UNIVERSIDADE D
COIMBRA

Carlos Alberto de Oliveira Henriques

STUDIES OF XENON MIXTURES WITH MOLECULAR ADDITIVES FOR THE NEXT ELECTROLUMINESCENCE TPC

Tese no âmbito do Doutoramento em Engenharia Física, ramo de Instrumentação, orientada pela Doutora Cristina Maria Bernardes Monteiro e pelo Doutor Luís Manuel Panchorrinha Fernandes, apresentada ao Departamento de Física da Faculdade de Ciências e Tecnologia da Universidade de Coimbra.

Dezembro de 2018

Faculty of Sciences and Technology

STUDIES OF XENON MIXTURES WITH MOLECULAR ADDITIVES FOR THE NEXT ELECTROLUMINESCENCE TPC

Carlos Alberto de Oliveira Henriques

Ph.D. thesis in Physics Engineering, in the field of Instrumentation, performed under scientific guidance of Dr. Cristina Maria Bernardes Monteiro and Dr. Luis Manuel Panchorrinha Fernandes, presented to the Physics Department of the Faculty of Sciences and Technology of the University of Coimbra.

December of 2018

UNIVERSITY OF COIMBRA

The research reported in this thesis was performed with financial support from the following institutions and programs:

- PhD grant number PD/BD/105921/2014 from Fundação para a Ciência e Tecnologia.
- Project PTDC/FIS-NUC/2525/2014 from Fundação para a Ciência e Tecnologia.

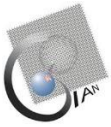

RESUMO

A eventual deteção do decaimento beta duplo sem emissão de neutrinos ($\beta\beta0\nu$) provará que não existe distinção entre neutrinos e antineutrinos, permitindo ainda calcular as suas massas. Esta descoberta poderá revolucionar a física de partículas, conduzindo a avanços para além do estabelecido no Modelo Padrão. A experiência NEXT pretende detetar o decaimento $\beta\beta0\nu$ do isótopo ^{136}Xe utilizando uma câmara de projeção temporal (TPC) baseada em eletroluminescência (EL), com enchimento a xénon a alta pressão. A discriminação eficiente de eventos de fundo através da sua topologia dos mesmos é crucial para a experiência, em virtude do elevado tempo de meia vida deste decaimento. Esta técnica apresenta limitações, principalmente devido à elevada difusão dos eletrões no xénon, a qual poderá ser reduzida pela adição de pequenas quantidades de gases moleculares, de modo a arrefecer os eletrões. Em contrapartida, o rendimento de EL é deteriorado e a resolução em energia poderá ficar comprometida. O trabalho bem como os resultados expostos nesta tese avaliam o impacto da adição de CO_2, CH_4 e CF_4 no rendimento de EL e na resolução em energia intrínseca, utilizando para esse fim um contador gasoso proporcional de cintilação (GPSC). A partir da análise da forma da onda à saída do foto-sensor, é possível compreender os processos físicos que ocorrem dentro do detetor, e estimar alguns parâmetros relacionados com a cintilação e o transporte de eletrões, tais como a probabilidade de cintilação, a captura de eletrões pelas moléculas, as flutuações na produção de cargas primarias e fotões de EL, a velocidade de deriva e a difusão longitudinal dos eletrões. Foi realizado um estudo sistemático de alguns destes parâmetros para várias concentrações de aditivos, as quais foram medidas utilizando um analisador de gases residuais (RGA). A comparação entre os três aditivos é efetuada tendo em conta as concentrações que permitem obter difusões semelhantes, de acordo com as simulações. O CF_4 demonstrou ter o menor impacto no número médio de fotões de EL produzidos por evento, mas com grandes flutuações relativas, devido à elevada captura de eletrões. Por outro lado, o CH_4 originou a maior redução do rendimento de EL, mas com flutuações relativas desprezáveis. Estes resultados foram ainda usados para extrapolar a resolução em energia da TPC do NEXT, onde o CH_4 demonstrou ter o melhor desempenho, e CF_4 o pior. Assumindo que o campo elétrico reduzido na zona de deriva é 20 V/cm/bar e a pressão é 10 bar (ou 15 bar), então a dispersão tridimensional dos eletrões por metro de deriva será 2.3 mm (ou 1.8 mm), com uma concentração de 0.37 % de CH_4, o que degrada ligeiramente a resolução de 0.33 % para 0.42 % (ou 0.38 %). O CH_4 mostrou ser bastante estável, ao contrário do CO_2 que reage com o sistema de purificação do gás.

PALAVRAS-CHAVE: Decaimento beta-duplo sem emissão de neutrinos, deteção de eventos raros, câmara de projeção temporal, contador gasoso de cintilação proporcional, cintilação, difusão de eletrões.

ABSTRACT

The detection of the neutrinoless double-beta ($\beta\beta0\nu$) decay might confirm that neutrinos are their own antiparticles and provide their absolute masses. Such breakthrough would have a profound impact on particle physics, bringing a new energy scale beyond the Standard Model. The NEXT experiment aims at searching for the $\beta\beta0\nu$ decay from the ^{136}Xe isotope, using a high-pressure xenon electroluminescence (EL) Time Projection Chamber (TPC). Given the long half-life of the $\beta\beta0\nu$ decay, efficient discrimination of background events through ionization tracks imaging is a major requirement for the experiment. However, it is mainly limited by the large electron diffusion in xenon. Sub-perceptual concentrations of molecular gases might be enough to cool down electrons, improving the TPC position resolution. On the other hand, the EL yield drops, and the energy resolution (ER) could be compromised. In this thesis the impact of CO_2, CH_4 and CF_4 on the EL yield and on the intrinsic energy resolution of xenon is evaluated using a driftless gas proportional scintillation counter (GPSC). The underlying dynamics of the driftless GPSC are accessed through the analysis of the photosensor waveforms, allowing estimating several fundamental parameters related with the scintillation mechanism and electron transport, such as the scintillation probability, electron attachment, fluctuations on the production of primary charges and EL photons, electron drift velocity and longitudinal electron diffusion. A systematic study has been carried out for several additive concentrations, measured with a Residual Gas Analyser (RGA). The comparison between the three additives is done for concentrations that reduce equally the electron diffusion according to simulations. The lowest impact on the mean number of EL photons produced per event was found to be for Xe-CF_4 mixtures, but with the largest relative fluctuations resulting from the high dissociative electron attachment. On the other hand, CH_4 showed the strongest impact on the EL yield due to the high quenching of xenon excited states, but fluctuations in the photon production remain as negligible as in pure xenon. The energy resolution achievable in the NEXT-100 TPC for each additive concentration was extrapolated based on these results, CH_4 presenting the overall best performance and CF_4 the worst. Assuming a reduced electric field in the drift region of 20 V/cm/bar and a gas pressure of 10 bar (or 15 bar), the 3-dimentional electron spread per drifted meter may be reduced down to 2.3 mm (or 1.8 mm), which is close to the thermal limit, with a CH_4 concentration of 0.37 %, resulting in a modest degradation of the energy resolution from 0.33 % to 0.42 % (or 0.38 %). From the technical point of view, CH_4 exhibited stability, while CO_2 was found to be very reactive with the gas purification system.

KEYWORDS: Neutrinoless double beta decay, rare event detection, Time Projection Chamber, Gas Scintillation Proportional Counter, scintillation, electron diffusion.

ACKNOWLEDGEMENTS

I would like to acknowledge to everyone who supported me along this thesis, especially to my supervisors **Luís Fernandes**, **Cristina Monteiro** and **Juan José Gómez-Cadenas**. I thank them for the trust they have put in me, and for the freedom they gave me to develop this work by myself, which I consider to be essential to my personal and professional progress.

To **Luís** for his openness, advice and patience during this journey. I am also very grateful for the guidance during abroad missions, and for the careful revision of this dissertation, largely improving its quality.

To **Cristina** for her orientation, teaching and availability every time I needed assistance, including reviewing the present dissertation. I thank her for having always faith in me to carry out the proposed PhD program.

To **Juan José** for giving me the opportunity to work on this project and to be part of the NEXT collaboration. Pursuing a common goal has been enormously motivating to me.

I would like to thank professor **Joaquim dos Santos** for the countless discussions, advice and feedback over the past years. Most of what I learned during my PhD thesis was taught by him. I am also grateful for his detailed review of this dissertation.

I acknowledge **Diego González-Díaz** for his persistent support and mentoring, especially in the theoretical realm. He always encouraged me to be more ambitious in the experimental method, in order to assess as much useful information as possible. Moreover, he provided simulation results that were indispensable to reach the general overview of the present work.

I would like to thank **Carlos Azevedo** for the many simulations he performed for the project. His work served as initial motivation for this thesis, and was crucial to sustain the experimental results, allowing to draw many of the conclusions presented here. I am also grateful for his guidance along the last years.

A sincere thanks you all my colleagues from GIAN for their friendship and willingness to help, especially the ones who contributed actively to the present thesis, **Elisabete Freitas** for her pioneer work in this field, and for transmitting me her expertise, **Daniel Mano** for his valuable instruction in the beginning of this work, **Pedro Silva** for the help in the experimental setup assembly, and to **Andreia Fernandes,** who worked exclusively in this project during the last two years, I am deeply grateful for her commitment, contribution and organization skills.

I would like to express my gratitude to **GIAN** for giving me the scientific knowhow and resources to develop this project. The spirit of mutual help and good working environment I found here were certainly decisive.

I acknowledge the **NEXT** collaboration for integrating me in their team. Here, I had the opportunity to meet inspiring and wise individuals. It has been an amazing experience to be part of such a large experiment, where I learned so much about multidisciplinary coordination. I am particularly grateful to **Neus March** with whom I had the opportunity to work closer; she always made me feel part of the team.

To all those who supported me during the last years and made this thesis possible, a warm hug. To my friends for their priceless companionship, to my family for their unconditional love, and to my parents, **Maria** and **José**, for their sacrifices which brought me here.

Last but certainly not least, I thank **Daniela Sousa** for all the love, tenderness and everlasting support.

CONTENTS

LIST OF ABBREVIATIONS AND ACRONYMS

CF_4	Tetrafluoromethane
CH_4	Methane
CL	Confidence level
CO_2	Carbon dioxide
DP	Number of detected photons
EL	Electroluminescence
E/p	Reduced electric field
ER	Energy Resolution
F	Fano Factor
FWHM	Full width at half maximum
GPSC	Gaseous Proportional Scintillation Counter
HPXe	High pressure xenon
MCA	Multichannel analyser
PMT	Photomultiplier tube
ROI	Region of interest
S1	Primary scintillation signal
S2	Secondary scintillation signal
SiPM	Silicon photomultiplier
SM	Standard Model
SP	Scintillation probability
TPC	Time Projection Chamber
VUV	Vacuum ultraviolet
WIMP	Weakly interacting massive particle
Xe	Xenon
Y	Electroluminescence yield
Y/p	Reduced electroluminescence yield
ββ0ν	Neutrinoless double beta decay
ββ2ν	Two-neutrino double beta decay

INTRODUCTION

Time Projection Chambers (TPCs) are able to image the three-dimensional tracks produced by ionizing particles. This technology has been recently employed and committed in many frontier physics large scale experiments [1], mostly based on rare-event detection, such as double-beta decay [2–5], dark matter WIMP direct detection [6–9] and directional detection of galactic WIMP signals [10, 11]. One such experiment is NEXT-(Neutrino Experiment with a Xenon Time Projection Chamber), to search for the ^{136}Xe neutrinoless double-beta ($\beta\beta0\nu$) decay using a high-pressure xenon (HPXe) electroluminescence (EL) TPC [12].

The detection of the $\beta\beta0\nu$ decay could solve some of the most important open questions in physics. The occurrence of this hypothetical process proves that the neutrino is truly a neutral particle, i.e. indistinguishable from its antiparticle. Such breakthrough implies the existence of a new energy scale in particle physics, beyond the Standard Model, which would boost our understanding of the mechanism of symmetry breaking, the origin of mass and the flavour problem. The $\beta\beta0\nu$ decay violates the leptonic number conservation law, providing an explanation for the matter-antimatter asymmetry observed in the universe, through the so-called leptogenesis process [13].

The present half-life limit of the ^{136}Xe $\beta\beta0\nu$ decay is ~10^{26} years (about 10^{15} longer than the universe age) [14]. Therefore, the large-scale technology implementation and the discrimination of background events are the biggest challenges in this kind of experiments. HPXe electroluminescence TPCs, as the one developed by the NEXT collaboration, offer two crucial advantages in background discrimination when compared to liquid Xe TPCs, i.e. good energy resolution (0.5-0.7 % FWHM in the region of interest, $Q_{\beta\beta}$ = 2.45 MeV) and the visualization of the unique topological signature of a double beta decay [2].

In such large HPXe TPCs, the spatial resolution is mostly limited by the diffusion of electrons in xenon, resulting from the reduced amount of energy lost in elastic collisions. This is a serious constraint for the NEXT topology-based background discrimination efficiency [15]. Doping xenon with a molecular gas could reduce the mean kinetic energy of electrons

and, hence, their diffusion, as new energy transfer channels are made available (i.e. low energy vibrational or rotational states). However, this kind of solution is also known to considerably degrade the EL yield and the energy resolution [16, 17]. Yet, a compromise might exist between the spatial resolution improvement and the energy resolution degradation, so that the overall sensitivity of the NEXT TPC to the ^{136}Xe $\beta\beta0\nu$ half-life is maximized. This is the main motivation of the work described in the present dissertation.

A driftless Gaseous Proportional Scintillation Counter (driftless GPSC) was used to evaluate the impact of CO_2, CH_4 and CF_4 additives on the Xe secondary scintillation yield and respective fluctuations. These studies were carried out at pressures of about 1.2 bar and the Xe admixtures were excited by means of a 5.9-keV x-ray beam. The molecular additive concentrations were measured in real-time through a Residual Gas Analyser (RGA). The driftless GPSC provides estimates for several parameters related to the scintillation and electron transport mechanisms, enabling the accurate extrapolation of our detector performance to other detector specifications, such as the NEXT-100 TPC. The ultimate goal of this experimental work is to find the additive, and its respective concentration, for which the electron diffusion can be significantly decreased with a minimal degradation of the energy resolution.

In chapter 1, basic concepts of the $\beta\beta0\nu$ decay physics are introduced. The state of the art is summarized, with special a focus on the NEXT experiment. The concept of the NEXT TPC is described, along with the main results already obtained with several NEXT prototypes.

In chapter 2, the main physical and instrumental constraints of the NEXT TPC spatial resolution are itemised. Then, some theoretical concepts behind the electroluminescence mechanism and electron transport are introduced, including the impact of molecular additives. Finally, some of the few experimental and theoretical studies reported in the literature regarding this subject are discussed.

In chapter 3, the full RGA system, designed and assembled especially for this work, is presented. The main technical difficulties that were found are discussed, such as the high gaseous backgrounds inside the RGA chamber, the reading dependence on room temperature, and the CO_2 reactiveness with the gas purification system. Finally, the method used to calibrate the RGA, to subtract the background, and to measure the concentration of the three additives during the driftless GPSC operation, is described.

In chapter 4, the driftless GPSC design and operation are described, including the two data acquisition systems used along this work. Subsequently, the undesirable effect produced in the results by the x-ray penetration in the GPSC, arising from the driftless nature of our detector, is presented.

In chapter 5, the waveforms produced by the detector's photosensor are analysed. This study was motivated by the need for an accurate method to correct the x-ray penetration effect

in former data. The organization of the waveforms according to their duration discloses the driftless GPSC underlying dynamics and operation.

In chapter 6, a new methodology based on the shape of the waveforms is proposed to improve the energy resolution of the driftless GPSC, minimizing the x-ray penetration effect. Several radioactive sources are used to characterize this technique which is, then, validated though the comparison of the results, including the intrinsic energy resolution, with those obtained with standard instrumentation, as well as with other results reported in the literature.

In chapter 7, some proof-of-concept techniques developed to estimate scintillation and electron transport related parameters are described, including the attachment coefficient, scintillation probability, longitudinal electron diffusion and electron drift velocity, this being possible only after a deep understanding of the GPSC waveforms. Some simple simulations were performed to interpret the results which are, in turn, compared with Magbotz simulations and with theoretical approximations found in the literature. These new parameters are crucial to understand the impact of molecular additives on the NEXT TPC performance.

In chapter 8, the response function of the driftless GPSC when it is combined with standard instrumentation is constructed. Two response functions with different levels of complexity are developed based on the knowledge acquired in chapters 4, 5, 6 and 7. In this way, a better estimate for the intrinsic fluctuations in the EL production can be obtained from the data, where the x-ray penetration effect is sizable.

In chapter 9, the EL performance of our GPSC is reported for several concentrations of CO_2, CH_4 and CF_4 additives. These experimental results were acquired before the studies described in chapters 5, 6, 7 and 8, but those were necessary to access some fundamental parameters, such as the scintillation probability and the relative fluctuations in the EL photon production.

In chapter 10, the results obtained in chapter 9 are extrapolated considering the NEXT TPC specifications, for several working conditions. The simulations and results reported in chapter 7 are here employed to properly scale the experimental data. Based on the figure of merit, we debate the several advantages and disadvantages of each molecular additive, from both the technical and the physical point of view. Finally, the best additive candidate for the NEXT experiment is identified, as well as the concentrations of interest.

The work developed in this thesis, especially the results reported in chapters 9 and 10, produced two publications in international peer-reviewed journals:

- NEXT Collaboration, C. A. O. Henriques *et al*., "Secondary scintillation yield of xenon with sub-percent levels of CO2 additive for rare-event detection," *Phys. Lett. B*, vol. 773, pp. 663–671, (2017)

- NEXT Collaboration, C. A. O. Henriques *et al*., "Electroluminescence TPCs at the thermal diffusion limit," *JHEP* (accepted) http://arxiv.org/abs/1806.05891

and four oral communications in scientific conferences:

- C. A. O. Henriques *et al*., "Secondary scintillation of xenon with sub-percent concentrations of molecular additive (CO2, CH4 and CF4) for HPXe optical TPCs", *Eighth International Symposium on Large TPCs for low-energy rare event detection*, Paris, France, (2016)
- C. A. O. Henriques *et al*., "Secondary scintillation yield and energy resolution for xenon with molecular additives (CO2, CH4 and CF4)", *Joint Iberian Meeting on Atomic and Molecular Physics (IBER)*, Barcelona, Spain, (2017)
- C. A. O. Henriques *et al*., "Secondary scintillation yield and energy resolution of Xe-CO2/CH4/CF4 mixtures for the NEXT electroluminescence TPC", *Light detection in noble elements (LIDINE)*, Stanford, California, USA, (2017)
- (RD51 collaboration meeting) C. A. O. Henriques *et al*., "Xe-Mx mixtures for the NEXT EL TPC", *18th RD51 Collaboration Meeting*, Aveiro, Portugal, (2016)

The results presented in chapter 9 were also used to develop and validate the theoretical model described in:

- NEXT Collaboration, C.D.R. Azevedo, D. González-Díaz, S.F. Biagi, C.A.B. Oliveira, C.A.O. Henriques *et al*., "Microscopic simulation of xenon-based optical TPCs in the presence of molecular additives," *Nucl. Instrum. Methods Phys. Res. A*, vol. 877, pp. 157–172, (2018)

Additional publications are planned to be submitted, presenting the techniques developed in chapter 7, and the results obtained for pure xenon and xenon admixtures, namely the attachment coefficient, scintillation probability, longitudinal electron diffusion and electron drift velocity.

1 NEUTRINOS AND NEXT

The neutrino is an elementary particle with half-integer spin, a lepton. In contrast to other leptons (e.g. electrons), neutrinos only interact by means of the weak force and gravity, making them hard to detect. Therefore, neutrinos remain a mystery in modern physics. Their existence was firstly proposed to explain the continuous energy distribution of the beta decay, otherwise, both momentum and energy conservation laws would be violated.

There are neutrinos of three flavours: electron neutrinos ν_e, muon neutrinos ν_μ and tau neutrinos ν_τ, associated to electron, muon and tau particles, respectively. There is a corresponding antiparticle for each neutrino, the antineutrino. In the Standard Model of physics (SM), neutrinos are assumed to be massless, as no right-handed neutrinos (i.e. the linear momentum having the same direction as the spin) have ever been observed.

1.1 Neutrino oscillations

Neutrino oscillation experiments have demonstrated that neutrinos oscillate between their flavors during their flight, which is only possible if each flavor has a different mass. In this framework, the flavor eigenstate is in fact a linear superposition of three mass eigenstates. Therefore, it has been unambiguously proven that neutrinos have a non-zero mass, in contrast to the SM prediction [18].

Despite the success of neutrino oscillation experiments, they are only sensitive to the squared differences of the three mass eigenstates m_i, remaining the absolute mass scale unknown. Solar and reactor experiments have measured the so-called solar mass splitting ($\Delta m^2_{sol} = m_2^2 - m_1^2$), while atmospheric and accelerator-based experiments have measured the so-called atmospheric mass splitting ($|\Delta m^2_{atm}| \equiv |m_3^2 - (m_1^2 + m_2^2)/2|$). The flavour content of each neutrino mass eigenstate can be estimated from these two experimental data sets [19]. Accordingly, two possible ordering of the mass eigenstates may exist, the so-called *normal hierarchy* (m_3 being the heavier mass) and *inverted hierarchy* (m_2 being the heavier mass).

This discovery has risen a number of fundamental questions about the neutrino nature. All other fermions in the SM (e.g. quarks and charged leptons) have their mass described by one Dirac mass term alone. However, the neutrino being chargeless, it could have an additional Majorana mass term, providing a simple explanation for its lightness (in contrast to other particles) through the seesaw mechanism [20]. The Majorana nature of neutrinos could lead to processes in which the lepton number would not be conserved. The possibility of such violation, together with the Charge-Parity (CP) violation in the lepton sector might explain the observed cosmological asymmetry between matter and antimatter (through leptogenesis) [21].

1.2 Neutrinoless double beta decay

A possible way to experimentally verify if neutrinos are Majorana particles and what is their absolute mass scale, would be the detection of the neutrinoless double beta decay.

Predicted in 1935 [22], the regular double beta ($\beta\beta 2\nu$) decay, i.e. two simultaneous beta decays with emission of two antineutrinos ($(Z, A) \rightarrow (Z + 2, A) + 2e + 2\bar{\nu}_e$) may occur when the parent nucleus is less bound than its daughter, and both nuclei are more bound than the intermediate $Z + 1$ nucleus, for which the transition is forbidden. Such condition is fulfilled by 35 nuclides in nature, although as a second order weak process, leading to an extremely low decay rate. For this reason, it has only been detected in 1950 [23], and directly observed in a TPC in 1987 [24]. Since then, $\beta\beta 2\nu$ decay has been observed for several nuclides, such as ^{76}Ge, ^{100}Mo, ^{130}Te or ^{136}Xe, with measured half-lifes typically of the order $10^{18} - 10^{21}$ years [13].

On the other hand, the neutrinoless mode of the double beta decay ($(Z, A) \rightarrow (Z + 2, A) + 2e$) has never been observed experimentally, although it was proposed already in 1939 [25]. In this decay, the antineutrino emitted by one neutron is absorbed as a neutrino by the other neutron. Consequently, the sum of the kinetic energies of both emitted electrons (K_e) is approximately equal to the total energy released in the nuclear transition (Q), allowing to distinguish both decay modes by measuring the energy of the electrons.

The distributions of K_e/Q produced by $\beta\beta 2\nu$ and $\beta\beta 0\nu$ are illustrated in figure 1, considering a detector energy resolution of 5 % [26]. The importance of the energy resolution in these measurements is demonstrated in the top right corner of the same figure. Since the $\beta\beta 0\nu$ mode is much more infrequent than the $\beta\beta 2\nu$, only an exceptional energy resolution could make the small peak of the $\beta\beta 0\nu$ distinguishable from the $\beta\beta 2\nu$ tail. More information about $\beta\beta 0\nu$ and related experiments can be found in the reviews [27–33].

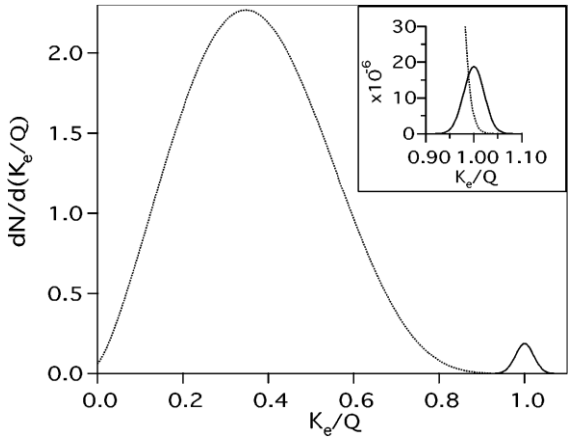

Figure 1: Illustration of the K_e/Q spectra produced by both decay channels. The ββ2ν spectrum area is normalized to the unit (dotted curve), while the ββ0ν spectrum is normalized to 10^{-2} (10^{-6} in the top right corner plot). All spectra are convoluted with an energy resolution of 5 % [26].

1.3 Decay rate of ββ0ν

From the theoretical point of view, the ββ0ν decay can occur through any mechanism where the lepton number is violated, for instance emitting one or two Majorons (hypothetical bosons), or being mediated by the exchange of heavy Majorana or sterile neutrinos. However, the simplest mechanism in which ββ0ν is mediated by a virtual exchange of light Majorana neutrinos is usually considered to be dominant at low energies [34]. Accordingly, the ββ0ν half-life ($T_{1/2}^{0\nu}$) is given by equation (1) [13, 35]:

$$(T_{1/2}^{0\upsilon})^{-1} = G_{0\upsilon}\,|M_{0\upsilon}|^2\,m_{\beta\beta}^2 \tag{1}$$

where $G_{0\nu}$ is the phase-space factor that depends on the energy of the decay ($Q_{\beta\beta}$) and on the nuclear charge (Z), $|M_{0\nu}|$ is the nuclear matrix element (NME), which has to be evaluated theoretically, and $m_{\beta\beta}$ is the effective Majorana mass of the electron neutrino, given by equation (2) [13, 35]:

$$m_{\beta\beta} = \left|\sum_i U_{ei}^2\, m_i\right| \tag{2}$$

where m_i are the neutrino mass eigenstates, and U_{ei}^2 are the elements of the neutrino mixing matrix.

While $G_{0\upsilon}$ can be analytically computed with accuracy, only approximated estimates exist for $|M_{0\nu}|$, where results from different nuclear models can vary by a factor of 2 to 4, [35]. An additional uncertainty comes from the dependence of the NME on the square of the axial-vector coupling constant, g_A. When g_A is estimated from the ββ2ν measured half-lives, it tends to decrease from its vacuum value g_A ~1.27 down to ~0.8 [36]. If the same happens

in the ββ0ν decay, experimental constraints on $T_{1/2}^{0\nu}$ could translate into $m_{\beta\beta}$ 6 to 34 times lower than currently assumed [30].

According to equation (1), the experimental measurement of $T_{1/2}^{0\nu}$ provides direct assessment of $m_{\beta\beta}$. On the other hand, if ββ0ν is not found for a given $T_{1/2}^{0\nu}$ sensitivity, the result is taken as the upper limit for $m_{\beta\beta}$. This measurement combined with the results from oscillation experiments enables the determination of the absolute neutrino mass eigenstates (m_1, m_2 and m_3), through equation (2) (albeit with sizable uncertainties from nuclear and neutrino physics).

Figure 2 shows $m_{\beta\beta}$ as a function of the lightest m_i (m_1 in the normal ordering, or m_3 in the inverted one), considering the two possible hierarchies. The regions limited by the black dotted curves represent the 3σ constraints imposed by the neutrino oscillation parameters (intervals are computed from the variation of the complex phases). The shadowed areas (inverse hierarchy in green and normal hierarchy in red) include the constraints in $\sum m_i$ coming from cosmological observations, for different confidence levels (1σ, 2σ and 3σ) [32].

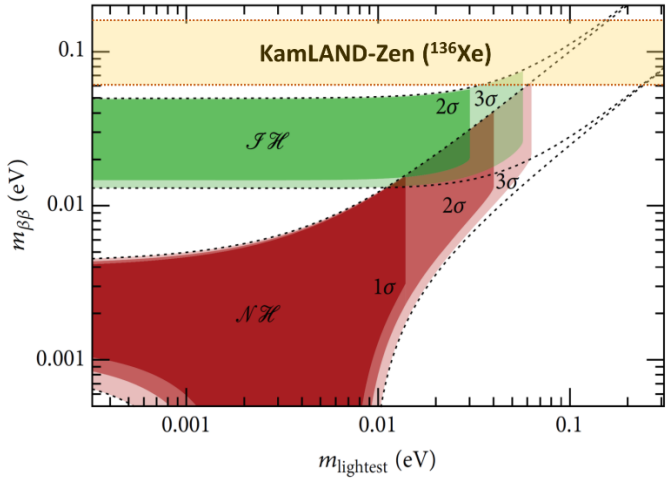

Figure 2: $m_{\beta\beta}$ as a function of the lightest m_i, considering the 3σ constraint imposed by the neutrino oscillation parameters, delimited by dotted curves. The shadow areas (green for the inverted hierarchy, and red for the normal hierarchy) include the $\sum m_i$ boundaries coming from cosmological observations for different confidence levels. The yellow band presents the current experimental $m_{\beta\beta}$ upper limit, established by the KamLAND-Zen experiment [14]. The figure was adapted from ref. [32].

1.4 State of the art on ββ0ν detection

The sensitivity of a ββ0ν experiment to $m_{\beta\beta}$ is directly proportional to $(b\Delta E/Mt)^{1/4}\,\varepsilon^{-1/2}$, where b is the background rate, ΔE is the energy resolution, Mt is the exposure (i.e. the data acquisition time interval multiplied by the mass of the ββ emitting isotope), and ε the signal detection efficiency [12, 37]. A good energy resolution is essential to distinguish ββ0ν against

ββ2ν, or other background sources, while b must be kept as low as possible, forcing the underground operation of the detector, which has to be shielded and constructed from carefully selected radiopure materials. The scalability to larger masses and long term stable operation are other important factors that increase the sensitivity of the experiment.

Naturally, the simultaneous optimization of all these parameters is very difficult. Therefore, many distinct experimental techniques have been exploited during the last decade, each of them having advantages and disadvantages. In the following paragraphs, the major experimental achievements in the ββ0ν detection are highlighted.

KamLAND-Zen consists of a balloon with 13 tons of xenon liquid scintillator (320 kg of xenon enriched to 91 % in isotope ^{136}Xe) surrounded by Photomultiplier Tubes (PMTs). The energy resolution and background within the $Q_{\beta\beta}$ region is about 9.9 % and $1 \times 10^{-3}\ cts/(keV \cdot Kg \cdot yr)$, respectively [38]. The current $m_{\beta\beta}$ upper limit is held by the KamLAND-Zen collaboration, corresponding to 61-165 meV ($T_{1/2}^{0\nu} > 10.7 \times 10^{25}\ yr$) [14]. This boundary is also presented in figure 2.

EXO-200 is a symmetric liquid xenon (LXe) TPC, deploying 110 kg of active xenon (enriched to 80.6 % in isotope ^{136}Xe). EXO uses the ratio between primary scintillation and ionization signals to discriminate alpha events, and the TPC tracking capability to discriminate gamma Compton multi-site events. The energy resolution is about 3.9 % and the background about $1.5 \times 10^{-3}\ cts/(keV \cdot Kg \cdot yr)$ [39]. Thus far, the $m_{\beta\beta}$ upper limit is 190-450 meV ($T_{1/2}^{0\nu} > 1.1 \times 10^{25}\ yr$) [5].

GERDA uses germanium diodes with a total mass of 35 kg (enriched to 86-88 % in the isotope ^{76}Ge), which serve as both ββ0ν source and detector. This technology provides an excellent energy resolution, 0.20-0.28 %, and can discriminate multi-site background events based on the signal pulse shape, achieving a background of $1 \times 10^{-3}\ cts/(keV \cdot Kg \cdot yr)$. Recent data establishes a $m_{\beta\beta}$ upper limit of 120-260 meV ($T_{1/2}^{0\nu} > 8 \times 10^{25}\ yr$) [40].

MAJORANA Demonstrator comprises 44.1 kg of Ge detectors (29.7 kg enriched in isotope ^{76}Ge). The main difference with respect to GERDA is the ultra-pure cooper innermost shielding. Recently, a $m_{\beta\beta}$ upper limit of 240-520 meV ($T_{1/2}^{0\nu} > 1.9 \times 10^{25}\ yr$) was reported [41].

CUORE-0 is based on the bolometric technique, using a total fiducial mass of ~11 kg of non-enriched Te (^{130}Te has a natural abundance of ~35 %,). TeO_2 crystals are cooled down to 10-15 mK with helium, inside a multi-layer copper cryostat. The energy deposited by ββ0ν is registered as temperature increments by thermistors, enabling to reach an impressive energy resolution of 0.20 %. Combining data from CUORE-0 and its predecessor, CUORICINO, an $m_{\beta\beta}$ upper limit of 110-520 meV has been currently established ($T_{1/2}^{0\nu} > 1.5 \times 10^{25}\ yr$) [42].

Up to now, a wide range of experimental techniques have been exploited, leading to different systematic errors. Data from different experiments can be combined in order to improve the $m_{\beta\beta}$ upper limit. In 2015, an upper limit for $m_{\beta\beta}$ in the region of (83.7-157.1) meV was obtained using data from ^{76}Ge, ^{100}Mo, ^{130}Te and ^{136}Xe sources [43]. Since then, KamLAND-Zen [14] and GERDA [40] have brought important advances to the field. As shown, the current generation of ββ0ν experiments is still far from the full coverage of the inverted hierarchy. Over the last few years, the scientific community has been investing huge resources in research and development of the next ββ0ν experiments, aiming to cover entirely the inverted hierarchy region (down to $m_{\beta\beta}$ ~15-20 meV). Such detectors require larger exposure times (with masses within the ton scale), lower backgrounds, a good energy resolution and preferably additional techniques to discriminate background events.

Some of the most promising upcoming experiments are: nEXO, an upgrade of EXO-200, although deploying 5 ton of enriched liquid Xe [44]; KamLAND-Zen 800, a ~750 kg upgrade of the actual 320 kg of xenon [45]; SNO+, consisting of 780 ton of liquid scintillator doped with natural Te [46]; Super-NEMO, using foils of source material (100 kg of ^{82}Se) and magnetized tracking volumes on both sides [47]; AMoRE, using the technique of cryogenic scintillating bolometers to detect ββ0ν in 200 kg of $^{40}Ca^{100}MoO_4$ crystals [48]; LUCIFER/CUPID, a collaboration between the LUCIFER and CUORE projects to develop an upgrade of CUORE-0, with particle identification capabilities [49]; NEXT-100, consisting of a HPXe TPC (100 kg of enriched xenon) with electroluminescence readout, providing an excellent energy resolution and background rejection based on event topology [12]; and PandaX-III, similar to NEXT, but with charge readout, known as Microbulk Micromegas [3].

1.5 The NEXT experiment

The present work has been developed under the NEXT collaboration, hence particular focus needs to be put on the NEXT experiment. NEXT intends to search for ββ0ν of the isotope ^{136}Xe using an electroluminescence TPC filled with 100 kg of enriched xenon gas at 10-15 bar, the NEXT-100 TPC. This detector has three key features when compared with the competitors: good energy resolution (ER), lower than 1 % Full Width at Half Maximum (FWHM) at $Q_{\beta\beta}$; the ability to track the ββ0ν decay, enabling active rejection of background; and the possibility to scale the technology to large masses [2, 12, 50]. NEXT-100 is foreseen to start operations in 2019, in the Laboratorio Subterráneo de Canfranc (LSC), Spain [51]. Since 2016, LSC hosts a 1:2 prototype of NEXT-100, called NEXT-White (NEW). The NEXT collaboration comprises institutions from Spain, Portugal, USA, Russia, Israel and Colombia.

In this section, the NEXT-100 concept is introduced, and a brief description of the prototypes and the archived results are presented.

1.5.1 The NEXT concept

The use of xenon in the ββ0ν research has some advantages over other elements. Being a noble gas, its enrichment and continuous purification is relatively easy and cheap. The energy released in the ^{136}Xe ββ decay is high, $Q_{\beta\beta} = 2458$ keV, which is advantageous as the decay rate of the ββ0ν mode is faster at high energies, and the background is generally lower. In addition, the decay rate of the ββ2ν mode is slow, $\sim 2.3 \times 10^{21}\ yr$, contributing, thus, less to the background [38, 52].

Xenon can act at the same time as the source and the detection medium, as is the case of the EXO LXe TPC. However, a HPXe TPC can reach a much better energy resolution (ER), due to the lower Fano factor (i.e. the relative variance in the number of primary electrons produced per event), which is about 0.15, much lower than the value ~20 for LXe [53]. On the other hand, a HPXe TPC requires a larger volume to contain the same mass as a LXe TPC. In the NEXT TPC, the amplification of the ionization signal produced by ββ0ν is performed through electroluminescence processes. EL has been chosen due to the negligible contribution to ER, in contrast to electron avalanche amplification [54]. Therefore, the expected ER in NEXT-100 is about 0.5-0.7 % FWHM (intrinsic limit ~0.3 %), well below the ER values reported by the two main Xe-based competitors of NEXT, EXO-200 and KamLAND-zen which present ER values of 3.9 % and 9.9 %, respectively [2].

Another advantage of a HPXe TPC is the possibility to reconstruct the ββ0ν event topology, whose track is acceptably long, about 15 cm at 15 bar. When electrons (with energy < 12 MeV) move through xenon gas, they lose energy by ionizing and exciting the Xe atoms at an approximately fixed rate, until they become non-relativistic [55]. Afterwards, the electron effective energy loss (dE/dx) increases, producing a blob at the end of the ionization track. Therefore, the signature of a double beta emission consists of a single track with two blobs at the ends, allowing to distinguish it from the single electron produced by a background gamma with the same energy. In figure 3, two simulated topologies are shown, one being produced by ββ0ν decay and the other one by a single electron with the same energy; the identification of the blobs is also presented. This background discrimination technique (using deep neuronal networks) may yield a suppression factor of about ~11 (~21 with enhanced electron diffusion), while the ββ0ν sensitivity is kept at ~80 % [15].

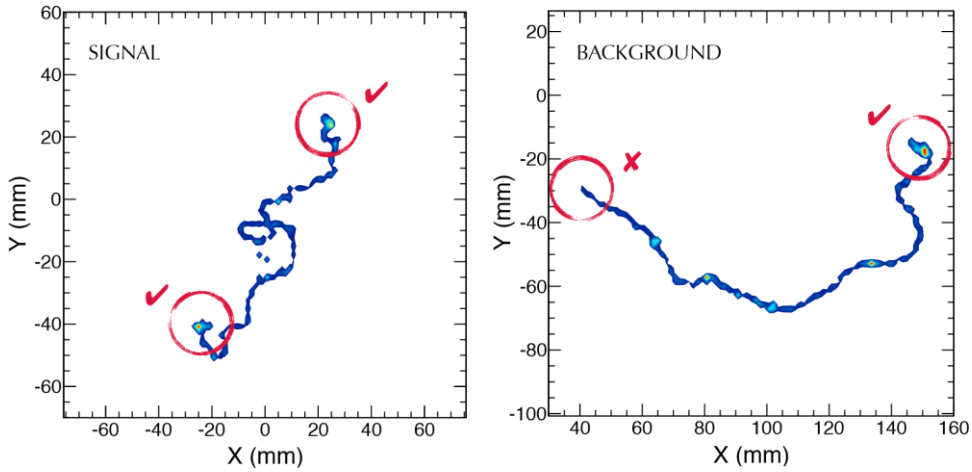

Figure 3: Monte Carlo simulation of the ionization tracks produced by ββ0ν decay, on the left, and a background event consisting of a single electron with the same energy, on the right. A xenon pressure of 15 bar was assumed. The detected blobs are identified [15].

In the NEXT TPC, tracking and energy measurements are both provided by the electroluminescence signal. However, two different optical readouts optimized for each function are used, the tracking plane consisting of a 1-cm pitch array of silicon photo-multipliers (SiPMs), and the energy plane formed by large-window PMTs. This concept is known as SOFT (Separated, Optimized Functions) and is presented in figure 4, together with the main components of the NEXT TPC.

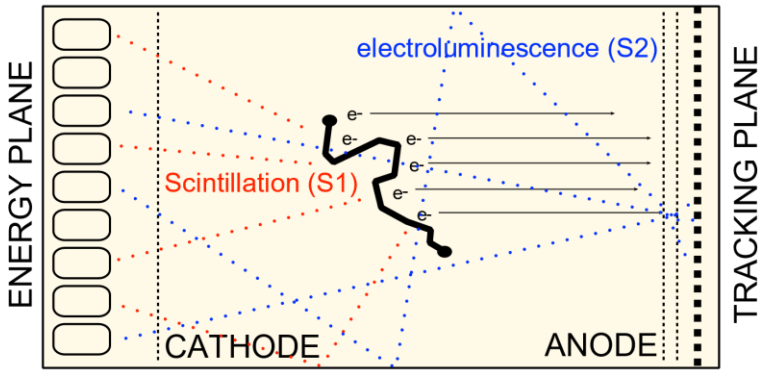

Figure 4: Conceptual presentation of the NEXT TPC. On the left, the energy plane consisting of PMTs. On the right, the tracking plane consisting of an array of SiPMs. During an event, primary scintillation (S1) and a track of electrons are released. S1 is detected on the energy plane, establishing the start-of-event. Electrons are guided towards the EL region, where the secondary scintillation signal (S2) is produced. S2 is detected on both the tracking and the energy plane, rendering the topology and energy of the event, respectively [15].

The detection process (schematically depicted in figure 4) can be described as follows. At first, interacting particles deposit their energy in the medium, ionizing and exciting Xe atoms along their path, leading to the production of VUV scintillation photons (around 172 nm). This first scintillation signal (S1) is recorded by the PMTs in the energy plane, establishing the start-of-event (t_0). A weak electric field is set between the cathode and the

gate electrodes, in order to prevent the track ionization charges from recombining and to guide the electrons to the EL region (i.e. the small gap between the gate and the anode electrodes). In this region, they are accelerated through a stronger electric field, producing EL photons, while the secondary ionization is kept negligible. This secondary scintillation signal (S2) is recorded on both the energy and the tracking plane. The first one provides an accurate measurement of the total energy released in the event, while the second one provides the two-dimensional image of the ionization track, since the SiPMs array is positioned just behind the EL region. The coordinate along the electric field is computed from t_0 (knowing the electron drift velocity), allowing full 3-dimentional topology reconstruction. A more detailed description of the NEXT TPC operation can be found in the conceptual design report [56].

1.5.2 The NEXT-100 TPC

The NEXT-100 TPC deploys 100 kg of Xe at 15 bar in a cylindrical active volume of approximately 1.15 m^3. External radiation is prevented from reaching the detection region by means of a 20-cm thick lead castle and by a 12-cm thick copper shield. The energy plane is formed by 60 PMTs (Hamamatsu R11410-10), sealed into individual vacuum-tight copper enclosures coupled to sapphire windows, positioned behind the cathode (coverage area of about 30 %). The tracking plane includes 7100 square SiPMs of 1 mm^2 (1792 SensL C series), positioned in a 1-cm pitch array.

An open-ended high-density polyethylene (HDPE) cylindrical shell surrounds the active volume, providing structural stiffness and electric insulation. The drift region, 106-cm thick and 107-cm in diameter, is limited by two highly transparent stainless-steel wire meshes, the cathode and the gate. The EL gap, 5-mm thick, is limited by the gate and a fused-silica window, 1-cm thick and conductive due to an indium tin oxide coating, which separates the EL gap from the SiPMs. A reduced electric field (i.e. the electric field divided by the gas pressure) of 0.03-0.05 and 2-3 kV/cm/bar is set in the drift and in the EL region, respectively.

To improve the light collection efficiency, most of the TPC's inner surfaces are coated with a wavelength shifter, tetraphenyl-butadiene (TPB), which converts the xenon VUV light into blue light, around 440 nm, corresponding to the peak sensitivity of SiPMs. Areas covered by TPB include the side ring structure, the fused silica window in front of the SiPMs, and the sapphire windows in front of the PMTs. Additional technical details can be found in [50], or in more recent references [2, 12, 57].

The major background events expected to fall within the $Q_{\beta\beta}$ region in NEXT-100 are 2447 keV gammas and Compton electrons resulting from 2614 keV gammas, produced by ^{214}Bi and ^{208}Tl, respectively, both being found in the detector materials. Another significant source of these two isotopes is radon (isotopes ^{222}Rn and ^{220}Rn), which is difficult to control

due to its gaseous nature. More information on background prediction and experimental measurements are found in [12, 58–61].

Despite using radio-pure materials and background shielding, NEXT-100 takes advantage of background discrimination techniques. Only events taking place far from the walls and with a double-blob and a single-track topology are considered as potential ββ0ν decay events. In this way, the most part of the background is rejected, as well as the ionization tracks that were partially lost to the walls or distorted by local electric field non-uniformities in that region.

Combining these rejection factors with the theoretical background model and direct screening of materials, a background rate lower than $5 \times 10^{-4}\ cts\ keV^{-1}Kg^{-1}\ yr^{-1}$ is expected in NEXT-100 [12, 58]. Therefore, a sensitivity to $T_{1/2}^{0\nu}$ of $6 \times 10^{25}\ yr$ should be achieved after running for 3 effective years. This corresponds to $m_{\beta\beta} < (67 - 187)\ meV$ [12].

1.5.3 NEXT prototypes

During the last years, the NEXT collaboration has developed an extensive R&D program in order to study and demonstrate the concept of NEXT-100. In this section, some of the most important prototypes that have been used or are currently in use are described.

1.5.3.1 NEXT- DBDM

Operating at the Lawrence Berkeley National Laboratory, in USA, NEXT-DBDM is a small chamber (8 cm in the drift region) without tracking capabilities, employing ~1 kg of Xe, which was used mostly for energy resolution studies, and characterization of neutrons in HPXe. At 15 bar, an energy resolution of 1 % (FWHM) was measured with 662-keV gammas, extrapolating to 0.5 % at $Q_{\beta\beta}$ (assuming dominance of Poisson statistics) [62].

1.5.3.2 NEXT-DEMO

NEXT-DEMO is a small TPC similar to NEXT-100 operating at Instituto de Física Corpuscular (IFIC), Valencia, Spain. The pressure vessel is 60 cm long and 30 cm in diameter, containing 1-2 kg of xenon at a maximum pressure of 15 bar. Featuring the SOFT concept (19 PMTs in the energy plane and 256 SiPMs coated with TPB in the tracking plane), NEXT-DEMO demonstrated being able to achieve a good energy resolution value of 1.62 % at 511 keV, which extrapolates to 0.74 % at $Q_{\beta\beta}$ [63], and background discrimination based on topology recognition, where the two-blob track was mimicked by electron-positron pairs created from 2614 keV gammas (from ^{208}Tl), while the background was mimicked by single electrons produced from 1275 keV gammas (from the ^{22}Na chain) [64]. Together with these

achievements, DEMO showed a good operational performance, with no leaks and only a few sparks, as well as a long electron lifetime (larger than 10 ms) [65].

1.5.3.3 NEXT-White

The NEXT-White (NEW) is a ~1:2 scaled prototype of NEXT-100 (~50 cm thick drift region), with about 20 % of the photosensors (12 PMTs and 1792 SiPMs), containing ~10 kg of Xe in the active volume at 15 bar. It is operating at LSC since 2016. The main objectives of NEW are the in-situ measurement of background and $\beta\beta2\nu$ with full event reconstruction, validating the background model and the technology chosen for NEXT-100. In preliminary tests, NEW has shown a good and stable performance, with an acceptable electron lifetime close to 2 ms (although after several weeks of continuous gas purification) [66]. A good linearity within approximately 1 % (between 30-1592 keV) and a good energy resolution of 1 % extrapolated to $Q_{\beta\beta}$ were recently established. Nonetheless, a significant improvement of the energy resolution in near future is foreseen [67]. Recent measurements of the radon background and electron transport parameters in NEW can be found in [51, 68].

1.5.4 Future prospects for NEXT

The HPXe EL TPC developed by NEXT has the potential to become the most sensitive detector at this scale. Nevertheless, in order to cover the entire inverted hierarchy (figure 2), NEXT-100 technology needs to be upgraded to the ton mass scale, also improving the efficiency of the background rejection methods. New ideas currently being investigated or developed are described in the following paragraphs.

Perhaps the most viable upgrade of the NEXT TPC in the near feature relies on the reduction of the electron diffusion to improve the spatial resolution and, consequently, the topology-based background discrimination efficiency. A possible way to accomplish this comprises the addition of a small amount (concentration lower than 1 %) of a molecular gas to Xe, thus reducing the mean kinetic energy of drifting electrons, this being the subject of the present work. As an alternative, helium could be used to reach the same goal, though a larger amount will be required (concentrations of 10-20 %). Both approaches have been actively investigated and developed by the NEXT collaboration [16, 17, 69–72].

Under a moderate magnetic field, $\beta\beta$ electrons produce a double helix track, while single electrons produce a single helix track. This additional topological information may improve the background rejection by one order of magnitude [57]. However, there are some technical issues in the implementation of this technique, such as the incompatibility of a magnetic field with PMTs, requiring their replacement by SiPMs.

A more ambitious way to discriminate the $\beta\beta$ decay against the background is through the in-situ detection of its daughter product, Ba^{++}. This might be achieved using a technique

known as single molecule fluorescence imaging (SMFI). The molecule typically consists of a dye bonded to a receptor that traps the barium ion, becoming fluorescent. It can be subsequently detected with an electron multiplying CCD (EM-CCD), after emission and excitation light being separated via dichroic filters. Recently, the NEXT collaboration demonstrated the single Ba sensitivity using this methodology [68].

2 MOLECULAR ADDITIVES IN XENON

One of the key features of the NEXT detector is the ability to reconstruct the topology of events. The characteristic signature of ββ decays, consisting of a single track with two blobs at both ends is used to reject the background events, whose tracks have usually a single blob at one end. The effectiveness of this method is determined by the TPC position resolution, which can be improved adding molecular gases to xenon to reduce the electron diffusion. Unfortunately, such technique may lead to a significant degradation of scintillation parameters of the NEXT TPC, and consequently deteriorate the energy resolution.

In this chapter, we summarize some of the theoretical concepts behind the additive role in the electron diffusion and the scintillation process, as well as the state of the art on these studies.

2.1 Tracking limitations in the NEXT TPC

The position resolution of an optical EL TPC is determined by either physical or instrumental constraints. For the latter, we consider the readout technology currently used in NEXT-White, i.e. a 6 mm long EL gap placed 5 mm away from the 10-mm pitch SiPMs array [66].

The spatial distribution in the plane transverse to the drift direction for a point-like energy deposition in the gas is affected by the light spread and the SiPMs pitch. A simulation of the point spread function projected on the tracking plane due to isotropic light emission was performed, including light reflections, resulting in a 3.8 mm RMS spread [72], while the upper limit on the mean bias in transverse position reconstruction is ~2.9 mm ($pitch/\sqrt{12}$), assuming no light sharing between neighbouring SiPMs. Nonetheless, this value can be considerably reduced taking advantage from the SiPMs light sharing (e.g. the local barycentre technique, allowing a resolution of ~1 mm [63]) and more elaborate algorithms [73].

Ultimately, the transverse resolution could be improved, for example, decreasing the SiPMs pitch or the distance between the EL region and the tracking plane.

The longitudinal resolution depends on the time between the start-of-event, provided by the primary scintillation signal (S1), and the arrival-time of electrons to the EL region, provided by the secondary scintillation signal (S2). The spread introduced by the uniform light emission over the 6 mm wide EL gap is expected to be about 1.7 mm RMS, being hard to improve significantly this value in a large TPC, due to the difficult reduction of the EL gap. Finally, there is an additional contribution coming from the photo-detector waveform sampling in the TPC time domain. However, this effect should be less than a 0.3 mm mean bias in the longitudinal position reconstruction [72].

On the other hand, the effect of the electron diffusion in pure Xe might even overcome these instrumental constraints. For instance, transverse and longitudinal spreads of about 10 mm and 4-5 mm are expected, respectively, after electrons drift one meter in Xe, under a drift-like electric field [51]. Therefore, the effectiveness of the background discrimination based on the events topology is mostly limited by the large electron diffusion in Xe. This effect is demonstrated in figure 5, where two events, a ββ0ν (top left) and a ^{214}Bi gamma (bottom left) are reconstructed, considering either a 2-mm (middle) or a 10-mm diffusion spread (right).

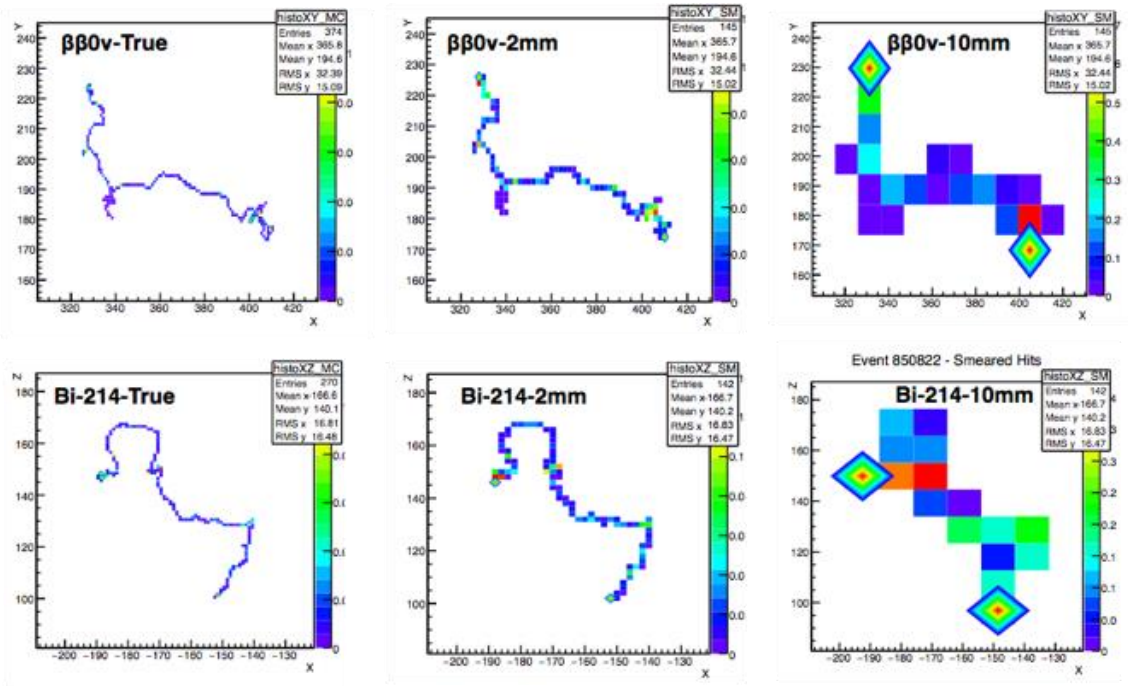

Figure 5: Impact of the electron diffusion on the NEXT TPC tracking performance. Two simulated events are shown, a ββ0ν on the top, and a ^{214}Bi background gamma on the bottom. From the left to the right, the true event topology, the event reconstruction after 2 mm electron spread, and the event reconstruction after 10 mm spread (expected for 1 m drift in pure Xe).

Some of the original track details are still visible for a 2 mm spread, such as the two blobs in the ββ0ν and the single blob in the background event. On the other hand, the topology

reconstruction is significantly degraded after electrons drift 1 m in pure Xe (i.e. for a 10 mm spread), leading to the inaccurate identification of background events.

In a recent study of the NEXT collaboration, where deep neuronal networks were used to discriminate background events, the background acceptance was found to decrease from 6.6 % to 2.5 % when voxels of 2 × 2 × 2 mm^3 are used rather than 10 × 10 × 5 mm^3, which is only possible if the electron diffusion is reduced down to same level [15]. In addition, the signal efficiency is increased from 66.7 % up to 69 %. This improvement may shorten considerably the time required to reach a given $T_{1/2}^{0\upsilon}$ sensitivity. For instance, a 9 $years \cdot ton$ exposure is needed to achieve $T_{1/2}^{0\upsilon} = 5 \times 10^{26}\ years$, but if the electron diffusion is enhanced to the $2mm/\sqrt{m}$ level, the same could be accomplished in only 3 $years \cdot ton$ [15]. Therefore, reducing the large electron diffusion in pure Xe is one of the main goals of the NEXT experiment.

2.2 Electron diffusion with molecular additives

Due to the small mass of electrons, they scatter isotropically while moving in a gas. The electron energy follows the Maxwell energy distribution, since they are in thermal equilibrium with the medium. Accordingly, their motion can be described by a mean instantaneous velocity *v*, given by $\varepsilon = mv^2/2 = 3kT/2$, where ε is the mean energy of electrons, *m* their mass, *T* the temperature and *k* the Boltzmann constant), and an isotropic diffusion coefficient *D*. Assuming a Gaussian density distribution, $\sigma_x^2 = \sqrt{2Dt}$, where σ_x is the mean squared deviation of electrons, and *t* is the elapsed time.

When an electric field is applied, in addition to the random thermal velocity *v*, electrons begin to drift according to the electric field direction with a mean drift velocity *u*, where *u* is much smaller than *v*. In these conditions, diffusion is no more isotropic, and there is a coefficient for longitudinal diffusion D_L, i.e. along the electric field, which can be quite different from the transverse diffusion coefficient D_T. Besides the dependence of ε on the thermal energy ($3kT/2$), ε is also affected by the electric field intensity, since electrons are accelerated between collisions (ε is determined by the balance between the energy lost in collisions and energy gained between them). More detailed information on electron transport in gas under electric fields, and the relevance of the electron diffusion and velocity in TPCs can be found in [74–77].

In noble gases, drifting electrons with ε below ~8 eV suffer only elastic collisions with the atoms, as demonstrated by the cross sections of the several available energy transfer channels with Xe, depicted in figure 6. The fraction of energy ($\delta\varepsilon/\varepsilon$) that is lost by an electron (with mass m) through an elastic collision with a Xe atom (with mass M) is approximately given by $2mM/(m+M)^2$, which corresponds to only $\sim 10^{-5}$, since m is much smaller than

M. Consequently, electrons keep their average kinetic energy high, leading to a large diffusion, in particular for low reduced electric fields (E/p, where p is the gas pressure). Naturally, under strong fields, inelastic collisions may occur, through the excitation or ionization of Xe atoms. However, these processes are not desirable inside the drift region of a TPC. Therefore, E/p is kept below the ionization and excitation thresholds, being high enough to prevent the electron-ion recombination (in NEXT, E/p is in the 20-50 V/cm/bar range).

On the other hand, electrons may transfer a significant amount of energy in inelastic collisions with molecules, whose vibrational or rotational states are available even for low energy electrons. This property is also demonstrated in figure 6, where the electron scattering cross sections of CH_4 are represented [17]. In this example, the first vibrational state can be already excited for ε of about 0.2 eV.

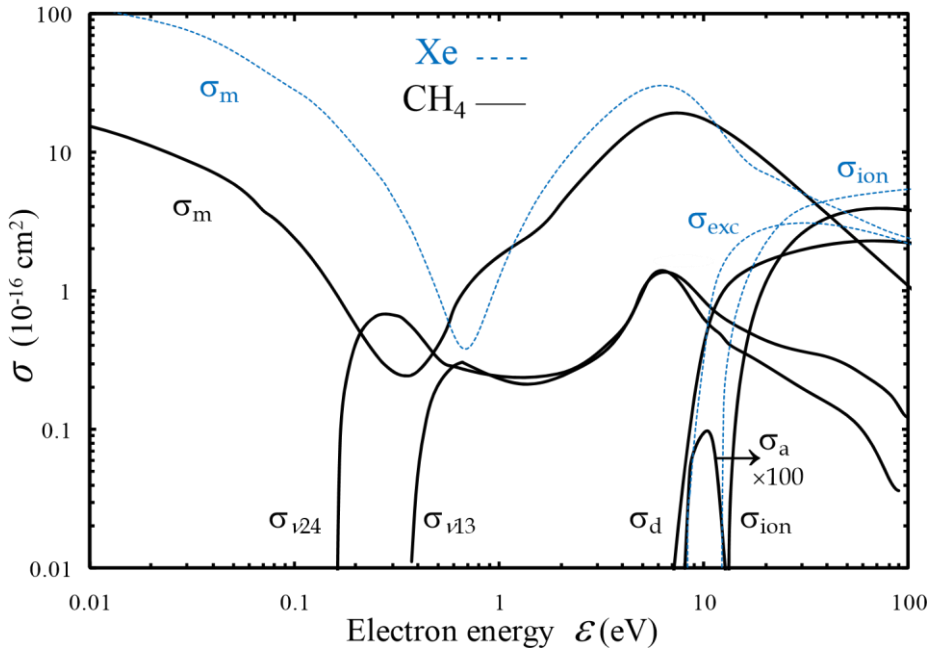

Figure 6: Electron scattering cross sections for pure Xe and CH_4, obtained from Monte Carlo simulations: elastic momentum transfer (σ_m), vibrational excitation (σ_v), electron attachment (σ_a), neutral dissociation (σ_d), electronic excitation (σ_{exc}), and ionization (σ_{ion}). The electron-xenon elastic cross section (σ_m) presents a minimum near 1 eV, known by Ramsauer-Townsend minimum.

Despite the cross sections for elastic collisions being generally higher with respect to the inelastic ones, the large amount of energy transferred in the latter provides an efficient electron cooling, even using sub-perceptual concentrations of a molecular gas in xenon. In mixtures, the electron energy distributions become mildly non-thermal, tending to build up around the energy of the first vibrational level of the molecule. Consequently, the longitudinal and transverse diffusion coefficients are significantly smaller. On the other hand, the drift velocity can be maximized by adjusting the electric field, so that ε approaches the so-called Ramsauer-Townsend minimum of the Xe elastic cross section.

In figure 7, the simulated transverse (a) and longitudinal (b) diffusion (in units of spread per root square of the drifted path length), as well as the drift velocity (c), are plotted as a function of the additive concentration, for Xe-CF_4, Xe-CO_2 and Xe-CH_4 mixtures.

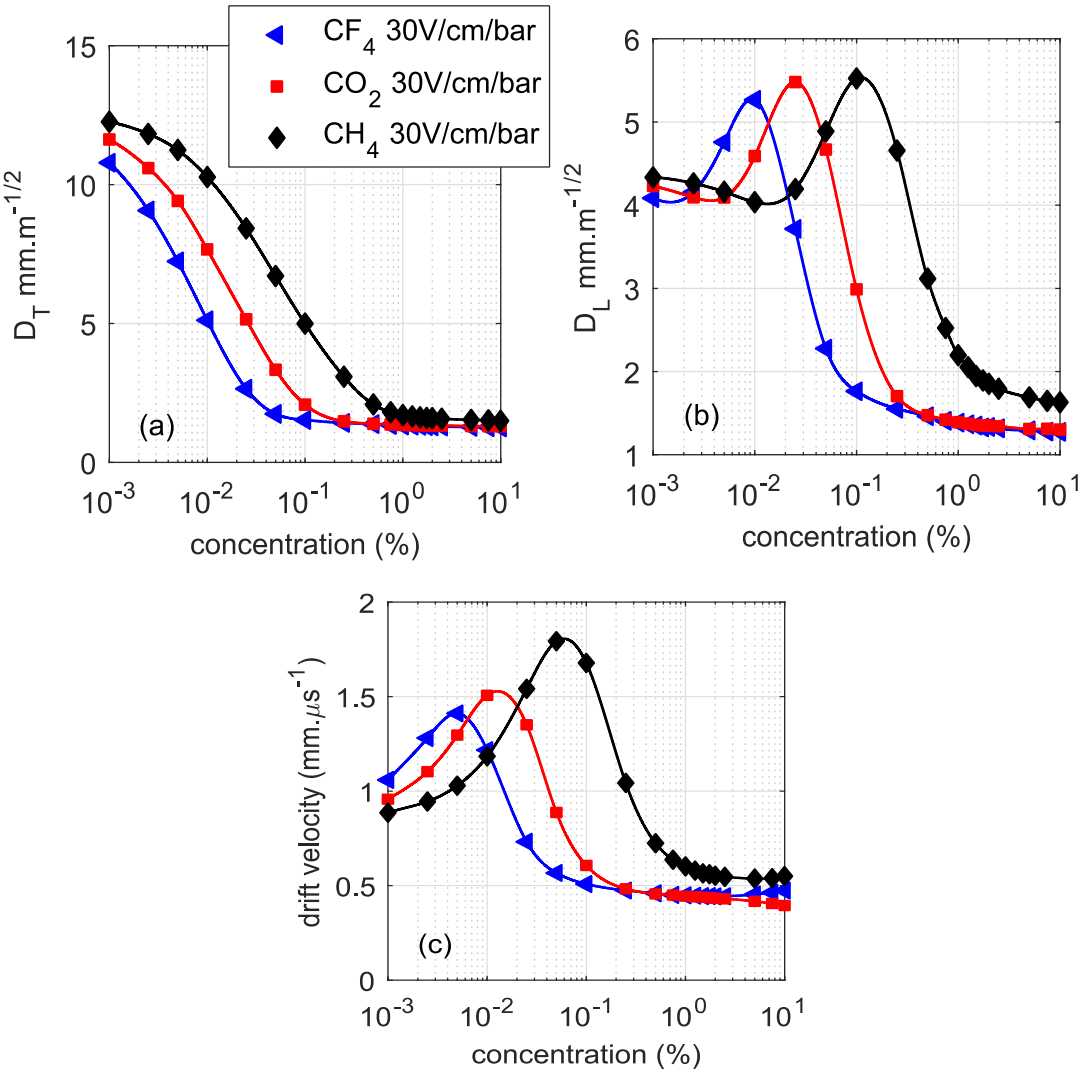

Figure 7: Transverse (a) and longitudinal (b) diffusion (spread per root square of the drifted path length) and drift velocity (c) of electrons as a function of the additive concentration, obtained from Magboltz simulations for Xe-CO_2, Xe-CF_4 and Xe-CH_4 mixtures, under a drift reduced electric field of 30 V/cm/bar, and a pressure of 10 bar.

According to the simulation predictions of figure 7, the electron diffusion could be decreased down to the 2 mm level, with only 0.04 %, 0.1 % and 0.6 % of CF_4, CO_2 and CH_4 additives, respectively. The drift velocity is approximately doubled when compared to pure xenon for concentrations of about 0.005 %, 0.01 % and 0.06 % of CF_4, CO_2 and CH_4, respectively, but it falls below the pure xenon drift velocity for higher concentrations. Therefore, an electron diffusion of a few mm seems to be incompatible with a good drift velocity. Nevertheless, this may not be problematic for the NEXT TPC, as the detection rate is low. On the other hand, molecular additives are also known to degrade significantly the performance of electroluminescence-based detectors, even for such minute concentrations.

2.3 Scintillation with molecular additives

In this section, the effects that molecular additives may have on the scintillation production are summarized. There are two scintillation signals of interest in the NEXT TPC, primary scintillation (S1), produced during the radiation interaction by highly energetic charges, and the secondary scintillation (S2), produced in the electroluminescence region by the drifting electrons. S1 is used as a start-of-event trigger and must remain detectable, while S2, which is more intense than S1, provides information on the event energy, thus fluctuations in this signal should be as low as possible.

2.3.1 Primary scintillation and ionization

When the xenon gas is crossed by energetic charged particles, atoms are either ionized or excited. These processes also occur when electromagnetic radiation (x-rays and gammas) interacts with the gas, since high energy electrons are usually produced (e.g. a photoelectron is emitted by a Xe atom upon absorbing an x-ray). Despite the wide distribution of Xe excited states usually produced in those events, they cascade quickly to the lowest lying metastable $^3P_2$ and resonant $^3P_1$ states [70].

At pressures above a few tens of mbar [78], the main channel of de-population of these excited atoms (Xe^*) is through the formation of excimers (Xe_2^{**}), in three-body collisions with xenon atoms (Xe), as described by equation (3):

$$Xe^* + Xe + Xe \rightarrow Xe_2^{**} + Xe \quad (3)$$

For pressures above 400 mbar, Xe_2^{**} loses their high vibrational energy mostly upon collisions with a ground state atoms [79]:

$$Xe_2^{**} + Xe \rightarrow Xe_2^{*} + Xe \quad (4)$$

Finally, the lower vibrational states, Xe_2^* ($^1\Sigma_u^+$ and $^3\Sigma_u^+$, with characteristic lifetimes of (5.5 $\pm$ 1) ns and (96 $\pm$ 5) ns, respectively [80]) decay emitting a scintillation photon ($h\nu$):

$$Xe_2^{*} \rightarrow Xe + Xe + h\nu \quad (5)$$

These photons form a vacuum ultraviolet (VUV) continuum, the so-called *second continuum*, centered at 172 nm, with a FWHM of 14 nm [79].

In order to avoid the recombination of electrons an electric field is applied across the TPC drift region (E/p higher than ~5 V/cm/bar [81]), guiding the electrons to the signal amplification zone. Even so, recombination (geminate or columnar) may occur, especially within a high-density media (e.g. liquid Xe), or for particles with high energy loss per unit of path length. This process consists usually of the formation of a molecular ion in three body collisions ($Xe^+ + Xe + Xe \rightarrow Xe_2^+ + Xe$), and the thermalization of the electron through

excitations/ionizations and elastic collisions, allowing the dissociative recombination of both ($Xe_2^+ + e \rightarrow Xe^{**} + Xe$). After the resulting highly excited atom relax ($Xe^{**} \rightarrow Xe^* + heat$), the reactions of equation (3), (4) and (5) may occur, leading also to a VUV photon emission in the Xe second continuum [82]. In this way, the primary scintillation and the ionization signals are often anti-correlated. One may even take advantage from this property to improve the detector energy resolution, as recently demonstrated using the NEXT-DEMO with alpha particles [83]. However, the recombination is expected to be minimal in the NEXT experiment, due to the low ionization charge density generated in the beta emission.

The primary scintillation and ionization yields are usually quantified by w_s and w_i, which refer to the mean energy necessary to produce a VUV photon and an electron-ion pair, respectively. A value $w_i = 22 \pm 1$ eV was obtained using either x-rays, gammas or electrons [84–86]. On the other hand, a large range in the experimental w_s value is reported in the literature, from 34 to 111 eV [70, 83, 87]. Generally, the lower values are obtained with alpha particles, and the higher ones with x-rays. The origin of this tendency is not fully understood.

Studies on the impact of molecular additives on primary scintillation are scarce. In ref. [88], the ionization and primary scintillation yields were measured with Xe-CH_4 mixtures at 26 bar, with concentrations in the 0.2-2 % range. A 50 % and 75 % relative reduction of the scintillation and ionization yields were found, respectively, with only 0.4 % of CH_4, for E/p = 25 V/cm/bar. Due to the use of alpha particles, charge recombination plays an important role in the results of both parameters, since the ionization yield was found to increase whereas the primary scintillation yield was found to decrease with the electric field.

The lower amount of charge produced in Xe-CH_4 mixtures is attributed to the higher probability of recombination, which could be promoted by the enhanced cooling of the electrons in the event track, while the reduction of the light yield is explained by the quenching of the Xe excited atoms by the CH_4 molecule. The quenching of the first Xe metastable level may occur through the following process:

$$Xe(^3P_2) + CH_4(^1S_0) \rightarrow Xe(^1S_0) + CH_4^* \quad (6)$$

Due to the large contribution of the charge recombination to the scintillation yield that was measured in that study, we cannot draw reliable conclusions about the quenching probability in Xe-CH_4 mixtures.

Additional quenching mechanisms besides the one presented in equation (6) may exist, such as the de-activation of Xe^* through a 3-body collision with Xe and CH_4, or the de-activation of Xe_2^* upon colliding with CH_4. The latter case leads to a significant increase of the quenching probability as higher the total gas pressure is. Additional information regarding these hypotheses can be found in the simulation studies reported in [17, 70] and references

therein. Nevertheless, the Xe excimer or atom quenching in mixtures needs to be evaluated experimentally, as well as its dependence on pressure.

The S1 signal can also be reduced in mixtures due to the low transparency of the additive to VUV photons, which is expected for instance in Xe-CO_2 mixtures. This is particularly important in large TPCs as the NEXT-100 one, where scintillation photons may travel long path lengths before reaching the photosensors. Other concern regarding the use of additives is the attachment in the drift region, especially in the case of electronegative molecules.

In the present work, we do not evaluate directly the impact of molecular additives on S1 or on the amount of ionization electrons. However, the accurate quantification of w_i or w_s in such conditions should be a priority in future experimental studies.

2.3.2 Secondary scintillation

When thermalized electrons drift under a strong electric field, they may acquire enough kinetic energy between collisions to excite the Xe atoms (when ε is higher than ~8 eV, as seen in figure 6). Because of the low energy of these electrons (when compared to the energy of the particle that produces the event track), Xe is predominantly excited in the lowest lying metastable $^3P_2$ and resonant $^3P_1$ states. Therefore, the same processes leading to the primary scintillation take place, as described by equations (3), (4) and (5). The subsequent emission of VUV photons in the Xe second continuum (~173 nm) is called secondary scintillation or electroluminescence (EL). There is also atomic emission of photons in the 820-885 nm range [89]. However, the VUV continuum is one order of magnitude more intense, and most of the photosensors are not sensitive within this range. Therefore, only the VUV second continuum is considered.

The energy lost by electrons in elastic collisions with Xe atoms is residual (due to the large difference between masses), hence EL is a very efficient process. In fact, about 95 % and 80 % of the energy gained by electrons from the electric field is spent exciting the Xe atoms, and producing VUV photons, respectively, for a E/p value of 4 kV/cm/bar [90, 91]. Nevertheless, this process becomes less efficient for E/p lower than 2 kV/cm/bar, being near zero for E/p below ~0.76 kV/cm/bar, which is known by the scintillation threshold [92]. Detailed information on the electroluminescence of Xe and other noble gases can be found in the following theoretical and experimental studies [79, 87, 90, 93–95].

2.3.2.1 Electroluminescence yield

One of the most relevant parameters that characterizes the EL process is the EL yield (Y), defined as the average number of VUV photons emitted per primary electron and per unit of drift length. The EL yield is usually represented as a function of the applied electric field (E). However, this relation depends on the atomic density of the gas (N, i.e. the number of atoms

per unit of volume) because the energy transferred from the electric field to electrons between collisions is higher as longer their mean free path is. For this reason, both parameters are usually normalized to N, thus, the relation between the reduced yield (Y/N) and the reduced electric field (E/N) is valid for any macroscopic conditions of the gas phase. For convenience, this normalization is sometimes performed to the gas pressure (p) instead. Nevertheless, in such cases, the gas temperature (T) should also be considered, as N depends on both T and p.

The amount of energy gained by electrons is directly proportional to the electric field, leading to an almost linear dependency of Y/p on E/p. The slight deviation from the linearity arises from the variation of the EL efficiency with E/p, which is sharper for E/p below ~2 kV/cm/bar. For E/p values above the ionization threshold Y/p grows exponentially with E/p.

The dependence of Y/p on E/p is represented in equation (7). This relation was derived based on an experimental study reported in [92], where a Xe driftless-GPSC was used, at 1.5 bar and 20 ºC. The scintillation and ionization thresholds were found to be about ~0.76 kV/cm/bar and ~4.6 V/cm/bar, respectively.

$$\frac{Y}{P}\left(\frac{photons}{electron \cdot cm \cdot bar}\right) = 140\,\frac{E}{p}\left(\frac{kV}{cm \cdot bar}\right) - 116 \tag{7}$$

The linear relations between Y/p on E/p found in other experimental works or using simulation show usually a good agreement with equation (7) [90, 92].

2.3.2.2 Energy resolution

Different sources of fluctuations contribute to the energy resolution of an EL-based detector, defined by $R_E = FWHM/C$, where $FWHM$ is full width at half maximum of a monoenergetic peak and C is its centroid. Since these contributions are statistically independent, they can be summed in quadrature, thus R_E is given by equation (8) [96]:

$$R_E = 2\sqrt{2\,ln\,2}\,\sqrt{\frac{\sigma_e^2}{\overline{N}_e^2} + \frac{1}{\overline{N}_e}\left(\frac{\sigma_{EL}^2}{\overline{N}_{EL}^2}\right) + \frac{\sigma_{pe}^2}{\overline{N}_{pe}^2} + \frac{1}{\overline{N}_{pe}}\left(\frac{\sigma_G^2}{\bar{G}^2}\right)} \tag{8}$$

where $2\sqrt{2\ln 2}$ is the relation between the $FWHM$ and the standard deviation (σ) for a Gaussian distribution. The first term inside the square root is related with fluctuations in the number of primary electrons produced per event (N_e), the second term is related to fluctuations in the number of EL photons produced per primary electron (N_{EL}), the third term is related to fluctuation in the number of photoelectrons extracted from the PMT photocathode per event (N_{pe}), and the fourth term is related to fluctuations in the number of electrons reaching the PMT collector per electron extracted from the photocathode (i.e. the PMT gain *G*).

Fortunately, fluctuations in primary charge generation are not purely statistical, leading to a relative variance lower than 1, as it would be expected from Poison statistics. The Fano factor ($F = \sigma_e^2/\bar{N}_e$) is often used to describe this characteristic of the detection medium. F has been experimentally and theoretically estimated in pure Xe, but results obtained are in a wide range, from 0.13 to 0.25 [85, 86]. $\bar{N}_e$ is given by $\bar{N}_e = E/w_i$, where E is the energy released in the event, an w_i is the average energy necessary to produce an ion-electron pair.

The fluctuations in the production of scintillation are usually described by the parameter Q given by equation (9).

$$Q = \left(\frac{\sigma_{EL}}{\bar{N}_{EL}}\right)^2 \tag{9}$$

It is also common to find the parameter $J = \sigma_{EL}^2/\bar{N}_{EL}$ in the literature, which is related with Q as $Q = J/\bar{N}_{EL}$.

The extraction of photoelectrons from the PMT photocathode by VUV scintillation photons is expected to follow a Poison distribution. Consequently, the variance on the number of photoelectrons is equal to the mean value, $\sigma_{pe}^2 = \bar{N}_{pe}$. The fluctuations in the charge multiplication gain of the PMT is typically described by $(\sigma_G/\bar{G})^2$, which is often assumed to be ~1, but it depends on the PMT and other technical specifications (e.g. bias voltage ripple). Naturally, $\bar{N}_{pe}$ is directly proportional to $\bar{N}_{EL}$ and $\bar{N}_e$, $\bar{N}_{pe} = k\,\bar{N}_e\,\bar{N}_{EL}$, where the proportionality constant k corresponds to the ratio between the number of EL photons detected and the number of EL photons produced. This parameter depends on several technical characteristics, for instance the PMT coverage area, the material reflectivity, the anode transparency, or the PMT photocathode quantum efficiency. Therefore, equation (8) can be simplified into equation (10) [96]:

$$R_E = 2\sqrt{2\,ln\,2}\,\sqrt{\frac{F}{\bar{N}_e} + \frac{Q}{\bar{N}_e} + \frac{1}{k\bar{N}_e\bar{N}_{EL}}\left(1 + \frac{\sigma_q^2}{\bar{G}_q^2}\right)} \tag{10}$$

In figure 8, R_E expected for the ββ0ν decay in NEXT-100 is plotted as a function of E/p, considering only the contributions represented in equation (10), for two possible k values, 0.005 and 0.06, and assuming $(\sigma_G/\bar{G})^2$, F, w_i and E_x to be 1, 0.15, 21.9 eV and 2.458 MeV, respectively, while $\bar{N}_{EL}$ comes from the simulated Y/p [96]. The three terms of equation (10) are also represented individually, being related to contributions of the Fano factor, Q factor and PMT.

In pure xenon, Q is expected to be negligible when compare to F, as demonstrated in figure 8 (purple curve). This is only valid up to an E/p value of ~4 kV/cm/bar, above which Q increases considerably, as Xe ionizations become relevant. On the other hand, the PMT contribution decreases with E/p, due to the larger $\bar{N}_{EL}$. Therefore, an optimal range of E/p

exists, for which the R_E value is minimized. Obviously, this depends on the relative importance of the photosensor contribution to R_E. In the example of figure 8, the optimal E/p falls in the range of 3-4 kV/cm/bar for $k = 0.06$, but it is about 5 kV/cm/bar for $k = 0.005$, due to the larger contribution of the PMT statistics. In the first case, R_E is almost flat within the optimal E/p range, since it is mostly limited by the Fano factor contribution that does not depend on the electric field.

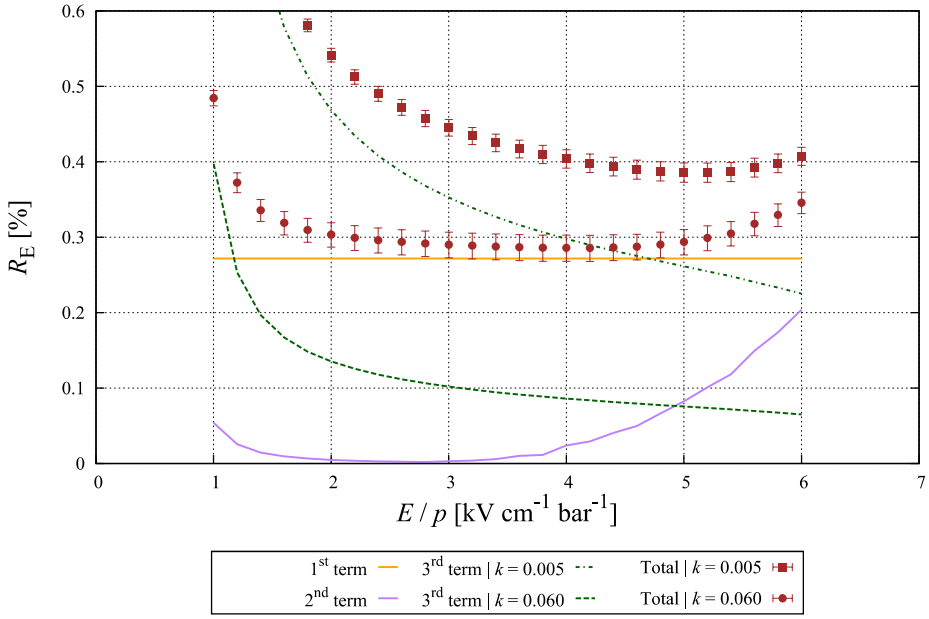

Figure 8: Energy resolution (R_E) expected for the ββ0ν decay in NEXT-100 as a function of E/p, obtained using equation (10), assuming k values of 0.005 or 0.06. The Fano factor, Q factor and PMT contributions are also represented individually. The figure was adapted from [96], where more details on the simulation could be found.

2.3.2.3 Impact of molecular additives

EL-related studies with minute concentrations of molecular additives in Xe are scarce, in addition to the preliminary experimental work developed in [97–100] and simulations performed for the NEXT experiment [16, 17, 70]. Nonetheless, the spectral EL response was measured with mixtures of argon with several molecular gases [101]. It was found that concentrations as low as 0.02 % of CH_4 and 0.004 % of CO_2 reduce the electroluminescence intensity by 70 % and 80 %, respectively, when compared to pure argon. This degradation was attributed to electron cooling and Ar excimer quenching. Other studies related with molecular additives in noble gases can be found, for instance, in [102, 103].

Historically, the reduction of the electron diffusion in noble gases provided by molecular additives has been assumed to be incompatible with the use of electroluminescence as amplification mechanism. However, a compromise may exist, for which the diffusion is improved, while the electroluminescence intensity is still maintained at acceptable levels. From this point of view, the Xe gas is gifted with a crucial feature with respect to argon, i.e.

the fast decay of the scintillation process, whose slower component ($^3\Sigma_u^+$) has a time constant of only ~100 ns, while the corresponding decay channel of argon has a much longer time constant ~3 μs [104]. This key aspect may lead to a smaller quenching probability in Xe mixtures, when compared to the results obtained with Ar [101].

As discussed in section 2.2, the mean kinetic energy of electrons is lower in the presence of molecular additives. Naturally, this cooling mechanism also affects the electron transport in the EL region. In order to produce the same EL yield as in pure Xe, a stronger electric field is required, thus compensating the energy loss to the vibrational or rotational excitations of molecules. This shift in the secondary scintillation threshold is intimately related with the electron diffusion reduction, hence being a necessary evil.

On the other hand, molecular gases show usually additional undesirable features, motivating our search for the additive and concentration where those are minimized. The EL signal intensity may be reduced through the quenching of Xe_2^* or Xe^* by the additive molecules, or as a result of the drop in the mixture transparency to VUV photons, like in the case of primary scintillation, as described in section 2.3.1. In addition, the dissociative attachment of electrons to the gas molecules may occur under EL-like electric fields, as this channel is only available for higher electron energies (e.g. figure 6). Consequently, the EL signal intensity is also reduced.

These mechanisms, i.e. electron cooling, quenching, gas transparency and attachment, contribute to the degradation of the TPC energy resolution, through the PMT contribution (because of the lower $\bar{N}_{EL}$, equation (10)) and the increase in the Q factor, especially in high attachment mixtures. The PMT contribution can be attenuated, for instance, by increasing the light collection efficiency (k), while the Q factor degradation is harder to avoid. Regarding the Fano factor contribution, it is not expected to change significantly when compared to pure xenon, in particular for low additive concentrations [17].

In a recent simulation study, the NEXT collaboration identified CO_2, CF_4 and CH_4 as promising additive candidates to reduce the electron diffusion, with an acceptable energy resolution compromise [16]. Previously, CF_4 and CH_4 were also proposed to be used in the NEXT-100 TPC [17]. The anticipated characteristics of the three molecules are distinct, the quenching in CH_4 is the largest and the attachment is the lowest, the opposite being expected for CF_4, while CO_2 is somewhere in the middle, with an additional low transparency to VUV photons. Yet, these EL degrading mechanisms needed to be verified experimentally. Therefore, the experimental study reported in the present document focuses on EL response of Xe doped with CO_2, CF_4 and CH_4 additives.

Additional operational issues must be taken into account in the molecular additive choice, for example the reactiveness of the molecular gas with the TPC materials or the gas purification system, handling risks and hazards to human life, the accuracy in the mixture

preparation and concentration monitoring, long term stability, or the recovery of the xenon after being mixed with the molecular gas. Some of these details were also investigated in the present study.

2.4 Gas Proportional Scintillation Counter

The Gas Proportional Scintillation Counter (GPSC) is an electroluminescence-based detector introduced by Policarpo and Conde in 1964 [105]. This device is commonly used in x-ray spectrometry, for energies up to 100 keV, in applications such as medical instrumentation, x-ray astronomy and high-energy physics. The key feature of this detector is the good energy resolution when compared to the conventional proportional counter, due to the absence of electron avalanche. In addition, it can provide high counting rates, large detection areas and reduced space charge effects.

The GPSC consists of a chamber containing usually a noble gas, with a drift region, where x-rays are absorbed, and an electroluminescence region, where the ionization electrons are accelerated in order to produce scintillation photons. The VUV photons are generally detected with a PMT, or an Avalanche Photodiode (APD). Energy resolutions near the Fano factor limit can be achieved, e.g. 8 % and 4 % for 5.9 keV and 22 keV, respectively. An extensive review of this technology can be found in ref. [95], and other relevant works can be found in [87, 92, 106–111].

The operating principle of an optical EL TPC is similar to the GPSC, except the lack of positioning capabilities in the latter. In the present study, a variant of the traditional GPSC was used, without drift region (driftless GPSC), to evaluate the impact of additives on the EL response of xenon. This detector has some advantages over the conventional GPSC for this kind of studies, as discussed in chapter 4.

3 THE RESIDUAL GAS ANALYZER

The present study searches for the optimal additive concentration for which the electron diffusion can be considerably reduced, keeping as much as possible the EL yield and energy resolution of the detector. Therefore, the concentrations that are tested must be accurately known. In the past, the additive concentration has been measured at the time it is prepared, using pressure gauges [97–100]. However, the measured EL yield with mixtures did not agree with simulation, raising the possibility of the additive concentration during the detector operation being different from the initial one, what is reasonable considering the minute additive concentrations used. A significant amount of additive could be absorbed or adsorbed by the many materials inside the detector, including hot getters used to purify the xenon gas. For this reason, a real-time gas monitoring system is crucial for the study here developed.

A Residual Gas Analyser (RGA) is a highly sensitive mass spectrometer, commonly used in the characterization of high vacuum systems, contamination and leak detection [112]. The RGA is usually composed by three main parts, the ionizer, the quadrupole mass-filter and the ion detector. A hot filament produces electrons, which are accelerated by an electric field (up to ~70 eV), and the gas molecules are ionized by electron impact. The ionized molecules are focused into the quadrupole, where a combination of radio-frequencies and static electric fields selects the mass-to-charge ratio of the ions, which can pass through the filter with stable oscillations. The number of surviving ions is measured by a very sensitive electrometer. Naturally, this process is only feasible in high vacuum, otherwise the hot filament would burn (in the presence of oxygen), or the ions would collide with the medium molecules before being collected. Therefore, the correct RGA operation is usually limited to a maximum total pressure of about 1×10^{-4} mbar. In order to analyse the gas inside a high-pressure chamber,

like in our detector, a minute amount of gas is sent into the RGA vacuum chamber, using for instance a capillary or a leak valve.

In this chapter, we describe the system used for the RGA sampling, calibration and preparation of mixtures. The gas background on the RGA side is characterized, either when pure Xe is sampled or when the chamber is in high vacuum. Some technical issues such as the influence of the room temperature on data are reported. The RGA is calibrated, and the methodology used to measure the driftless GPSC additive concentration is described, with some examples. Finally, the stability of the three additives and their compatibility with getters is discussed.

3.1 RGA sampling and gas mixing system

The electroluminescence studies were carried out at about 1.2 bar. The RGA used in this work (model RGA200 from Stanford Research Instruments) can be operated at pressures as high as 10^{-4} mbar. However, according to the manufacturer, linearity is only assured for pressures below 10^{-5} mbar. Therefore, the driftless-GPSC pressure needs to be reduced by a factor of 10^{8}. This large pressure differential is provided by a stainless-steel narrow capillary, which is strangled in one end, at the detector side, allowing the fine tuning of the gas flow rate.

The probability of a molecule to be ionized or cracked in the RGA ionizer depends on several factors, such as the mean kinetic energy of electrons. Even a small misalignment between the ionizer grids may have a severe impact on the RGA sensitivity or cracking pattern for a given gas. Indeed, we found relative differences larger than 50 % between the real concentrations and the ones computed from the manufacturer's gas sensitivity factors. We had also the opportunity to assemble another identically RGA (same model) in the same chamber. Despite the two RGAs being operated with the same settings, the uncalibrated concentration obtained with the new one for a Xe-CH_4 mixture was about 20 % higher than the first one. Therefore, a proper calibration of the RGA must be performed. Usually, each pure gas is introduced into the RGA chamber, being the total pressure measured with an independent vacuum gauge. However, this kind of calibration does not consider, for instance, the capillary conductance to different molecules. For this reason, two small volumes were assembled near the driftless GPSC, in order to calibrate the RGA in combination with the sampling system. The full gas system is depicted in figure 9.

The volume 2 (red box) is filled with xenon, while the volume 1 (green box) is filled with additive, both pressures being precisely measured by two capacitive pressure gauges. Then, the two volumes are joined and the valve between them is closed during a few seconds to measure the final pressure, since this valve modifies the sum of volumes when it is open. Finally, the additive concentration is estimated, according to the ideal gas law at a constant

temperature ($PV = nRT$, where P, V, n, T and R are the gas pressure, volume, number of moles, absolute temperature, and ideal gas constant). The amount of additive that may become adsorbed is assumed to be negligible, since the area of the calibration volumes is small, and there are not additional materials inside. Therefore, the RGA calibration is made using the concentration values calculated from the pressures at the time the mixture is prepared. The same capillary is used for the RGA calibration and the driftless GPSC sampling, thus eliminating the need for two identical capillaries. During the RGA calibration, the two volumes are isolated from the detector through a valve.

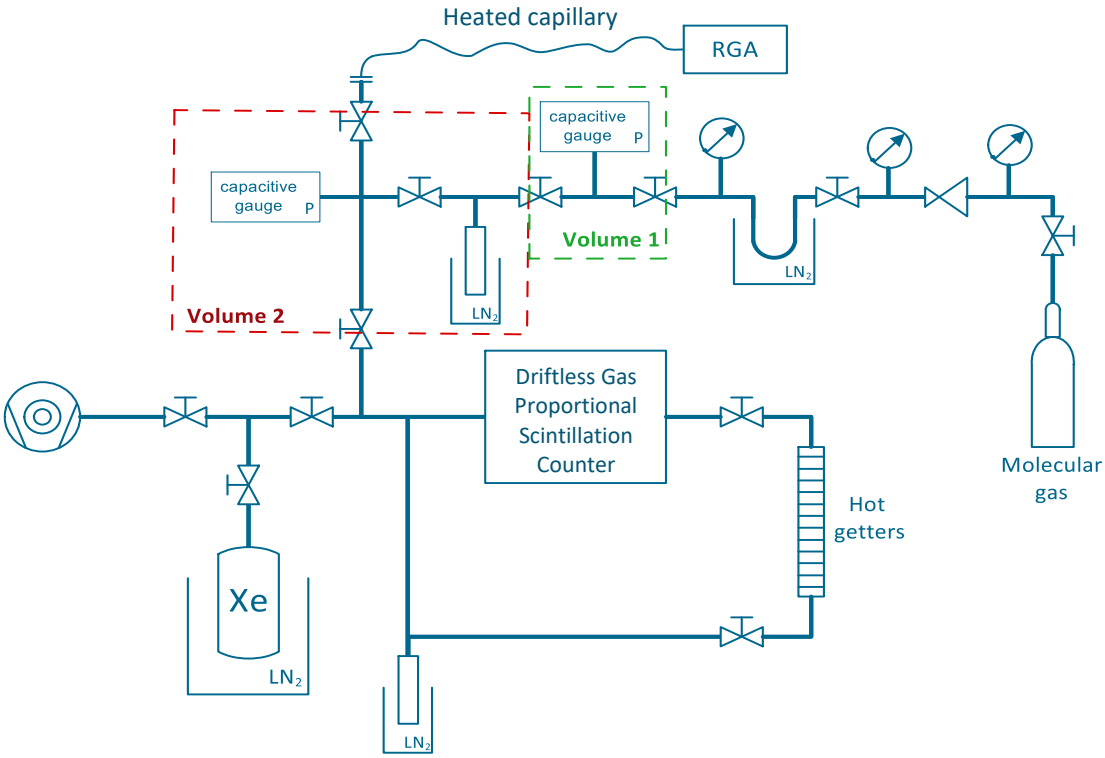

Figure 9: Illustration of the gas system used in the present work, including the driftless GPSC, the RGA, and the two calibration volumes.

In figure 9, the U-shape tube is used to accurately set the desired additive pressure on volume 1, through the slow evaporation of the molecular gas when the temperature rises from liquid nitrogen temperature to room temperature. The same technique is employed to introduce xenon in volume 2. Two additional small vessels are place in the system, one in volume 2 and the other in the detector recirculation loop. Both are used to liquefy/solidify the mixture at the liquid nitrogen temperature, either in the calibration volumes or in the detector. This procedure is made immediately after the mixture preparation to speed up the homogenization process. The preparation of mixtures inside the detector is done similarly to the calibration mixtures, except that the detector system and volume 2 act as a single volume, which is filled with pure Xe, while the volume 1 is filled with additive. The valve between

the xenon volume and volume 1 remains open after preparing the mixture either for the RGA calibration or for the driftless GPSC operation, thus eliminating the risk of part of the additive being trapped inside volume 1.

Non-evaporable hot getters (St-707 from SAES) are used to purify either xenon gas or mixtures, through the recirculation loop, whose flow is maintained by convection. The getters are operated at 250 ºC for pure Xe. This temperature is decreased down to 80 °C for Xe-CO_2 mixtures, and 120 °C for Xe-CF_4 and Xe-CH_4 mixtures, to avoid the quick absorption of these molecules.

In order to reach a more profound understanding of the concentration measurements and backgrounds over time, the RGA was continuously operated during the whole CF_4, CH_4 and CO_2 campaigns. A turbo-molecular pump is exclusively dedicated for the RGA pumping, which is isolated from the rest of the system to avoid chamber contamination and to keep the background stable. The capillary strangulation was adjusted so that the pressure in the RGA chamber is $\sim 4 \times 10^{-6}$ mbar, when the pressure on the driftless GPSC side is about 1.2 bar. In this way, we minimize the risk to operate the RGA in the non-linear region, though with the expense of dynamic range.

A complete mass scan from 1 to 140 a.m.u. is done every 3 min (using a low scanning speed, to improve precision), hence including most of the background species as well as all the xenon masses. To reduce the amount of memory required by data, instead of saving the full analogic mass spectra, each peak maximum is previously computed to build a discrete spectrum.

3.2 Background characterization

After assembling the RGA system, a 200 ºC bake-out was performed to the RGA probe, chamber, capillary and pipe system during 48 h. In this way, the gas background was considerably reduced, especially for H_2O. After that, the RGA system is operated at the room temperature, except the capillary that is maintained at 170 ºC, to reduce the adsorption of molecules to the walls.

In figure 10, the discrete mass spectrum obtained with the RGA chamber in vacuum is shown (in red). The most intense mass peaks and the respective probable gas species are listed as follows: 1, 2 (H^+, H_2^+) from hydrogen; 16, 17, 18 (O^+, HO^+, H_2O^+) from water (or oxygen for 16); 28 (N_2^+ or CO^+) from nitrogen or carbon monoxide; 32 (O_2^+) from oxygen; and 44 (CO_2^+) from carbon dioxide. As expected, these are common impurities found in vacuum systems.

The several background species have an exponential-like decrease over time, although at different rates. After several days of continuous pumping, the background can be considerably reduced. The partial pressures of H_2O, CO_2 and N_2 are usually pumped out faster

than O_2. At the beginning of our tests, the amount of O_2 was residual when compared with CO_2 or N_2. However, upon a long pumping period (several weeks), the amount of O_2 became similar to CO_2 and N_2, as noticeable in figure 10.

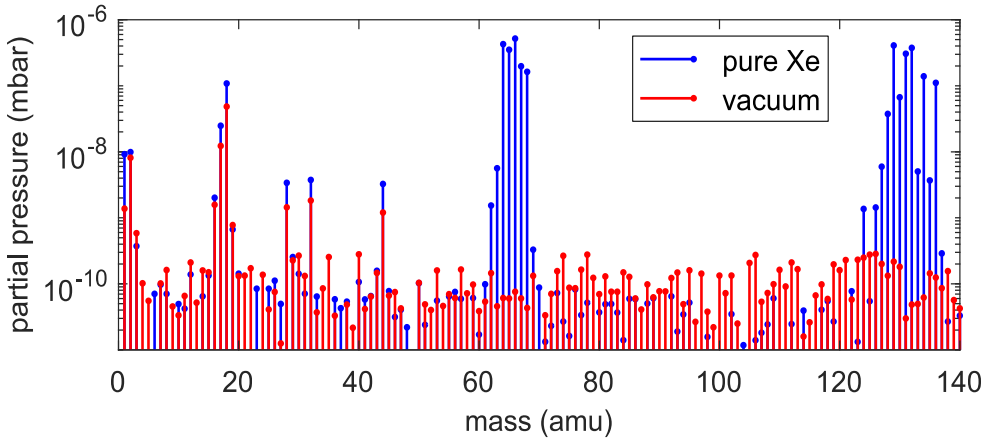

Figure 10: Discrete RGA mass spectrum obtained in vacuum (red), at a total pressure of $7 \times 10^{-7} mbar$, and with pure Xe flowing through the capillary, at a total pressure of $4 \times 10^{-6} mbar$, coming from the driftless GPSC at a pressure of about 1.2 bar, purified with hot getters at 250 ºC.

The large CO_2 background in the RGA chamber hampers the measurement of the CO_2 concentrations in the detector, since they are in the same order of magnitude. On the other hand, CH_4 and CF_4 backgrounds are residual, as it can be observed in figure 10 for the respective main masses: 15 and 16 a.m.u. for CH_4 (16 is dominated by water), and 69 a.m.u. for CF_4.

After the background measurement of figure 10, the driftless GPSC was pressurized at about 1.2 bar of pure xenon, with the getters being operated at 250 ºC to ensure maximum purity. Xenon was allowed to flow through the capillary, and the RGA mass spectrum was acquired, as depicted in figure 10 (in blue). As expected, the xenon mass signature becomes the major contribution in the spectrum: from 124 to 136 a.m.u., corresponding to the several natural isotopes, and from 62 to 68 corresponding to the respective double ionizations (because the RGA measures the mass-to-charge ratio of ions). One also observes that the partial pressures of the main background gases increased by a factor of approximately 2. If we assume that this additional amount of impurities comes from the detector, we can estimate their concentrations, using the theoretical cracking patterns and relative sensitivities [112]. Concentrations of about 500 ppm, 600 ppm, 400 ppm, 20000 ppm and 400 ppm, were found for CO_2, O_2, H_2, H_2O, and N_2, respectively.

Simulations using the same method reported in [16] suggest that such high concentrations would have a significant impact on the EL yield, electron attachment and energy resolution of the detector [113]. However, we have measured a near-zero attachment in the EL region (details in section 7.1), dxand obtained good energy resolutions, about 7.4 % for 5.9 keV x-rays (details in chapter 6), which is near the intrinsic energy resolution of xenon,

and it agrees with the best results reported in the literature [85, 95, 108]. Our driftless GPSC was developed with state-of-art technology, known to provide a very clean noble gas operation. Moreover, when the gas circulation through the getters is closed, the EL yield takes hours to be decreased by 20 %, while the original performance is reached in only 10 minutes, once the gas circulation is reopened. Therefore, the xenon purity in normal detector operation is similar or even better than the gas inside the commercial bottle (4.8 grade), containing less than 1 ppm of the main molecular impurities.

Based on these arguments, we believe that the partial pressures of most of additional impurities arising after the xenon flow is established comes from molecules adsorbed in the capillary and chamber walls, upon being hitas by high velocity Xe atoms. For this reason, the RGA background is measured with pure Xe sampled from the driftless GPSC, where getters are operating at 250 ºC. Before each mixture is prepared, the background is measured during several hours, until readings are stable. This is particularly important in Xe-CO_2 mixtures, because the concentration measurement is highly dependent on the CO_2 background, which in turn fluctuates over time.

We found the additive concentration measured by the RGA to depend on the total pressure of the mixture, probably because the capillary conductivity to Xe or molecules changes. In addition, the background partial pressures in the RGA chamber also vary with the xenon flow rate. Therefore, the background and the mixture measurements are performed always at about the same total pressure in the detector or calibration volumes.

3.3 Perturbations from temperature variations

During the preliminary testes with the RGA, several mass partial pressures were found to fluctuate periodically over time. The air conditioning system positioned above the RGA was identified as a possible source of those fluctuations, given their characteristic pattern (~20 min period). A temperature sensor was assembled near the RGA probe to understand how the room temperature could influence the RGA readings. Indeed, a strong correlation between the air temperature and the fluctuations on partial pressures was found. Since then, air conditioning is always turned off when mixture concentrations or backgrounds are measured with the RGA.

Even without air conditioning, fluctuations are still observed in data, although smaller. The source of these perturbations is again the room temperature that varies along the day, depending on the weather. In this case, the fluctuation period is usually 24 h rather than a few minutes, making it possible to perform stable measurements overnight. In figure 11, the partial pressures of several masses corresponding to the main gases inside the RGA chamber are plotted as a function of time, together with the temperature of the room near the RGA probe.

The first 49 h were obtained with pure Xe flowing from the detector, after that a 0.62 % Xe-CH_4 mixture was prepared.

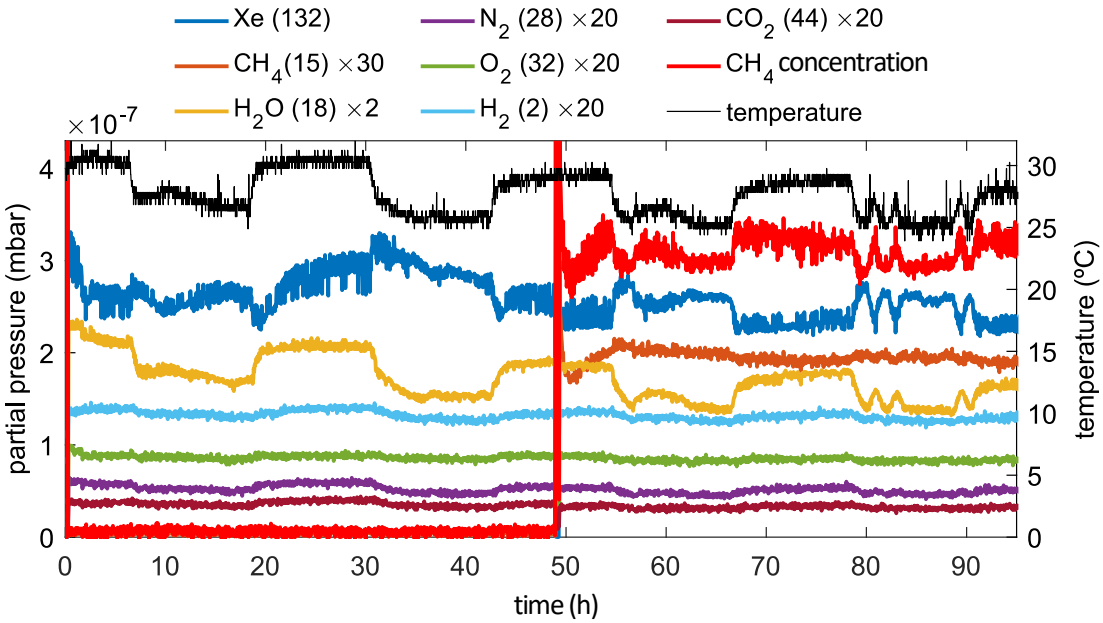

Figure 11: Partial pressures measured by the RGA as a function of time for different masses, which were mostly produced by Xe (^{132}Xe isotope), CH_4, H_2O, N_2, O_2, H_2 and CO_2. Some partial pressures were scaled to facilitate their visualization (the scaling factors are shown in the legend). The non-calibrated CH_4 concentration is also plotted in arbitrary units. The room temperature (black curve) is shown in the right-hand vertical axis. The first 49 h correspond to pure Xe flowing from the detector, after that period a Xe-CH_4 mixture is sampled.

As demonstrated by the example of figure 11, the larger relative fluctuations can be observed in the H_2O partial pressure (mass 18), for which the correlation with the temperature is clear. When the room temperature is high (about 30 ºC, during day), the partial pressure of H_2O is larger, the opposite being observed when the temperature is low (about 25 ºC, during night). This behaviour is also observed, in a smaller scale, in the main masses of CO_2, O_2, H_2, and N_2 (masses 44, 32, 2, 28, respectively). On the other hand, the partial pressure of Xe (mass 132) and CH_4 (mass 15) decreases when the temperature is higher. Although the temperature does not fluctuate for more than 5 ºC, this could be enough to boost the degasification of background gases from the RGA chamber walls, while the dilatation of the stainless-steel capillary could cause a lower gas flow (the heating mantle assembled in the capillary works at a constant power, so its temperature is affected by the external one). These two effects may explain the different dependence of the background gases (H_2O, CO_2, O_2, H_2, and N_2) and the sampled gases (Xe and CH_4) with the temperature.

Despite the similar variation of Xe and CH_4 with the room temperature, they are not quantitatively equal. Therefore, the concentration is affected by temperature fluctuations, as demonstrated in figure 11 (red curve, in arbitrary units). To deal with this technical problem that may produce a 20 % relative error in the calculation of concentrations, the measurements

are always done during a period where the temperature of the room is stable and around 25 ºC. In the example of figure 11, the background with pure Xe could be measured between 39 h and 40 h, and the CH_4 concentration between 64 h and 65 h.

We still tried to find a simple mathematical relation that could predict the variation in the measured additive concentration based on the outside temperature, thus, allowing removing these perturbations from data. However, none of attempts produced satisfactory results.

3.4 Measurement of concentrations

The additive concentration measurements are done in a similar way for the RGA calibration and for the detector operation. Therefore, both procedures are described in this section, and results are discussed.

3.4.1 RGA calibration

There are several kinds of calibrations of the RGA that must be performed periodically, such as the total pressure, the sensitivity factors and the mass scale. These procedures are not described here as they are standard and explained in the RGA documentation. Here, we report the concentration calibration of the RGA system, including the capillary, for the three studied additives.

The most intense mass peaks of CO_2, CH_4 and CF_4 are 44, 16 and 69 a.m.u., respectively. Therefore, 44 and 69 a.m.u. peaks are used to measure the respective additive concentrations. However, the 16 a.m.u. peak from CH_4 is superimposed with the O^+ peak from water and oxygen, whose background partial pressures are usually high (figure 10). For this reason, mass 15 is used instead of mass 16, its peak intensity being slightly lower. These masses represent ~80 % of all the theoretical molecule cracking probabilities of the three additives. For this reason, we do not consider the less intense peaks, as no significant improvement of the detection sensitivity would be achieved. Since the main Xe masses are not superimposed with any peak from the major residual gases (see figure 10), they are all summed (124-136 and 62-68 a.m.u.) to reduce fluctuations in the Xe partial pressure.

During the RGA system calibration with CO_2, the background oncentration was found to variate significantly over time. When volume 2 (figure 5) is filled with pure Xe (after being purified with getters at 250 ºC) and isolated from the detector, the CO_2 background concentration increases linearly. This behaviour is represented in figure 12, where the CO_2 concentration (in blue) was directly obtained from the partial pressure of the mass 44 (in purple), and all the Xe masses summed (in brown).

Although the flow of gas through the capillary is low, the reduction of the total pressure inside the calibration volumes after some hours is noticeable (brown curve). Naturally, if the

amount of Xe decreases and the CO_2 background on the RGA chamber is constant, the concentration will increase with time, hence explaining the linear-like CO_2 concentration increase over time. In addition to this effect, the background partial pressure of CO_2 (purple curve) presents a subtle increase with time in this case, while it was found to decrease in other cases. It might be produced either on the RGA side or on the volume 2 side, for instance by a leak, degasification, or induced by the RGA hot filament.

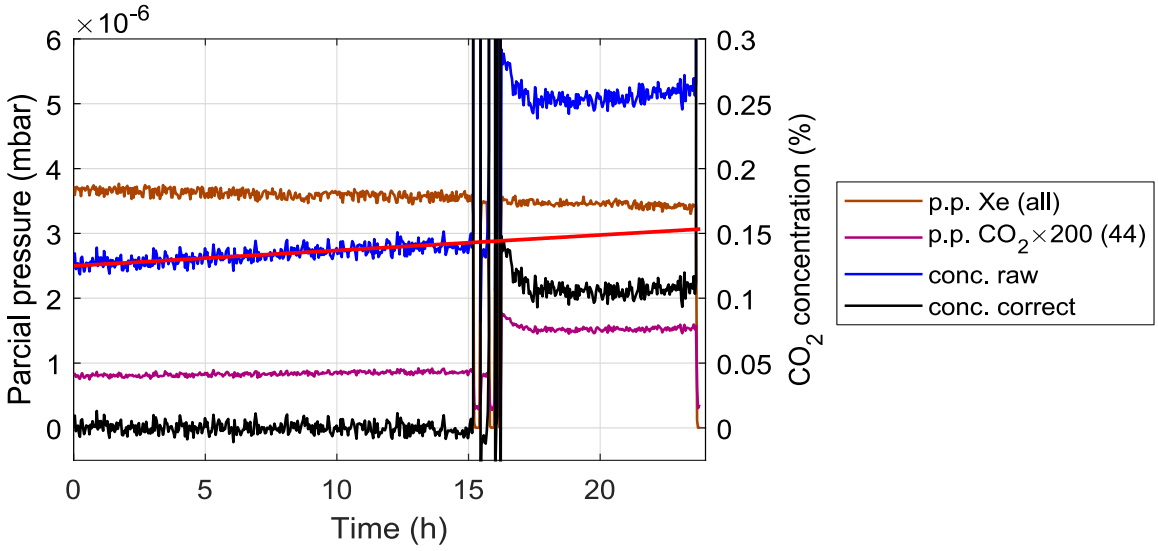

Figure 12: Partial pressures of all the Xe masses summed together (brown) and the CO_2 mass 44 (purple, $\times 200$), as a function of time. The concentration of CO_2 (blue) measured directly from the respective partial pressures and a linear fit performed within the background region, i.e. before volumes 1 and 2 were joined, are shown in the right hand vertical axis. The concentration (not calibrated) obtained after subtracting the background is also represented (black).

After 15 h in figure 12, a Xe-CO_2 mixture with CO_2 concentration of 0.088 % was prepared, joining together volumes 1 and 2. The mixture concentration measured by the RGA seems to follow the same linear trend of the background concentration (blue curve). To lead with this issue, a line is fitted to the CO_2 concentration before the mixture being prepared, thus the CO_2 background concentration can be extrapolated to the following hours. This technique is also demonstrated in figure 12, where the corrected CO_2 concentration (black curve) was obtained from the subtraction of the raw CO_2 concentration (blue curve) and the respective linear fit (red line). The result shows constant trend over time, being about zero before the mixture preparation. The background-subtracted concentration accounts only for the amount of CO_2 that was added in volume 1 (measured with the pressure gauge), allowing to perform a reliable calibration of the RGA.

The subtraction of the CO_2 background is done in this way, either for the RGA calibration or during the driftless GPSC operation. Fortunately, the CF_4 and CH_4 backgrounds are approximately zero, even when measured with pure Xe flowing through the capillary. The partial pressures are in the 10^{-10} mbar scale, which is near the RGA sensitivity limit

(measured using the 21 a.m.u. peak for which it is unlikely to have background molecules), determined by the noise level. Therefore, the mean CF_4 or CH_4 background concentration is measured before each mixture (with pure Xe flowing), within a given time interval (usually about 1 h, to reduce the fluctuations), when the room temperature is as near 25 ºC. The additive concentration curve over time is then subtracted by this value (the background is not extrapolated like in the CO_2 case).

Although the CF_4 background is almost zero, the required concentrations to operate the driftless GPSC are equally low. Therefore, the fluctuations on the background concentration have a profound impact on the accuracy of the mixture concentration measurement, in contrast to the CH_4 case. In addition, after CF_4 being added to Xe, its concentration that is slightly above the background also fluctuates considerably over time (as it will be shown in figure 14). The large statistical error introduced by this technical limitation is minimized, computing the average concentration over a long period of time, usually 5 h, either to measure the background or to measure the additive concentration in the mixture. The RGA sensitivity to CF_4 may be improved by weakening the capillary strangulation in order to increase the total pressure in the RGA chamber. However, the risk of operating in the non-linear regime would be higher, and the previous calibration lines obtained with CO_2 and CH_4 would not be valid anymore.

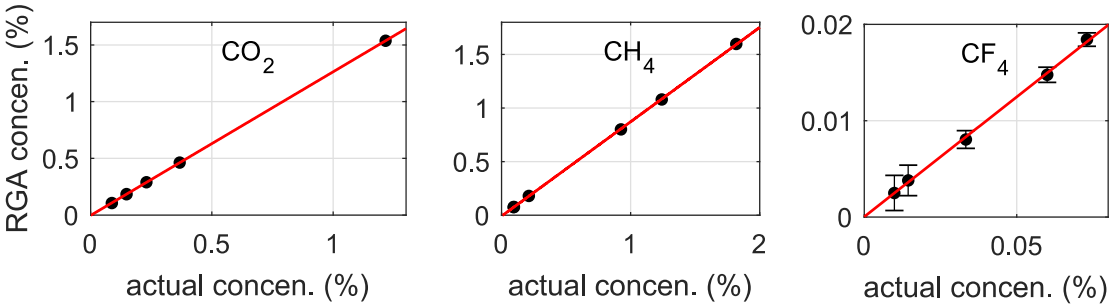

Figure 13: Calibration lines of the RGA system for the three studied molecules, i.e. the concentration obtained from the RGA partial pressures as a function of the concentration measured with the pressure gauges on volumes 1 and 2. The error bars for CO_2 and CH_4 are within the symbol sizes.

In figure 13, the RGA calibration lines obtained for each of three additives studied in this work are shown, i.e. the concentration obtained from the RGA partial pressures as a function of the concentration given by the initial and final total pressures in volumes 1 and 2 (following the ideal gas law). The error bars that correspond to the standard deviation of the RGA concentration measurement (including the contribution of the background subtraction) are only represented for CF_4, because they are within the symbol sizes in the other two cases. The RGA response shows a good linearity, and a negligible offset, showing the robustness of the methods here develop to deal with additive backgrounds in the RGA chamber and with the room temperature issue.

3.4.2 Detector operation

During the driftless GPSC operation with molecular additives, the concentrations are measured as follows. First, the relative concentration of the mixture is corrected by the background, which is measured for a few hours before with pure Xe at about the same pressure. Then, the absolute additive concentration is obtained directly from the respective calibration line (figure 13). Like in the background measurement, the driftless GPSC is ideally operated when the room temperature is about 25 ºC and after the concentrations are stable, so that reliable concentration measurements can be obtained.

In figure 14, the absolute CH_4 and CF_4 concentrations (already corrected by the background and the calibration lines) inside the detector are shown in (a) and (b), respectively, as a function of time. A moving average is plotted in the CF_4 case (black curve) to facilitate the visualization of the mean concentration. The time interval that was used to compute the background concentration is represented in red. Plot (b) illustrates well the low accuracy of the concentration measurements with Xe-CF_4, due to the large noise in the 68 a.m.u. partial pressure for such minute amounts of additive.

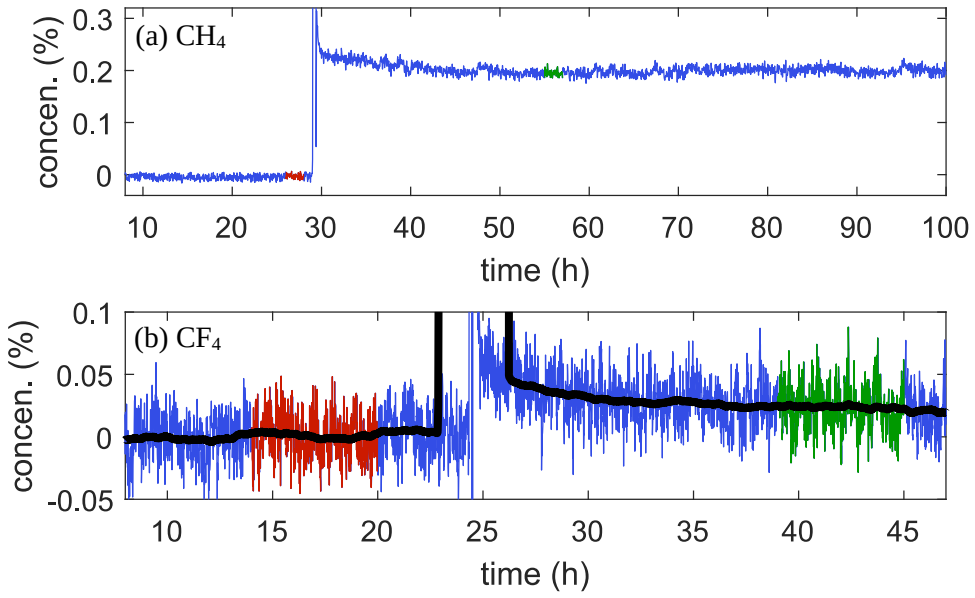

Figure 14: Concentrations of CH_4 (a) and CF_4 (b) inside the detector as a function of time, obtained with the RGA after the background was subtracted and the calibration line was applied. The red region represents the interval used to compute the mean background concentration, while the mixture concentration is obtained from the average over the green region, when the EL studies were performed. The black curve in (b) is a moving average of the concentration to assist the trend visualization.

After adding CH_4 (30 h in (a)) or CF_4 (25 h in (b)) to Xe, the concentration decreases in the first few hours, tending to stabilize afterwards. Therefore, these molecules are not continuously absorbed or converted into other species by the detector materials or getters (at 120 ºC), at least within this time range. The same is not verified with Xe-CO_2 mixtures, as it will be shown in the following sections. In our preliminary tests, we realised that the time

required for the additive concentration to stabilize after being added was more than 12 h, in contrast to the ~2 h observed in the two examples of figure 14. To speed up the homogenisation process, two mixing vessels were added to the system, one for the calibration volumes, and the other one for the detector (see figure 9). Thus, after adding the molecular gas to xenon, the mixture is liquified/solidified into the respective vessel using liquid nitrogen, and the

n let to return to the vapor phase. This simple procedure takes no more than 10 min, and it has been used successfully in all mixtures either for the RGA calibration or detector operation.

In the examples of figure 14, the EL-related measurements were performed at the centre of the green intervals, over which the average concentration is computed. In these cases, the measured concentrations are (0.201 ± 0.011) % and (0.024 ± 0.007) % for CH_4 and CF_4, to be compared with the initial concentrations of 0.240 % and 0.033 %, respectively. In general, the CH_4 concentration measured by the RGA is similar to the initial one measured with the pressure gauges. On the other hand, the CO_2 and CF_4 concentrations decrease by 25-80 % and 30-40 %, respectively, with respect to the initial ones. This drop could be explained by the absorption, adsorption or conversion of these molecules in getters or other detector materials. This observation justifies the need for an accurate real-time concentration measurement system. It is also a possible explanation of the discrepancies between previous EL-related experimental data and simulated results found with Xe-CO_2 mixtures [99, 100].

The error in the concentration measurements that will be presented from now on was estimated taking into account the standard deviation of the respective RGA partial pressures, the contribution from background subtraction, the calibration line, and the room temperature induced-fluctuation (because not all the measurements were performed at 25 ºC). Nonetheless, an additional systematic error may exist, for example due the amount of additive that becomes adsorbed in the 2 calibration volumes wall, hence affecting the calibration lines.

3.5 Real-time concentration and electroluminescence yield

In this section, the electroluminescence yield and energy resolution obtained in the driftless GPSC are compared with the additive concentration as a function of time. This study was performed for the three additives, however we show only the CO_2 case, since the variation of its concentration over time is usually sharper.

In figure 15, we depict the absolute reduced EL yield (normalized using the experimental data of [92]), the CO_2 concentration, and the detector energy resolution (measured using the method described in section 4.2.1) as a function of time, for an initial concentration of 0.24 % (measured with the pressure gauges).

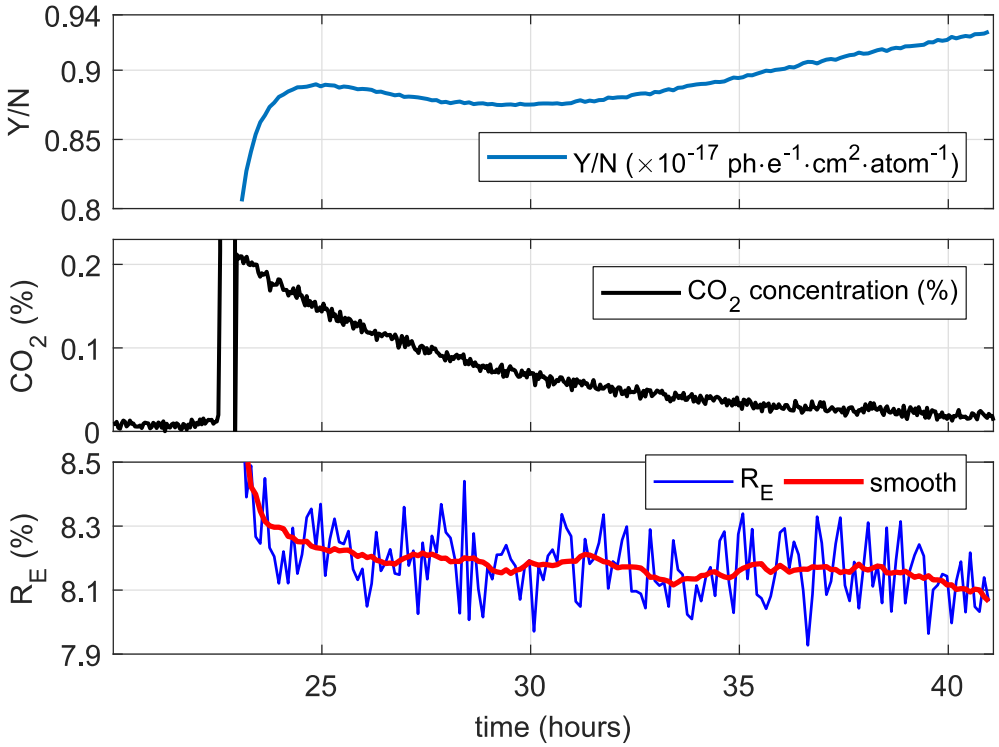

Figure 15: Absolute reduced EL yield (top), RGA calibrated CO_2 concentration (centre), and detector energy resolution (bottom), as a function of time. The red curve in the bottom plot is a moving average to assist the trend visualization. The molecular gas was added after 22.5 h, then the mixture was liquified/solidified in the mixing vessel at the liquid nitrogen temperature to speed up the homogenization process.

In opposite to the CH_4 and CF_4 cases (figure 14), the CO_2 concentration inside the detector decreases continuously over time, contrasting with the stability observed inside the calibration volumes (figure 12). This result is most likely related to the getters, despite the low temperature used with Xe-CO_2 mixtures (80 ºC). Generally, the higher the initial concentration, the lower the relative loss of CO_2 in the first 24 h, probably because the superficial sorption sites of the getters become saturated, and the impurities diffuse slowly to the inner part of the getters at 80 ºC (according to the manufacturer).

The detector EL yield presents a peculiar variation in the first 5 hours, showing a sharp growth followed by a slow decrease. This observation is not compatible with the real-time concentration measurement. In our gas system, the capillary is placed far away from the detector (figure 9). Consequently, the RGA readings are not reliable to evaluate the additive concentration inside the EL region, until the mixture become homogeneous. Therefore, this strange variation of the EL yield at the beginning could be produced by local non-uniformities of the mixture. After that, the yield increases with time, which is consistent with the observed reduction of the CO_2 concentration. The energy resolution is close to the one obtained for pure Xe (~8 %), with a slight decrease with time, as expected from the EL yield variation.

Considering the long homogenisation time (even using the mixing vessel), the EL studies with the three additives were only performed several hours (usually more than 20 h) after the molecular gas was added. In this way, the risk of the measured concentration being much different from the real concentration inside the EL region is minimized. Special care was taken with Xe-CO_2, because its concentration is continuously changing. In addition to these facts, our RGA sampling system introduces a long delay in measurements. For instance, if there is a dead volume at the capillary entrance of 1 cm^3, it takes about 1.5 hours to be drained. In applications requiring faster response times, a larger flow is usually used and deviated through a primary vacuum pump, a small fraction of this flow being analysed by the RGA.

3.6 Additive compatibility with getters

Since the full RGA mass spectrum is recorded over time, possible byproducts of the three additives can be latter identified. No significant increase in any mass partial pressure was found with Xe-CH_4 and Xe-CF_4 mixtures. However, with Xe-CO_2, the 28 a.m.u. peak grows considerably after the molecular gas is added to the driftless GPSC. The second most intense peak of CO_2 is 28 a.m.u., however this contribution cannot explain the continuously increasing tendency, because the CO_2 concentration decreases over time.

The more likely impurities that could produce this result are nitrogen (N_2) and carbon monoxide (CO), 28 a.m.u. being the main peak in both. In order to distinguish them, the secondary peaks are also analysed. All the N_2 masses (28, 14 and 29) are common with CO, but some secondary masses of CO are independent from N_2, such as the second more intense peak, 12 a.m.u. (from C^+). First, the contribution of CO_2 to the masses 12 and 28 needs to be subtracted. These ratios are provided by the RGA manufacturer molecule library, but they may deviate significantly from experimental values. For this reason, the RGA data obtained during the CO_2 calibration is used to quantify accurately the CO_2 impact in masses 12 and 28, considering that N_2 and CO remain constant. We should note that the partial pressures in masses 12, 28 and 44 are roughly constant over time inside the calibration volumes, in contrast to the mixtures inside the detector.

The ratio between the secondary CO_2 peak $P_{12}^{CO_2}$ or $P_{28}^{CO_2}$ and the main one $P_{44}^{CO_2}$ is obtained from the increment in the 12 or 28 a.m.u. partial pressure divided by the increment in the 44 a.m.u. peak when CO_2 is added to Xe in the calibration volumes. The experimental factors we obtained after averaging over several mixtures are $P_{12}^{CO_2}/P_{44}^{CO_2} = 1.9$ % and $P_{28}^{CO_2}/P_{44}^{CO_2} = 4.7$ %, which are lower than the theoretical values of 6.0 % and 11.0 %, respectively, given by the RGA manufacturer. Using these experimental factors, the contribution of CO_2 can be excluded from the readings in masses 12 and 28.

In figure 16, we depict the partial pressures of the peak 28, CO_2 (in mass 44) and Xe (all masses summed) as a function of time. In the first 25 h, pure Xe flows through the capillary (getters as 250 ºC), after that a 0.37 % Xe-CO_2 mixture (measured using the pressure gauges) was prepared inside the detector, with the getters at 80 ºC up to 40 h. The partial pressure of mass 28 is also plotted, after the respective CO_2 contribution (4.7 % relative to peak 44) and the background (measured with pure Xe) were subtracted. We assume that the background comes mostly from nitrogen that remains constant, hence this curve represents the relative amount of CO over time.

Due to the minute contribution of CO to the peak 12 a.m.u., theoretically 4.6 % relative to peak 28, the partial pressure in this mass after the CO_2 being subtracted (1.9 % relative to peak 44) is near zero. Therefore, it is hard to evaluate any trend over time, since the readings are at the level of the RGA sensitivity limit. A moving average with a large span (~15 h) is used as an attempt to overcome this limitation, the result being also shown in figure 16. The Xe and the 12 peak partial pressures were scaled to facilitate their visualization. The blue arrows represent periodic perturbations (every ~24h) produced by room temperature variations, which affect all the data sets, especially the Xe partial pressure.

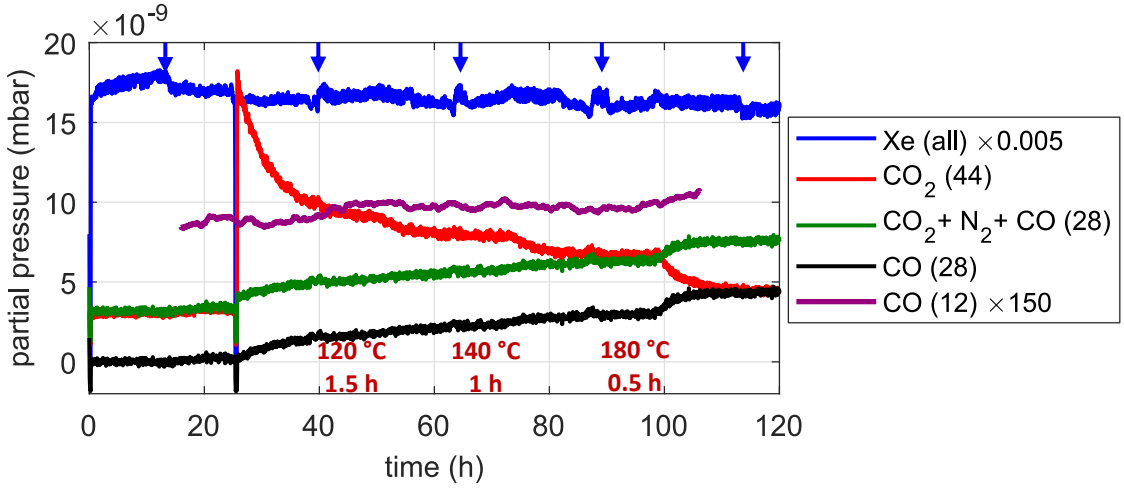

Figure 16: Partial pressure as a function of time, measured in the peaks 28 a.m.u. (green), 44 a.m.u. (red) and all the Xe masses summed together (blue). The partial pressure of mass 12 (purple, moving average with a span of ~15 h) and mass 28 (black), after the CO_2 contribution was subtracted, as well as the background (mostly produced by N_2) in the latter case. In the first 25 h, pure Xe flows from the detector, where getters are at 250 ºC. Then, their temperature is decreased to 80 ºC and CO_2 is added. After 50 h, 70 h and 100 h, the temperature of the getters was set to 120 ºC, 140 ºC and 180 ºC during 1.5 h, 1 h and 30 min, respectively. The blue arrows indicate periodic (~24 h) perturbations in all data sets produced by room temperature changes.

The impact of CO_2 in the mass 28 is visible in figure 16 (green curve), as the respective partial pressure jumps to a higher value when the molecular gas is added (after 25 h). Once this contribution is subtracted (black curve), the 28 a.m.u. partial pressure increases gradually right after the mixing, while it is zero before, when pure Xe is sampled.

To evaluate the getter influence on peak 28, the temperature was increased to 120 ºC during 1.5 h (after 50 h), being then dropped again to 80 ºC. This procedure was repeated in the next two days, first increasing to 140 ºC during 1 h (after 70 h) and finally to 180 ºC during 30 min (after 100 h), the results being depicted in figure 16. A common behaviour is observed, when the getter temperature increases, the CO_2 decreasing tendency is boosted. On the other hand, the pressure in the mass 28 excluding the CO_2 contribution (black curve) increases sharper, especially when the highest temperature is set. This result suggests that the additional molecules detected in the 28 peak are likely CO rather than N_2, as they seem to be produced from CO_2, most likely inside the getters. Despite the high noise (not shown here) in peak 12 readings obtained after subtracting the CO_2 contribution, the average trend over time (purple curve) seems to agree qualitatively with the corrected 28 a.m.u. partial pressure, reinforcing our belief that the peak 28 increases due to CO rather than N_2.

Despite a proper calibration was not done for CO, its concentration can be estimated from the corrected partial pressure in mass 28 a.m.u., assuming the same sensitivity factor of CO_2. In normal conditions, with getters at 80 ºC, the concentration of CO may reach 0.04 % at most. According to simulations (using the method described in [16]), the impact of such concentration in the EL yield measurements would be 10 % for the worst-case scenario, i.e. for the lower CO_2 concentration, where the ratio between CO and CO_2 is higher [113]. For this reason, we do not consider the effect of CO in our EL results. It is worth mentioning that the decrease of the partial pressure in the mass 44 a.m.u. is larger than the increase in the peak 28 a.m.u., suggesting that only a small part of CO_2 is converted into CO.

For Xe-CH_4 and Xe-CF_4 mixtures, concentrations inside the detector with the getters at 120 ºC have shown to be stable, at least up to 44 days and 5 days, respectively. However, with a Xe-CH_4 mixture with a concentration of ~0.03 %, it was observed a 10 % drop of the EL yield after 7 days, increasing to 30 % after 44 days. The relative degradation of the energy resolution was 5 % and 10 %, respectively. It was not found any substantial increase in the partial pressures of the main impurities. Nonetheless, since the detector performance with such low CH_4 concentrations is near the pure xenon one, even a small amount of impurity could be enough to produce this result. At some point the getters temperature was raised to 250 ºC, but the EL response of the detector and the CH_4 concentration remained unchanged, probably because the getter surface was saturated. After carrying out a reactivation of the

getters[1], their performance was restored, being able to purify efficiently pure Xe continuously during 19 days, without any degradation of the EL yield or the energy resolution.

These results suggest that some kind of incompatibility between the getters and CH_4 may exist. However, a more detailed study must be done with new getters, and at different temperatures. The getters we used in the present work are in operation during several years with molecular additives, hence their performance could be considerably worse than the initial specification.

[1] The getters reactivation is a procedure used to migrate the impurities sorbed in the getter surface into the getter bulk, allowing the surface sites to be active again. To accomplish this, the temperature of the getters is gradually increased up to about 370 ºC, being kept at this level for about 1 h in vacuum.

4 THE DRIFTLESS GPSC

The main goal of this work is to evaluate the influence of molecular additives in the EL response of Xe, which can be easily accessed using a Gaseous Scintillation Proportional Counter (GPSC). However, in a traditional GPSC the EL signal also includes the effect that the additive may have in the drift region, such as its impact on the electron lifetime or on the electron cloud size. Moreover, to reduce the contribution of low transparency mixtures to the EL signal, the photosensor should be placed near the EL gap, and the detector made compact, thus shortening the path length of reflected photons. For these reasons, we have opted to use a driftless GPSC, i.e. without drift region, which was already used in previous studies [114–116]. With this apparatus we measured the EL response of Xe-CO_2, Xe-CH_4 and Xe-CF_4 mixtures.

In this chapter, we describe the experimental setup used in the present study, including two different data acquisition configurations, the *direct* and *standard method*. Then, the unique response of this detector is shown, and modulated on a purely theoretical basis, either in the presence or in the absence of attachment.

4.1 Driftless-GPSC experimental setup

In a conventional GPSC, most of the x-rays interact in the drift region, where the applied electric field is high enough to avoid the recombination of the produced electron-ion pairs, but below the gas scintillation threshold. Under this electric field, the electrons drifts to the scintillation region, where the electric field intensity is kept between the scintillation and ionization thresholds. Consequently, the electroluminescence process takes place, while the electron charge avalanche gain is negligible. In a driftless GPSC, the drift region is eliminated, and x-rays are absorbed inside the scintillation region.

Besides the motivations supporting our choice for the driftless GPSC in the present study, this kind of configuration has additional advantages. For instance, the interaction of soft x-rays in a region with a stronger electric field reduces the probability of primary

electrons being lost to the detector window, hence reducing lower amplitude events in the pulse-height distributions [117]. Furthermore, the absence of a grid separating the drift and EL regions avoids electron loss in this boundary. Because of the stronger electric field in the driftless configuration, additional adverse effects are minimized, such as electron-ion recombination, lateral diffusion of electrons, or even electron attachment to impurities as the number of collisions is lower [116, 118].

In figure 17, the schematic diagram of the driftless GPSC used in this work is depicted. The EL region (2.5 cm thick) is delimited by a Kapton radiation window (8 mm in diameter, mounted on a stainless-steel holder, aluminised on the inner side) and by the PMT quartz window, vacuum-evaporated with a chromium grid (100 µm thick wires with 1000 µm spacing), electrically connected to the photocathode pin of the PMT. The PMT (model EMI D676QB with 52-mm in diameter, but 48-mm of effective cathode) is epoxied to a Macor disc coupled to the lower part of the detector (about 10 cm in diameter), made of stainless steel and connected to the gas circulation tubing. The gas purification system consists of a closed loop, forcing the gas to flow through non-evaporable getters (SAES St707), which are heated by an external heating mantle. A continuous flow through the getters is ensured by convection.

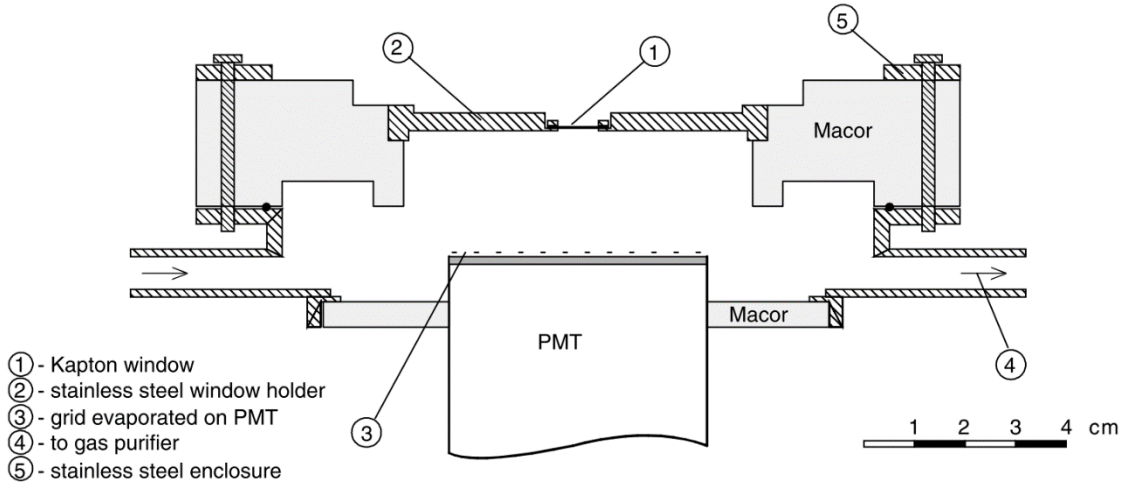

Figure 17: Scheme of the driftless GPSC used in this work, adapted from [115].

4.1.1 Data acquisition: standard method

In the standard data acquisition method used in the present studies, the PMT signal is integrated in a charge sensitive preamplifier (CANBERRA model 2005, with a decay time constant of about 50 µs) configured to a sensitivity of 22.7 millivolts per picocoulomb. Its output signal is shaped by a linear amplifier (Tennelec model TC243, configured to deliver unipolar output), hence reducing the pile-up probability and improving the signal-to-noise ratio. Since the conventional and the driftless GPSCs rely on the total amount of collected scintillation photons, long integration (RC) and differentiation (CR) time constants (several

μs) are necessary to embrace the full PMT waveform. The output of the linear amplifier consists of Gaussian-like pulses, with height proportional to the total charge delivered by the PMT in each x-ray interaction. A Multi-Channel Analyser (MCA) is then used to construct a histogram of pulse heights, known as pulse-height distribution. This arrangement of electronics (from now on called *standard method*) is typical in x-ray, gamma and other ionizing radiation spectroscopy.

4.1.2 Data acquisition: direct method

With modern analog-to-digital converters (ADC) reaching good voltage and time resolutions at impressive high sampling rates, the PMT signal can be digitalized with minimal loss of time or voltage information, for instance using a pico-ammeter or an oscilloscope (there are commercial oscilloscopes reaching a sampling rate of 240 GS/s, corresponding to a bandwidth of 100 GHz). This kind of solution when combined with high gain photosensors like a PMT can be very sensitive and deliver a good signal-to-noise ratio, making it possible to design an accurate system with good linearity and repeatability. Moreover, the amount of hardware needed to operate a detector such as the driftless GPSC is considerably reduced and simplified, being even cheaper if the required time resolution is modest. Noise filtering, background discrimination or other basic operations can be post processed by software.

After analyzing data recorded using the standard method with Xe-CO_2, Xe-CH_4 and Xe-CF_4 mixtures, a deeper understanding of the driftless GPSC phenomenology was needed. For this purpose, output signals from the PMT were directly connected to an oscilloscope (Lecroy, WaveRunner 610Zi), with an analog bandwidth of 1 GHz. In this data acquisition configuration, from now on called *direct method*, one needs to convert first the current delivered by the PMT into a voltage. Accordingly, the 50 Ω DC coupling of the oscilloscope was used to match the cable impedance, thus avoiding wave reflections. The typical 1 MΩ input impedance is not suitable for this task, because it would act together with the cable capacitance as a slow differentiator (i.e. like the preamplifier).

In some measurements for weak EL electric fields, the energy resolution of the detector was found to be significantly degraded by low frequency fluctuations on the oscilloscope baseline, whose standard deviation was found to be about 120 μV (measured with the lower vertical scale, 1 mV/div). The major source of this noise is the oscilloscope itself, since fluctuations remain almost unchanged when the input is grounded. No relation with the external electromagnetic environment or the power supply grid was found. To reduce the effect of these fluctuations on low current acquisitions, a resistor of 273 Ω is placed at the oscilloscope input to increase the voltage of the PMT signal, with the 1 MΩ DC coupling being used in those cases. Although the cable impedance does not match the resistor, no significant distortion on the typical waveforms for a given duration interval was observed.

The trigger threshold of the oscilloscope (made on the rising edge) is set manually for each run. When the amplitude of waveforms is too low, the high frequency noise hampers a proper triggering; in these cases, a 200 MHz cut-off is applied to the incoming signal, as well as a weighted moving average-like filter (known as ERES filter, which decreases the bandwidth down to 290 MHz when set to 2 bits). Waveforms are then saved in memory, each in a single binary file for post processing.

4.2 Effect of the x-ray penetration on the pulse-height distribution

In contrast with a regular GPSC, the response of a driftless GPSC depends on the x-ray penetration, since the total amount of produced EL photons is related to the distance travelled by the electrons across the scintillation region. Consequently, the MCA pulse-height distribution obtained with monoenergetic x-rays (when the standard method is used) corresponds to the convolution of a Gaussian distribution with an exponential distribution (according to the absorption law of x-rays in matter).

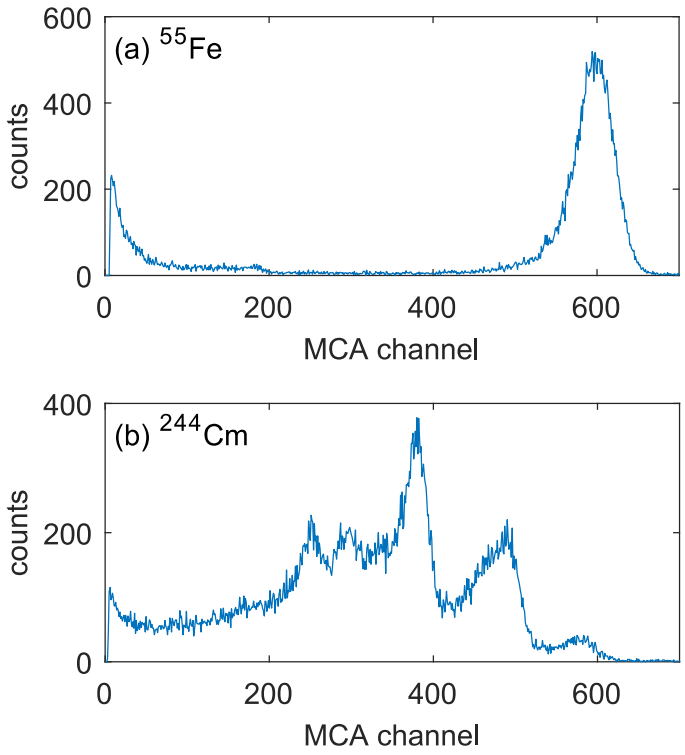

Figure 18: Typical pulse-height distributions produced by the driftless GPSC filled with pure xenon when radiated by 5.9 keV x-rays (from ^{55}Fe) in (a) and by a ^{244}Cm radioactive source (the main x-ray energies are 8.3, 11.1, 9.4, 14.2, 17.3, 18.3 and 21.4 keV) in (b).

When low energy x-rays are absorbed, the penetration distance is short when compared to the 25-mm thick EL region. For instance, for the Kα line (5.9 keV) of the ^{55}Fe source, the absorption length in 1 bar of xenon is about 2.7 mm. Therefore, the full absorption peak of the pulse-height distribution is still roughly similar to a Gaussian function, as shown in figure

18 (a), in contrast with the left-tailed photopeaks produced by higher energy x-rays (because of their deeper penetration into Xe), as shown in figure 18 (b).

Despite the 5.9 keV source have been used in our studies with CO_2, CH_4 and CF_4 mixtures, the accurate quantification of the impact of the additives on the GPSC intrinsic energy resolution is still limited by the x-ray penetration effect. In practical terms, the energy resolution of a driftless GPSC through the standard method includes this effect. However, in a TPC as the one used by the NEXT experiment, events occur in the drift region and, consequently, the electron cloud produces secondary scintillation always along the same path length. Therefore, to extrapolate the impact that the additives may have in other detectors being operated at different conditions, such as the NEXT-100 TPC, the penetration effect must be corrected from our results.

4.2.1 Single Gaussian fit methods

A possible way to avoid the x-ray penetration effect on the pulse-height distribution without further hardware implementation is by reducing both the differentiation and the integration time constants of the linear amplifier. Thus, pulses coming from the linear amplifier become like the original PMT waveforms as shorter the shaping constants are. Since the MCA records only the height of the pulses, the full absorption peak will correspond to the amount of light collected during a short time interval just before the electron cloud being collected by the anode grid [2], rather than the total amount of EL light collected by the PMT. The relative amount of 5.9 keV x-rays interacting near the PMT window is negligible, hence the left tail observed in the full absorption peak is small.

The main disadvantage of this method is most likely the degradation of the energy resolution, due of the lower number of photons that are included (because PMT fluctuations follow the Poison statistics). Nevertheless, this effect can be reduced by making the shaping time constants longer, thus, integrating more light during the final stage of the electron path way. However, the penetration effect becomes higher too, as more x-rays may interact inside the region that is considered. Therefore, depending on the x-ray energy, a compromise exists between the reduction of the penetration effect and the degradation of the energy resolution due to shorter integration times. In our study with this method, an optimal energy resolution of 7.61 % for 5.9 keV x-rays was found for a shaping time constant of 1 μs, with an EL

[2] Here, we are assuming that the intensity of the light reaching the PMT is maximum when the electron cloud is at the nearest point to the photocathode. However, the electron cloud has a finite size, consequently the maximum light intensity will happen when a few electrons were already collected, and the remaining ones are very close to the PMT's window. In the presence of high electron attachment, the maximum light intensity might even occur at the beginning of the drift pathway, because, despite the solid angle being larger at the end, just a few electrons survive up to there.

reduced electric field of about 3.4 kV/cm/bar applied. It is worth highlighting that these results depend on the EL electric field because, for different electron drift velocities, the same integration time will cover different lengths near the PMT window.

In the presence of molecular additives, the EL yield can be considerably reduced, consequently this method could result in an additional degradation of the energy resolution. Moreover, in mixtures that promote electron attachment, the amount of light produced during the final stage of the electron drift is no more constant, depending strongly on the x-ray penetration. Therefore, the above method was not used in our study with mixtures, and the linear amplifier time constants were set long, so that the total amount of produced EL light is considered.

In a first approximation, to estimate the energy resolution corrected from the x-ray penetration effect, one can fit a Gaussian to the right side of the photopeak, including also a small part of the left side. In this single gaussian fit method, most of the left tail coming from the x-ray penetration effect will be excluded, while the Gaussian centroid can still be accurately determined. Nonetheless, the corrected energy resolution obtained in this way is overestimated, since the right side of the full absorption peak do not corresponds exactly to the right side of the Gaussian produced by the zero penetration x-rays (this can be visualized in figure 20 (a)).

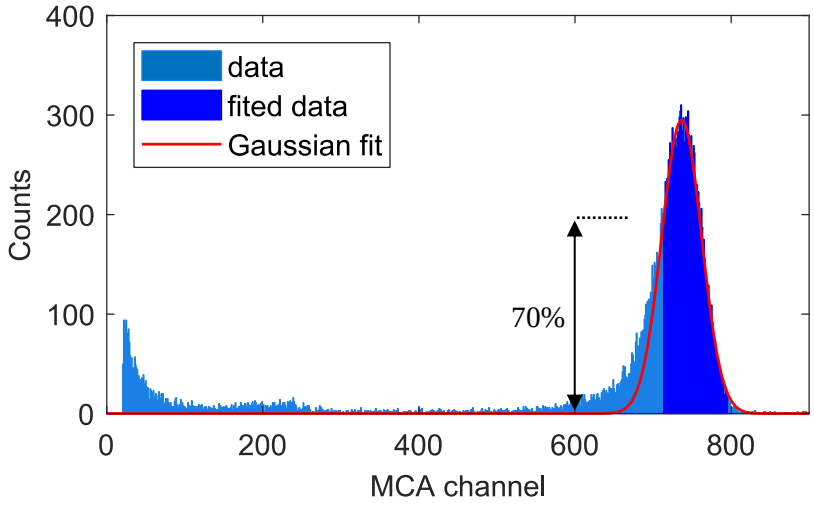

Figure 19: In blue, the pulse-height distribution obtained with the driftless GPSC filled with pure Xe and irradiated with 5.9 keV x-rays (for an E/p of 3.4 kV/cm/bar and a pressure of 1.18 bar). The red curve shows a Gaussian fit to data, including the right side of the full absorption's peak and the left side above 70 % of the peak height (the fit region is represented in dark blue).

This method was used in former studies with the driftless GPSC [97–100], as well as in the preliminary data analysis of the present study. For standardization proposes, we fixed the left threshold across measurements, corresponding to the portion of the photopeak above 70 % of its average height, as demonstrated in the example of figure 19. Since just few points on

the left side are used in the fit, there is a significant uncertainty on the estimation of the FWHM (when short MCA acquisition times are used). Therefore, 4 additional fits are made for small variations of the threshold (within (70 $\pm$ 15) %), with the mean FWHM being computed from the 5 fits. With this method, a corrected energy resolution of about 8 % is obtained for pure xenon in contrast to the real value, 9 %, i.e. obtained from the FWHM of the full absorption peak.

The impact of the CO_2 addition to xenon on the detector energy resolution was first evaluated using this single Gaussian fit method. However, to isolate the fluctuations on the production of EL photons (see section 2.3.2.2) from the overall energy resolution, the fluctuations on primary charge production and ones produced by the PMT should be subtracted. Therefore, even a small mismatch between the rough approximation obtained from the aforementioned fit method and the real corrected energy resolution can have a significant impact on the calculation of the EL-related fluctuations.

4.2.2 Theoretical detector response function

In order to improve the accuracy of the corrected energy resolution determination, it was then estimated by deconvoluting the full absorption peak into a sum of a large number (250) of Gaussian functions, corresponding to x-ray interactions at successive depths, in intervals (Δz) of 0.01 cm.

All these Gaussians have the same relative FWHM, which was left as a free parameter. The Gaussian areas decrease according to the exponential absorption law for 5.9 keV x-rays. The attenuation coefficient was computed considering the x-ray energy, the measured gas pressure, and the estimated gas temperature. The centroid of each Gaussian follows the integration of the solid angle subtended by the PMT photocathode along the path corresponding to each x-ray penetration (assuming a point-like electron cloud with no diffusion over time). The centroid of the rightmost gaussian (i.e. the one corresponding to the zero-x-ray penetration) is also left as a free parameter.

Nevertheless, this simplification of the system response function cannot be perfectly fitted to experimental data, as shown in figure 20 (a). Some neglected effects might explain this mismatch, for example: the divergence of the x-ray beam; the non-uniform sensitivity of the PMT photocathode; the reflection of VUV photons on the PMT window or on detector materials; the initial size of the electron cloud and diffusion; the exact temperature of the gas (affecting the calculation of the attenuation coefficient); non-uniformities on the electric field, most likely near the detector window (which is visually deformed outwards due to the inner higher pressure). Some of these effects (reflected light, x-ray beam divergence and PMT effective photocathode radius) were introduced in the response function as free parameters.

As demonstrated in figure 20 (b), the modified response function fits better to the experimental pulse-height distribution obtained with pure Xe, which is used to estimate the additional parameters. After this procedure, the *theoretical response function* is build considering always the same values, as they are not expected to depend on the mixture. Therefore, the energy resolution and the centroid of the rightmost Gaussian are the only parameters left free in the fits to data obtained with mixtures.

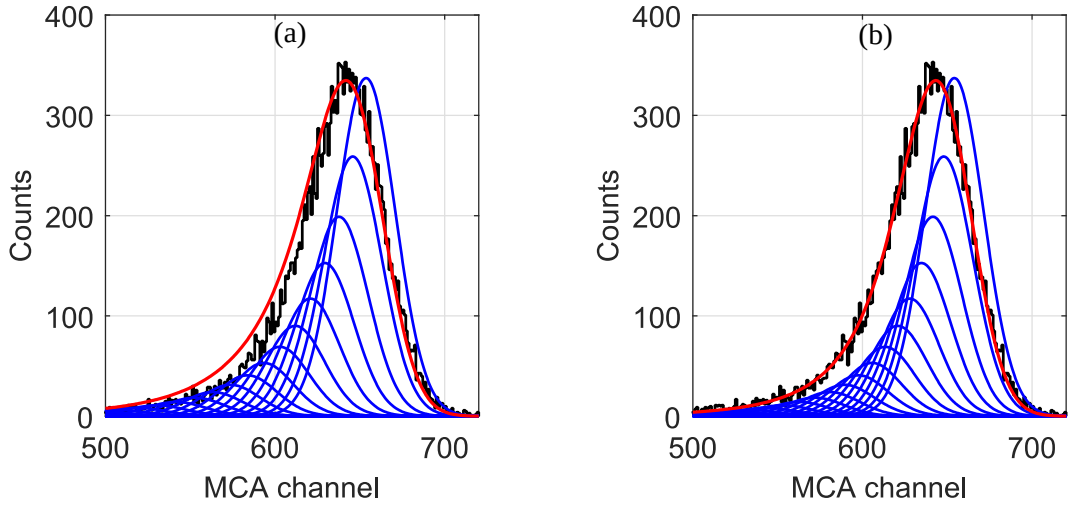

Figure 20: Pulse-height distribution (in black) obtained with the driftless GPSC filled with pure Xe and irradiated with 5.9 keV x-rays for an E/p of 3.1 kV/cm/bar and a pressure of 1.18 bar. In (a) the simplified response function (red curve) was fitted to data, while in (b) the same function is shown but including additional effects. About 10 % of the Gaussians used to produce the response functions are also depicted (in blue), in arbitrary units.

When the full absorption peak centroid is estimated using the single gaussian fit method, a deviation of just 2 % in relation to the rightmost Gaussian centroid is observed (figure 20 (b)). On the order side, the corrected energy resolution obtained with the theoretical response function is somewhat below 7 %, which is significantly lower than the 8 % obtained with the single gaussian fit method (figures 19 and 20 (b)).

4.2.3 Theoretical response function and the electron attachment

The theoretical response function was developed to improve our estimation of the corrected energy resolution, despite a systematic error being likely introduced. This function was used with pulse-height distributions obtained with the standard method, for pure Xe, Xe-CO_2 and Xe-CH_4 mixtures. However, when the driftless GPSC was operated with Xe-CF_4 mixtures, a clear right-sided tail in the full absorption peak was observed (see the example of figure 21), instead of the expected left-sided tail.

The source of this effect is the high dissociative attachment of electrons, which is induced by the CF_4 molecule under EL electric fields. In this way, electron clouds produced by less penetrating x-rays will lose more electrons, when compared to those from deeper

absorptions. If the electron attachment is high enough, the overall number of EL photons collected by the PMT could be even higher when x-rays penetrate deeper. In those cases, there are more electrons reaching the region near the PMT window, where the solid angle is larger, thus compensating the lower overall number of EL photons emitted along the full path length. Therefore, the distribution of Gaussian centroids of the theoretical response function (which was obtained by integrating the solid angle for each path length) should also include the electron loss along the drift path.

In a uniform EL electric field, the probability of electrons to become attached follows an exponential distribution. Accordingly, this effect was introduced in the simulation, with the attachment coefficient being left as an additional free parameter. In figure 21, the resulting response function fitted to experimental data (for a mixture with a high concentration of CF_4) is shown, and some of the Gaussians used to produce this function are also depicted in arbitrary units.

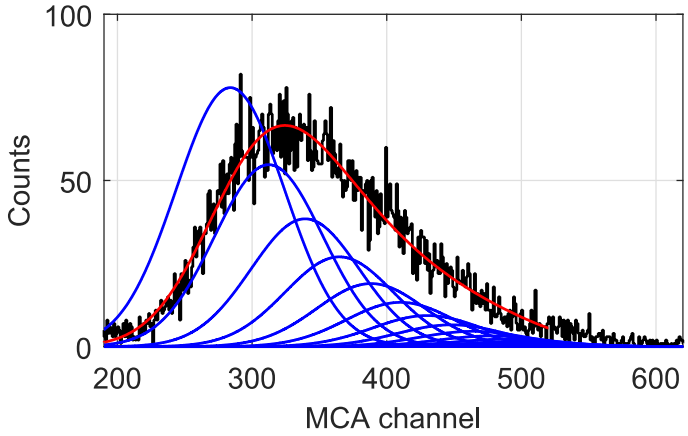

Figure 21: Pulse-height distribution (in black) obtained with the driftless GPSC filled with a mixture of Xe-CF_4 (with a CF_4 concentration of about 0.09 %), irradiated by 5.9 keV x-rays for an E/p value of 3.1 kV/cm/bar and a pressure of 1.21 bar. The detector response function (red curve) including the effect of electron attachment was fitted to data. 10 % of the Gaussians used to produce this function are also depicted (in blue) in arbitrary units.

A good agreement between the theoretical response function and the experimental data can be observed in figure 21. However, when the attachment probability is just moderate, the full absorption peak can be almost symmetric, and, in those situations, this fitting method is not accurate in estimating the corrected energy resolution. Moreover, the effects introduced in the theoretical response function in order to improve the quality of the fit (from figure 20 (a) to (b)) are speculative, leading to a possible systematic error in results.

For these reasons, the direct method was used, connecting the PMT directly to a digital oscilloscope, to investigate in detail the unique response function of the driftless GSPC, correcting properly the x-ray penetration including the attachment effect. This study was

started only after performing the data acquisition campaigns with Xe-CO_2, Xe-CH_4 and Xe-CF_4 mixtures.

5 ANALYSIS OF PMT WAVEFORMS

In this chapter, it is shown how the signal produced in the PMT is sampled, and how the events are organized according to their duration. Standard waveforms corresponding to the average PMT signal for different durations are presented. Finally, some EL parameters are obtained as a function of the duration of events, which is intrinsically related to the respective x-ray penetration. These parameters include the average number of EL detected per event, the energy resolution and the number of events taking place at each depth. In this way, the detailed operation of the driftless GPSC is accessed.

5.1 PMT waveforms' acquisition

The study of the waveforms produced by the PMT was carried out mainly with pure Xe at a pressure of about 1.25 bar. The detector was irradiated with 5.9 keV x-rays from a ^{55}Fe radioactive source, the 6.5 keV line being efficiently eliminated by a chromium filter. Because of the low voltage of the PMT signal recorded by the oscilloscope (with 50 Ω DC coupling), the PMT's polarization voltage was kept at 1400 V (which is near the maximum value specified by the manufacturer), rather than 850 V as in most measurements with CO_2, CH_4 and CF_4. Nevertheless, no degradation on the energy resolution obtained using the standard method was found when the voltage of the PMT was increased up to 1400 V. For this reason, we believe such higher voltage has no adverse effects on the results (this subject will be discussed in more detail in section 6.5.2.1).

The PMT waveforms are sampled and saved in memory for post processing as described before when the direct method was introduced. To achieve good statistics, the maximum memory of the oscilloscope is used every time a run is made, corresponding to 10^5 files, each

file having a single waveform with a timing resolution of 100 picoseconds (while the vertical resolution is 8-bits; up to 11-bits when the ERES filter is used).

Due to the long acquisition time that is required (about 100 minutes), fluctuations in the detector's working conditions (e.g. room temperature, bias voltages) may have a sizeable impact on measurements, especially on the energy resolution. Therefore, the integral of each PMT waveform is plotted as a function of time, together with a moving average and a linear fit to data, to visualize the variation of the mean energy of the events over time. Usually, the response of the detector is constant for the same run. In cases where a clear instability is observed, the entire run or at least part of it is discarded. In fact, we found out that every run should be prepared about 2 hours before taking data (allowing for stabilization of the instrumentation), to get optimal energy resolutions.

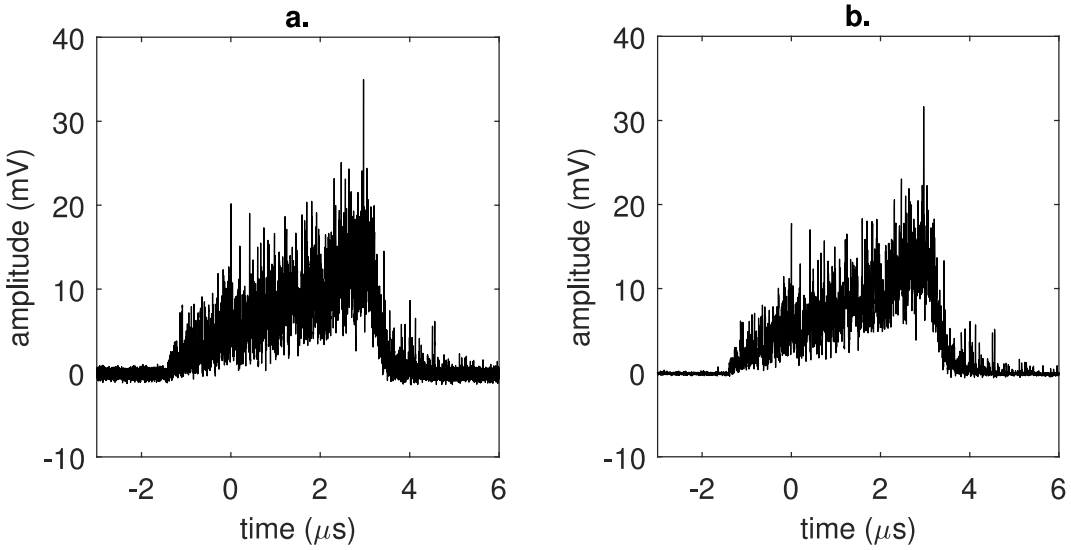

Figure 22: Randomly chosen waveform obtained directly from the PMT, in (a), and after the 20 times size reduction, in (b), for pure Xe at a pressure of 1.21 bar, E/p = 2.32 kV/cm/bar, PMT bias voltage of 1400 V and 50 Ω DC coupling.

About 60 GB of memory is consumed for each run, making it impossible to process all data at once using the RAM memory found in an ordinary computer. Therefore, a simple algorithm was introduced to reduce the amount of information contained in each file by averaging 20 successive points of each waveform, being the 10^5 acquisitions subsequently saved in a single file. In this way, the amount of memory used can be reduced by 20 times, while high frequency noise is also attenuated. The timing resolution is degraded from 0.1 to 2 ns, nevertheless it is still appropriate for the analysis performed. In figure 22, a typical PMT waveform is shown, in (a) the signal obtained directly from the PMT, and in (b) the same signal after the size reducing method. As expected from the solid angle subtended by the PMT window towards the electron cloud, the amount of light collected grows as the cloud drifts. When most of the electrons are collected by the anode, the light signal drops sharply. Then, some small spikes for several microseconds can be observed.

The full understanding of the waveforms produced during x-ray detections is only possible after evaluating the individual response of the PMT. To this end, a blue LED was placed in front of the detector entrance window and connected to a square wave voltage generator. A wide range of LED pulse durations was study, however, only two cases are reported here, a short pulse less than 10 ns width, and long square pulse with a duration of about 4 μs, matching the typical driftless GPSC waveform duration. An example of the PMT response for each situation is shown in figure 23 (a) and (b), respectively.

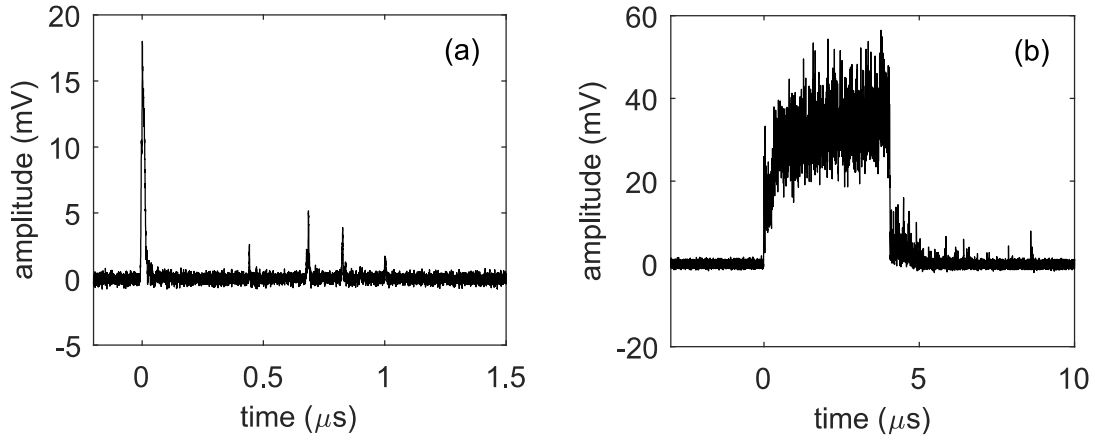

Figure 23: PMT response obtained with a short LED pulse (less than 10 ns width) in (a), and with a long square LED pulse (about 4 μs) in (b). The waveforms were directly obtained from the PMT, without any kind of noise filtering.

The FWHM of the first pulse depicted in figure 23 (a) is just 17 ns, demonstrating the fast response of the PMT (with a rising time of 4 ns according to the manufacturer), when compared to the typical drift times of electrons in the driftless GPSC. One may also observe four *afterpulses* occurring several hundreds of nanoseconds after the light burst detection. When a longer light pulse is used, as in figure 23 (b), the combined effect of the afterpulsing becomes similar to the spikes observed at the end of the driftless GPSC waveforms (e.g. figure 22 (a)). These events are most likely generated by ionized residual gases inside the PMT that return to the photocathode (ion feedback) [119]. Here, they may generate many photoelectrons, whose signal depends on the type of ion and the position where it was produced. The time delay of the afterpulses with respect to the detected signal varies with the PMT bias voltage (as it affects ion velocities), and it may range from several hundreds of nanoseconds to a few microseconds. This effect, known by the PMT manufacturers, is responsible for the degradation of the energy resolution of scintillation-based detectors and it is mostly attributed to the aging of PMTs. The large afterpulsing observed in our detector is justified by the 20 years old age of the PMT.

Despite the LED being connected to a square wave generator, the PMT response shown in figure 22 (b) is not perfectly square. This effect could be produced by the LED itself, whose

light intensity might take some time to stabilize after a given voltage being applied. A second light sensor could be used in the future to understand the source of this observation.

5.2 Background rejection

A second algorithm rejects background events, as well as waveforms that were not correctly sampled. This *background rejection algorithm* starts by rejecting waveforms with sharp negative spikes, given that the waveforms are positive (the negative signal coming from the PMT is previously inverted by the oscilloscope software). Saturated signals that are mainly produced by high energy cosmic rays are also rejected, as demonstrated by the example of figure 24 (a).

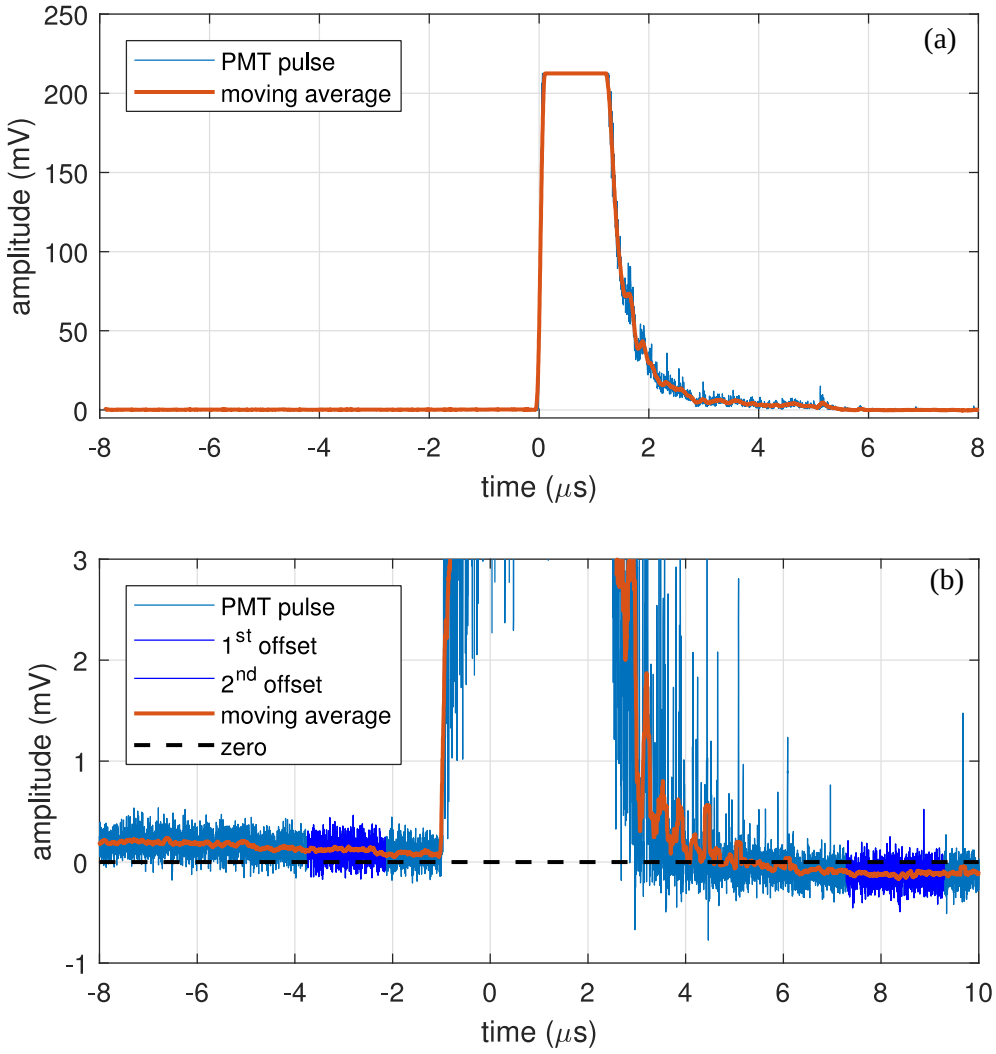

Figure 24: Two examples of rejected events: (a) saturation of the oscilloscope, probably produced by background radiation; (b) high offset of the baseline when compared to the maximum voltage of the waveform (10 mV, not shown here).

In the next stage, the PMT waveforms are identified in time, i.e. when they start and end. To reduce the probability of triggering noise spikes, a moving average is performed previously. Then, this smoother waveform is used to find both start and end times of the

events, with the first threshold being defined just above the baseline (usually at about 1% of the waveform maximum height), and the last threshold at 50 % of the smooth waveform maximum height. The baseline offset is measured just before the event begins and after it ends (at a longer distance from the end to avoid afterpulsing). If one of these two offsets are strongly deviated from zero, or between themselves, the waveform is rejected. If offsets fall within the predefined interval, the waveform passes to the next stage, with a straight line between offsets being subtracted to full waveform. This method to reject events or compensate their offsets was found to be crucial to improve the detector energy resolution (that is strongly affected by baseline fluctuations). In figure 24 (b) an example of a rejected waveform based on the offset is shown.

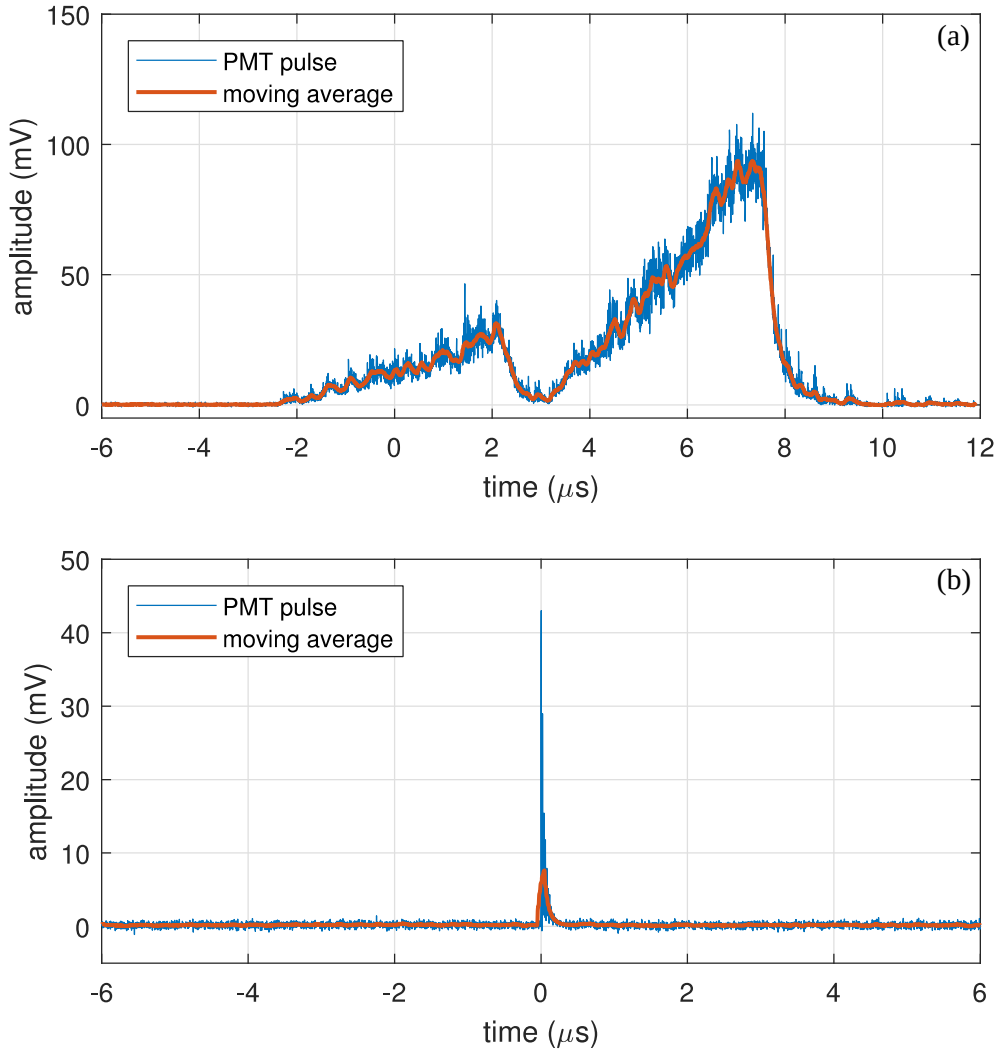

Figure 25: Two examples of rejected events: (a) excessively long waveform, a clear result of two followed events; (b) excessively short waveform.

Next, the algorithm verifies if the waveform is too long (as in the case of two successive events) or too short (for instance, when the oscilloscope triggers spikes from background photons). Waveforms that are significantly deviated in time from the trigger instant are also

rejected. In figure 25 two examples of rejected events due to the excessively long or short waveform durations are shown.

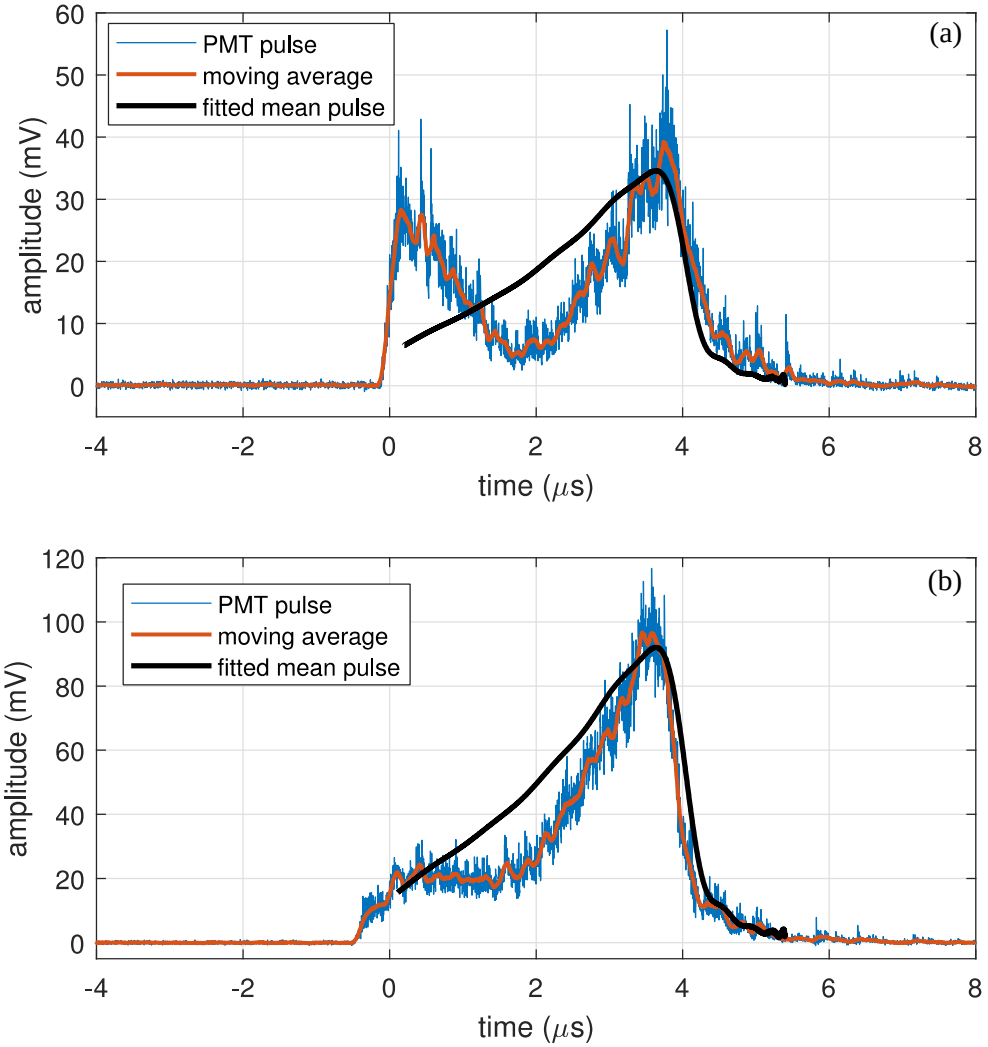

Figure 26: Two examples of rejected waveforms based on their shape. The experimental waveform is shown in blue, together with a moving average in orange. The standard waveform for the same duration interval (computed for the same run) is shown in black.

Finally, a given number (usually 1200) of the first waveforms passing through all these conditions are saved in memory to be used in the last background rejection stage. These waveforms are organized according to their durations, and an average over all waveforms within the same duration interval is used to create the standard waveforms. After this calibration, which is made at the beginning of each run, the following waveforms are fitted to the standard waveform of the respective duration, and the R-squared is computed. If R-squared is below a given boundary (usually 0.9) the event is rejected, since it is most likely a distorted waveform (for instance, produced by background radiation or xenon L-escape x-rays which may interact far from the electron cloud). This ultimate rejection method has shown to be decisive, when detailed information about waveform shapes are required. In figure 26 two examples of rejected waveforms based on their shape are shown.

5.3 Duration and alignment of waveforms

An accurate determination of the duration of every waveform is needed to perform an effective x-ray penetration's correction on the energy spectrum. The correct alignment in time of the waveforms is also critical for other measurements that depends on the waveform shape (e.g. attachment and longitudinal diffusion). Accordingly, the start and end instants are computed again after the background rejection algorithm, but now following a more accurate and computationally heavy methodology.

If the start or end thresholds are absolute values, the waveform duration will slightly depend on the number of primary charges produced in each event, compromising the x-ray penetration correction of the energy spectrum. For this reason, the two thresholds should be set according to the waveform height, which is proportional to the total number of primary electrons. The waveform average height is measured just before the time the maximum height is reached, thus avoiding fluctuations in the waveform fall stemming from the electron cloud size. This instant is determined by using a large span moving average to reduce fluctuations near the maximum height. The waveform average height is obtained from an average over the raw waveform amplitude within a given path length interval (4 mm width). The conversion factor between time and path length is estimated assuming that the waveform duration interval gathering more events corresponds to a path length of 2.5 cm. This procedure is demonstrated in figure 27, where the average height of the raw waveform is presented in green.

The start threshold is defined for each single waveform as a percentage of its average height, usually about 1 %. To avoid triggering into noise spikes, a small span moving average is used to find the waveform start time. The ending threshold is defined as 50 % of the waveform maximum height. The average ratio between the waveform maximum height and the average height is preliminarily computed for each run. The instant at which the waveform falls below this threshold is found using a larger span moving average to minimizing jitter. Most of our analysis depends on the careful alignment of the several waveforms, which is made using the end threshold. The 50 % threshold is also advantageous because a sharp variation of the waveform amplitude takes place in this region, thus providing a reliable way to align the several waveforms (for instance, a threshold of 20 or 90 % would produce larger fluctuations on the time alignment between waveforms). From the physical point of view, the waveform end time corresponds approximately to the instant when the middle point of the electron cloud reaches the anode.

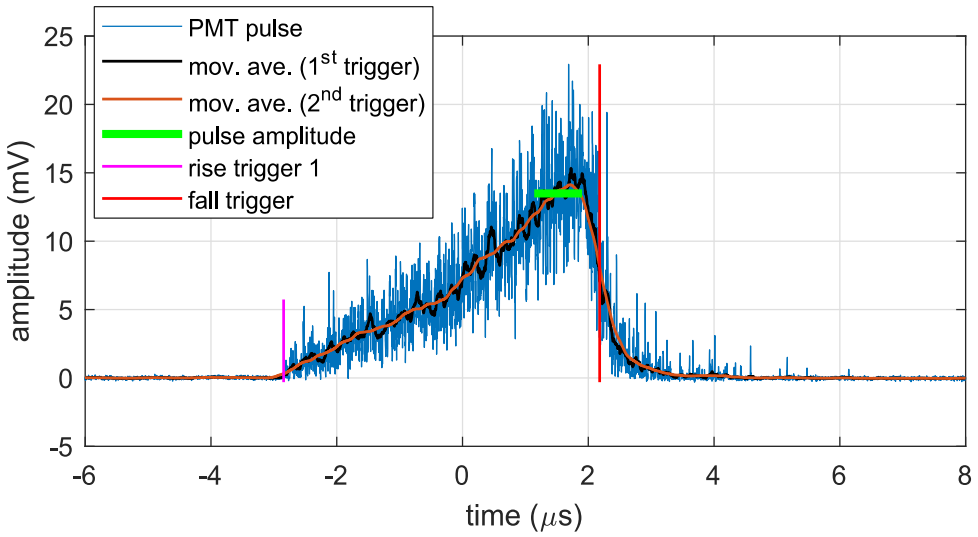

Figure 27: An example of a PMT waveforms (in blue), together with the respective start and end times (magenta and red), computed using the two moving averages (black and orange) and the waveform average height (in green).

In summary, three different smooth curves are generated, one to find the instant of the waveform maximum height (to compute the waveform average height), another one to find the waveform end time, and the last one to find the waveform start time, the moving average span being 500, 250 and 50, respectively. In figure 27, an example of a PMT waveform and respective start and end times is shown.

Since the electric field in the driftless GPSC is uniform, a linear relation between the electron drift times and the penetration of x-rays is expected. Accordingly, to gather the events corresponding to the same depth into the EL region, the waveforms are organized according to their duration (within a given interval), which is determined from the difference in time between the end and start instants. In this way, the waveform durations extend from the instant when the first VUV photons are produced to the instant when about half of the electron cloud was collected by the anode.

5.4 Standard waveforms

To obtain the standard profile of the PMT waveforms produced at similar depths, an average over all the waveforms within the same duration interval is made. In figure 28 (a), some of these standard waveforms, corresponding to different duration intervals (40 ns wide) are depicted. For the sake of clarity, only 25 % of the standard waveforms are show.

In the legend of figure 28 (a and b), the mean path length travelled by the electrons is presented instead of the waveform duration (presented in the horizontal axis), to make possible the direct identification of the respective x-ray penetrations. Despite the EL region being 2.5 cm, the path lengths extend from 1.5 to 2.6 cm (in steps of 1 mm). Next in this

chapter, the conversion between both quantities will be discussed, and this apparent inconsistency will be explained.

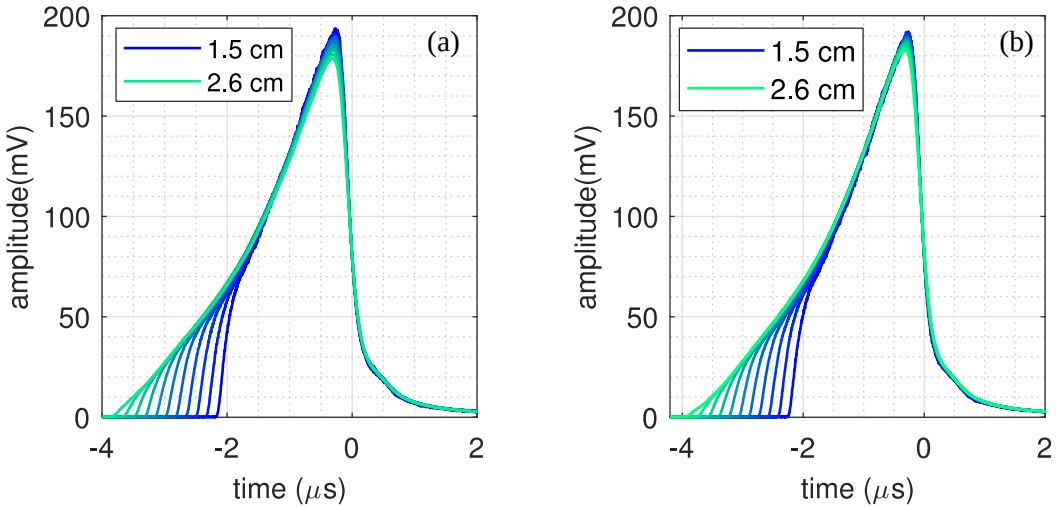

Figure 28: Standard waveforms for different duration intervals (40 ns wide), in steps of 160 ns (corresponding to a path length of 1 mm), before (a) and after (b) their areas are normalized to the respective full absorption peak centroids. The legend shows the mean electron path length extrapolated directly from the waveform durations. Data were obtained with pure Xenon irradiated with 5.9 keV x-rays, at a pressure of 1.24 bar, a reduced EL field of 3.2 kV/cm/bar and a PMT voltage of 1400 V (the PMT signal cable was terminated with a 273 Ω resistor).

After a sharp drop in the fall of the standard waveform, a much slower decrease is observed. The de-excitation time constant of the xenon scintillation process (about 100 ns [120]) cannot explain this long tail extending to the µs scale. The average effect of several spikes coming from afterpulsing (e.g. figure 22) is likely the source of this observation.

Considering solely the variation of the solid angle subtended by the PMT effective photocathode relative to a point-like electron cloud drifting at a constant speed through the EL region, the expected waveform for each total path length (Δx) is described by:

$$W(t) = 1 - \cos\left(\tan^{-1}\left(\frac{r}{\Delta x - v \cdot t}\right)\right) \qquad (11)$$

$W(t)$ is the waveform in arbitrary units as a function of time, r is the effective photocathode radius and v the electron drift velocity. In figure 29, the standard waveform obtained experimentally (one of those represented in figure 28) for a mean electron path length (Δx) of 2 cm is shown together with the corresponding theoretical waveform computed using equation (11), for a r of 2.4 cm, and a v of 6.68 mm/µs. The drift velocity was estimated from experimental data, as it will be discussed later (figure 31). However, v is here overestimated, since additional effects contributing to the waveform broadening are not considered (e.g. decay time constant of the EL process, or longitudinal diffusion).

Independently from the waveform duration, the experimental waveform does not match in shape with the respective theoretical curve. The observed discrepancy can be attributed to

the non-zero size of the electron cloud, electron diffusion, excitation and de-excitation times of the xenon scintillation process, or even reflection of EL photons on detector materials, including the PMT window. Our detector is mostly build from stainless steel, Macor and aluminium (vacuum evaporated on the Kapton entrance window). The high reflectivity of these materials to scintillation photons (57 % and 70 % experimentally obtained for stainless steel and aluminium [121]) suggest that the waveforms could be strongly influenced by reflected photons, whose intensity may change along the electron path way. Thus, the estimate of the amount of collected scintillation light based solely on solid angle considerations is not sufficient.

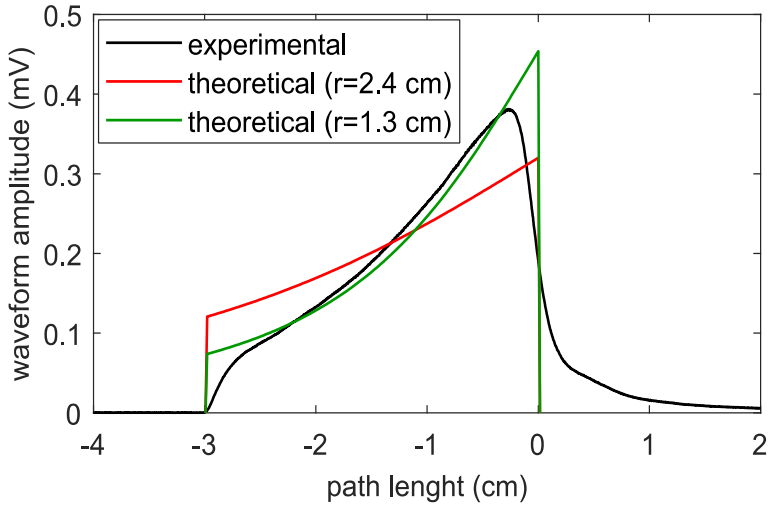

Figure 29: Experimental standard waveform (in black), corresponding to an estimated mean electron path length of 2 cm, and the respective theoretical waveform computed from the solid angle variation, when a point-like electron cloud drifts across the EL region starting 2 cm away from the PMT, either considering a photocathode radius of 2.4 cm (in red) or 1.3 c, (in green). The areas of the theoretical curves were normalized to the area of the experimental waveform between the start and end threshold.

It is still interesting to notice that the observed sharp growth of the waveform amplitude (with respect to the theoretical curves) seems to be compatible with a significantly smaller PMT photocathode radius, about 1.3 cm (as seen in figure 29). Therefore, a non-uniformity of the PMT photocathode favoring the central region could also contribute to the observed discrepancy.

5.5 Histogram of waveform integrals

To represent the detector energy spectrum for a given x-ray penetration interval, all the waveforms whose durations fall within the respective interval are integrated. Fluctuations on the PMT signal occurring before or after the waveform can be avoided by adjusting the integration interval. Therefore, this integration extends from each waveform start, minus 100 ns (ensuring no part of the signal is missed, while most of noise spikes before the waveform are excluded), up to each waveform end, plus 150 ns (thus including the full waveform, while

part of the afterpulsing is still excluded). These time intervals were chosen because the best energy resolutions were found for those conditions. It is worth highlighting that this kind of analysis is not feasible with the standard method, as the time constants cannot be dynamically adjusted for each single waveform duration. Thus, the direct method might deliver a better energy resolution. Nonetheless, it does not allow to exclude completely the afterpulsing, since part of it is contained within the waveform.

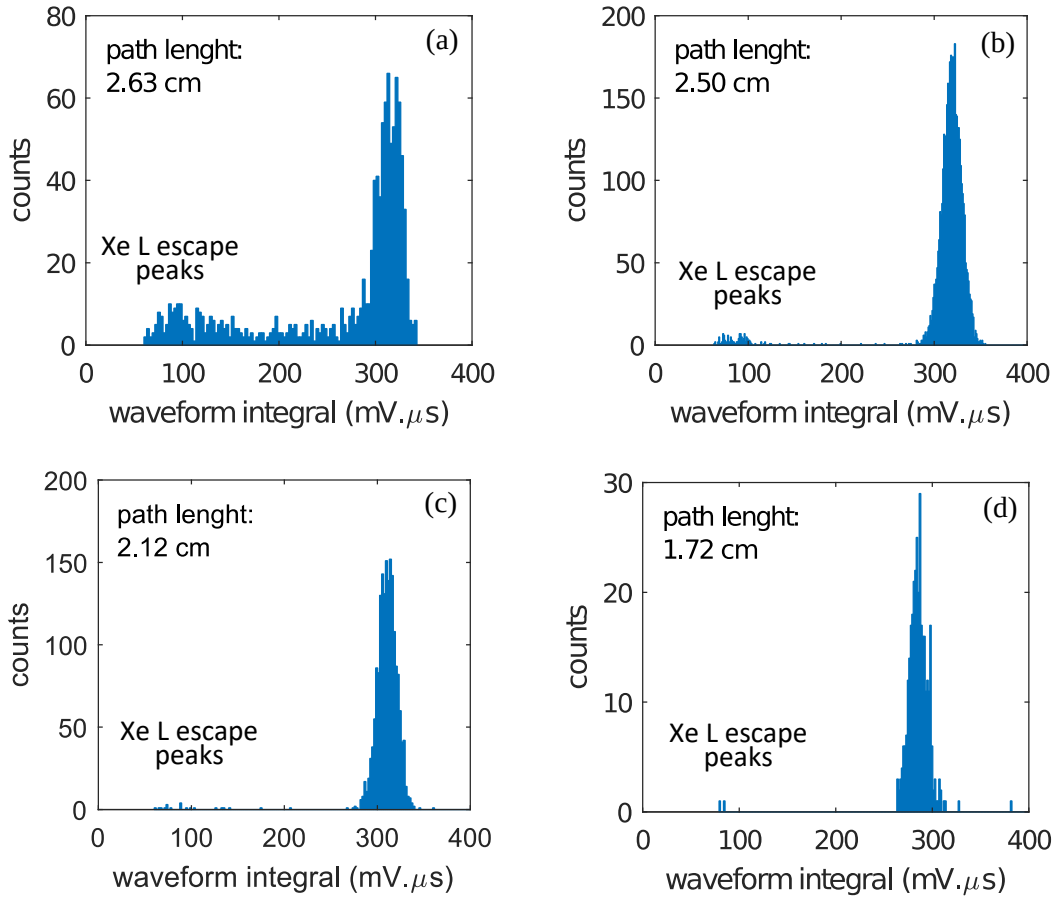

Figure 30: Uncalibrated energy spectra produced by the K-α line of a ^{55}Fe radioactive source, for different waveform durations. The respective mean path lengths drifted by electrons are indicated in each plot. Data were obtained with the detector filled with pure xenon, at a pressure of about 1.24 bar and a reduced EL field of 3.2 kV/cm/bar.

A histogram of the waveform integrals is computed for each waveform duration interval [3]. The full absorption peak has now a gaussian-like shape for any duration interval, as the x-ray penetration effect becomes negligible. Several histograms of waveform integrals for different duration intervals are depicted in figure 30. For longer durations, corresponding

[3] This histogram is analogous to the *pulse-height distribution* produced by the MCA. However, while the MCA measures the heights of the amplifier pulses, the waveform integrals are measured here (waveform heights could also be used, albeit leading to a low-resolution energy spectrum). In order to avoid confusion between both techniques, we call this distribution *histogram of waveform integrals*.

mainly to events taking place near the detector window, several counts extending to lower energies are observed, an effect attributed to the partial loss of primary electrons to the window and to the higher relative intensity of the xenon-L escape peaks.

Gaussian functions are fitted to the full absorption peak of the histogram of waveform integrals for each duration interval (only the region of the peak with more than 10 % of the peak height is included in the fit). In this way, the dependence of the total amount of collected VUV photons as well as the energy resolution on the x-ray penetration can be evaluated, by computing the Gaussian centroid and the FWHM for each waveform duration interval, respectively. However, before that, the conversion factor between the waveform duration and the corresponding x-ray penetration needs to be estimated.

5.6 Histogram of waveform durations

The x-ray attenuation's profile in xenon is accessed by counting the number of events occurring for each waveform duration interval. Only events with energies within either the full absorption peak or the xenon L-scape peaks are included. The resulting distribution is shown in figure 31 (waveform durations are shown in the upper axis), together with the theoretical exponential attenuation curve (in red) expected for 5.9 keV x-rays in xenon at a pressure of ~1.24 bar and a temperature of ~305 K. As seen, the data points follow the theoretical exponential law, except for longer waveform durations.

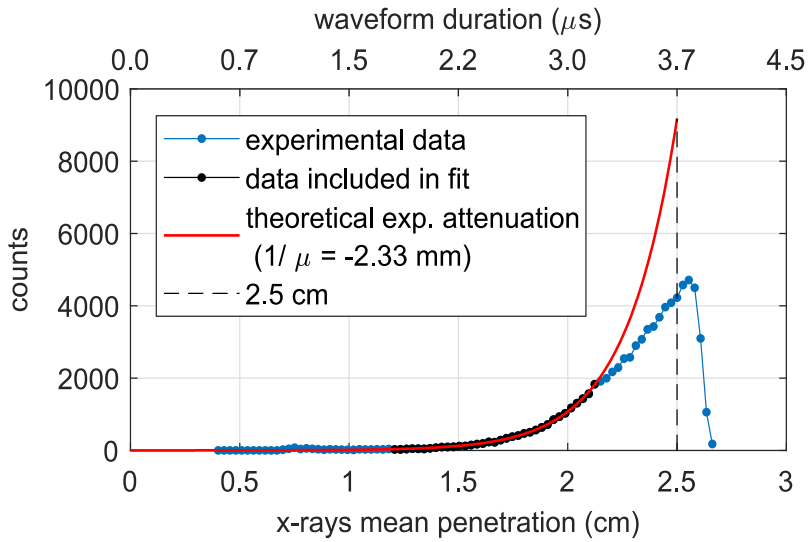

Figure 31: Histogram of waveform durations (blue and black points), which was fitted to the theoretical exponential attenuation law (red curved), in order to find the conversion factor between the duration of waveforms (upper axis) and the corresponding penetration of x-rays (bottom axis). The horizontal amplification was left as a free parameter, and zero duration corresponds to zero path length.

Unfortunately, the duration of a waveform cannot be accurately converted to the penetration of the respective x-ray because there are also fluctuations on the duration of the

VUV photon burst. This effect is clearly seen on the right part of the distribution plotted in figure 31, where events occurring likely at about the same depth in xenon have distinct durations. This effect will be discussed in more detail in section 6.4. Therefore, there is a mean duration of the events produced at 2.5 cm away from the anode, which is obtained by fitting the waveform duration distribution to the theoretical exponential law, computed considering the same operation conditions. The conversion factor, that may be interpreted as the electron drift velocity, is left as a free parameter. The points that clearly deviate from the exponential trend are excluded from the fit (represented in blue in figure 31).

To cross-check this procedure, the area between the waveform duration distribution and the theoretical exponential law below 2.5 cm path length (black dashed line in figure 31) is compared to the integral of the waveform duration distribution above the same path length. The conversion factor is adjusted so that those areas are made equal. In this way, the number of events in the theoretical curve matches the number of events in the waveform duration distribution. The conversion factors computed using both methods are usually in good agreement (with relative differences lower that 10 %).

The electron drift path length axis also shown in the figure 31 (on the bottom axis) is obtained from the multiplication between the waveform duration axis and the conversion factor. To make the following analysis more intuitive, we will talk most of the times in terms of the electron drift path length rather than the respective waveform duration. However, this is still a mean path length, thus, values above 2.5 cm may exist, although the EL region is 2.5 cm long in our detector (neglecting the outwards deformation of the Kapton window produced by the pressure differential).

5.7 Mean number of collected photons

From the histogram of waveform integrals for a given mean path length (figure 30), the centroid of the Gaussian function that is fitted to the respective full absorption's peak is extracted. The centroid is directly proportional to the mean number of photons collected by the PMT for the events occurring at that depth. This procedure is repeated for all the path length intervals. Thus, the peak centroids can be plotted as a function of the mean path length of electrons. The resulting distribution of centroids is depicted in figure 32.

Within the theoretical realm, a simplification of the distribution represented in figure 32 can be obtained by integrating the solid angle of equation (11) for the several total path lengths (z from 0 to 2.5 cm):

$$C(z) = \int_0^z 1 - \cos\left(\tan^{-1}\left(\frac{r}{x}\right)\right) dx \qquad (12)$$

$C(z)$ is the distribution of centroids and x the distance between the electron cloud and the PMT window ($x = \Delta x - v \cdot t$, from equation (11)). Solving equation (12) for a PMT photocathode radius (r) of 2.4 cm, one obtains:

$$C(z) = z - \frac{z\sqrt{\frac{25z^2}{144} + 1}}{\left(\sqrt{\frac{25z^2}{144} + 1} + 1\right)\sqrt{\frac{144}{25z^2} + 1}} \tag{13}$$

Since z is positive, equation (13) can be rearranged to:

$$C(z) = \frac{12}{5} + z - \frac{1}{5}\sqrt{144 + 25z^2} \tag{14}$$

The plot of the equation (14) for path lengths (z) ranging from 0 up to 2.6 cm is shown in figure 33, together with the experimental distribution of centroids of figure 32.

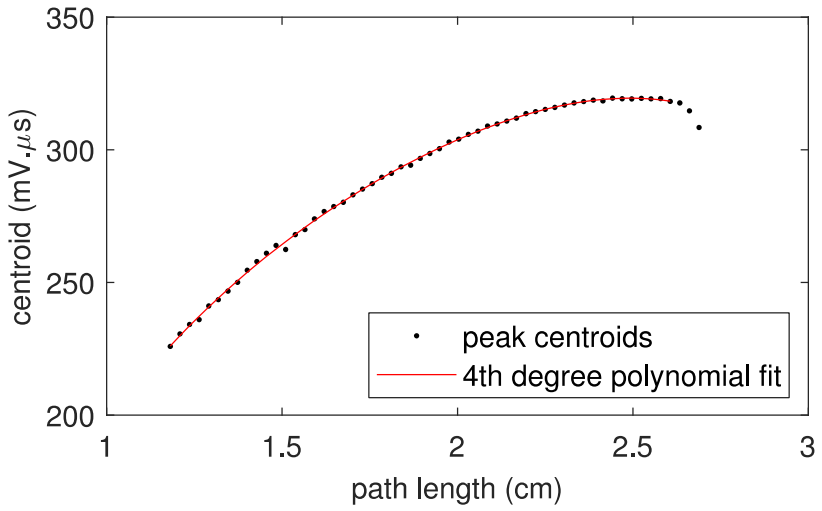

Figure 32: Distribution of centroids computed from the histogram of the waveform integrals obtained for each path length. The black points are the experimental data, while the red curve is a 4th degree polynomial fit to data, though excluding the last 3 points for the longer path lengths.

The simplified theoretical distribution deviates significantly from the experimental distribution, especially for higher path lengths. Part of the disagreement arises from the difference between the real waveform shape, and the theoretical solid angle variation (figure 29), used to compute the distribution. In addition, the path length intervals gathering the longer waveforms are not representative, because they only contain a part of the events that took place just below the detector window, the ones with longer photon burst durations. It is worth to notice, the theoretical distribution assuming a photocathode radius of 1.3 cm ($r =$ 1.3 cm in equation (12)) fits better to the experimental distribution, as demonstrated in figure 33.

In figure 32, at longer path lengths the centroid of the full absorption's peak remains almost unchanged. This observation reinforces the hypothesis that, despite having distinct

durations, most of these longer waveforms were produced by events occurring at about the same depth, i.e. just below the detector window. For these reasons, rather than fitting the theoretical function, a 4th degree polynomial function is fitted to data points in figure 32. This function will be used to correct the x-ray penetration effect on the energy spectrum of the driftless GPSC.

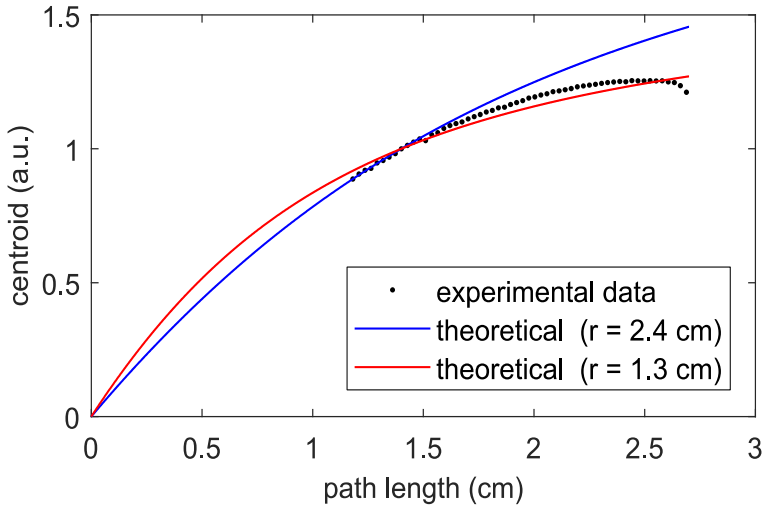

Figure 33: The simplified theoretical distribution of centroids considering either a photocathode radius of 2.4 cm (in blue) or 1.3 cm (in red), and the experimental distribution (black points, same distribution of figure 32), both being normalized to unity for the path length of 1.4 cm.

Integrating the standard waveforms of figure 28 (a), one obtains the relative average number of collected photons for each event interaction depth, analogous to the distribution of centroids of figure 32. However, the distributions deviate for higher path lengths. This mismatch is mostly attributed to events where some electrons were lost to the detector window, resulting in an asymmetric full absorption's peak (see figure 30 (a)). Consequently, the mode of the histogram of waveform integrals is different from the mean. For this reason, the integration of each standard waveform must be normalized to the respective full absorption peak's centroid (figure 32), which is less affected by this asymmetry. The result is shown in figure 28 (b), where the difference between waveforms before and after the normalization is easily observed near the maximum height.

Once the standard waveforms are correctly normalized, more information can be extracted from their shape. For instance, one may conclude that no significant electron attachment is taking place in pure xenon, since all the standard waveforms have almost the same amplitude at a given instant (e.g. 1 μs) before the end (figure 28 (b)).

5.8 Energy resolution

Figure 34 (a) depicts the energy resolution obtained for 5.9 keV x-rays from the FWHM and centroid of the Gaussians fitted to the distribution of waveform integrals produced for each

path length. The large fluctuations observed come from the low number of events occurring within each interval of x-ray penetrations. This effect is naturally more significant at higher x-ray penetrations. For this reason, the energy resolution values shown in figure 34 are not accurate, they are shown here just to demonstrate the dependence of the energy resolution on the mean path length of electrons.

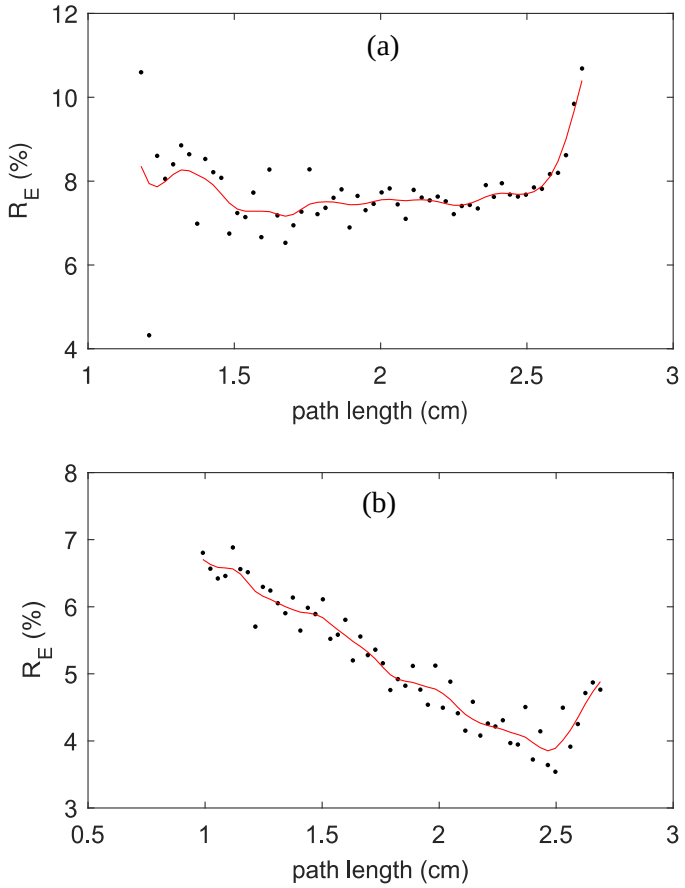

Figure 34: Energy resolution (R_E) as a function the electron path length obtained for 5.9 keV x-rays (a), and for 22 keV x-rays (b), absorbed in pure xenon. The red curve serves only to guide the eye. The reduced EL electric field, PMT cable termination, and PMT bias voltage are in (a) 3.2 kV/cm/bar, 273 Ω and 1400 V and in (b) 2.9 kV/cm/bar, 50 Ω and 1100 V, respectively. In both cases the pressure is 1.24 bar.

The energy resolution is expected to degrade with the decrease of the path length because the total number of collected photons is lower, leading to a larger contribution of the PMT photon statistics. Still, we observe a constant tendency between 1.8 cm and 2.5 cm in figure 34 (a). This result can be explained by the large light collection efficiency in our detector, combined with the short penetration of 5.9 keV x-rays. However, for more energetic x-rays (e.g. 22 keV), a considerable number of events takes place at deeper depths, exposing the energy resolution degradation for shorter path lengths (between 1 cm and 1.8 cm), as demonstrated in figure 34 (b). Nonetheless, if we subtract the PMT contribution (experimentally measured as described next in section 6.5.2.1) to these results, the energy

resolution value still increases with the decrease of the path length. This trend seems to be stronger as higher the x-ray energy is.

Since the energy resolution is better for more energetic x-rays (because of the $1/\sqrt{E}$ Poison-statistics scaling), the relative importance of additional fluctuation sources (e.g. the solid angle variation due to the x-ray beam divergence) becomes higher. In addition, the initial electron cloud produced by high energy x-rays is broader, leading to larger fluctuations in the photon burst duration. The variation of the total number of collected photons between two consecutive path lengths is higher for deeper events (figure 32). Consequently, fluctuations on the photon burst duration have a larger relative impact on the energy resolution for low path lengths, thus contributing to the trend observed in figure 34 (b).

For path lengths longer than ~2.5 cm the energy resolution is also degraded, as observed in figure 34. This effect can be related to the partial loss of electrons to the detector window; the distorted electric field near the window; or the simple fact of the waveform organization being not representative in this region, as discussed previously in this chapter.

6 *INTRINSIC ENERGY RESOLUTION*

In the present work, the intrinsic energy resolution is perhaps the most important feature, yet one of the hardest to measure with accuracy in a the driftless GPSC, as demonstrated in chapter 4. The intrinsic energy resolution is here defined as the relative FWHM obtained for a monoenergetic x-ray line due to fluctuations on charge and EL photon production, thus excluding both the x-ray penetration effect and the fluctuations on the photosensor.

In chapter 5, the driftless GPSC waveforms were sampled and organized according to their duration. Now, this information can be used to compensate each measured event energy by the respective absorption depth in the EL region, in order to produce a penetration-corrected energy spectrum. In this way, the energy resolution (ER) corrected from the x-ray penetration can be directly measured.

Before analyzing the ER obtained with molecular additives, this parameter must be deeply understood and the driftless GPSC should fully characterized, since only a few studies were reported in literature on this topic. The intrinsic resolution that is obtained with pure xenon must be compared with the results found in literature, which are well established for xenon. In this way, the methodology here developed can be validated. The knowledge acquired in this study can be used as initial motivation to build the detector response function, allowing an accurate estimation of the corrected ER of previous MCA pulse-height distributions obtained in the presence of additives.

The integrals of the waveforms are first corrected from the respective durations, and then, the intrinsic energy resolution of the driftless GPSC is measured for several x-ray energies, using the PMT photon statistics that was measured experimentally.

6.1 Method to correct the x-rays penetration

In this section, a simple method to compensate event energies based on their pulse duration is described. The full methodology developed here is only possible using the direct method. For simplicity, the study is performed with a single 5.9 keV x-ray line. The integral of each recorded waveform is divided by the centroid expected for the respective path length that is, in turn, computed from the waveform duration. This centroid is obtained from the 4th degree polynomial fit to the centroid distribution (figure 32). In this way, the 5.9 keV full absorption peaks obtained for the several path length intervals become naturally superimposed, centered in the unit. For convenience, the corrected event energies are normalized to the centroid corresponding to the path length of 2.5 cm.

The centroid distribution is not expected to change significantly with the x-ray energy, since it is mostly dependent on the solid angle and other geometric parameters. Nonetheless, the size of the electron cloud that is larger for higher x-ray energies may affect the mean solid angle subtended by the PMT window. Consequently, the centroid distribution could depend slightly on the x-ray energy. In figure 35 we depict the 4th degree polynomial functions fitted to the centroid distributions obtained for three different x-ray energies at different working conditions.

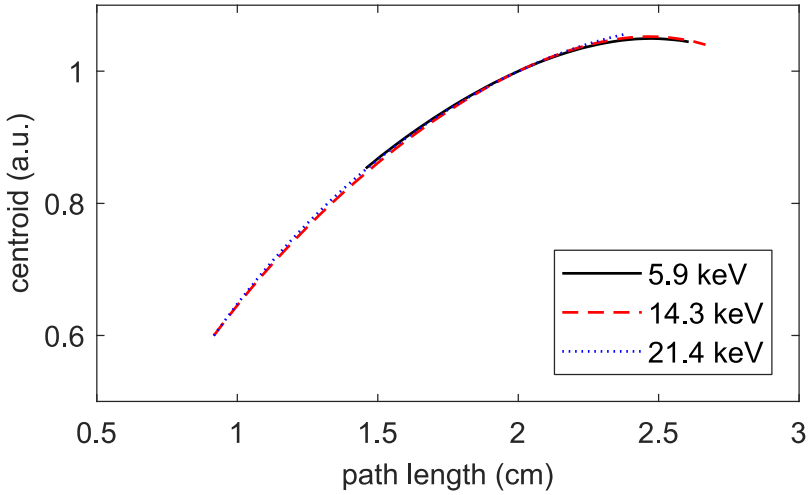

Figure 35: 4th degree polynomial functions fitted to centroid distributions obtained for three different x-ray energies (5.9, 14.3 and 21.4 keV), for reduced electric fields in the scintillation region of 3.2, 2.9 and 2.9 kV/cm/bar, respectively, at a pressure of 1.24 bar. The three curves were normalized to the unity for a path length of 2 cm.

Despite small deviations, all the three centroid distributions follow the same trend. This result shows that the variation of total amount of collected EL photons with the electron path length does not dependent significantly on the x-ray energy. In addition, since different working conditions were used, the consistency between data sets of figure 35 demonstrates also the robustness of the entire methodology, including the measurement of the waveform

durations, the organization of events according to their duration, and the conversion between waveform durations and electron mean path lengths. Even so, the centroid distribution is computed independently for every run, being then used to correct the waveform integrals according to the respective durations, thus avoiding a further degradation of the energy resolution resulting from slight variations of the centroid distribution over runs, or for different working conditions.

Since the energy spectra obtained for longer path lengths show worse energy resolutions (figure 34), this region is excluded from the present analysis (path length usually above 2.45 cm are excluded). Nevertheless, about 70 % of events are still accounted for (a 100 % detection efficiency would imply a 1 % relative degradation of ER). In addition, energy spectra for shorter path length intervals are also excluded because the statistics is too low (intervals with less than 150 events are excluded), this cutoff having a negligible impact on the detection efficiency.

In figure 36 (a), an example of the corrected energy spectrum obtained with 5.9 keV x-rays is shown. The full absorption's peak is on the right side of the plot while the xenon L-escape peaks are on the left side. This spectrum comes from the histogram of waveform integrals, after the aforementioned correction method is applied. To make it more intuitive, the histogram of integrals was calibrated by the respective theoretical x-ray energies. This procedure is explained in the next section. Therefore, the energy spectrum of figure 36 is shown in absolute units of energy. In figure 36 (b) and (c), zooms of the full absorption's peak and the xenon L-escape peaks are shown, respectively. Gaussian functions fitted to the data are also represented. As seen, the full absorption's peak of the penetration-corrected energy spectrum has now a Gaussian-like shape, yet with a minor tail on the left side. However, this residual artefact is negligible when compared with the tail of the uncorrected energy spectrum of figure 18 (a).

The low background observed in figure 36 (a) results from the high effectiveness of the background rejection algorithm based on the shape of waveforms (section 5.2). The small number of events under the xenon L-escape peaks observed in figure 36 (a) results from the exclusion of longer path lengths in this analysis, given that the probability of the xenon florescence x-rays to escape is higher near the detector window, as observed in figure 30 (b) and (c).

The full absorption's peak of the penetration-corrected energy spectrum has now a gaussian-like shape, yet, with a minor tail on the left side. The source of this residual tail is not fully understood; however, it is negligible when compared with the penetration tail of the uncorrected energy spectrum (figure 18 (a)).

Finally, the energy resolution of the detector for the 5.90 keV is estimated from the relative FWHM of the Gaussian function that is fitted to the full abortion's peak (including

only the region above 10 % of the peak height) in figure 36 (b). A value of (7.42 ± 0.02) % was found, which represents a large improvement with respect to the ~9 % value obtained with the uncorrected energy spectrum (figure 18 (a)), or the ~8 % value estimated with single gaussian fit method (figure 19). Therefore, one may conclude that despite the short mean penetration of 5.90 keV x-rays into the EL region, its impact on the energy resolution is still significant.

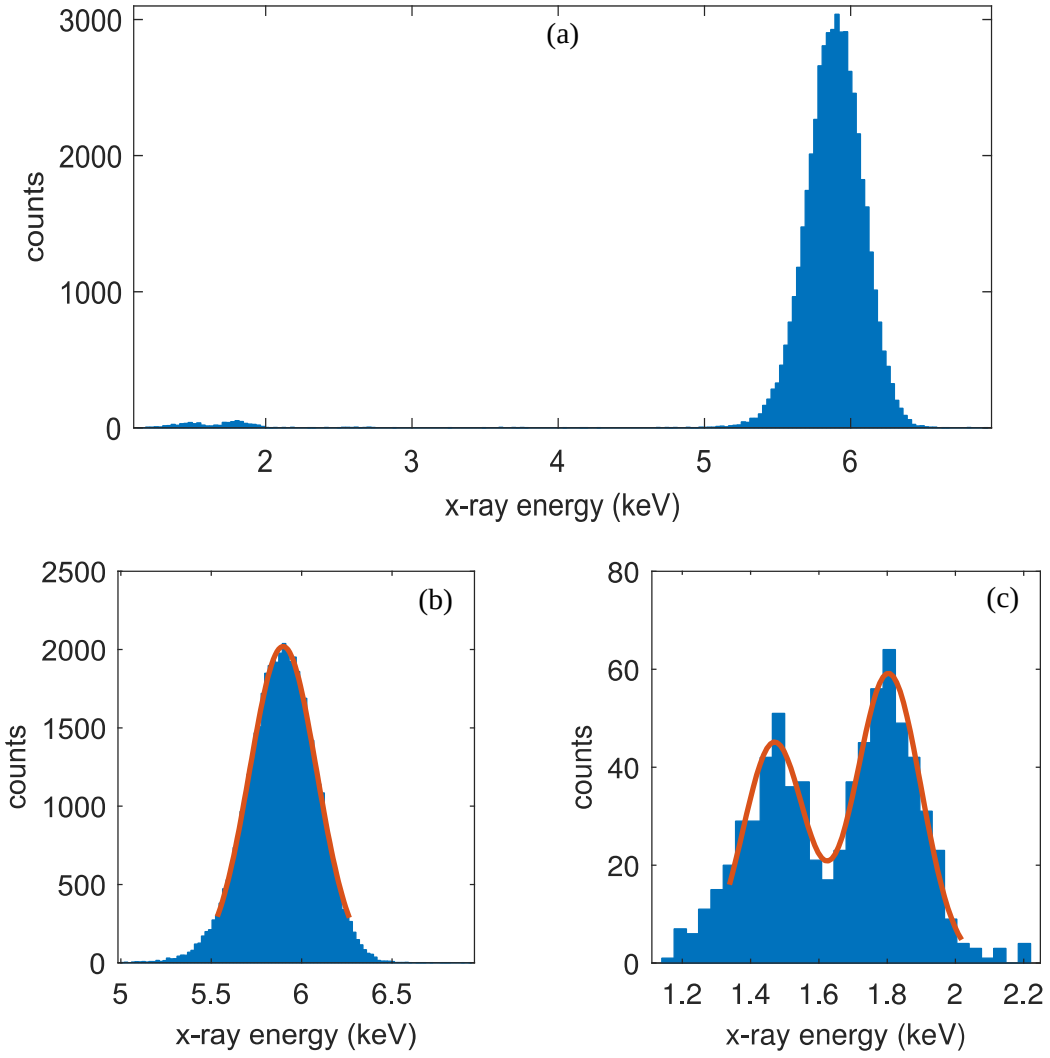

Figure 36: Energy spectrum corrected by the penetration effect obtained with a 5.9 keV x-ray beam for an EL electric field of 3.2 kV/cm/bar. The full spectrum is shown in (a), a zoom on the full absorption's peak is shown in (b), and a zoom on the L-escape peaks of xenon is shown in (c). Gaussian functions are fitted to data.

The uncertainty in the energy resolution value comes from the confidence intervals of the fitting parameters (68 % CL), except when other error estimation method is specified. The high number of events in each run, about 70000 (acquisition times of 1.5 h), explains the low uncertainty on the ER estimate. After performing several runs in the same working conditions, the standard deviation on ER is found to be ~0.05 %. This value is not far from the confidence

intervals of the fitting parameters (68 % CL), being unknown the correlation between both statistical errors. The presence of a systematic error in the ER values produced by the present method is not discarded.

The energy resolutions of the 1.79 and 1.48 keV L-escape peaks in figure 36 (c) are (12.33 $\pm$ 0.45) % and (15.11 $\pm$ 0.85) %, respectively. Compared to the values 13.47 % and 14.81 %, expected from the $1/\sqrt{E}$ scaling with reference to 5.90 keV, the better ER value obtained for 1.79 keV could be explained by the smaller size of the electron cloud produced at low x-ray energies, which may lead to lower geometrical fluctuations, while the worst ER value obtained for 1.48 keV could be due to the superposition with the L-β_2 escape. In any case, the low statistics of the xenon L-escape peaks prevent us to draw reliable conclusions.

6.2 Calibration of the energy spectrum

The xenon L-escape peaks with energies of 1.48 and 1.79 keV together with the 5.90 keV x-ray beam are used to obtain the energy calibration line, as plotted in figure 37 (a). This calibration line is then applied to the corrected histogram of waveform integrals in order to obtain the energy spectrum in absolute units, like the one represented in figure 36.

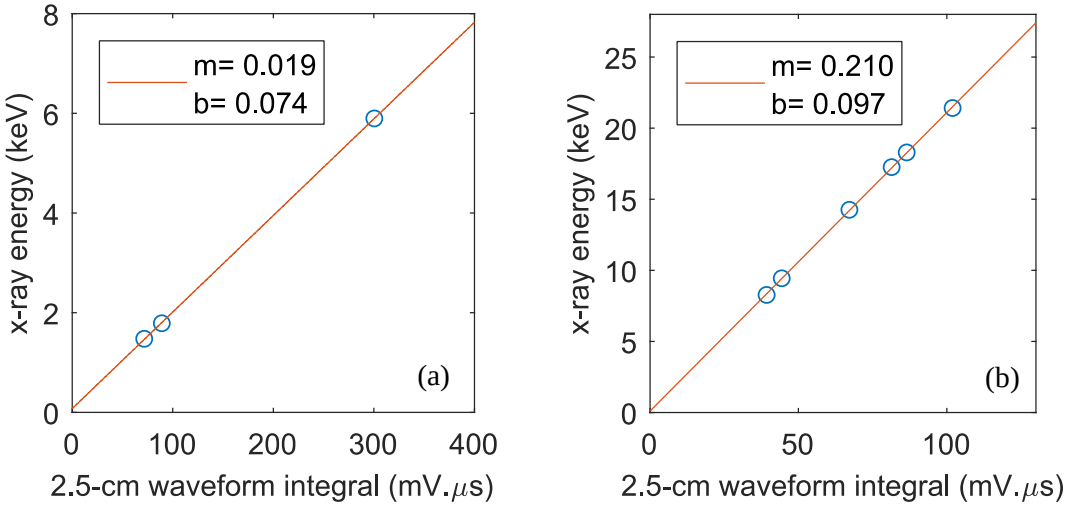

Figure 37: Two energy calibration lines of the detector, using (a) a ^{55}Fe radioactive source (with a chromium film to remove the 6.49 keV line); (b) a ^{244}Cm source (21.42, 18.29, 17.26, 14.28, 9.44 and 8.27 keV). The two data sets were obtained at different working condition.

In figure 37 (b), another energy calibration line is depicted for higher energy x-rays, emitted by a ^{244}Cm radioactive source (see figure 39). In both cases, figure 37 (a) and (b), a good linearity and a low offset are observed, reinforcing the robustness of the direct method and the software here developed to analyse the PMT waveforms. The offset was found to be always positive, usually around 0.08 keV. Despite being small, the offset has a measurable impact on the energy resolution calculation, which is slightly improved (~1 % relative at most). The reason for the distinct slopes of the calibration lines depicted in figure 37 is the

fact that those runs were carried out at different working conditions, including the gas pressure, the EL E/p and the load resistance at the oscilloscope input. The x-axis in figure 37 corresponds to the average over the 2.5-cm waveform integrals, whose natural units are mV.µs. If these values are normalized according to the different working conditions, the slopes of the two calibration lines become similar, as expected.

6.3 Corrected energy spectra

Xe-CO_2, Xe-CH_4 and Xe-CF_4 mixtures were studied only with 5.90 keV x-rays. However, the full characterization of the driftless GPSC, as well as the validation of the complex analysis developed along this work, is only complete if a wide range of energies is tested. Therefore, in this section, the corrected energy spectra obtained with the direct method for several radioactive sources are shown, together with the energy resolutions estimated for more energetic x-ray peaks.

6.3.1 Spectra from a ^{55}Fe radioactive source

In figure 38, the spectrum obtained with a ^{55}Fe source is shown, but this time without any chromium filter. In figure 38 (a), the K-$\alpha_{1,2}$ and the K-β lines from Mn are visible, while in figure 38 (b), the xenon L-$\alpha_{1,2}$, L-β_1 and L-β_2 escape peaks from the Mn K-$\alpha_{1,2}$ are depicted.

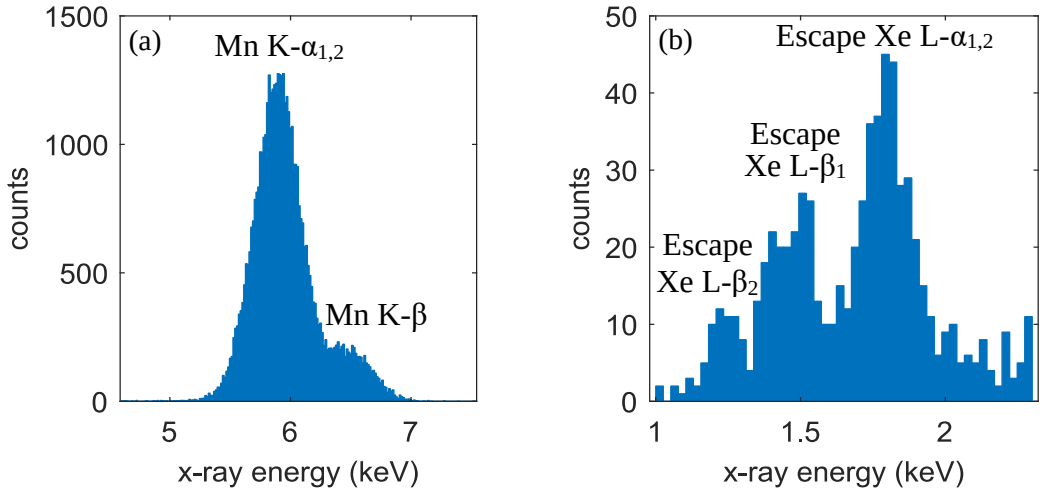

Figure 38: Corrected energy spectrum produced by a ^{55}Fe radioactive source: (a) zoom on both the K lines of Mn; (b) zoom on the L-escape lines of xenon with respect to the 5.9 keV Mn line (L-escape lines from the 6.49 keV line are hidden on the right). An EL reduced electric field of 2.9 kV/cm/bar was used.

The ER values obtained from the fit of two Gaussians to the Mn K-α (5.9 keV) and K-β (6.49 keV) peaks are (7.39 ± 0.03) % and (6.77 ± 0.16) %, respectively. The ER obtained for the 6.49 keV line is slightly better than the 7.04 % expected from the $1/\sqrt{E}$ scaling (considering an ER of 7.39 % as obtained for the 5.90 keV peak).

6.3.2 Spectra from a ^{244}Cm radioactive source

In section 5.8, the ER at high energies was found to degrade considerably for lower electron drift path length (see figure 34 (b)). Therefore, to improve the ER obtained with more energetic x-rays, the waveforms corresponding to shorter path lengths (usually shorter than 2 cm) are also excluded from the corrected spectrum. A drawback of this procedure is the considerable reduction of the detection efficiency, since many events still occur at these depths due to the larger attenuation length of x-rays. In figure 39, the corrected energy spectrum produced by a ^{244}Cm source is depicted. The principal x-ray peaks detected are labeled.

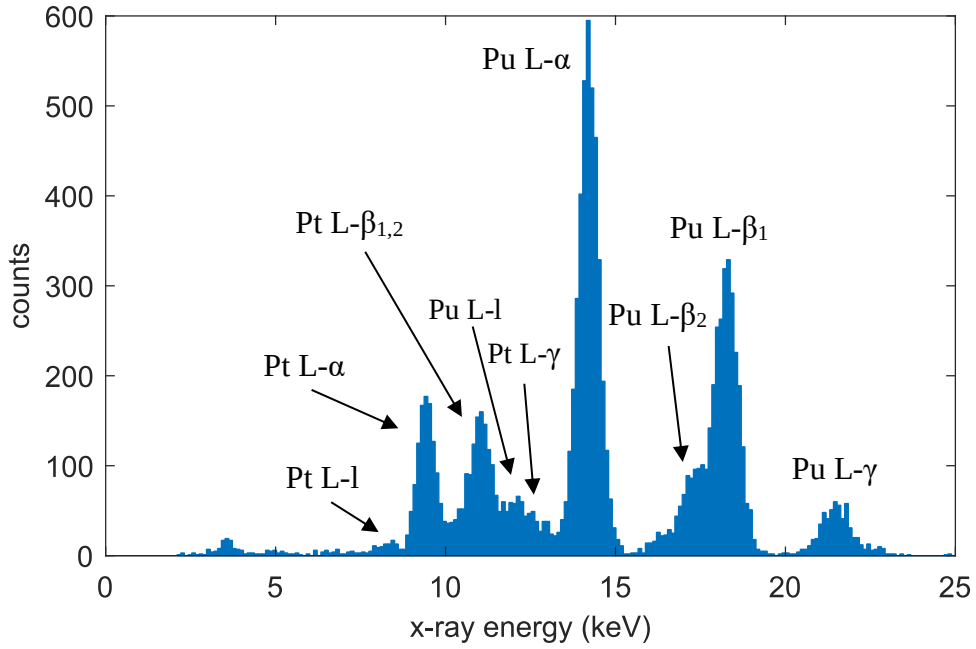

Figure 39: Corrected energy spectrum produced by a ^{244}Cm radioactive source. The principal peaks result from ^{240}Pu fluorescence, together with some peaks from Pt, which is present in the holder. An EL reduced electric field of 2.9 kV/cm/bar was used.

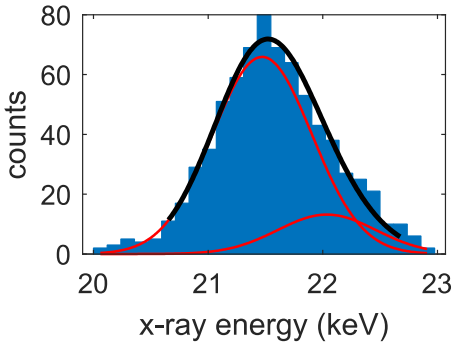

Figure 40: Pu L-$\gamma_{1,3}$ lines from the ^{244}Cm energy spectrum, after corrected by the x-ray penetration, demonstrating the double-Gaussian fit procedure. The two red curves are the fitting Gaussians corresponding to the two L-γ lines, and the black curve is the sum of them. An EL reduced electric field of 2.4 kV/cm/bar was used.

To accurately determine the energy resolution of the detector, the several mono-energetic x-rays present in the spectrum were considered. Therefore, a double-Gaussian function is fitted to each Pu series, including L-α_1 (14.28 keV) and L-α_2 (14.08 keV) lines, and L-γ_1 (21.42 keV) and L-γ_3 (21.98 keV) lines (as the difference between energies is not negligible). This fit may not converge properly in the presence of two x-ray lines with very close energies. In those cases the double Gaussian function is defined so that the ratio between energies and areas comes from the literature [122, 123], while the $1/\sqrt{E}$ scalling is used for FWHMs. This procedure is demonstrated in figure 40, where the asymmetry of the peak clearly suggests the existence of more than one x-ray line (corresponding to the Pu L-γ_1 and Pu L-γ_3 lines).

The ER values obtained for the main line energies of 21.42 keV, 18.29 keV, 17.26 keV and 14.28 keV are (4.23 ± 0.11) %, (4.43 ± 0.1) %, (4.66 ± 0.3) % and (4.59 ± 0.06) %, respectively. The ER value of the Pu L-α (4.59 %) is slightly below the value expected from the $1/\sqrt{E}$ scalling (4.76 %), while the opposite is observed for the remaining peaks. The ER values of the two Pu L-β lines are likely overestimated due to the superposition with the xenon L-escape peaks of the Pu L-γ lines. In addition, for higher x-ray energies, the larger size of the electron cloud may boost undesirable geometrical effects, justifying the worse energy resolution obtained for the Pu L-γ peak.

6.3.3 Spectra from a ^{109}Cd radioactive source

A ^{109}Cd radioactive source was also analyzed with the present setup, the corrected energy spectrum being depicted in figure 41 (a), where some of the main peaks were labeled. In figure 41 (b), an example of a double-Gaussian fit performed to the Ag fluorescence lines L-β_1 (24.93 keV) and L-β_2 (25.46 keV) is also shown.

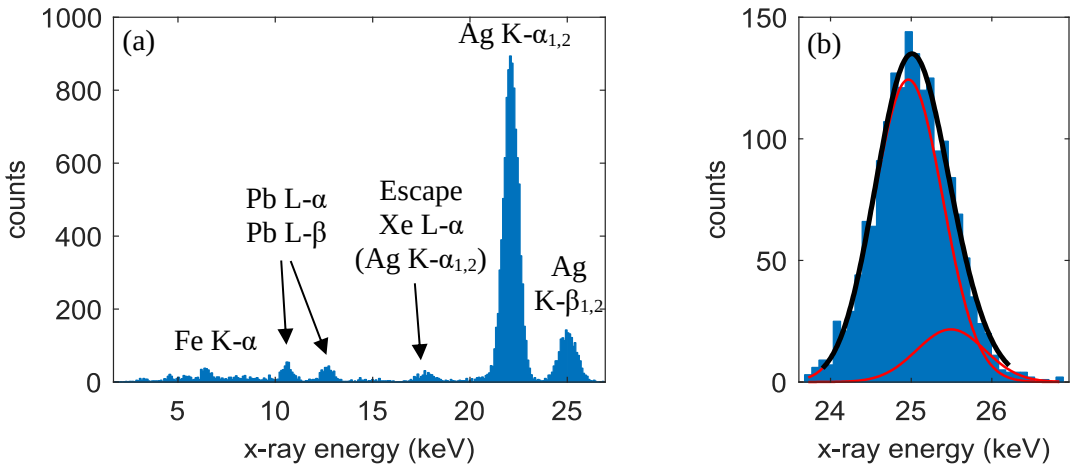

Figure 41: Corrected energy spectrum produced by a ^{109}Cd radioactive source: (a) full energy spectrum; (b) zoom on the Ag K-$\beta_{1,2}$ lines, together with a double Gaussian fit. An EL electric field of 2.9 kV/cm/bar was used. The PMT bias voltage is 1100 V rather than 1400 V.

The energy resolutions obtained for the Ag K-α_1 (22.16 keV) and K-β_1 (24.93 keV) lines were (3.82 $\pm$ 0.02) % and (3.69 $\pm$ 0.08) %, respectively, both values being in good agreement with the $1/\sqrt{E}$ scalling.

6.4 Second-order correction of the waveform integrals

The energy resolution obtained from the energy spectra corrected from the x-ray penetration effect is still an upper limit, since the extrapolation of the electron path length from the respective waveform duration is not exact (the same x-ray penetration may produce different waveform durations). Quantifying the impact of this effect on the corrected ER is crucial to accurately determine the intrinsic resolution and the Fano factor.

In order to understand the source and magnitude of the fluctuations on the photon burst duration, a simple simulation was carried out, attempting to reproduce the experimental distribution of waveform durations, stemming from the exponential absorption law of x-rays in matter (see figure 31). This simulation is described in appendix A, where the respective results are shown and discussed. The simulation was not able to predict satisfactorily the experimental distribution of waveform durations. However, data suggests that the mismatch between the experimental and exponential distributions observed for long path lengths is mostly produced by events taking place near the detector window, for which larger fluctuations on the waveform duration may occur. This hypothesis is supported by the outwards deformation of the Kapton window, which can distort the EL electric field in this region. Nonetheless, this effect would not degrade significantly the ER, as the longer path lengths are excluded from the energy spectra.

Smaller additional fluctuations are likely to occur for the full range of path lengths, hence degrading the ER of the corrected energy spectra. Some sources of these fluctuations include variations on the initial electron cloud shape [4], on the excitation and de-excitation times of the xenon scintillation process, on the longitudinal diffusion of electrons, or even on the PMT response function, which includes afterpulsing (see figure 23). It is worth mentioning that the mean initial shape of the electron cloud is not expected to be Gaussian. The radial profile has a sharp almost point-like density near zero, mainly produced by Auger electrons, and a second maximum far away from the center, resulting from secondary ionizations performed by the photoelectron. Naturally, the cloud size is larger for higher x-ray energies.

[4] The electron cloud size may depend on several factors, for instance, the photoelectron trail and the Auger electrons produced in the vacancy cascade, or even the excitation of the Xe L-shell, followed by the emission of the respective x-ray, which can deposit its energy far away from the initial position, resulting in a double-cluster electron cloud.

To minimize the impact that fluctuations on the photon burst duration may have on the corrected energy resolution, a second organization of the waveforms within each duration interval is performed, so that events with higher probability to have been produced at similar depths will be grouped together. This additional partitioning must rely on a parameter that is correlated with the penetration of the x-rays, or with the source of fluctuations on the photon burst duration. The waveform fall-time seems to be a viable choice, since it depends mostly on the final electron cloud size. In this way, a distribution of centroids analogous to the one depicted in figure 32 can be obtained for each interval of waveform durations, being used to make the 2^{nd}-order correction of the waveform integrals. The detailed description of the second-order correction is in appendix B.

Significant improvements of the energy resolution were possible using the 2^{nd} order correction method based on waveform fall times (appendix B.1): from (7.42 ± 0.04) % to (7.23 ± 0.06) % for the 5.9 keV peak, from (4.59 ± 0.08) % to (4.49 ± 0.10) % for the 14.3 keV peak, and from (3.82 ± 0.04) % to (3.69 ± 0.12) % for the 22.2 keV peak. Those energy resolutions are not estimated, but direct measurements of the relative FWHM of the two-fold corrected energy spectra. Thus, the driftless GPSC together with the software devolved in this work shows an impressive ability to resolve two nearby x-ray energies.

In addition to the duration and fall-time of the waveform, more information about the event interaction depth is most likely contained in the waveform shape. Therefore, the full potential of the driftless GPSC could be in theory unlocked using a more complex pattern recognition algorithm. In appendix B.2, we summarize some additional attempts to improve the performance of the detector using the waveform shape. Unfortunately, none of these simple ideas has shown to be as successful as the 2^{nd} order correction method based on fall-times.

6.5 Determination of the Fano factor

The relative fluctuations on primary charge production are usually quantified by the Fano factor. To estimate the Fano factor, the remaining contributions to the overall energy resolution must be subtracted. In a driftless GPSC those contributions may include fluctuations on the following parameters: the total path length drifted by the electron cloud inside the EL region (depends on the x-ray penetration); the number of photons produced in the EL process per primary electron (quantified by the *Q* factor); the number of photoelectrons extracted from the PMT photocathode per event; the PMT gain; the number of electrons lost to the detector window or to gas impurities; the overall solid angle subtended by the PMT window, which depends on the electron cloud size and on the x-ray beam divergence; or even the acquired electric signal.

Some of these fluctuation sources were minimized through the following techniques. The x-ray penetration effect is considerably reduced using both the duration and the fall-time of the waveforms. The PMT is operated at high polarization voltages to achieve high gains ($\sim 7 \times 10^5$ at 850 V, and $\sim 3 \times 10^7$ at 1400 V), so that the output signal is large compared to the electronic noise. The x-ray beam divergence is minimized with a narrow x-ray collimator (7 mm thick, 2 mm in diameter), which was placed 2 mm way from the detector window, whereas the remaining geometrical effects can be neglected in a compact detector like ours. The electron loss for the detector window or to gas impurities is minimal, since the longer waveforms are excluded from the energy spectra, and the gas purity is efficiently maintained by hot getters. Neglecting the aforementioned effects, the energy resolution (R_E) of the detector can be described by equation (10).

In pure xenon, the relative fluctuations on the EL photon production are low when compared to the fluctuation on primary charge production [96], thus equation (10) can be simplified into equation (15), where both sides of the equality were squared.

$$R_E^2 = \left(2\sqrt{2ln2}\right)^2 \left(\frac{F}{\bar{N}_e} + \frac{1}{c\bar{N}_e\bar{N}_{EL}}\left(1 + \frac{\sigma_q^2}{\bar{G}_q^2}\right)\right) \quad (15)$$

The Fano factor (F) is defined as the relative variance on the number of electrons produced during the interaction, $F = \sigma_e^2/\bar{N}_e$.

Equation (15) is a simple linear relation between R_E^2 and $1/\bar{N}_{EL}$, since the remaining variables do not change for a given x-ray energy. The constant term on this equation corresponds to the intrinsic energy resolution of the detector, which is determined by fluctuations in charge production, while the factor multiplied by $1/\bar{N}_{EL}$ is related to the fluctuations taking place in the PMT. This linear equation makes the determination of the Fano factor more intuitive and it will be used in the following sections.

6.5.1 Fano factor extrapolated at the limit of infinite number of EL photons

In this section, the Fano factor is estimated from the intrinsic energy resolution extrapolated at the limit of infinite number of EL photons ($\bar{N}_{EL} \to \infty$), when the PMT contribution becomes null in equation (15). The accuracy of this well-known method relies on the use of weak EL electric fields, for which the PMT contribution to the ER becomes larger, which is particularly important in our detector due to the high k. An E/p range from 0.9 up to 3.4 kV/cm/ bar was used for this measurement. For the resulting low intensity EL signals, the fluctuations on the oscilloscope baseline become relevant, degrading the ER obtained with the direct method. Therefore, the intrinsic R_E extrapolation for $\bar{N}_{EL} \to \infty$ is here exemplified using data obtained with the standard method (section 4.1.1). For the direct method, the Fano factor is computed using other methodology, without these limitations, as it will be demonstrated in section 6.5.2.

Unfortunately, the standard method does not allow to correct the energy of the events according to the respective durations. Consequently, ER contains the undesirable contribution of the x-ray penetration. In order to minimize this effect, the improved detector response function, introduced in section 8.2, is fitted to the MCA pulse-height distribution. Due to the low drift velocities resulting from the weak EL fields used in this study, the preamplifier and the linear amplifier may produce a sizeable distortion of the pulse-height distribution (because the ballistic deficit is larger for long waveforms). This fact justifies our choice for the improved response function over the simplified one, introduced in section 8.1, since the first one includes the effect of electronics. This fitting methodology will be described in chapter 8.

The corrected energy resolution provided by the fit of the response function to the standard method's pulse-height distribution is just an estimation, assuming all events take place at the very beginning of the EL region. On the other hand, the ER obtained from the direct method in combination with the x-ray penetration correction algorithm is a direct measurement of the relative FWHM, thus evaluating the real ability of this setup to resolve two close peaks.

In accordance with the linear relation of equation (15), the corrected R_E^2 is plotted in figure 42 as a function of the reciprocal of the relative $\overline{N}_{EL}$ $(1/A)$, together with a linear fit to data. The experimental values were obtained at different EL electric fields, with the driftless GPSC filled with pure xenon, configured with the standard method. The R_E and A values were obtained from the FWHM and centroid of the 2.5-cm path length Gaussian that is estimated by the improved response function fitted to each MCA pulse height-distribution. The error bars shown in figure 42 come from the corrected R_E uncertainty, whereas the error in $1/A$ is not show due to the low statistical uncertainty in the Gaussian centroid.

In figure 42, R_E^2 deviates from the linearity when $1/A$ is low, suggesting the existence of additional fluctuations in this region. A similar deviation from the linearity can be also observed in other GPSC studies, e.g. ref. [109]. The highest $1/A$ point seems to be also deviated from the linearity in figure 42. The electronic noise is a possible explanation for the latter case, since its relative standard deviation is larger for lower intensity PMT signals. A possible systematic error introduced by the detector response function fitting method could also explain the deviation from the linearity, observed either at low or high E/p values. In any case, those data points were excluded from the linear fit of figure 42 (black points).

The intrinsic energy resolution estimated from the y-interception of the fitted line shown in figure 42 is 6.66 %, from which the Fano factor is directly obtained (assuming no additional fluctuations contributing to the R_E constant term). For 5.9 keV x-rays, about 269 electrons are produced on average per x-ray interaction with the gas ($\overline{N}_e$), assuming an energy $w_i =$

21.9 eV required to produce an ion-electron pair [86]. Accordingly, using equation (15), a Fano factor of 0.216 ± 0.020 is obtained. The error was estimated by varying the number of points in the fit of figure 42 and evaluating the effect on F. This Fano factor agrees with other results found literature [85].

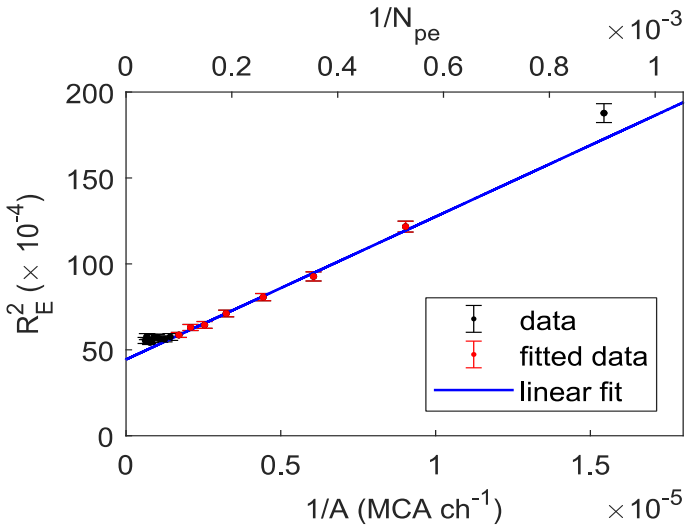

Figure 42: R_E^2 as a function of $1/A$, obtained with pure xenon. The blue line represents a linear fit to the data points in red, the black points being excluded from the fit. The corrected R_E and A were estimated using the improved response function. A PMT bias voltage of 850 V was used.

One should highlight that the electric field variation used in this method does not modifies solely the number of photons detected by the PMT, other parameters may also be affected such as: the electron loss to the grid between the drift and scintillation regions (in a regular GPSC), or to the entrance window (in a driftless GPSC); the electron attachment induced by impurities, which depends on the electron mean energy or on the number of collisions; the recombination of primary charges; geometrical effects that may depend on the electron velocity and diffusion; the power supply stability or sparks occurring at high bias voltages. These field-dependent effects may also modify (likely overestimating) the slope of the linear trend of figure 42 in relation to real PMT photon statistics line. Therefore, we do not consider this methodology reliable to accurately determine the Fano factor, despite it had been largely used in the literature, e.g. [85, 107–109].

6.5.2 Fano factor obtained directly from the energy resolution

In opposite to method described in the previous section, the PMT photon statistics is now directly measured using a pulsed LED. In this way, the influence of additional fluctuations that depend on the EL electric field is excluded, and the contribution of the electronic noise is minimized, since low intensity photon bursts are not required. Finally, the Fano factor is directly computed from several energy resolution measurements obtained with different x-ray

energies and EL electric fields, after the PMT contribution being subtracted. This approach is exemplified using data produced by the direct method.

6.5.2.1 PMT photon statistics

To measure the PMT photon statistics, a blue LED was placed in front of the detector Kapton window and connected to a pulse generator (BNC, model PB-5). Despite the reduced transparency, the amount of light crossing the window is enough for this study. The pulse duration, rise and fall times were made similar to the PMT typical waveform obtained with the driftless GPSC. The range of intensities of the LED pulses was chosen so that the integrated PMT signal covers the full range of waveform integrals obtained with x-rays.

Possible long-term fluctuations of the LED intensity were investigated. The average integral of the PMT waveforms along time was monitored, for consecutive acquisitions of 1 second. The average value was found to decrease significantly within the first 5 min after the LED starts to be operated at a given frequency and voltage. The temperature variation could be a possible explanation for this effect. Therefore, every time the LED voltage was changed, we waited 10 min before taking data. Moreover, the frequency of the pulses was set to 500 Hz, which is high enough to use short acquisition times, of about 10 s, within which long-term fluctuations are negligible. Although this frequency is high, there is enough time between pulses for the PMT and electronics to stabilize. The output of the PMT was directly connected to the oscilloscope through the 50 Ω DC coupling. The waveforms resulting from the LED pulses pass through the same analysis algorithm used previously with x-rays, including the background rejection method and the waveform integration technique (described in the chapter 5).

In the present method, the LED light is directly collected by the PMT. Therefore, the constant term of equation (15) (i.e. the Fano factor) becomes null, and the energy resolution is determined exclusively by the relative fluctuations produced in the PMT (R_{PMT}). R_{PMT}^2 is then given by the linear relation:

$$R_{PMT}^2 = \left(2\sqrt{2ln2}\right)^2 \left(1 + \left(\frac{\sigma_G}{\bar{G}}\right)^2\right) \frac{1}{\bar{N}_{pe}} \qquad (16)$$

The histogram of waveform integrals produced for each LED intensity consists in a Gaussian distribution, from which the centroid (A) and R_{PMT} ($R_{PMT} = FWHM/A$) can be measured. Varying the LED intensity, R_{PMT}^2 is computed as a function of $1/A$. Since $\bar{N}_{pe}$ is directly proportional to A, the slope of the resulting line describes the PMT photon statistics that is determined by the relative standard deviation of the PMT gain ($\sigma_G/\bar{G}$). This value is expected to be constant, at least for the same PMT operation conditions.

The standard method was also used to measure the PMT photon statistics line, allowing to cross check the results obtained with the direct method, and with the methodology described in the previous section (figure 42). The PMT output was connected to the preamplifier, followed by the linear amplifier (with a shaping constant of 8 μs, large enough to embrace the full PMT waveform) and by the MCA. Even setting the linear amplifier gain to the minimum, the signal amplitude at the MCA input was saturated for almost the full range of the LED pulse amplitudes, when the PMT bias voltage is 1400 V. Therefore, the measurements with the standard method were performed at a lower PMT bias voltage of 950 V. This voltage reduction leads to a relative improvement of the R_{PMT} value of about 15 % and 7 %, for the standard and the direct method, respectively. The high afterpulsing of the PMT might explain this effect, since it depends strongly on the PMT bias voltage (as the feedback ions inside the PMT are accelerated by the same electric field).

Another evidence that the afterpulsing degrades considerably R_{PMT} lays on the relative 4 % improvement of the R_{PMT} value that is generally obtained with the direct method when compared to the standard one (both using a bias voltage of 1400 V, and a low LED intensity to avoid saturation). The exclusion in the direct method of the afterpulsing occurring at the end of the waveforms is a possible explanation for this difference. Nevertheless, when the PMT output signal is low, the R_{PMT} value obtained with the direct method becomes worst in relation to the standard method, due to the larger impact of fluctuations in the oscilloscope base line.

Despite the R_{PMT} degradation at high PMT bias voltages being noticeable, it does not have a measurable impact on the overall detector ER, since the contribution of fluctuations related to the Fano factor is far superior. This fact was confirmed for two x-ray energies, 5.9 keV and 22.2 keV. No significant change of the respective energy resolutions was found when the PMT voltage is variated in the 850-1400 V range.

In figure 43, R_{PMT}^2 is plotted as a function of $1/A$, (a) using the direct method, and (b) using the standard method. Linear fits are also shown. As expected from equation (16), data follow a linear relation with a zero y-interception. Since A is obtained from the MCA's pulse-height distribution in the standard method, it has units of *MCA channel* (normalized according to the amplifier gain) rather than $mV^1\mu s^1$. In contrast to the previous methodology demonstrated in figure 42, the two data sets of figure 43 do not show any deviation from linearity, suggesting that the PMT is not the source of such effect. The slope of the PMT photon statistics line obtained directly with the pulsed LED is 632 *MCA ch* (figure 43 (b)), whereas the slope of the line obtained varying the EL electric field is 831 *MCA ch* (figure 42). This mismatch seems to confirm our belief that the former methodology is not reliable to measure the PMT contribution to the detector ER.

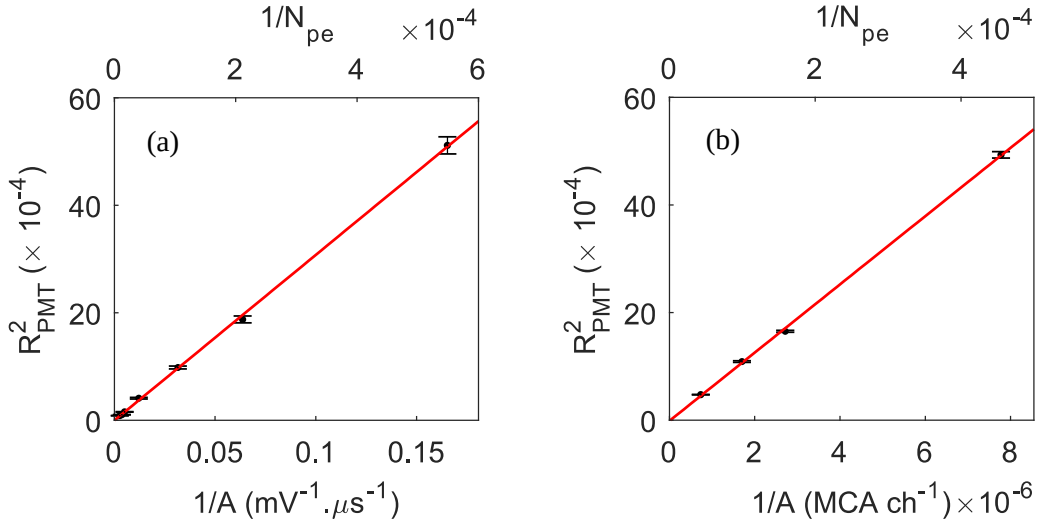

Figure 43: R^2_{PMT} as a function of $1/A$, (a) obtained using the direct method for a PMT voltage of 1400 V; (b) obtained using the standard method for a PMT voltage of 950 V. A line fitted to data is shown for each case. In both plots, $1/\bar{N}_{pe}$ is shown in the upper axis, it was obtained from $1/A$ using the PMT single-photon response (see appendix C.1).

From the lines represented in figure 43, the contribution of the PMT to the overall R_E can be determined for any x-ray energy and electric field, if the respective mean waveform integral is known. Each line of figure 43 should be used with data produced by the respective method, since additional fluctuations could depend on the data acquisition system and analysis (e.g. the afterpulsing at the end of waveforms that is excluded in the direct method). In this way, as those contributions are present in R_E as well as in R_{PMT}, they will cancel themselves during the intrinsic ER calculation.

In order to compare the two plots of figure 43 (allowing to cross check the results), the $1/A$ must be converted to absolute units, i.e. $1/\bar{N}_{pe}$ ($\bar{N}_{pe} = k\,\bar{N}_e\,\bar{N}_{EL}$), which is achieved using the PMT average gain ($\bar{G}$), obtained from the PMT single-photon response. This is a trivial procedure with the standard method, but there are some technical details when the direct method is used due to the large electronic noise. Since this study is not essential for the present work, it is described in appendix C. Through a careful oscilloscope triggering and post-processing analysis, it was possible to obtain the single-photon distribution of waveform integrals with the direct method. Both spectra obtained with the direct and with the standard method are presented in appendix C.1. In this way, the PMT average gain ($\bar{G}$) and the relative standard deviation ($\sigma_G/\bar{G}$) are estimated for the two data-acquisition systems: $\bar{G} = 3.32 \times 10^{-3}$ mV. µs and $\sigma_G/\bar{G} = 0.37$ for the direct method, and $\bar{G} = 58.5$ ch and $\sigma_G/\bar{G} = 0.56$ for the standard method.

In figure 43, $1/\bar{N}_{pe}$ is represented in the upper x-axis. The slopes of the fitted lines are 9.3 (a) and 10.8 (b). The small mismatch could be explained by the afterpulsing at the end of the waveforms that is excluded in the direct method. The afterpulsing could increase the slope

of the PMT photon statistics line in two ways, degrading R_{PMT} and overestimating N_{pe} due to the additional PMT current that was not produced by the detection of photons. An alternative independent way to compute these slopes is still possible using the measured $\sigma_G/\bar{G}$, through equation (16), as explained in appendix C.1.

Finally, in appendix C.2, $\overline{N}_{pe}$ produced by a given x-ray energy and E/p is compared with the expected value, considering the reduced electroluminescence yield reported in ref. [92] and the technical parameters of our apparatus.

6.5.2.2 Results of the Fano factor

In order to compute R_{PMT} for a given x-ray energy and electric field using the line represented in figure 43 (a), one needs to know precisely A (in $mV \cdot \mu s$), i.e. the mean integral of the PMT waveforms. However, in a driftless GPSC this value is not fixed, depending on the event interaction depth. Therefore, the mean integral of waveforms obtained for each path length is weighted by the respective number of events (i.e. the distribution of centroids of figure 32 is weighted by the distribution of durations of figure 31), to compute the overall mean integral of waveforms.

Table 1 shows some energy resolution values obtained from the corrected energy spectra, for several x-ray lines and electric fields, with the driftless GPSC filled with pure xenon at a pressure of 1.24 bar. The improved R_E obtained from the 2nd-organization of waveforms according to their fall-times is also shown in table 1 (this method is described in appendix B.1), together with the intrinsic R_E obtained by subtracting the R_{PMT} to the improved R_E.

The uncertainties on the R_E and improved R_E values represented in table 1 comes from the confidence intervals of the fit parameters (68 % CL), which were quadratically summed to an additional statistic error estimated from the x-ray penetration correction method. Nonetheless, the existence of a systematic error produced by the entire methodology here developed is not discarded. The uncertainty in the remaining values of table 1 comes only from the improved R_E error, since the contribution of the PMT statistics line is negligible.

The mean energy required to produce an ion-electron pair ($w_i = E_x/\overline{N}_e$) is expected to depend slightly on the x-ray energy (E_x), with sharp rises near the xenon absorption edges. Therefore, the w_i-values obtained from Monte Carlo simulation in [86] are assumed, in order to compute the Fano factor from the corresponding intrinsic R_E values, for each x-ray energy, through equation (15). The results are shown in table 1.

The intrinsic R_E and the Fano factor determined in this study should be interpreted as upper limits, since the unknown contribution of the fluctuations on the photon burst duration were not considered. This effect is expected to be stronger for more energetic x-rays. Even

so, the Fano factor values of table 1 agree with the experimental values found in the literature, between 0.12 and 0.26, as reported in [85] and references therein.

Table 1: Energy resolution, R_E, correct from the x-ray penetration, obtained with the driftless GPSC for several x-ray energies and E/p values. Intrinsic R_E and the Fano factor computed from the improved R_E considering the w_i-values found in [86]: 22.4 keV (for 5.9 keV x-rays), 21.9 keV (for 14.3 keV x-rays) and 21.8 keV (for 21.4 keV, 22.2 keV and 24.9 keV x-rays). The detector was operated with pure xenon at a pressure of about 1.24 bar, with a PMT bias voltage of 1400 V, except for the last two energies, where a voltage of 1100 V was used. The PMT cable was terminated by the oscilloscope input resistance, 50 Ω, except in the three first cases, where a resistor of 273 Ω was used.

x-ray (keV)	E/P (kV/cm/bar)	R_E (%)	Improved R_E (%)	Intrinsic R_E (%)	Fano factor
5.9 (K-$\alpha_{1,2}$)	2.4	7.70 ± 0.06	7.45 ± 0.10	6.89	0.226 ± 0.007
5.9 (K-$\alpha_{1,2}$)	2.9	7.43 ± 0.03	7.23 ± 0.05	6.77	0.220 ± 0.004
5.9 (K-$\alpha_{1,2}$)	3.2	7.42 ± 0.04	7.23 ± 0.06	6.83	0.222 ± 0.004
14.3 (L-α_1)	2.4	4.95 ± 0.10	4.59 ± 0.15	4.14	0.201 ± 0.016
14.3 (L-α_1)	2.9	4.59 ± 0.08	4.49 ± 0.10	4.11	0.198 ± 0.008
21.4 (L-γ_1)	2.4	3.96 ± 0.20	3.75 ± 0.30	3.40	0.204 ± 0.040
21.4 (L-γ_1)	2.9	4.23 ± 0.15	3.87 ± 0.20	3.59	0.228 ± 0.027
22.2 (K-α_1)	2.9	3.82 ± 0.04	3.69 ± 0.12	3.38	0.209 ± 0.016
24.9 (K-β_1)	2.9	3.69 ± 0.15	3.46 ± 0.25	3.16	0.206 ± 0.035

Despite the Fano factor being initially considered independent from the x-ray energy, simulation and experimental results have shown sharp increases near the xenon absorption edges (L and K atomic subshells), above which the Fano decreases slowly. These observations are explained in terms of the relative importance of the photoelectron and Auger cascading electron processes [86, 124]. Indeed, the Fano factor values obtained for 5.9 keV (just after the L xenon subshells) in table 1 are slightly larger than the values obtained for higher energies, which are, in turn, likely more overestimated.

6.6 Conclusions

In this chapter, we characterized the driftless GPSC configured according to the direct method. The detector was connected to a wide bandwidth oscilloscope, and the sampled waveforms were organized based on their durations. In this way, the event energies were corrected according to the respective x-ray penetrations. Using information about the waveform fall-times, the energy resolution of the energy spectra has been further improved.

With a simplified hardware setup (only the detector and the oscilloscope), together with software especially developed for this work, some of the best energy resolutions reported in the literature for GPSCs were achieved (for instance, 7.23 % and 3.69 % for 5.9 and 22.2 keV

x-rays, respectively) [85, 95, 108], even compared with other studies with the driftless GPSC [114–116]. Nevertheless, the performance of our detector could be improved using a PMT with lower afterpulsing, and a more complex pattern recognition method to reduce the contribution of the fluctuations on the photon burst duration to the ER value.

Finally, the Fano factor was estimated through the infinite light extrapolation technique and the subtraction of the PMT contribution, using the standard and direct methods, respectively. The detailed study of the PMT photon statistics was carried out using both conventional amplification electronics and no electronics at all. The PMT large afterpulsing was found to have a significant impact on these results. The Fano factor values obtained with both the methodologies agree within the error, showing the robustness of the analysis here developed. Nevertheless, we consider that the Fano factor computation using the standard method is not reliable, since the corrected energy resolution is an estimation, in contrast to the direct measurement of the relative FWHM performed with the direct method. Moreover, the dependence of gas-related fluctuations on the electric field may compromise the intrinsic resolution extrapolated at infinite EL light.

7 OTHER PARAMETERS EXTRACTED FROM WAVEFORMS

The initial motivation of the waveform analysis was the possibility to estimate accurately the energy resolution corrected from the x-ray penetration effect from the pulse-height distributions obtained with mixtures using the standard method. However, the direct method has shown potential besides the initial goal, providing energy spectra with very good resolutions, at the level of a regular GPSC, as shown in chapter 6. Apart from that, the direct method revealed to be a powerful tool to obtain other gas parameters that may be affected by the additive, such as the longitudinal diffusion of electrons, the dissociative electron attachment taking place in the EL region, and the scintillation probability.

The electron attachment is one of the most important parameters to be measured experimentally, because it has a profound impact on the detector energy resolution. Therefore, the knowledge of the attachment coefficient is crucial to extrapolate our results to other detector operating conditions, such as NEXT-100. In addition, the attachment coefficient provides a link to the electron transport theoretical model. In section 7.1, a detailed study of the dissociative electron attachment in Xe-CF_4 mixtures is described. First, the experimental method to measure the attachment coefficient is introduced, the obtained results are discussed and cross checked through an alternative method. Afterwards, the impact of the attachment coefficient on both the energy resolution and EL yield is experimentally quantified. A simple simulation is developed to understand the results, and to address the important role played by the PMT solid angle variation along the electron cloud path, which must be considered in any detector design when operated with attachment-inducing mixtures.

Another remarkable feature of the direct method is the ability to measure the scintillation probability. Despite this parameter being measured using the secondary scintillation yield, its knowledge helps to evaluate the impact of mixtures also on the primary scintillation signal, as the primary and secondary scintillation probabilities are expected to be roughly the same. Moreover, the scintillation probability can be used to evaluate the quenching theoretical model. In section 7.2, measurements of the scintillation probability for two Xe-CF_4 mixtures are reported, this being only possible due to the experimental quantification of the attachment effect on the EL yield.

Despite the absence of an absorption region in the driftless GPSC, the longitudinal electron diffusion under EL-typical electric fields is measured through the fall-times of the standard waveforms in section 7.3. This is possible through a careful organization and alignment of the PMT waveforms described in chapter 5. The results are compared with Magboltz simulated data. The technique here developed opens a new possibility to study experimentally the impact of mixtures on this parameter, providing also an additional way to evaluate the electron kinetic model.

Unfortunately, we were not able to perform a systematic study of these parameters in the studied mixtures using the direct method, because this work was only developed after the Xe-CO_2, Xe-CH_4 and Xe-CF_4 campaigns. Yet, the techniques described in this chapter were validated through cross-checking with other experimental methods and several simulations. Therefore, they are proof of concepts, and will be optimized in future to be extensively used in studies with mixtures.

7.1 Electron attachment

The secondary scintillation intensity is proportional to the number of drifting electrons. Therefore, the knowledge of the PMT signal as a function of time raises the possibility to evaluate the electron attachment under EL electric fields. The x-ray penetration effect in the driftless-GPSC is here advantageous, because it allows to determine the number of electrons reaching a given distance from the anode, starting at different locations.

7.1.1 Method to measure the attachment coefficient

In section 5.4, the normalized standard waveforms corresponding to several path lengths were obtained, as seen in figure 28 (b). The same procedure is applied to data produced by 5.9 keV x-rays interacting in the driftless GPSC with Xe-CF_4 mixtures (the CF_4 molecule is known to induce dissociative attachment). The standard waveforms were chosen because they contain information about the average number of electrons within the electron cloud along its path.

In figure 44, the standard waveforms obtained from different path lengths (between 1.3 and 2.5 cm) with a mixture of Xe-CF_4 are shown, together with the respective waveforms

obtained from pure xenon. The measurements were performed at similar EL E/p, 2.23 and 2.24 kV/cm/bar, for Xe-CF_4 and pure xenon, respectively. The amplitude of the Xe-CF_4 standard waveforms was normalized so that waveforms from pure xenon and the mixture overlap at the initial region, since the initial number of electrons is the same. In this way, the absolute impact of the electron attachment can be directly observed. The effect of the dissociative attachment is clear in figure 44. Unsurprisingly, the longer the path length covered by the electron cloud, the flatter the EL signal growth with time will be.

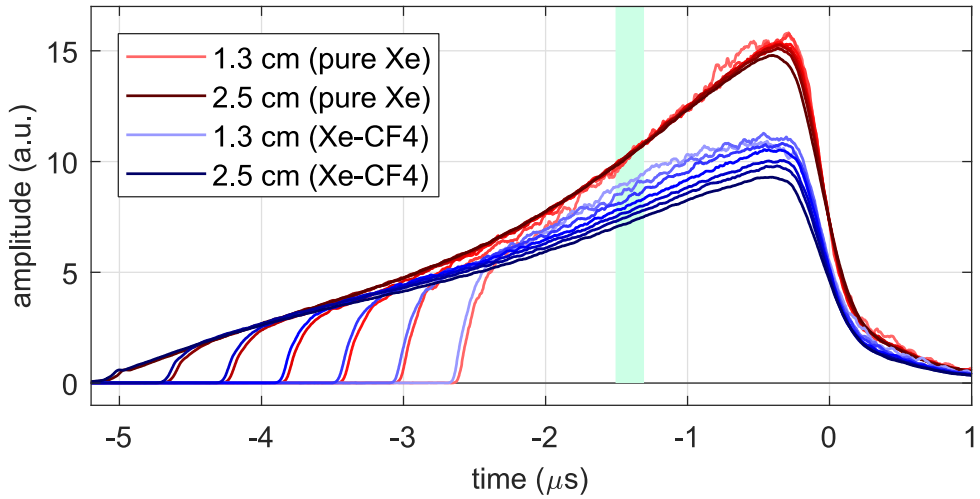

Figure 44: Standard waveforms obtained with 5.9 keV x-rays absorbed in pure xenon (in red), and in a mixture of xenon with 0.0115 % of CF_4 (in blue). The Xe-CF_4 waveforms were normalized to the pure xenon ones considering only the initial part. The green area represents the region from which $A(7mm)$ is measured. An E/p and pressure of 2.23 kV/cm/bar and 1.22 bar were used with Xe-CF_4, and 2.24 kV/cm/bar and 1.25 bar with pure xenon, respectively.

As seen in figure 44, the waveform maximum height is no more constant, growing with the x-ray penetration, since the total number of attached electrons decreases. Therefore, the method to organize the waveforms according to their durations (described in section 5.3) is slightly modified for these mixtures. The waveform start threshold is now fixed, rather than being proportional to the waveform average height, thus avoiding this effect to influence the results. For each run, the threshold is chosen as low as possible (usually about 0.2 mV), but above the baseline spikes. The end threshold is kept at 50 % of the waveform maximum height, given that the end of the event was defined as the instant when about half of the electron cloud is collected.

In order to determine the attachment coefficient, the amplitude of the several standard waveforms at a fixed instant before the end is measured, corresponding to the time when the electron cloud is at a given distance from the PMT window (the conversion between time and distance is done as described in section 5.6). We chose to use 7 mm, because the amplitude of the standard waveforms coming from pure xenon does not change in this region (as seen in figure 44). To reduce fluctuations on the measurement of the standard waveform amplitude,

a narrow interval (7 mm $\pm$ 0.5 mm for the considered position) is used rather than a single point. This procedure is demonstrated in figure 44, where the average amplitude of each mean waveform ($A(7mm)$) is measured within the region represented in green. Then, the mean path length drifted by the electron cloud up to the 7-mm point (Δx) is computed for each standard waveform (i.e. the total drifted path length subtracted by 7 mm). Finally, $A(7mm)$ is represented as a function of Δx. The result is shown in figure 45, for pure xenon and two different Xe-CF_4 mixtures (circles). The units of $A(7mm)$ (represented in the y-axis) are normalized as it will be explained in the following paragraphs.

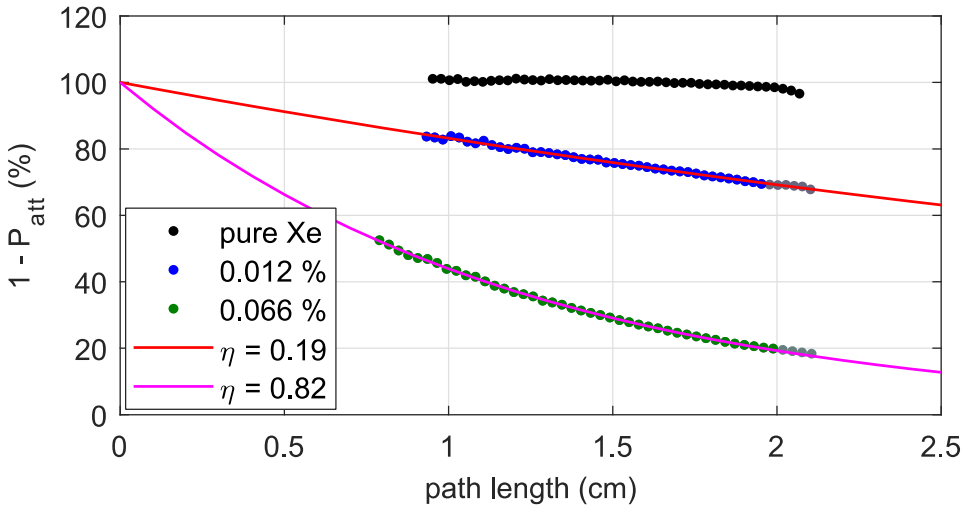

Figure 45: The average PMT signal amplitude when the electron cloud is at about 7 mm from the anode ($A(7mm)$) as a function of the path length drifted up to that point (Δx), for pure xenon (1.25 bar, 2.24 kV/cm/bar) and two mixtures of Xe-CF_4 with initial concentrations of 0.012 % (1.22 bar, 2.25 kV/cm/bar) and 0.066 % (1.23 bar, 3.26 kV/cm/bar). Two exponential functions were fitted to Xe-CF_4 data, though excluding longer path lengths (grey circles). The Xe-CF_4 data were normalized so that the exponential functions correspond to 100 % for $\Delta x = 0$, while the average value for pure xenon is normalized to 100 %. The attachment coefficient (η) can be directly extracted from the fitted functions.

For a constant drift velocity (v_d), the probability of electrons to survive along their path length ($\Delta x = v_d \Delta t$, where Δt is the elapsed time) decreases exponentially with Δx, the decay rate being defined as the attachment coefficient (η). Therefore, the probability of electrons getting attached (P_{att}) after drifting a given distance (Δx) is given by:

$$P_{att} = 1 - e^{-\eta \Delta x} \tag{17}$$

This exponential relation is clear in figure 45, especially for the higher CF_4 concentration. Nevertheless, in some cases, a small deviation from the exponential trend may be noticeable for the longer path lengths, which correspond to the longer waveform durations. As discussed before, the organization of waveforms according their durations is not accurate in this region. Accordingly, these points are excluded from the fit of figure 45 (grey circles).

On the other hand, the PMT signal obtained with pure xenon is almost independent from the path length drifted by the electron cloud (figure 45, black circles), confirming our belief that the gas purification system is highly efficient. To facilitate the direct comparison between the data sets in figure 45, the Xe-CF_4 curves were normalized, so that the respective exponential fits correspond to 100 % when the path length is zero, as no electrons are attached at this position, while the mean value obtained with pure xenon is made equal to 100 %, as no attachment is expected at all. Thus, the y-axis corresponds to $1 - P_{att}$.

From now on, $P_{att}(2.5cm)$ will refer to the percentage of electrons lost after the cloud drifts 2.5 cm ($\Delta x = 2.5\ cm$). In this way, $P_{att}(2.5cm)$ can be directly inferred from the fitted exponential curves of figure 45 for the path length of 2.5 cm, yielding 37.5 % and 87.2 %, for CF_4 concentrations of 0.012 % and 0.066 % [5], respectively.

The method used here to estimate η may produce a systematic error in the results, since additional mechanisms may affect the waveform shape along the x-ray penetration. If the 7-mm width that is used to compute $A(7mm)$ is slightly changed ($\pm$ 3 mm), a variation on η of 5 % at most is observed. The errors in η are estimated in this way. Although $A(7mm)$ obtained with pure xenon does not follow a clear exponential dependence along the Δx (black circles in figure 45), η can still be estimated, being 0.011 cm^{-1} at most. This observation could arise from a real residual attachment as a result of small concentrations of impurities, or it may be a side effect of other processes, like the electron diffusion or the x-ray beam divergence. In the latter case, the η obtained with pure xenon can be interpreted as an estimation of the systematic error of the method.

7.1.2 Method to cross check the results

To cross-check the previous results, the electron attachment can be also evaluated by comparing the standard waveforms obtained with mixtures with the reference waveforms obtained with pure xenon. In contrast to the former method, the results here obtained are relative, nonetheless, they can be considered absolute as the attachment in pure xenon is negligible.

Since the electron drift velocity depends on the EL electric field and on the CF_4 concentration, the time scale of the standard waveforms must be normalized. In this way, the duration of the standard waveform for the same path length is equal for the mixture and pure xenon, allowing their direct comparison. In the presence of a molecular additive, the number of collected photos can be affected through several mechanisms apart from attachment, e.g. xenon excimer quenching or gas transparency to VUV light. Accordingly, when the

[5] The CF_4 concentrations reported in this chapter correspond to initial values, i.e. at the time the mixtures were prepared, measured using the initial and final pressures of the two mixing volumes.

waveforms from a specific mixture are compared with the ones from pure xenon, other effects degrading the EL yield must be excluded. Therefore, the amplitude of the standard waveform from the mixture is normalized in such a way to be superimposed with the respective pure xenon waveform, in the start region. Thus, the difference between waveforms from the mixture and from pure xenon is determined by the attachment only.

An example of this procedure is depicted in figure 46 (a), where two standard waveforms for different path lengths, obtained with a Xe-CF_4 mixture, were normalized in amplitude and time to the respective waveforms obtained with pure xenon.

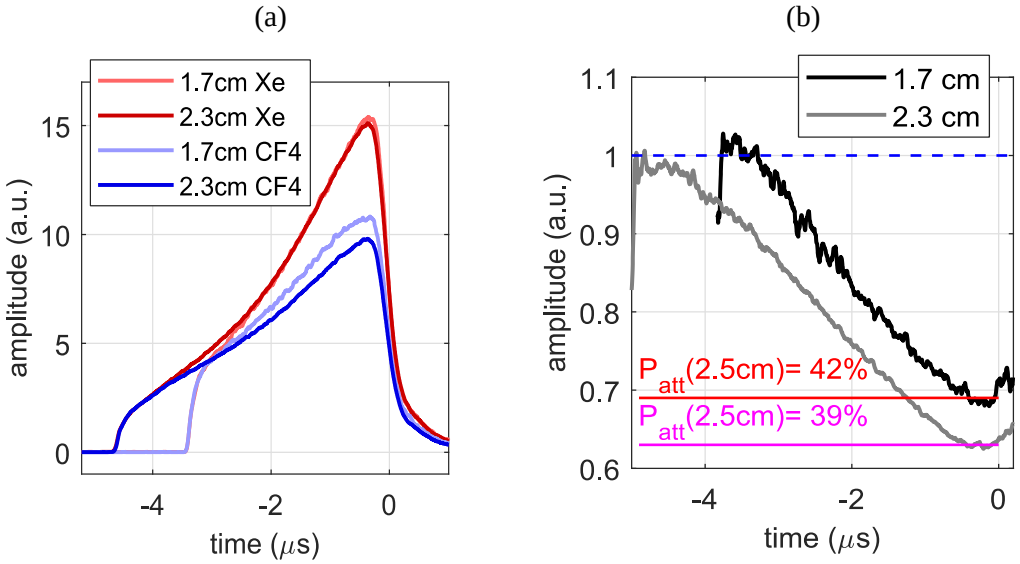

Figure 46: In (a), a comparison between the standard waveforms, for two different path lengths, obtained with pure xenon and with a Xe-CF_4 mixture with initial concentrations of 0.012 %, after normalization of their duration and their amplitude in the start region. In (b), the ratio between the Xe-CF_4 and pure xenon waveforms represented in (a), from which $P_{att}(2.5cm)$ is estimated.

$P_{att}(2.5cm)$ or η can now be measured for each path length by analyzing the ratio between the standard waveforms from the mixture and from pure xenon (as shown in figure 46 (b) for the two path lengths of figure 46 (a)). The ratio just before the end of the waveforms, corresponding approximately to the minimum observed before time 0 μs in figure 46 (b), determines the relative number of electrons that survived after drifting the respective total path lengths (1.7 cm and 2.3 cm). Therefore, these minima are used to extrapolate η or $P_{att}(2.5cm)$, through equation (17).

In contrast to the previous method, η can be measured with a single x-ray penetration. For this reason, this technique could be used with a regular GPSC, where the path length drifted by electrons in the scintillation region is always the same. The η or $P_{att}(2.5cm)$ values should not depend on the standard waveform chosen, even so, in the example figure 46 (b), the two obtained $P_{att}(2.5cm)$ are slightly different. The obtained $P_{att}(2.5cm)$ and η are generally higher for longer path lengths. Some physical effects that were excluded from the analysis may explain this difference, for instance the influence of the electron diffusion

on the waveform shape; the normalization procedure of the standard waveforms based on their start amplitude; or the accurate alignment between of the standard waveforms from both data sets. These effects may have a significant impact on the ratio curve of figure 46 (b) within the narrow region used for the measurement.

Based on these remarks, we do not consider this method as accurate as the previous one, being presented here just to cross check the results and to evaluate the systematic error that may exist in this kind of methodologies. The fairly good agreement between results obtained with these two independent methods ($P_{att}(2.5cm) = 37.5$ % in figure 45, and $P_{att}(2.5cm) =$ 39 % and 42 % in figure 46) reinforces the robustness of our measurements.

7.1.3 Attachment coefficients obtained with several Xe-CF_4 mixtures

In figure 47, the attachment coefficient and the probability of attachment for a 2.5-cm path length experimentally measured for 3 different CF_4 concentrations are shown for several EL electric fields, obtained using the method described in 7.1.1. For comparison, the expected values obtained from Magboltz simulations (version 9.0.1, for a pressure of 1 bar and a temperature of 20 ºC) are also plotted, but for different CF_4 concentrations [125]. Due to the large fluctuations in the simulated values, the respective curves were smoothed.

The attachment coefficient is expected to scale approximately with P/P_0 (considering the temperature constant), where P_0 and P are the reference and scaled pressures, respectively [1]. Accordingly, the experimental η values were scaled for the pressure of 1 bar, to be compared to the simulated values. The errors associated to the experimental data were estimated by varying slightly some of the analysis parameters (e.g. the conversion factor between the waveform duration and the path length). The simulated attachment probabilities obtained for a pressure of 10 bar and an EL gap of 0.5 cm in ref. [17] are also shown in figure 47, after these values being scaled to a pressure of 1 bar and gap of 2.5 cm.

From figure 47, the experimental attachment coefficient seems to be higher for lower electric fields, as predicted by simulations for CF_4, opposite to the case of CO_2, where η is expected to be roughly constant in the E/p range of 2-4 kV/cm/bar [70]. There is an acceptable good agreement between simulations and experimental data, especially for the lowest concentration. For a CF_4 concentration of 0.029 %, there is a systematic deviation of the experimental values with respect to the Magboltz simulation. However, the large fluctuations of the simulated data (relative variations of about 25 %, which are not shown here) prevent us to extract precise conclusions. The experimental data points are consistent with the simulated results of ref. [17]. These measurements will be crucial to reconstruct the driftless GPSC response function, as it will be shown in chapter 8.

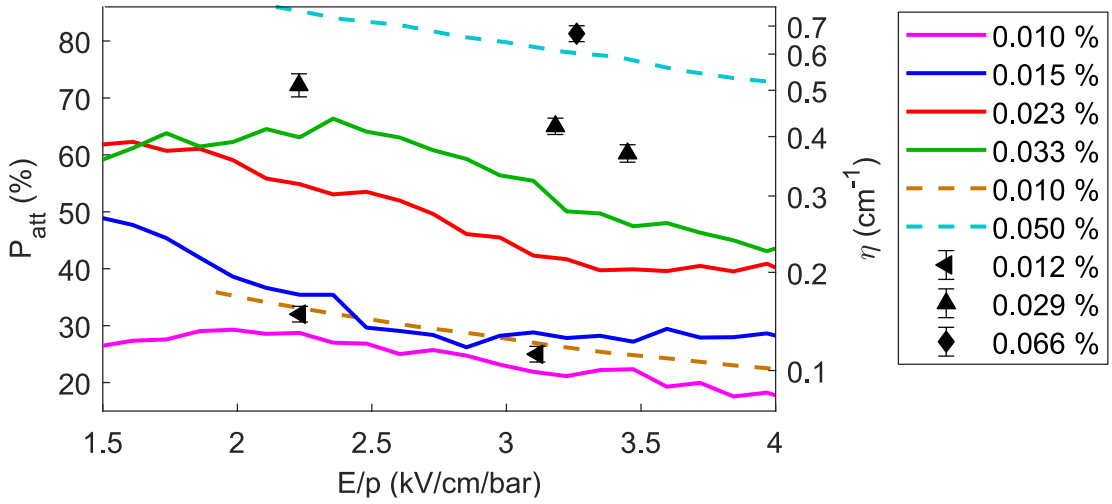

Figure 47: Probability of attachment for a 2.5-cm path length as a function of E/p for different CF_4 concentrations, obtained from Magboltz simulation (coloured solid curves, smoothed) for a pressure of 1 bar [125], and from ref. [17] after data being scaled to 1 bar (coloured dashed curves). The experimental values (extrapolated to 1 bar) measured in the present work with 3 different CF_4 concentrations are also plotted (black points). The corresponding attachment coefficient is shown on the right axis. The two lower E/p points of the 0.029 % Xe-CF_4 mixture were obtained 1 month after the mixture being prepared.

7.1.4 Experimental relation between η and Q

Similar to the Fano factor, fluctuations on the secondary scintillation light production are quantified by the Q factor, which is defined as the squared relative standard deviation on the number of EL photons produced per primary electron. There are three main contributions to Q: fluctuations in the number of excited states, fluctuations in the quenching process, and fluctuations due to electron loss. In Xe-CF_4 mixtures, the degradation of the EL yield that is observed comes mostly from the dissociative attachment (as it will be demonstrated in section 7.2). Consequently, Q is determined by attachment, as the remaining contributions are negligible. As proposed in ref. [70], in such conditions, Q can be described, in the limit of small attachment, by:

$$Q = \frac{1}{3}\eta\Delta x \tag{18}$$

Where Δx is the total path length drifted by electrons, and η is the attachment coefficient.

The Q factor for a given Δx in Xe-CF_4 mixtures can be estimated from the subtraction of the Fano factor ($F \cong 0.225$, for 5.9 keV x-rays, table 1) and the PMT contribution (figure 43) to the overall corrected energy resolution, obtained for the same Δx using a 5.9 keV x-ray beam (following the procedures described in section 6.1 and 6.4). A Δx of 2.28 cm was chosen for this study. To improve the accuracy in the determination of the energy resolution, events within a wide range of path lengths are included (Δx = (2.1-2.4) mm, since the mean

path length (2.28 cm) in an exponential distribution does not correspond to the middle point (2.25 cm)). The Q factor expected from equation (18) is also calculated assuming a Δx of 2.28 cm, using the parameter η that was measured experimentally (section 7.1.1). In this way, we can verify the theoretical relation of equation (18).

Table 2 shows the experimental Q factor (Q_{exp}) for a mean Δx of 2.28 cm obtained for several CF_4 concentrations and E/p values. The theoretical Q factor (Q_{th}), computed from equation (18), is also represented for each experimental η value, considering the same Δx (2.28 cm).

Table 2: The experimental attachment coefficient (η) and the Q-factor (Q_{exp}) obtained for a mean path length $\Delta x = 2.28$ cm, for several CF_4 concentrations and E/p values. The Q-factor (Q_{th}) obtained from equation (18) for the experimental η value is also shown, considering the same path length (Δx = 2.28 cm). The ratio between both terms (Q_{th}/Q_{exp}) is shown in the last column.

CF_4 (%)	E/p (kV/cm/bar)	η (cm^{-1})	Q_{th}	Q_{exp}	Q_{th}/Q_{exp}
0.012	3.12	0.14 ± 0.01	0.11 ± 0.01	0.18 ± 0.01	61 %
0.012	2.23	0.19 ± 0.01	0.14 ± 0.01	0.23 ± 0.02	61 %
0.029	3.45	0.45 ± 0.02	0.36 ± 0.02	0.56 ± 0.04	64 %
0.029	3.18	0.53 ± 0.02	0.40 ± 0.02	0.67 ± 0.05	60 %
0.029	2.23	0.64 ± 0.04	0.49 ± 0.01	0.92 ± 0.09	53 %
0.066	3.26	0.82 ± 0.04	0.62 ± 0.03	1.15 ± 0.14	54 %

A systematic trend is noticeable in table 2, the Q values computed from the attachment coefficient are 53 % to 64 % of the experimental Q values. The mismatch seems to be consistent within the studied range of η values**,** including the lower values where the approximation of equation (18) should be reliable, and the experimental uncertainties are smaller. Even a possible underestimation of the experimental η**,** in combination with an overestimation of the energy resolution, can hardly explain this discrepancy. As discussed in chapter 6, the energy resolution corrected by the x-ray penetration effect is overestimated, due to the fluctuations in the waveform duration. However, since Q_{exp} is computed based on the difference between the ER squared obtained for pure xenon and for Xe-CF_4 mixtures, a possible overestimation of Q_{exp} would be reduced. Nonetheless, other sources of systematic error affecting only the Xe-CF_4 data are not fully discarded.

7.1.5 Simulation of Q as a function of η and Δx

A possible source of the discrepancy between the experimental and theoretical Q factor summarized in table 2 could be the sharp variation of the solid angle subtended by the PMT photocathode along the electron cloud path, which was not considered in the deduction of

equation (18) [70]. In order to evaluate this effect, a simple simulation was performed, being described in appendix D. The influence of the solid angle variation on the total number of collected photons and respective standard deviation is demonstrated. Using this simulation, the Q-factor was estimated for the full range of experimental η values.

In figure 48, the simulated Q factor for a path length of 2.28 cm is depicted as a function of η, either when the solid angle is considered or not. The experimental values of table 2 are also plotted, together with the theoretical line predicted by equation (18).

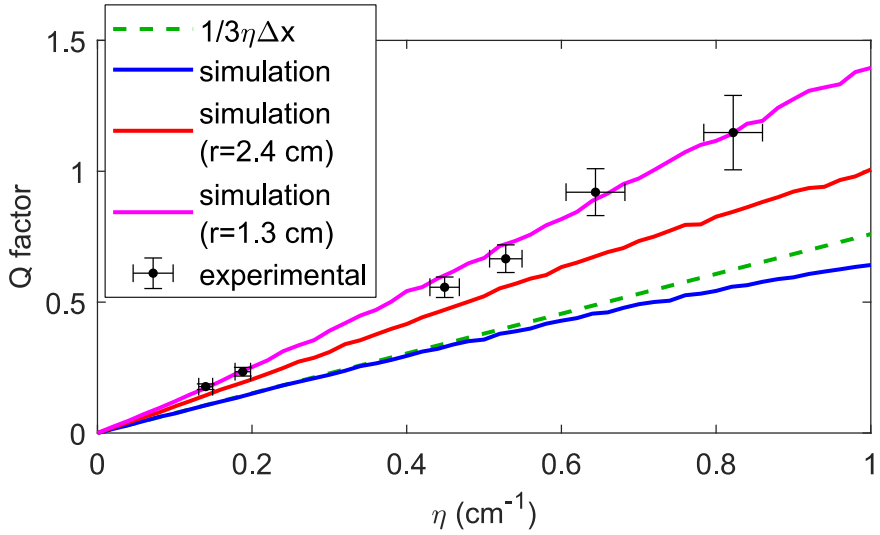

Figure 48: Experimental (in black) and simulated Q factor dependence on η, when the solid angle variation is neglected (in blue), or considered, either for a photocathode radius of 2.4 cm (in red) or 1.3 cm (in magenta). The approximated trend of equation (18) is also plotted (dashed line in green). Both experimental and simulated data were computed for a path length of 2.28 cm.

As expected, the simulated trend neglecting the solid angle variation is reproduced by equation (18), especially for lower η values, where this approximation should be valid. When the variation of the solid angle is introduced, the simulated Q factor is considerably larger, reproducing more closely the experimental data.

As discussed in section 5.4, other effects apart from the solid angle may influence the number of photons detected by the PMT along the electron cloud path. In figure 29, it was observed that the real PMT waveforms increase sharper in comparison with the expected solid angle variation. In fact, the experimental waveforms are more compatible with the solid angle assuming a circular PMT photocathode with a radius of 1.3 cm, instead of the real radius of 2.4 cm. Therefore, the simulation described in appendix D was also performed for a photocathode radius of 1.3 cm, which is here used just to modulate the observed PMT signal variation along time. The result is also shown figure 48. The simulated Q is fully compatible with the experimental values for the full range of η, demonstrating that the solid angle variation effects deeply the energy resolution of detectors operating with attachment-inducing mixtures.

Equation (18) also predicts a linear relation between Q and the total path length drifted by electrons (Δx). However, since the overall variation of the solid angle depends on the event depth, one may also anticipate a considerable deviation from the linear equation (18) in our apparatus. The same simulation described in appendix D is here employed to address the dependence of Q on Δx (finishing always at the PMT window), assuming a photocathode radius of 1.3 cm. The result is shown in figure 49 for several η values. The trend obtained with the same simulation although excluding the solid angle variation is also shown, together with the prediction from equation (18), for $\eta = 0.5$ cm^{-1}.

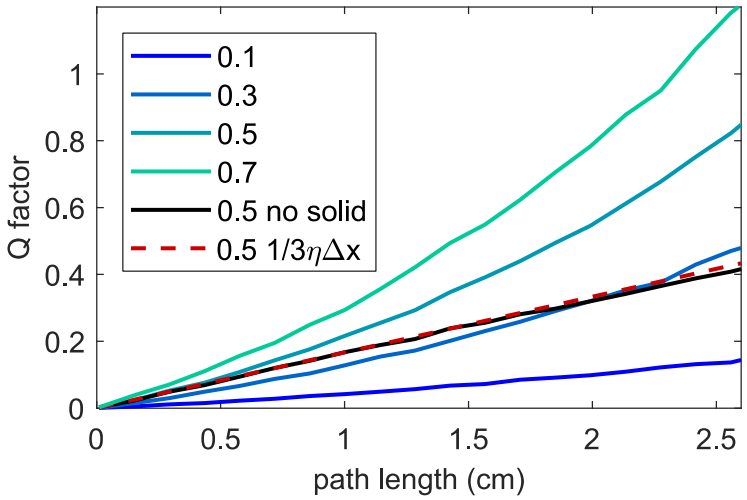

Figure 49: Q factor obtained from simulation as function of Δx for several η values (units of cm^{-1}). The Q factor obtained with the same simulation excluding the solid angle variation is also shown for η = 0.5 cm^{-1} (black curve), together with the linear relation of equation (18) (red dashed line).

As expected, the simulation excluding the solid angle variation for an attachment coefficient of 0.5 cm^{-1} agrees with the trend of equation (18). However, despite being not shown in figure 49, for higher η values, the linear relation of equation (18) becomes overestimated with respect to the simulated one. We should recall that this approximation holds just for low η values, as stated in ref. [70]. On the other hand, the simulated Q factor considering the solid angle variation shows a non-linear dependence on Δx. The relative difference between this simulation and the one neglecting the solid angle variation is larger for longer path lengths (for $\eta = 0.5$ cm^{-1}).

Unfortunately, during the detector operation with Xe-CF_4 mixtures using the direct method, only 5.9 keV x-rays were used. Consequently, data do not allow us to evaluate accurately the variation of Q with Δx, since most of the events occur within a narrow range of penetrations. This subject will be addressed again in section 8.2, where a rough comparison between data and simulation is made.

7.1.6 Impact of attachment on the number of EL photons

The mean number of EL photons produced per primary electron for each path length is naturally reduced when electrons become attached along their drift path way. Quantifying this reduction is important to understand the detector response when operated with attachment-inducing mixtures. Moreover, this study will be crucial to estimate the scintillation probabilities in mixtures, as described in section 7.2.

In ref. [70], the ratio between the EL yield in the presence of attachment (Y_{att}) and in the absence of it (Y_0) is demonstrated to follow equation (19), which is valid in the limit of low attachment:

$$\frac{Y_{att}}{Y_0} = 1 - \frac{1}{2}\eta\Delta x \tag{19}$$

where η and Δx are the attachment coefficient and the total drifted path length, respectively. Equation (19) comes from the same theoretical deduction that produced equation (18), hence it does not include the solid angle variation along the electron path. The qualitative importance of the solid angle variation can be understood observing again the distributions simulated in appendix D, which presents the total number of collected EL photons per electron. The mean of the distribution that includes the solid angle variation is lower than the mean of the distribution without the solid angle correction. Despite the impact of this technical detail on the EL yield being lower than on the *Q* factor, it is still significant.

In order to accurately quantify Y_{att}/Y_0, three different methods are described in the following sections. Then, the results are compared and discussed.

7.1.6.1 Purely theoretical method

The simulation described in appendix D is here employed to predict the Y_{att}/Y_0 dependence on η, with electrons starting a 2 cm (Δx) away from the PMT window. The solid angle variation expected from a 1.3-cm radius photocathode is considered. For comparison purposes, we also simulated Y_{att}/Y_0 assuming a constant solid angle along the electron path.

7.1.6.2 Semi-experimental method

Y_{att}/Y_0 can also be quantified using the experimental standard waveforms obtained with pure xenon, rather than the theoretical ones considering only the solid angle (see figure 29).

Following the formalism adopted along this work, where η is defined in terms of distance (η in L^{-1} units), the waveforms must be represented as a function of the drifted path length, which is accomplished using the conversion factor discussed in section 5.6 (figure 31). Obviously, when the independent variable of the waveforms is converted from time to distance, the amplitude must be normalized so that the integrals of the mean waveforms still follow the respective centroid distribution (figure 32).

Since the waveform amplitude is proportional to the number of drifting electrons, the pure xenon standard waveforms (where attachment is considered zero) are multiplied by the exponentially decreasing probability of electrons to survive along the drifted path length (equation (17)), for a given η. In this way, the effect produced by attachment in the waveforms is modulated. A good agreement was found between the modulated waveforms and the ones produced by a Xe-CF_4 mixture, for the same η (as shown in section 8.2, figure 64).

Using this method, Y_{att}/Y_0 can be estimated from the ratio between the integrals of the waveforms, after and before applying the attachment modulation, for each η value and Δx within the range of experimental path lengths. Since the standard waveforms corresponding to path lengths longer than 2.3 cm are not representative, and for path lengths below 1.5 cm the statistics is too low for 5.9 keV x-rays, we decided to compute Y_{att}/Y_0 for Δx = 2 cm.

7.1.6.3 Fully experimental method

Fortunately, the direct method together with the analyses developed in this chapter give us access to the fully experimental Y_{att}/Y_0 ratio, for each individual run. First, the effect of attachment on the waveform amplitude needs to be isolated from other sources, such as the quenching, the electron cooling, the dependence on E/p and pressure, the PMT bias voltage or the oscilloscope input resistance. The relative impact produced by these effects and working conditions on the PMT signal is expected to remain constant over the several x-ray penetrations, while the attachment probability depends on the electron path length.

Based on these considerations, the amplitude of the standard waveforms obtained from a Xe-CF_4 mixture is extrapolated at the limit of no attachment. First, the standard waveforms are represented as a function of distance, as previously done in the semi-experimental method. Then, the amplitude of the mean waveforms is measured at a given distance (7 mm) from the PMT window, for the several total path lengths (Δx). Finally, the amplitudes at 7 mm distance, $A\,(7mm)$, are represented as a function of Δx.. This method is very similar to the one used to compute η in section 7.1.1 (figure 45), except for the present analysis $A\,(7mm)$ must be absolute, whereas relative values were sufficient to obtain η. Analogously to the previous analysis, an exponential function is fitted to data, and $A\,(7mm)$ is extrapolated from the fit at the limit of zero Δx ($A\,(7mm, \Delta x = 0)$), which corresponds to the parameter a of the fit function $f(x) = ae^{-b\Delta x}$.

This procedure is equivalent to measure the PMT signal from events produced at 7 mm away from the PMT, before any electron become attached. The ratio between $A\,(7mm, \Delta x = 0)$ obtained with a mixture and the average $A\,(7mm)$ over all path lengths obtained with pure xenon (since it is nearly constant along Δx) corresponds to the modification on the corrected full absorption peak that is produced by other sources apart from attachment. This ratio defines a conversion factor (C) that can be used to normalize either the standard waveforms

or the centroid distributions obtained with mixtures to the ones obtained with pure xenon, so that they contain solely the attachment effect. In figure 50, we depict some standard waveforms corresponding to a path length of 2 cm, obtained with several Xe-CF_4 mixtures and E/p values, after this normalization procedure was applied. The pure xenon standard waveform is also shown.

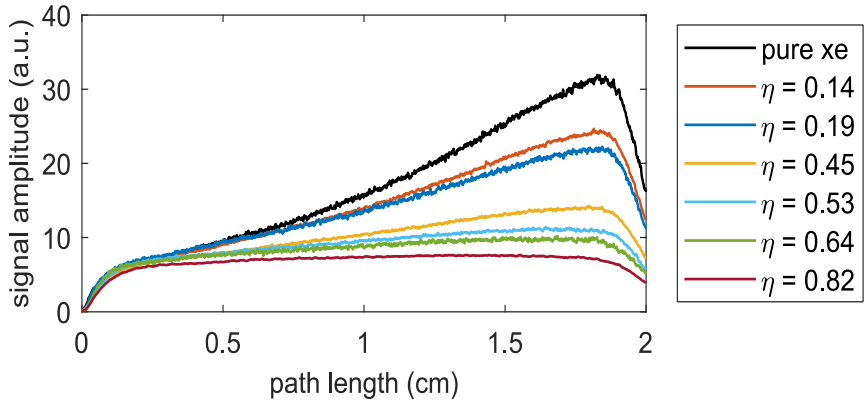

Figure 50: Standard waveforms experimentally obtained with pure xenon and three Xe-CF_4 mixtures, under several E/p values, after other effects besides the attachment being excluded. The waveforms for each η (in units of cm^{-1}) correspond to the same experimental data depicted in figure 51.

As expected, all the waveforms overlap at the beginning, where the number of attached electrons is zero. Then, the deviation with respect to the pure xenon waveform increases with the electron path length, being larger for higher η values. Finally, Y_{att}/Y_0 can be determined for any Δx (within the studied range) dividing the normalized centroid distribution obtained with mixtures by the pure xenon one. To maintain the consistency with the other two methods, this calculation is made for a Δx of 2 cm.

To cross check the results, instead of computing C as described above, it is manually adjusted so that the initial part of the waveforms become superimposed. Y_{att}/Y_0 is then estimated from the ratio between the integrals of the normalized Xe-CF_4 standard waveform and the pure xenon one, both corresponding to a Δx of 2 cm. The results obtained using this rough method agree within a 6 % relative error with the previous method. This value is used as an estimation of the error in the experimental Y_{att}/Y_0 values.

7.1.6.4 Results obtained with the three methods

We evaluated the dependence of Y_{att}/Y_0 on η through 3 different methods: the theoretical (considering or ignoring the solid angle variation), the semi-experimental and the experimental method. In figure 51, the results are compared, considering a Δx of 2 cm. The data points of the experimental method were obtained from several CF_4 concentrations and E/p, which are listed in table 2. For comparison purposes, the line predicted by equation (19) is also plotted.

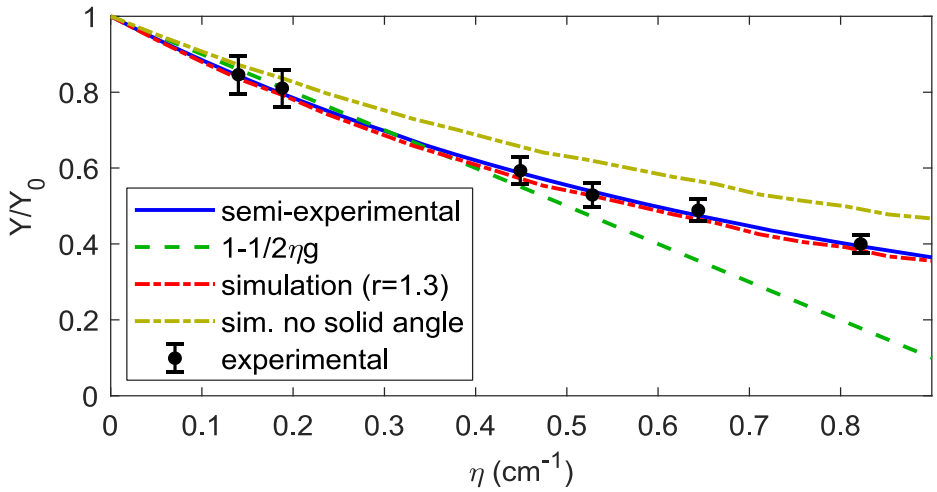

Figure 51: Ratio between the EL yield with and without attachment effect (Y_{att}/Y_0) obtained with three different methods as a function of η: in blue, the curve obtained from the pure xenon standard waveforms after the exponential attachment probability was modulated; in red and gold, the simulation results considering the solid angle variation (for a 1.3-cm radius photocathode), and a constant solid angle, respectively; in black, the experimental measurements performed with 3 different Xe-CF_4 mixtures, under several E/p values, the η values being the same ones reported in table 2. In green, the linear relation of equation (19).

The Y_{att}/Y_0 ratio from the linear relation of equation (19) (dashed green line) deviates considerably from the simulated curve neglecting the solid angle variation (dot-dashed gold curve), for η above 0.2 cm^{-1} (in contrast to Q, which deviates only for η values higher than ~0.4 cm^{-1}, as seen in figure 48).

From the two curves produced by the theoretical method (red and gold dot-dashed curves), one may conclude that the Y_{att}/Y_0 ratio is influenced by the solid angle variation, as anticipated. However, this effect is subtler than the one observed in the Q factor (figure 48). A remarkable agreement is observed between the simulated curve considering a photocathode radius of 1.3 cm and the semi-experimental curve. This confirms that the 1.3-cm photocathode was a good choice to modulate the solid angle variation. Both methods that rely on simulation (the theoretical and the semi-experimental ones) were validated by the experimental Y_{att}/Y_0 obtained for several CF_4 concentrations and E/p values. The good agreement between the three methodologies reinforces the robustness of the theoretical analysis developed in this chapter, as well as the accuracy of the experimental technique.

7.2 Scintillation probability

The scintillation probability (SP) is defined as the ratio between the number of VUV photons produced and the number of excited xenon atoms. In pure xenon, SP is about 97 % or higher [70]. For convenience, we will assume a SP of 100 % for pure xenon from now on. As mentioned before, one of the major drawbacks of using molecular additives is related to the quenching of excited states, which affects both the primary and secondary scintillation yields.

SP is expected to be nearly independent from the electric field, as the most populated states during the EL process (i.e. $1S_4$ and $1S_5$) are almost independent from the field, and the scintillation mechanism is similar for both atomic states. In addition, it is also expected that scintillation probability is similar for the primary and the secondary scintillation, since the higher energy states generally produced in the primary scintillation process decay quickly to low energy ones, thus, the additive impact on the initially populated states is negligible. Therefore, an experimental measurement of SP is crucial to understand the electroluminescence degradation, as well as to predict the possible reduction of the primary scintillation induced by the additive.

The reduced electroluminescence yield (Y/p) can be affected through several mechanisms apart from the excited states' quenching, like dissociative attachment, electron cooling or gas transparency, the latter being neglected in the present work given the compactness of the detector. In this way, SP can be estimated if we know the contribution of the remaining effects that degrade the EL yield.

The dependence of Y/p on the reduced EL electric field (E/p) is almost linear below the ionization threshold in pure xenon, a behaviour predicted by simulations and confirmed experimentally (chapter 9) [96]. The electron cooling induced by molecular additives shifts this line to higher E/p values, since more energy is required by electrons to excite the xenon atoms, thus, compensating the energy loss to inelastic collisions with molecules. This process is expected to affect solely the scintillation threshold, keeping intact the slope of the linear trend [70].

On the other hand, electron attachment may affect the Y/p (E/p) line slope, or even its linearity in some cases, due to the dependence of η on E/p (demonstrated for Xe-CF_4 mixtures in figure 47). Therefore, the attachment effect must be excluded from Y/p for each E/p value to restore the linearity, using the Y_{att}/Y_0 ratio measured in section 7.1.6 (figure 51). Thus, any subsequent slope difference with respect to the analogous pure xenon line is likely produced by quenching. In this way, SP can be obtained from the ratio between the slopes of the lines fitted to the attachment-corrected Y/p values as a function of E/p for mixtures and pure xenon.

Using the direct method, Y/p is obtained as follows. Only interactions occurring between 1.90 and 2.08 cm away from the PMT window are included, hence the mean path length covered by electrons is 2 cm. First, the histogram of waveform integrals is computed for each path length within this interval. In this way, the centroid distribution is obtained, being then weighted by the number of events for each path length. Finally, the mean centroid of the weighted distribution is calculated, and normalized according to the detector total

pressure and the PMT voltage (using the PMT gain dependence on voltage, which was obtained experimentally).

In figure 52, Y/p obtained for a mean path length of 2 cm is plotted in arbitrary units as a function of E/p, for two Xe-CF_4 mixtures (with initial concentrations of 0.012 % and 0.029 %), and for pure xenon. A line is fitted to the pure xenon data series. As expected, the number of collected EL photons for the same E/p is lower as higher the additive concentration is.

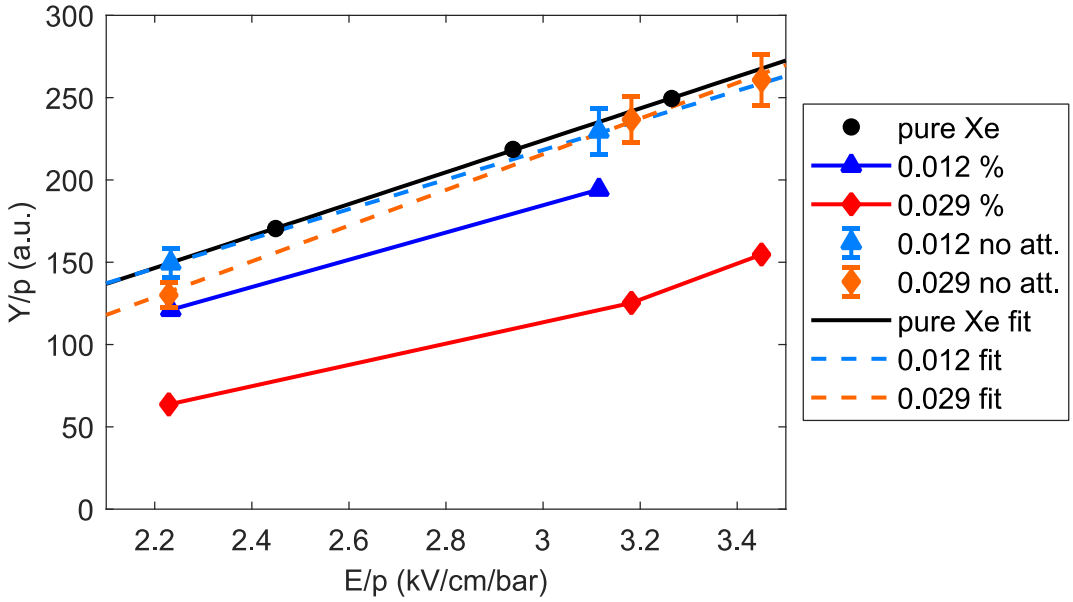

Figure 52: Reduced EL yield (Y/p) obtained for a path length of 2 cm (in arbitrary units) as a function of E/p, for two Xe-CF_4 mixtures with initial CF_4 concentrations of 0.012 % (blue triangles) and 0.029 % (red diamonds), and for pure xenon (black circles). The data points excluding the attachment effect for the two Xe-CF_4 mixtures are depicted (bright blue triangles, and orange diamonds), together with the respective linear fits (dashed lines). A linear fit to pure xenon data is also shown (black line). The two lower E/p points of the highest concentration mixture were acquired at about one month after the other point. The experimental data were obtained for a wide range of working conditions, such as the total pressure (1.2 to 1.3 bar), the PMT voltage (1200 to 1400 V), or the oscilloscope input impedance (50 or 273 Ω).

Finally, the Y/p data points are compensated by the ratio of secondary scintillation lost due to electron attachment (Y_{att}/Y_0), which was previously measured (figure 51, black circles). The results are also depicted in figure 52, together with the respective linear fits. The error bars arise from the uncertainties on the Y_{att}/Y_0 values represented in figure 51.

According to theoretical predications, the main source of EL yield degradation in Xe-CF_4 mixtures is the dissociative electron attachment [70]. When this effect is excluded, Y/p becomes similar to the one obtained with pure xenon, for the entire E/p range studied. Despite the few available data points for each run of figure 52, the linearity restoration after the Y_{att}/Y_0 correction can be roughly observed for the CF_4 concentration of 0.029 %. On the other hand, the Y/p trend is naturally linear in pure xenon.

The electroluminescence threshold of each mixture can be extrapolated from the interception of the lines fitted to the attachment-compensated Y/p data series (dashed lines in figure 52) with the E/p axis. Electroluminescence thresholds of 0.57 ± 0.55 and 1.02 ± 0.40 kV/cm/bar were estimated for mixtures with CF_4 concentrations of 0.012 % and 0.029 %, respectively. The threshold obtained for the pure xenon data series was 0.69 ± 0.04, which agrees with other experimental results [92].

SP is obtained for each mixture from the ratio between the slope of the respective fitted line (attachment-compensated Y/p) and the one from pure xenon. SP values of (93 ± 18) % and (112 ± 13) % were estimated for mixtures with CF_4 concentrations of 0.012 % and 0.029 %, respectively.

For the concentrations studied, the impact of CF_4 on SP is expected to be negligible, what may explain the near 100 % probabilities found. On the other hand, the increase of the EL threshold that is usually produced by electron cooling seems to be too modest in our experimental data, with respect to previous works [70]. Nonetheless, this parameter may have been wrongly estimated in the past due to the electron attachment dependence on E/p, which affects the Y/p (E/p) linearity. In any case, considering the error in our measurements, either the EL thresholds or SP agree with previous theoretical and experimental studies [70].

Despite the whole study detailed in this section being carried out for a mean total path length of 2 cm, other path lengths were also evaluated (1.8 and 2.2 cm). The results are consistent with the ones shown in figure 52. The analysis developed along this section is just a proof of concept, not a systematic study of the primary and secondary scintillation on Xe-CF_4 mixtures.

7.3 Drift velocity and longitudinal diffusion

The main goal of the present study is to reduce the electron diffusion in an optical xenon TPC using molecular gases to cool down the drifting electrons through non-elastic energy transfers Therefore, besides the impact of the additives on the scintillation response of xenon, the experimental evaluation of the electron diffusion and drift velocity is also relevant. Unfortunately, due to the absence of a drift region in our experimental apparatus, the diffusion and drift velocity cannot be measured for typical drift electric fields (0.02-0.5 kV/cm/bar). Nevertheless, the same kinetic model used to predict the reduction of the electron diffusion promoted by additives can be tested for EL typical electric fields.

In figure 53, the electron spread per unit of drifted path length (a) and the drift velocity (b), both obtained from simulation (Magboltz version 9.0.1), are plotted for a wide range of E/p values, for 3 different additives and pure xenon [125]. The additive concentrations correspond approximately to the same reduction of the three-dimensional spread of electrons

($\sim 2\ mm/\sqrt{m}$), expected for a drift E/p value of 20 V/cm/bar. The impact of additives is still noticeable for the strong electric fields typically used in the EL region, especially for E/p between 1 and 2 kV/cm/bar.

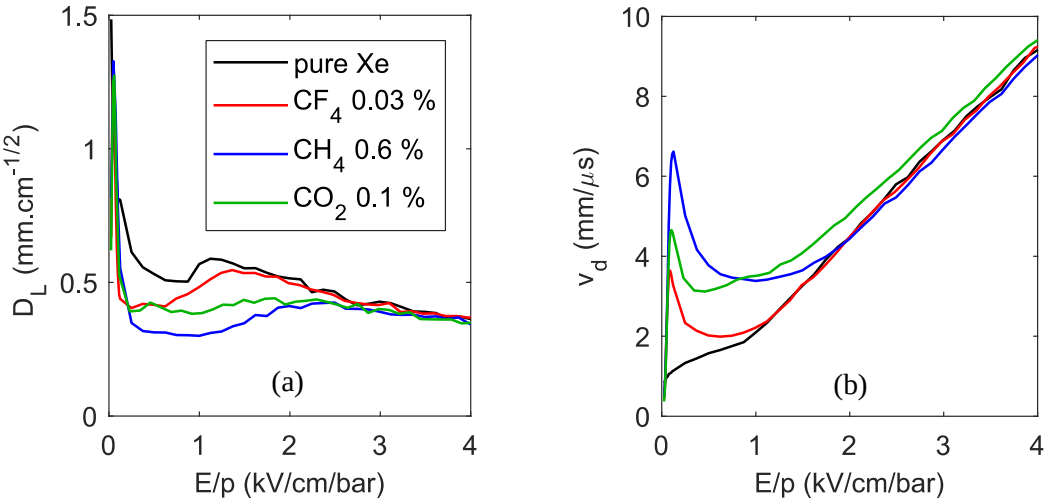

Figure 53: Electron longitudinal diffusion coefficient (spread per drifted root squared path length) D_L^* (a), and drift velocity v_d (b) as a function of E/p, obtained from Magboltz 9.0.1 simulation for a pressure of 1 bar and a temperature of 20 ºC. Three different additives are shown together with pure xenon [125].

In theory, both the transverse and longitudinal diffusion coefficients could be evaluated in a driftless GPSC, through the measurement of the PMT signal as the electron cloud drifts towards the PMT window, for different x-ray penetrations. However, from the practical point of view, it is impossible to measure the impact of the transverse diffusion on the solid angle along the electron path, due the large area of our PMT photocathode and the low path length covered by the electron cloud (2.5 cm maximum). On the other hand, the shape of the PMT waveforms at the end is determined by the electron cloud charge distribution along the drift direction, when it is collected by the anode. In turn, the final size of the electron cloud is stablished by the initial charge distribution produced by the x-ray interaction (depending on the energy), and the broadening induced by the longitudinal electron diffusion. Therefore, the variation of the final electron cloud size with the total path length covered by electrons give us direct access to the longitudinal diffusion coefficient, since the initial cloud size should not depend on the x-ray penetration.

7.3.1 Simulation of waveforms in the presence of longitudinal diffusion

In order to understand the effect that the longitudinal diffusion has on the PMT waveforms, a simple simulation was carried out. The evolution of the electron cloud along drift can be described by the hydrodynamic approximation of the Boltzmann equation [1]:

$$\frac{\partial N_e}{\partial t} + v_d \frac{\partial N_e}{\partial z'} - D_T \left(\frac{\partial^2 N_e}{\partial x'^2} + \frac{\partial^2 N_e}{\partial y'^2} \right) - D_L \frac{\partial^2 N_e}{\partial z'^2} = -\eta v_d N_e \tag{20}$$

where N_e is the density of electrons per unit of volume, D_T and D_L are the transverse and longitudinal diffusion coefficients, respectively, v_d the drift velocity and η the attachment coefficient. D_L defined here has natural dimensions, i.e. length squared per elapsed time, while in figure 53 (a) the diffusion coefficient has a different definition, more intuitive, $D_L^* = \sqrt{2D_L/v_d}$ which can be interpreted as the spread per root squared drifted length (e.g. mm per $\sqrt{m}$). Solving equation (20) one may obtain:

$$N_e(x', y', z', t) = \frac{e^{-\frac{(x'-x)^2+(y'-y)^2}{4D_T(t-t_0)}} e^{-\frac{\left((z'-z)+v_d(t-t_0)\right)^2}{4D_L(t-t_0)}}}{\left(4\pi D_T(t-t_0)\right)\left(4\pi D_T(t-t_0)\right)^{1/2}} \times \bar{n}_e e^{-\eta v_d (t-t_0)} \tag{21}$$

where (x', y', z', t) are the variables measurable by an observer, whereas (x, y, z, t_0) are the initial position and time of the ionization cloud, assumed to be point like and containing $\bar{n}_e$ electrons.

If the density of electrons (N_e in equation (21)) is projected in the z dimension (i.e. along the drift direction), and the electron attachment is neglected (a good approximation for pure xenon), equation (21) simplifies into a one-dimensional Gaussian function, whose standard deviation is directly proportional to the square root of time ($\sigma = \sqrt{2D_L \Delta t}$), and the centroid is directly proportional to time ($centroid = v_d \Delta t$).

The PMT waveforms can be simulated for different x-ray penetrations, assuming some approximations: the initial electron cloud distribution is point-like; the transverse electron diffusion and the electron attachment are neglected; the number of VUV photons detected by the PMT is only dependent on the solid angle subtended by each electron of the cloud and the PMT window, which is described by equation (11) (reflections are not considered); the EL process as well as the PMT time response are instantaneous; and finally, the x-ray beam divergence is neglected.

In figure 54 (a), the result of this simulation is shown for a longitudinal diffusion coefficient $D_L^* = 0.42\ mm/\sqrt{cm}$ and a drift velocity $v_d = 0.56\ mm/\mu s$. These values were obtained from the plots of figure 53, for E/p = 2.45 kV/cm/bar and a pressure of 1.23 bar. Despite the Magboltz simulation being performed for a pressure of 1 bar, the same results can be scaled for different working conditions: v_d is only dependent on E/p, while D_L^* is dependent on E/p and multiplied by the factor $\sqrt{P_0/P}$, where P_0 is the simulated pressure (1 bar), and P the actual pressure (1.23 bar), the temperature being considered constant [1].

In figure 54 (a), the effect of the longitudinal diffusion on the PMT waveforms is noticeable near the maximum height, and in the fall region. For longer path lengths, the

collection of the electron cloud starts sooner, resulting in lower waveform maximum heights, and the waveform fall time is longer (due to the larger tail of the cloud). Figure 54 (b) shows a zoom on the fall region of the simulated waveforms, where these features are clearly seen.

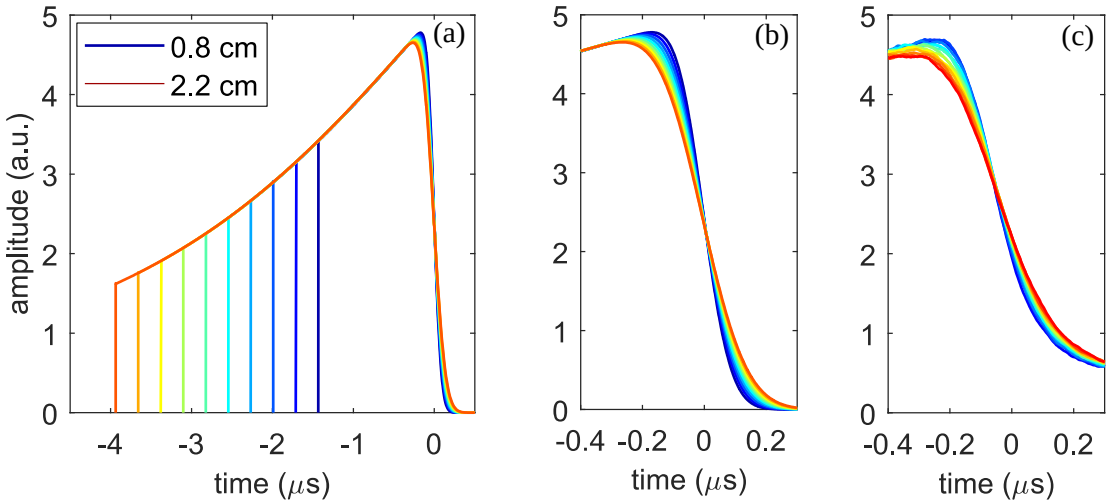

Figure 54: In (a), the PMT waveforms simulated for several drift path lengths, considering only the solid angle variation and the longitudinal electron diffusion, $D_L^* = 0.42\ mm/\sqrt{cm}$, for a drift velocity $v_d = 0.56\ mm/\mu s$. In (b), a zoom in the fall region of the waveforms plotted in (a). In (c), a zoom in the same region of the standard waveforms experimentally obtained for the same path lengths in similar working conditions. The experimental data were obtained with the driftless GPSC filled with pure xenon at a pressure of 1.23 bar, irradiated by 14.3 keV x-rays from a ^{244}Cm source, for an E/p value of 2.45 kV/cm/bar.

In figure 54 (c), an analogous zoom is made in the fall region of the standard waveforms experimentally obtained, with pure xenon at a pressure of 1.23 bar and an E/p value of 2.45 kV/cm/bar, the same conditions of the simulation of figure 54 (a,b). The standard waveforms were computed following the same methodology described in section 5.4 (figure 28 (b)). They were chosen instead of single waveforms because other factors affecting the fall region, like fluctuations in the initial size of the electron cloud, fluctuations in the EL process, fluctuations in the PMT signal, and afterpulsing in the PMT, will cancel during the standard waveform computation, revealing the subtle effect of the electron longitudinal diffusion.

Special care should be taken when standard waveforms are computed, such as the precise alignment between the several single waveforms, crucial to minimize the jitter, and the background rejection efficiency, important to reduce the standard waveform distortion. The algorithms developed in chapter 5 have made this possible.

The waveforms from shorter path lengths may still compromise the results, due to the lower number of events. Therefore, a higher energy x-ray beam should be used, rather than the 5.9 keV used in the attachment study. The x-ray energy must allow a deeper penetration into the gas to take advantage from the whole EL region to study the diffusion. On the other hand, the x-ray energy should not be too high in order to reduce the effects that large initial

electron clouds may have on the waveform decay profile. With this in mind, we have chosen 14.3 keV x-rays from a ^{244}Cm radioactive source.

In the presence of many x-ray energies, the mean initial size of the electron cloud is not constant along the x-ray penetration, hence producing an undesirable variation of the standard waveform fall-time. In addition, the calculation of the electron drift velocity is more difficult due to the superposition of the several energy exponential absorptions. For these reasons, the corrected energy spectrum is first computed, and then the events within the 14.3 keV peak are selected to be used in the computation of the drift velocity and standard waveforms (including figure 54 (c)).

There are other important factors to take into account in such a delicate analysis. Even a small geometrical effect may have a sizable impact on the standard waveform fall-time. Therefore, a narrow lead collimator (7 mm thick, 1 mm in diameter) was specially built for the longitudinal diffusion studies. The collimator and the radioactive source were placed as close as possible to the detector window (~3 mm away) to reduce the spread of the beam, and it was carefully aligned to the window axis. Furthermore, the full bandwidth of the oscilloscope was used together with the 50 Ω DC coupling, without any high frequency filter, to avoid distortions on the fall region of the waveforms.

The dependence of the waveform fall-time on the x-ray penetration predicted by simulation (figure 54 (b)) is also observed in the experimental data of figure 54 (c), despite the significant effect of the PMT afterpulsing that is perceptible at the end of the waveforms. This evidence suggests the possibility to evaluate the electron longitudinal diffusion with the present experimental setup. Nonetheless, the effect observed in figure 54 (c) could be produced by other physical processes (e.g. PMT after-pulsing that also depends on the x-ray penetration), or it could be an artefact of the waveform organization and alignment algorithms. Therefore, to verify the consistency of these results, several measurements were made in the same conditions, although for different reduced electric fields.

7.3.2 Analysis of waveform fall-times

In the present study, the fall-times of the standard waveforms are usually measured between 90 % and 60 % of the waveform maximum height, thus avoiding fluctuations near the maximum as well as part of the after-pulsing. In figure 55, the fall-times of the experimental standard waveforms are plotted as a function of the mean path length drifted by electrons, for three different E/p values. As seen, the fall-times are shorter for higher E/p values, which is expected since the drift velocities are higher. Since the parameter D_L^* corresponds to the spread per unit of square root path length, it does not depend on the drift time (because $D_L^* = \sqrt{2D_L/v_d}$). Nonetheless, D_L^* is also expected to be lower for higher E/p values, according to simulations of figure 53 (a).

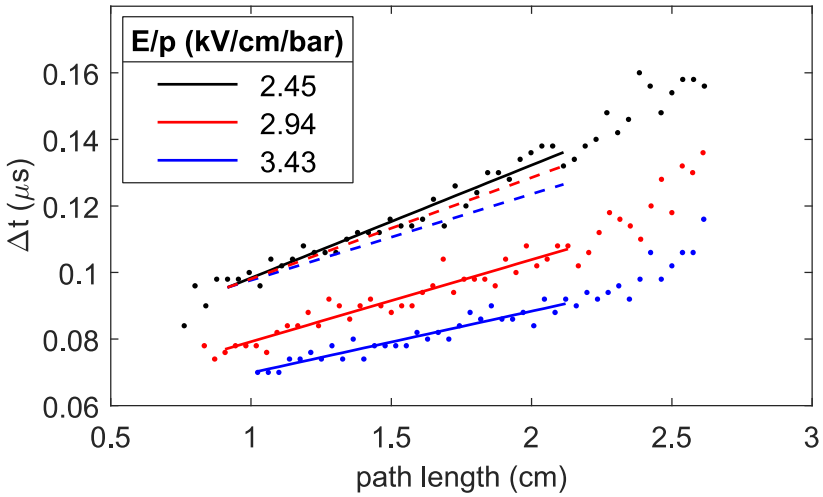

Figure 55: Fall-times (90 % down to 60 %) of the experimental standard waveforms (black, red and blue points) as a function of the mean path length drifted by electrons obtained for three different E/p values. Linear fits (solid lines) to the three data sets are also shown. In addition, the two lines corresponding to higher E/p were normalized to the first point of the lowest E/p line (dashed lines).

The fall-time of the standard waveforms increases almost linearly with the path length, except for the longer waveforms. After normalizing the lines that were fitted to the data, one may observe that the slope still decreases with E/p, suggesting that the variation on the fall-time is not produced by the different drift velocities only, but there is also a decrease of D_L^* as predicted by the simulations (figure 53 (a)). The consistency in these results proves that the standard waveform fall-times can be used in some way to evaluate D_L^* in the driftless GPSC.

7.3.3 Determination of the electron drift velocity

The experimental determination of the drift velocity is important to evaluate the kinetic model, but it is also necessary to compute D_L^*. In section 5.6, the method to compute the conversion factor between the waveform duration and the mean path length drifted by the electron cloud was described. However, v_d obtained in this way is an overestimation, since the waveform duration is measured between the very start moment (i.e. when the waveform rises above ~ 1 % of its height) and the instant at which half of the electron cloud is collected (i.e. when the waveform falls below 50 % of the height). Thus, the waveform duration includes not only the electron drift time, but also the broadening of the PMT signal promoted by several processes, for example the xenon excitation and deexcitation times, the electron cloud initial size and longitudinal diffusion, the PMT response function and after-pulsing, or the cable and oscilloscope impedances.

The same algorithm used to plot figure 54 (a,b) was adapted in order to include the electron cloud initial size and the EL process decay rate. The radial charge distribution of the initial electron cloud was taken from reference [126], which was obtained by simulation for

15 keV x-rays absorbed in xenon at 1 bar, similar working conditions as our experimental data. The ~100 ns exponential decay rate of the xenon 2nd continuum is added to the simulation by solving numerically the respective differential equation for the simulated waveform (because the waveform is not a step-function). The rise-time of the EL process is not considered as it is negligible when compared to the fall-time [70].

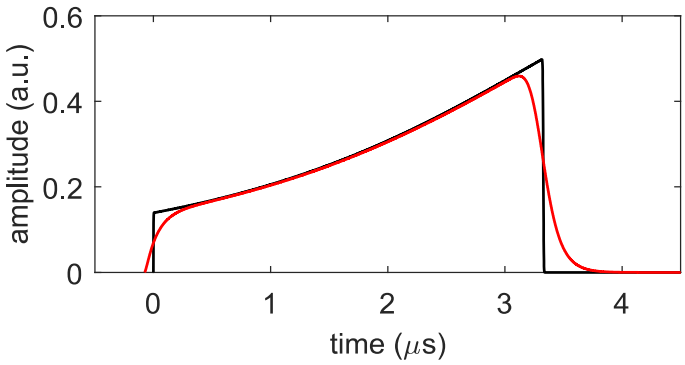

Figure 56: Simulation of the PMT waveform considering only the variation of the solid angle subtended by the PMT photocathode and the point-like electron cloud (in black); and considering the initial size of the electron cloud, the longitudinal diffusion and the EL decay rate (in red). The waveforms were generated for a path length of 2.5 cm, considering a v_d= 0.75 $mm/\mu s$, $D_L^* = 0.36\ mm/\sqrt{cm}$ and an initial cloud spread $\sigma = 140\ \mu m$.

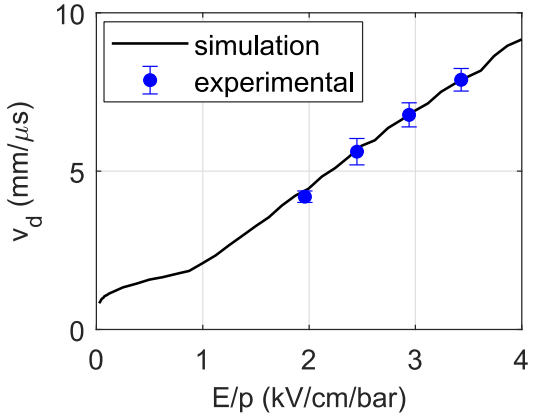

Figure 57: Electron drift velocity v_d obtained experimentally with the driftless GPSC filled with pure xenon at a pressure of 1.23 bar, as a function of the E/p (blue circles), together with data from Magboltz simulation (black curve) [125]. The error bars were estimated from the uncertainty associated to the conversion between the waveform duration and the mean path length drifted by electrons, no additional statistical or systematic errors were considered.

In figure 56, the impact of the simulated broadening sources on the PMT waveform is demonstrated, for $v_d = 0.75\ mm/\mu s$, $D_L^* = 0.36\ mm/\sqrt{cm}$ and initial cloud spread $\sigma = 140\ \mu m$. For this specific case, the waveform is 87 ns longer than the one obtained when only the solid angle is considered. Therefore, the actual v_d value is $0.73\ mm/\mu s$. Since this difference is still significant, the measurements of v_d reported from now on were individually corrected by the waveform broadening times computed for the respective simulated v_d and

D_L^* values (obtained from the Magbotz simulation of figure 53, for the same conditions of each experimental run), as described above.

In figure 57, v_d obtained experimentally with the driftless GPSC filled with pure xenon is plotted for several reduced electric fields, together with the expected values from Magboltz simulation [125]. The agreement between the experimental and simulated data is good. This experimental v_d values should be interpreted as an upper limit, since there are additional sources contributing to the waveform broadening that were not included in our corrections (e.g. the PMT time response and afterpulsing).

7.3.4 Determination of D_L^*

Using the experimental v_d values (figure 57), D_L^* can be determined through the same simulation developed to estimate the broadening of the waveforms (red curve of figure 56). The initial size of electron cloud and D_L^* are adjusted, so that the fall-region of the resulting simulated waveforms for the several path lengths is similar to the experimental one (e.g. figure 55 (c)).

In a first approach, the fall-times (between 90 % and 60 %) are measured as a function of the path length, for the simulated waveforms and for the experimental ones. Then, a linear fit is performed to each data set. The slope and the y-interception of this line are mostly dependent on D_L^* and the cloud initial size, respectively. Therefore, those two parameters are adjusted in the waveform simulation so that the two fitted lines match as far as possible. Using this method, the experimental D_L^* was evaluated in pure xenon for several E/p values. However, the statistical uncertainty associated to the D_L^* estimation is very high when compared with the small variation of D_L^* expected within the studied range of E/p (between 2 and 3.4 kV/cm/bar).

In theory, the effectiveness of this method could be further improved if all available information contained in the fall region of the standard waveforms was used, rather than a simple measurement of the time elapsed between two points. To accomplish that, a 3-dimentional function for the variation of the waveform amplitude with time and with path length is generated based on the same simulation discussed in the previous paragraphs. Then, this function is fitted to the analogous experimental 3-dimentional data, with D_L^* and the initial size of the electron cloud being left as the only free parameters, while v_d measured independently for each run is fixed. In figure 58, an example of the 3-dimentional plot of the experimental standard waveforms is shown for several electron path lengths.

Based on the same arguments discussed before, only part of the simulated function and experimental data are used in the fitting method, including the fall region between 90 % and 60 % of the waveform maximum height. The waveform amplitude is normalized to the waveform maximum height for each path length, resulting in a fixed range (90 % down to 60

%), while the range of time varies with the path length. To deal with this situation, the time becomes the dependent variable, whereas the relative voltage becomes the independent variable. This is done for both the experimental data and fit function. For each path length, the time of the voltage middle point (i.e. when the waveform is at 75 % of the maximum height) of the fit function is normalized to the respective time of the experimental data series. This procedure has some advantages, for instance, the experimental and fitted waveforms for each path length do not need to be aligned, neither their amplitude needs to be normalized. Thus, the possible number of free parameters is substantially reduced.

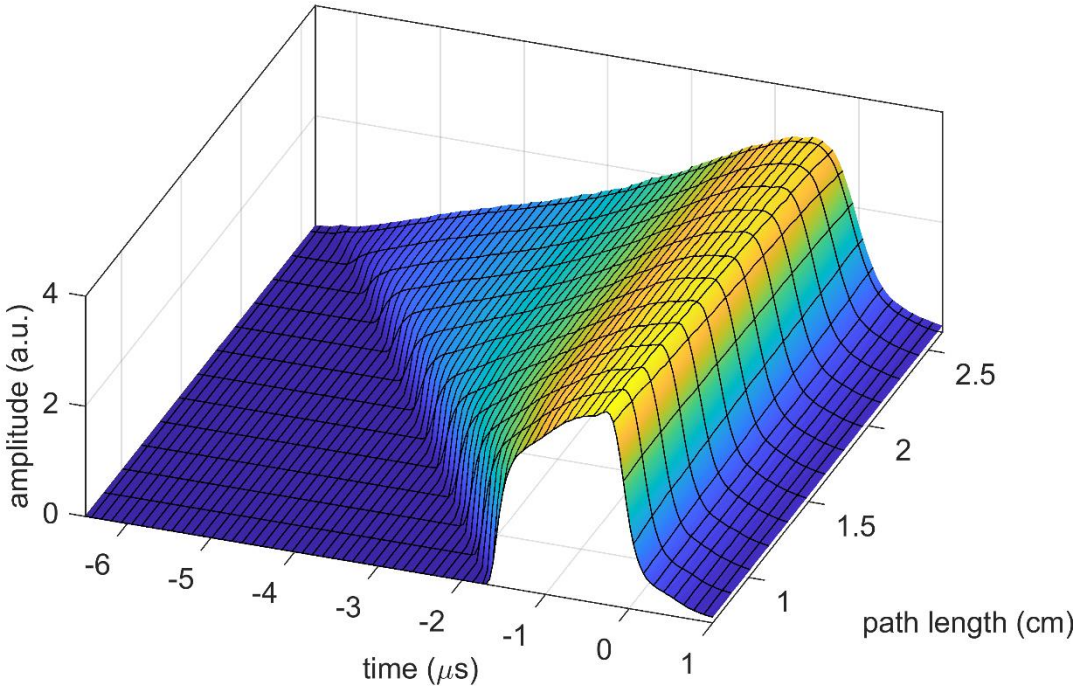

Figure 58: Experimental standard waveforms as a function of path length, obtained with pure xenon at 1.23 bar, for 14.3 keV x-rays from a ^{144}Cm source. Data was smoothed to assist the visualization.

The initial charge distribution obtained from the Monte Carlo simulations in ref. [126] used here for the waveform simulation was found to be computationally exhaustive, while its impact on the D_L^* estimation is negligible [6]. Therefore, the initial charge distribution along the drift direction is modulated by a Gaussian function. In this way, the code performance is considerably increased, since the initial cloud spread (σ_i) can be mimicked by a temporal shift in the diffusion process ($\sigma_i = \sqrt{2D_L(\Delta t + t_i)}$, t_i being the time added).

The 3-dimentional function is fitted to the experimental data by minimizing the sum of squares of the difference between both data sets ($\|f(x)\|^2$), a nonlinear least-squares solver being used for this propose. Because of the complexity of the problem, $\|f(x)\|^2$ has usually

[6] The radial initial charge distribution of the electron cloud has an atypical shape (due to the vacancy cascade electrons and the more energetic photoelectron). However, since the electron cloud spreads over time, its distribution becomes similar to a Gaussian function.

many local minima. To find the global minimum, several random distributed start points (D_L^*, σ_i) are generated. The run converging with the lower norm of the residuals is considered the global solution. This fitting method revealed to be extremely slow, but after the code was optimized and ran in parallel across several CPUs, acceptable computing times were achieved (less than 1 h).

In figure 59, some path length cuts of the 3-dimentional experimental standard waveform are plotted together with the respective cuts of the fitted function, after the global solution was found. The fitted function describes the fall region of the experimental waveforms with satisfactory precision, within the full range of path lengths. Since the fit is performed with the time being the dependent variable, whereas the relative waveform voltage is the independent variable, the waveforms of figure 59 are 90º rotated.

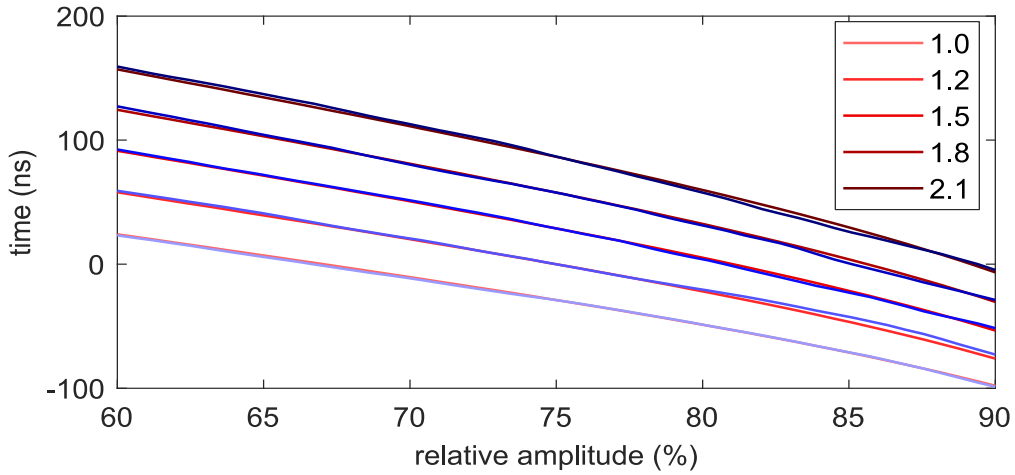

Figure 59: The fall region of the experimental standard waveforms (between 90 % and 60 %) for several path lengths in cm (curves in blue), and the respective simulated waveforms (curves in red) after the fit converged to a global solution. The waveforms were shifted in time to improve visualization (otherwise all the curves would intercept the 0 ns at the 75 % amplitude).

The aforementioned fitting method was applied to the experimental standard waveforms obtained with different E/p values, the driftless GPSC being filled with 1.23 bar of pure xenon and radiated by a ^{144}Cm source. The results of D_L^* estimated in this way are shown in figure 60, together with the Magboltz predictions obtained from figure 53, after performing the proper pressure scaling. The error bars represented in figure 60 include both the statistical uncertainty (68 % CL) of the D_L^* fit parameter and the error coming from the v_d measurement, being combined quadratically. No additional statistical or systematic errors were considered.

The fairly good agreement between the experimental data and the simulated trend demonstrates the accuracy and consistency of the methodology here developed. Nonetheless, our results might be slightly overestimated because the fit function did not include the effect of the afterpulsing. The number of feedback ions inside the PMT is expected to increase with the number of electrons extracted from the photocathode. Consequently, the afterpulsing may

also lead to longer waveform decay times for longer path lengths, since the number of collected photons is higher. In the future, the afterpulsing effect will be studied and introduced in the fit function, in order to improve the accuracy of this methodology.

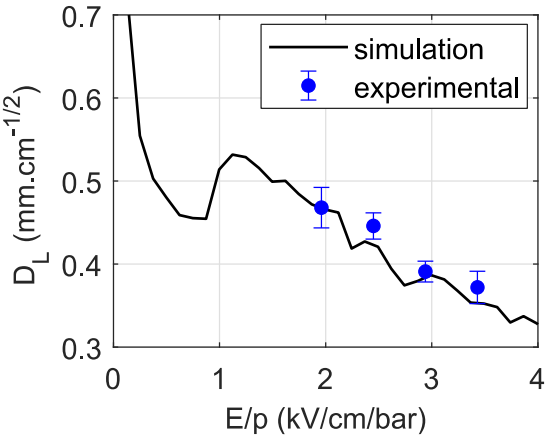

Figure 60: Experimental D_L^* obtained with pure xenon at a pressure of 1.23 bar for different E/p values (blue circles), and the Magboltz simulation results scaled for the same pressure (black) [125].

8 DETECTOR RESPONSE FUNCTION

The main motivation of the driftless GPSC waveform study was the possibility to build an accurate detector response function, which could be fitted to the MCA pulse-height distributions, which were obtained before the direct method being developed with Xe-CO_2, Xe-CH_4 and Xe-CF_4 mixtures. In this way, a better estimation of the energy resolution corrected from the x-ray penetration effect could be obtained and, consequently, a more accurate *Q* factor, which is essential to extrapolate our results to the NEXT-100 TPC, or any other detector.

In section 4.2.2, the theoretical response function was constructed based on some considerations, which were then found to be significantly deviated from direct observations. For example, the distribution of Gaussian centroids along the path length, which was previously computed based on the integration of the solid angle subtended by the PMT and the electron cloud. However, we verified that the typical PMT waveform does not follow this solid angle variation (as demonstrated in figure 29), most likely due to other mechanisms influencing also the PMT output (e.g. reflection of EL photons, non-uniformities of the electric field, the size of the electron cloud, the x-ray beam divergence, non-uniformities of the photocathode quantum efficiency, or the PMT after-pulsing).

In this chapter, the response function of the driftless GPSC obtained with the standard method (i.e. using a preamplifier, a linear amplifier and a multichannel analyser) is generated, based on direct observations of the PMT waveforms produced by events taking place at different depths. The detailed operation of the detector described in the previous three chapters is here assumed, including the electron attachment effect.

As starting point, the detector response function will be constructed based on rough approximations, called *simplified detector response* function. Then, this function will be upgraded with fine approximations, including the electronics contribution. Finally, the results

obtained with the new function, called *improved detector response* function, are compared with the ones produced by the simplified function.

8.1 Simplified response function

As demonstrated in figure 30, the full absorption peak produced by monoenergetic x-rays follows a Gaussian distribution when only events corresponding to the same x-ray penetration are selected, except for very long waveforms where the probability of part of the electron cloud being lost to the detector window is significant. Nonetheless, for 5.9 keV x-rays, the percentage of events suffering from this effect is negligible. This Gaussian-like shape seems to persist even in the presence of high dissociative attachment. Therefore, the detector response function can be modulated by a sum of Gaussians, corresponding to the several interaction depths into the EL region, as assumed before (section 4.2.2). However, the exact the distribution of centroids of these Gaussians (e.g. figure 32) is now known, hence there is no need to compute it based on theoretical solid angle considerations. This distribution has shown to be independent from the E/p value and from the x-ray energy, as demonstrated in figure 35. Still, the impact of the electron attachment on the centroid distribution must be accounted for, so that the detector response function can be fitted to CF_4 and CO_2 experimental data.

8.1.1 Distribution of centroids and electron attachment

The effect of the electron attachment on the PMT standard waveforms for a given x-ray penetration can be described by equation (22).

$$w^a(t) = e^{-\eta v_d t} w(t) \tag{22}$$

where w^a and w are the standard waveforms (voltage as a function of time) including and neglecting the attachment effect, respectively, η is the attachment coefficient and v_d the drift velocity.

The centroid of the full absorption peak for each path length (Δx) can be computed from the integration of the respective standard waveform, as described by equation (23):

$$M^a(\Delta x) = \int_{t_0}^{t_f} e^{-\eta v_d t} w_{\Delta x}(t)\, dt \tag{23}$$

where $M^a(\Delta x)$ is the centroid as a function of path length Δx considering the attachment. The integration interval from t_0 to t_f corresponds to the duration of the corresponding standard waveform $w_{\Delta x}(t)$.

Since the absorption length of 5.9 keV x-rays in our detector is small, the majority of the path lengths fall within a narrow interval. Therefore, when the attachment coefficient is not too high, one may consider the attachment probability dependence on Δx to be

aproximatly linear, as demonstrated in figure 45. In such case, $M^a(\Delta x)$ can be expressed as a function of the attachment probability corresponding to a path length of 2.5 cm ($P_{att}(2.5cm)$). Thus, equation (23) can be simplified into equation (24).

$$M^a(\Delta x) = M(\Delta x) - P_{att}(2.5cm)C^a(\Delta x) \quad (24)$$

Where $M(\Delta x)$ is the centroid distribution without the attachment effect (represented in figure 32), while C^a is a given constant for each Δx. The distribution of those constants, $C^a(\Delta x)$, can be calculated from equation (24) for a known $M(\Delta x)$, $M^a(\Delta x)$ and $P_{att}(2.5cm)$, which are in turn experimentally obtained with pure xenon and a Xe-CF_4 mixture ($P_{att}(2.5cm)$ is determined as described in section 7.1.1). For the correct computation of $C^a(\Delta x)$, other effects apart from the attachment must be excluded from the experimental $M^a(\Delta x)$ distribution. Therefore, the same procedure described in section 7.1.6.3 is here used to scale the $M^a(\Delta x)$ distribution, so that its difference with respect to the $M(\Delta x)$ distribution comes from the attachment only. After obtaining $C^a(\Delta x)$ for this calibration mixture, it can be used together with $M(\Delta x)$ to predict the centroid distribution for any $P_{att}(2.5cm)$.

The described procedure is demonstrated in figure 61, where $C^a(\Delta x)$ was computed using a the centroid distribution $M(\Delta x)$ from pure Xe and the distribution $M^a(\Delta x)$ from a Xe-CF_4 mixture (with a concentration of 0.012 %), for which an attachment probability of 37 % was measured. In order to improve the quality of the simplified response function fit, the centroid distributions shown in figure 61 were computed mimicking the integration of waveforms that is performed by the electronics (a preamplifier time constant of 50 μs and a linear-amplifier shaping constant of 8 μs). However, the variation of the electron drift velocity with E/p is not considered here. This rough correction of the centroid distribution is performed for a fixed E/p value of ~2.24 kV/cm/bar.

Additional centroid distributions are predicted for other $P_{att}(2.5cm)$ values through equation (24), these being also represented in figure 61. To validate the method, the centroid distribution obtained experimentally from a Xe-CF_4 mixture (with concentration of 0.029 %) with an estimated $P_{att}(2.5cm)$ value of 68 % is compared with the theoretical distribution predicted for the same $P_{att}(2.5cm)$; the result being shown in figure 61. Naturally, the experimental distribution was previously normalized to account for the attachment effect only. The agreement between the predicted and experimental distributions is satisfactory, thus validating the approximations performed (at least within this $P_{att}(2.5cm)$ range).

As demonstrated in the figure 61, if the electron attachment is too high (e.g. the orange curve),, most of the x-rays with larger penetrations could result in an overall higher number of collected EL photons when compared with less penetrating x-rays. Therefore, the MCA pulse-height distribution becomes right-tailed instead of left-tailed, while in the presence of

moderate attachment, Gaussians from deeper events could be on both the right and left sides with respect to the zero-penetration Gaussian.

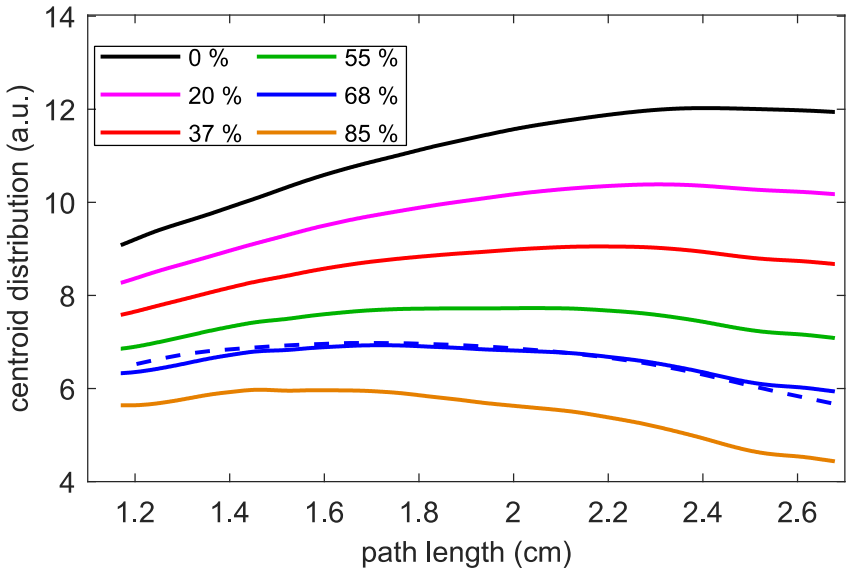

Figure 61: Centroid of the 5.9 keV peak as a function of the total path length drifted by electrons for several attachment probabilities. The solid black curve was obtained experimentally with pure xenon (E/p = 2.24 kV/cm/bar), while the red curve and the dashed blue curve come from Xe-CF_4 mixtures with 0.012 % of CF_4 (E/p = 2.24 kV/cm/bar) and 0.029 % of CF_4 (E/p = 3.45 kV/cm/bar), for which $P_{att}(2.5cm)$ values of 37 % and 68 % were measured, respectively. The orange, blue, green and magenta solid curves are simulated distributions (obtained through equation (24), using the red and black calibration curves) for $P_{att}(2.5cm)$ values of 85 %, 68 %, 55 % and 20 %, respectively.

8.1.2 Distribution of areas

The experimental distribution of centroids is computed as a function of the path length, which is in turn directly obtained from the waveform duration. Therefore, the areas of the several Gaussians used to produce the detector response function must follow the number of events observed for each waveform duration interval, rather than the theoretical exponential absorption law (figure 31). Logically the distribution of waveform durations also depends on the detector gas pressure.

The effect of the gas pressure on the distribution of durations is modulated as follows. First, the ratio between the distribution of durations and the exponential function that is fitted to data (including only the exponential part, as shown in figure 31) is computed for a given run. This measurement of the mismatch between the theoretical and experimental distributions can then be used to predict the distribution of durations for any pressure, multiplying the respective exponential function by the ratio data series. Despite being not ideal, this correction has shown to be reliable enough, since our campaign with molecular additives was carried out at similar pressures.

In figure 62, the distribution of waveform durations obtained experimentally with a CF_4 concentration of 0.012 % at a pressure of 1.22 bar is depicted, together with the exponential absorption law expected for the respective attenuation coefficient. For comparison, the same figure also shows the simulated distribution, which was computed from the experimental distribution obtained with pure xenon at a pressure of 1.25 bar, after correcting it by the different exponential function as explained above. The slight difference between the distributions of figure 62 and the one shown in figure 31 comes from a different criterium used to find the start instant of each waveform. A fixed threshold of ~0.3 mV was used in figure 62, while in figure 31 the threshold was ~1 % of the waveform height.

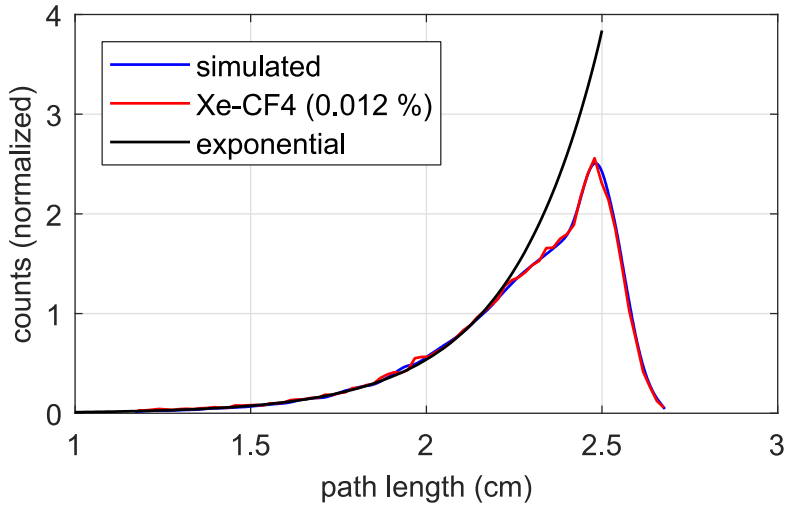

Figure 62: Distribution of waveform durations obtained experimentally with a CF_4 concentration of 0.012 % at 1.22 bar (in red), together with the theoretical exponential law (in black). The simulated distribution of waveform durations (in blue) was obtained multiplying the exponential curve (in black) by the ratio between the experimental and exponential distributions produced by a pure xenon run at a different pressure, 1.25 bar.

Despite the simulated distribution coming from pure xenon at a different pressure, it is superimposed to the Xe-CF_4 experimental distribution due to the correction associated to the different attenuation coefficient, thus validating this method (at least for a small range of pressures). One may also conclude that the additive has no significant impact on the distribution of waveform durations

8.1.3 Energy resolution considerations

As discussed in section 5.8, the energy resolution is expected to degrade with the x-ray penetration length, since the total number of collected photons is lower. However, the opposite may occur in the presence of electron attachment, because its probability is higher for longer path lengths. In any case, most of the interactions produced by 5.9 keV x-rays in xenon take place near the detector window (the attenuation length is 2.4 mm for a pressure of 1.2 bar), resulting in a narrow effective interval of path lengths. Therefore, to keep the detector

response function as simple as possible, the relative FWHM of the Gaussians is considered constant over the path length.

8.1.4 Results with the simplified response function

In summary, the detector response function fitted to the MCA pulse-height distributions is modulated by the sum of many Gaussian functions (about 5000), each one corresponding to a different penetration of x-rays (to be exact, they correspond to different waveform durations). The centroids of these Gaussians are given by the distribution experimentally determined with pure xenon plotted in figure 61, after this distribution being corrected by the attachment probability according to the approximation of equation (24). The Gausssin areas follow the experimental distribution of waveform durations of pure xenon, after the attenuation coefficient correction being applied according to the gas pressure of the respective run (as demonstrated in 62), all the Gaussians having the same relative FWHM. The attachment probability, the energy resolution and the centroid corresponding to the path length of 2.5 cm are left as free parameters in the fit.

Since all the Gaussians have the same relative FWHM, not depending on the respective path length drifted by electrons, the energy resolution obtained from the fit should be interpreted as an average value, which corresponds approximately to ER of the average path length, i.e. 2.5 cm subtracted by the attenuation length.

In figure 63, the detector response function is fitted to the MCA pulse-height distributions obtained with a Xe-CO_2 mixture with low attachment (a), a Xe-CF_4 mixture with high attachment (b), a Xe-CF_4 mixture with moderate attachment (c), and a Xe-CH_4 mixture with no attachment. Some of the Gaussian functions used to build the response function are also represented in arbitrary units.

There are Gaussians corresponding to path lengths longer than 2.5 cm, despite this being the length of the EL region. This peculiarity is explained by the fact that the several Gaussians do not correspond to real drifted path lengths, but to the mean path length obtained from the waveform durations. Nevertheless, since everything is performed in terms of waveform durations, this apparent inconsistency has no influence in the analysis. The path lengths are represented just to make the results more intuitive.

In figure 63, the effect of electron attachment on the driftless GPSC response is clear. In (a) and (d), the most penetrating x-rays produce more counts in the low energy region, while in (b), they produce generally more counts in the high energy region, resulting in a right-hand tail. When attachment is moderate, as in (c), the most penetrating x-rays may produce both higher energy events or lower energy events.

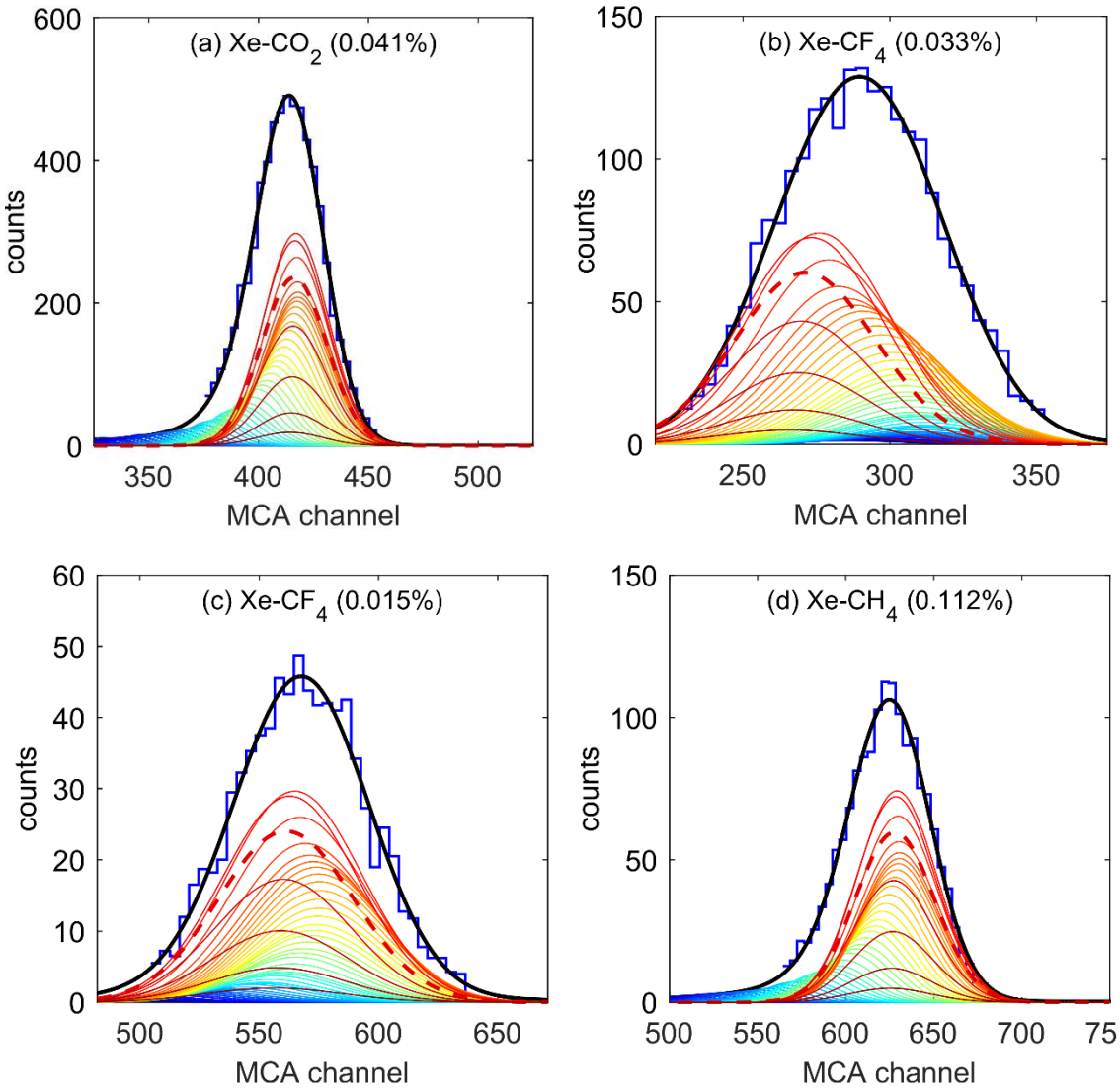

Figure 63: Pulse-height distribution obtained with the driftless GPSC radiated by 5.9 keV x-rays, for four different mixtures: (a) Xe-CO_2 (0.041%) at 1.15 bar and E/p = 3.1 V/cm/bar; (b) Xe-CF_4 (0.033%) at 1.20 bar and E/p = 2.8 V/cm/bar; (c) Xe-CF_4 (0.015%) at 1.25 bar and E/p = 3.4 V/cm/bar; (d) Xe-CH_4 (0.112%) at 1.23 bar and E/p = 3.6 V/cm/bar. The response function (in black) is fitted to the experimental MCA distribution (in dark blue), resulting from the sum of 5000 Gaussian curves, part of them being represented by solid thin lines from red to blue (in arbitrary units), corresponding to the longer and shorter path lengths, respectively. The dashed curve is the Gaussian corresponding to the path length of 2.5 cm. Attachment probabilities (after a 2.5-cm drift) of 7 %, 75 %, 36 % and 0 %, were estimated for (a), (b), (c) and (d) mixtures, respectively, while the respective corrected energy values are 8.3 %, 20.8 %, 11.8 % and 8.4 %.

Since the attachment probability for 2.5 cm and ER are left free in the fit, the method is not precise to estimate both parameters, as they are correlated. Occasionally, for some mixtures, especially the ones with almost symmetric pulse-height distributions (i.e. moderated attachment), extremely large fluctuations on the estimated $P_{att}(2.5cm)$ can be observed between measurements for close E/p values, for which such sharp variations are not expected. The confidence interval (68 % CL) of the $P_{att}(2.5cm)$ parameter could even reach

the magnitude of its own estimated value, for some MCA acquisitions. These $P_{att}(2.5cm)$ outlier values are however rare, usually the uncertainties for the remaining E/p values are lower. In such cases, the upper and lower limits of the $P_{att}(2.5cm)$ parameter are fixed, according to the smoothed trend of the $P_{att}(2.5cm)$ variation with E/p weighted by the respective uncertainties, for the same mixture. In this way, the accuracy of the ER estimation is improved for these cases where the fit converged to unrealistic $P_{att}(2.5cm)$ values.

Although the $P_{att}(2.5cm)$ parameter can have very large uncertainties, the relative uncertainty of ER is usually below 25 %. Therefore, despite the method not delivering a precise measurement of $P_{att}(2.5cm)$, the estimation of ER corrected by the x-ray penetration seems to be acceptably reliable. It is important to notice that the uncertainties on ER and $P_{att}(2.5cm)$ are considerably improved when long acquisition times are taken. Unfortunately, during the experimental campaign with Xe-CO_2, Xe-CF_4 and Xe-CH_4 mixtures, the detailed knowledge of the pulse-height distribution shape was not considered to be so important, hence the statistics level in the data is usually low. An additional systematic error in ER may still exist in measurements with high attachment, since the linear approximation of equation (24) is no more valid.

In order to validate this methodology, the corrected energy resolution (R'_E) estimated with the simplified response function is compared with the energy resolution (R_E) measured directly from the corrected energy spectrum obtained with the direct method (for a narrow interval of path lengths around 2.3 cm), as shown in table 3. The energy resolution (R''_E) measured at the FWHM of the full absorption peak (i.e. the non-corrected resolution) is also represented. For each energy resolution (R_E, R'_E and R''_E), the squared relative standard deviation of the total number of collected EL photons per electron (Q_{R_E}, Q'_{R_E} and Q''_{R_E}) is also listed in table 3. This value was obtained from the respective energy resolutions after subtracting the fluctuations in the primary charge production (using a Fano of about 0.225 as reported in table 1), and the fluctuations related with the photosensor signal (figure 43). In addition, the attachment probabilities for a 2.5-cm drift length estimated from the pulse-height distribution fits (P'_{att}) are compared with the respective values obtained directly from the standard PMT waveforms (P_{att}) reported in section 7.1.3.

Despite the low precision of the method to estimate the electron attachment level, there is an acceptable agreement between P'_{att} and the P_{att} measured directly from the PMT waveforms (naturally, the higher the P_{att}, the better this agreement will be because of the exponential dependence of the attachment probability on the attachment coefficient). A good agreement between R_E and R'_E is also observed, especially for lower attachment probabilities, where the relative difference is 5 % at most. Nonetheless, for the highest attachment case, R'_E seems to be overestimated by 15 %. On the other hand, R''_E that was

simply measured from the FWHM of the pulse-height distribution peak is considerably higher than R_E, even reaching a 56 % relative overestimation for the highest attachment case. Considering that the R_E measured using the direct method is close to the real driftless GPSC energy resolution for a path length of about 2.3 cm, the complex detector response function developed in this section showed to be a powerful tool to estimate this parameter, at least within the attachment probability range of table 3. Most of our previous measurements with Xe-CO_2, Xe-CF_4 and Xe-CH_4 fall within this range.

Table 3: Comparison between the corrected energy resolutions obtained for several Xe-CF_4 mixtures and E/p values, with the direct method (R_E), and with the standard method using either the simplified response function (R'_E) or a single Gaussian fit (R''_E). The Q factor computed from the energy resolutions resulting from the three methods is also presented. The attachment probability estimated from the simplified response function fit (P'_{att}) is compared with the one measured with the direct method (P_{att}). Data were taken for a total pressure of about 1.2 bar, and for 5.9 keV x-rays. All the energy resolution values and Q factors correspond to a mean path length of about 2.3 cm.

CF_4 conc. (%)	E/p (kV/cm/bar)	P_{att} (%)	P'_{att} (%)	R_E (%)	R'_E (%)	R''_E (%)	Q_{R_E}	Q'_{R_E}	Q''_{R_E}
0	2.90	-	-	7.3	7.6	8.8	-	-	-
0.012	3.12	29	19	9.5	9.5	10.3	0.18	0.18	0.26
0.012	2.23	38	31	10.3	10.6	11.3	0.23	0.27	0.34
0.029	3.45	68	72	13.1	13.8	17.5	0.56	0.65	1.21
0.029	3.18	73	75	13.9	15.1	19.1	0.67	0.83	1.50
0.029	2.23	80	84	16.1	18.9	25.2	0.92	1.40	2.74

As expected, the R'_E overestimation produced by the detector response function has a stronger impact on Q'_{R_E}, as the last depends quadratically on R'_E. The systematic relative error of Q'_{R_E} is usually about 20 %, reaching 50 % for the highest attachment probability. Nevertheless, this deconvolution of the MCA pulse-height distribution is far superior when compared to the method neglecting the x-ray penetration effect, for which the relative systematic error in Q''_{R_E} is about 100 %, reaching 200 % for the highest attachment probability.

This multifaceted fitting function has been able to describe acceptably the driftless GPSC output obtained with standard method, predicting the distinct dynamics of the three studied additives and pure xenon. However, there are still cases where this function does not fit well to the experimental data, usually at low E/p values (below ~2.2 kV/cm/bar), and for high electron attachment (η above 0.6 cm^{-1}). Some of the approximations and processes that were not modulated could explain these observations, for instance the non-inclusion of the electronics signal processing, the linear approximation of equation (24) used to predict the

attachment effect on the centroid distribution and the constant energy resolution assumed for the Gaussians obtained from different x-ray penetrations.

8.2 Improved response function

Aiming at a more profound understanding of the driftless GPSC, in combination with the standard method, some of the effects previously neglected are included in the improved version of the detector response function here described. In this way, a better interpretation of previous data obtained with Xe-CO_2, Xe-CF_4 and Xe-CH_4 mixtures is possible.

Although the electronics were neglected in the previous response function, they have a significant impact on the MCA pulse-height distribution. The way the preamplifier and the linear-amplifier integrate the PMT waveforms is distinct from the pure mathematical integration, resulting in a different distribution of centroids as a function of the x-ray penetration from the one observed with the direct method (figure 32). Due to the technical detail of this subject, the effect of the electronics on the detector response function and its modulation are described in appendix E. Nevertheless, some of the principal observations and ideas are summarized below.

Despite the long preamplifier decay time constant (50 μs), there is an observable ballistic deficit, whose impact on the pulse-height distribution is boosted by the penetration of the x-rays, as shown in appendix E.1. A similar effect is produced by the linear-amplifier, as described in appendix E.2. Both amplifiers lead generally to a larger dependence of the pulse-height distribution on the final part of the PMT waveforms when compared to the initial part. For this reason, the left-tail produced by the x-ray penetration becomes shorter in low-attachment mixtures, while the right-tail produced when attachment is high becomes considerably larger. This distortion induced by the electronics on the detector response is particularly remarkable when each one of the following conditions are verified: the linear-amplifier shaping constant is short (as in Xe-CO_2 acquisitions, 4 μs), the attachment coefficient is high (such in high concentrations of Xe-CF_4), or at low E/p values. Therefore, the electronics must be considered in the improved response function.

In appendix E, the preamplifier and linear-amplifier outputs are modulated through software. This effect can be introduced in the improved response function through the standard waveforms obtained with pure xenon (e.g. figure 28 (b)). However, instead of performing a pure mathematical integration of the standard waveforms, now they are integrated by virtual electronics. Thus, the Gaussian centroids corresponding for the several penetrations are directly given by these integrals, instead of using the centroid distribution produced by the direct method (as previously made in the simplified function, figure 61). Since the electronics effect depends on the working conditions (e.g. the E/p value that

influences the waveform duration), this centroid distribution must be computed for each acquisition.

8.2.1 Attachment effect on the standard waveforms

Before the integration of the pure xenon waveforms with our modulated-amplifiers, the waveforms must be corrected by the attachment effect. The duration of the standard waveforms is normalized for each E/p acquisition, according to the drift velocity scaling expected from Magbotlz simulations for the acquisition conditions (figure 53 (b)). In this way, pure xenon standard waveforms (obtained with E/p = 2.24 kV/cm/bar) can be extrapolated for any mixture and E/p. The attachment effect is directly introduced in the standard waveforms in the same way as explained in section 7.1.6.2, i.e. the standard waveforms are multiplied by the exponentially decreasing probability of electrons to survive along the path length, according to a given attachment coefficient (η).

In figure 64, the experimental standard waveform obtained with a Xe-CF_4 mixture for a path length of 2 cm is compared with the simulated one, which was generated from pure xenon data, after the drift velocity scaling (the result being shown in green) and the attachment correction (considering the same η measured for the mixture). The experimental pure xenon standard waveform used for the modulation is also plotted (in black).

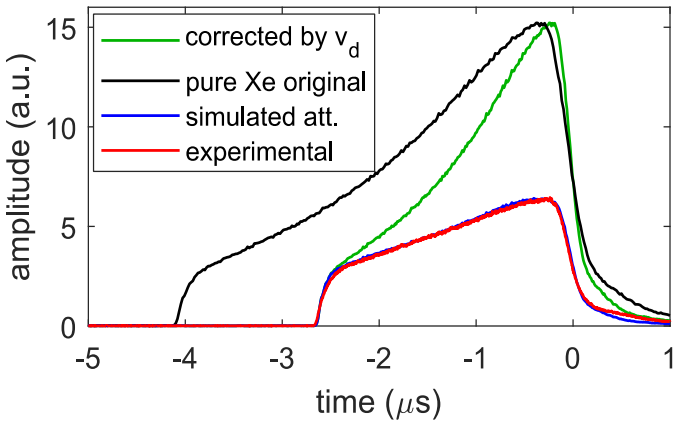

Figure 64: Experimental standard waveform (red) obtained with a Xe-CF_4 mixture (CF_4 concentration of 0.029 %) for a path length of 2 cm and the respective simulated waveform (blue), obtained from the experimental standard waveform produced with pure xenon for the same path length (black), after applying the drift velocity scaling (green), and then the attachment correction (considering η = 0.45 cm^{-1}, which is the same value measured with the Xe-CF_4 mixture). The experimental data were taken at a pressure of 1.25 bar and E/p = 2.23 kV/cm/bar for pure xenon, and 1.22 bar and 3.45 kV/cm/bar for the mixture, respectively.

The pure xenon standard waveform is much longer than the Xe-CF_4 one, most likely due to the lower E/p value. However, after the drift velocity scaling is applied, the resulting waveform matches the experimental one in terms of duration. Still, the Xe-CF_4 experimental waveform is flatter. This mismatch is solved after the attachment correction being applied,

resulting in an acceptable agreement between the modulated and the experimental standard waveform. The agreement was also observed for other path lengths, validating the method.

It is worth to refer that the attachment modulation is performed only between the waveform start and end instants, since most of the PMT signal after the waveform end is composed of afterpulsing rather than EL photon detections. Even so, the simulated waveform is underestimated in this region (as seen in figure 64). A detailed experimental study of the afterpulsing dependence on the amount of collected photons would be needed to address this issue. However, we do not consider it necessary for the present work due to the smallness of the observed deviation.

For the example of figure 64 the drift velocity scaling and η were measured experimentally from the waveforms sampled with the direct method. However, these parameters are unknown for the previous mixture measurements obtained with the standard method. Therefore, η is left as free parameter in the fit, while the drift velocity scaling comes from Magboltz simulations as they usually describe well the detector kinematics (as demonstrated in figure 57).

After the reference waveforms (obtained with pure xenon for $E/p = 2.24$ kV/cm/bar) corresponding to each path length are corrected by the drift velocity and attachment coefficient (according to the experimental conditions of each MCA pulse-height distribution), they are integrated by the software-implemented electronics (using the respective shaping constant), as described in appendix E. The centroids of the several Gaussians are given by the maximum heights of the pulses at the output of the modulated linear-amplifier, which is preceded by the modulated preamplifier.

8.2.2 Energy resolution dependence on the path length

For the simplified response function, the relative FWHM of the Gaussians was assumed to be constant over the x-ray penetration. However, this approximation is not accurate when electron attachment is too high, because of the large contribution of Q to ER. As shown in section 7.1.5, the Q factor depends on both the attachment coefficient and the path length drifted by electrons.

In figure 65, the experimental energy resolution obtained with the direct method for pure xenon and two Xe-CF_4 mixtures is plotted as a function of the drifted path length. As seen, the degradation of ER with the path length is clear, especially for the highest η value. On the other side, ER remains roughly constant for pure xenon, since Q is almost zero, and the variation of the PMT photon statistics is negligible for this narrow interval of path lengths.

The simulation developed in section 7.1.5 (considering the solid angle variation effect, as seen in figure 49) can be here exploited, aiming at modulating the energy resolution dependence on total electron path length ($R_E(\Delta x)$). First, the Q factor variation with the path

length ($Q(\Delta x)$) is interpolated from the data plotted in figure 49, for a given η. Then, $R_E(\Delta x)$ is computed from the $Q(\Delta x)$ using equation (10), considering the Fano factor and PMT contributions to be constant over the entire path length range. Therefore $R_E(\Delta x) = \sqrt{(R_Q(\Delta x))^2 + R_c^2}$, where $R_Q(\Delta x)$ is the contribution from $Q(\Delta x)$ and R_c the constant term (related with the Fano factor and the PMT). The result of this procedure is shown in figure 65, where η used in the $R_Q(\Delta x)$ modulation was measured from the same Xe-CF_4 data sets, while R_c was adjusted in order to fit the simulated curves to experimental data. For comparison, the result obtained for the pure xenon data set is also shown, where η was considered zero.

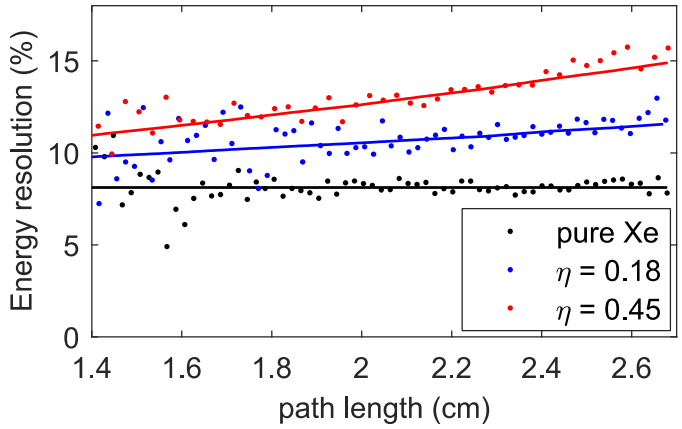

Figure 65: Experimental energy resolution (using only the 1st waveform organization method described in section 6.1) as a function of the path length Δx, obtained with pure xenon (black), and with two Xe-CF_4 mixtures, with CF_4 concentrations of 0.012 % (blue) and 0.029 % (red), corresponding to attachment coefficients of 0.18 and 0.45 cm^{-1}, respectively. The pure xenon and the Xe-CF_4 mixture (0.012%) were obtained at E/p = 2.23 kV/cm/bar, while Xe-CF_4 mixture (0.029%) was obtained at E/p = 3.45 kV/cm/bar. Solid curves represent the modulated dependence of ER on Δx considering the respective η values.

The agreement between the simulated curves and experimental points is acceptable, validating the reliability of this method to estimate the energy resolution variation with the x-ray penetration. Nonetheless, a slight deviation can be observed for the longer path lengths, most likely because these groups are not representative, as discussed in chapter 5.

The energy resolution of the several Gaussians composing the improved response function follow this modulation rather than being constant as in the simplified response function. For each MCA pulse-height distribution, $R_E(\Delta x)$ is generated according to η and R_c. The energy resolution of the 2.5-cm Gaussian is left as a free parameter, together with η.

8.2.3 Correlation between the energy resolution and the attachment

In theory, the precision of the detector response function to estimate the corrected energy resolution could be improved leaving a lower number of free parameters in the fit, for example fixing η to the value expected from simulation. Alternatively, the correlation between ER and

η could be exploited (similar to the $R_E(\Delta x)$ modulation demonstrated in figure 65). Thus, instead of η being left as a free parameter in the fit, it can be defined as a function of the FWHM and the centroid of the 2.5-cm Gaussian.

Since the major contribution to Q in attachment-inducing mixtures is usually the attachment itself, Q is considered to be only dependent on η, according to the simulated data shown in figure 49. Q is in turn obtained from energy resolution, after subtracting the Fano factor contribution (using data from table 1) and the PMT contribution (computed from figure 43, using the 2.5-cm Gaussian centroid to calculate $1/A$). In this way, for each pulse-height distribution fit, η is obtained from the FWHM and centroid of the 2.5-cm Gaussian, which are both left as the only free parameters in the fit.

This variant of the improved response function increased significantly the precision of the corrected ER estimation, reducing the relative statistical error down to 3 %. The accuracy is also better, at least for the cases where direct measurements of the corrected ER are available (table 3). However, despite the promising results, this method is not used here, due to the possible systematic errors introduced by the several assumptions. A more profound experimental and theoretical study of the Q dependence on η would be necessary, using also other attachment-inducing additives, such as CO_2. Still, the technique here developed to remove η from list of free parameters is an important starting point for a future work

8.2.4 Results with the improved response function

In summary, the improved response function of the driftless GPSC consists in a sum of about 5000 Gaussian functions, whose centroid distribution is computed from the experimental standard waveforms obtained for pure xenon with the direct method, after application of proper corrections. First, the standard waveforms are scaled according to the expected drift velocity for the acquisition conditions, obtained from Magboltz simulations. Then, the waveforms are corrected by the exponential probability of electrons to survive along the drifted path length, for a given η. Finally, the resulting standard waveforms pass through the software implemented electronics (preamplifier, followed by the linear-amplifier), using the same shaping constants of the experimental data acquisition. The centroid of each Gaussian is computed from the maximum height of the linear-amplifier simulated pulse obtained for each path length. The Gaussian areas follow the histogram of waveform durations obtained experimentally with pure xenon, after being corrected with the exponential x-ray attenuation law expected for the corresponding operating pressure and temperature, i.e. the same methodology used in the simplified response function (section 8.1.2). The energy resolution of the several Gaussians is computed from the simulated Q dependence on the path length (figure 49) for the respective η considering the Fano factor and PMT contributions equal for

all Gaussians. The centroid and energy resolution of the Gaussian corresponding to the 2.5-cm path length are left as free parameters in the fit, together with the attachment coefficient.

In figure 66, the MCA pulse-height distribution obtained with a CF_4 concentration of 0.066 % , for an E/p value of 2.27 kV/cm/bar, is fitted by the improved response function. To demonstrate the importance of the linear-amplifier modulation, two functions were fitted to data, one considering a shaping constant of 2 μs, i.e. the same value that was set on the physical linear-amplifier, and the other function considering 12 μs, which is comparable to the exclusion of the linear amplifier effect (since waveforms durations are about 4.5 μs). As expected, the fit function describes better the experimental pulse-height distribution when the correct shaping constant is used in the linear-amplifier modulation. If the linear-amplifier effect is not considered as in the simplified response function, the quality of the fit and the subsequent ER estimation are considerably degraded.

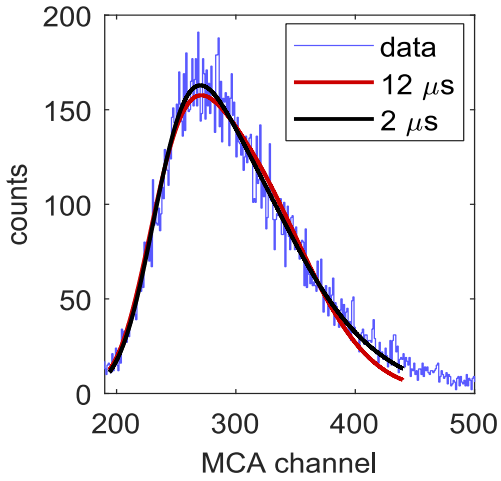

Figure 66: Two improved response functions considering either a shaping constant of 12 μs (red) or 2 μs (black), fitted to the MCA experimental pulse-height distribution (blue) obtained with a shaping constant of 2 μs. Experimental data and the fit function were obtained for 5.9 keV x-rays absorbed in a Xe-CF_4 mixture with a CF_4 concentration of 0.066 %, at 1.22 bar and an E/p value of 2.27 kV/cm/bar.

In figure 67, the corrected energy resolution (a) and the corresponding Q factor (b) estimated using the improved response function are compared with the respective values obtained with the simplified response function, for the same CO_2 mixture, for several E/p values.

Since the energy resolution variation with Δx is modulated in the improved response function, ER can be estimated for a 2.5 cm path length, but not in the simplified response function where ER is considered constant. In the latter case, the estimated ER is interpreted as the average value obtained for the mean path length (~2.25 cm). Therefore, in order to compare the results produced by both fit functions, Q obtained with the simplified function is scaled for 2.5 cm, considering a linear dependence of Q on Δx (for Xe-CO_2 mixtures,

$Q_{2.5cm} = 1.11 \times Q_{2.25cm}$). This approximation is valid given the closeness between the 2.5 cm extrapolated value and the mean path length (about 2.25 cm for CO_2 data, and 2.27 cm for CH_4 and CF_4 data). The analogous scaling of the corrected ER is obtained for each data point considering the Q scaling and its contribution to ER, as the Fano factor and PMT contributions almost do not change within this narrow Δx range.

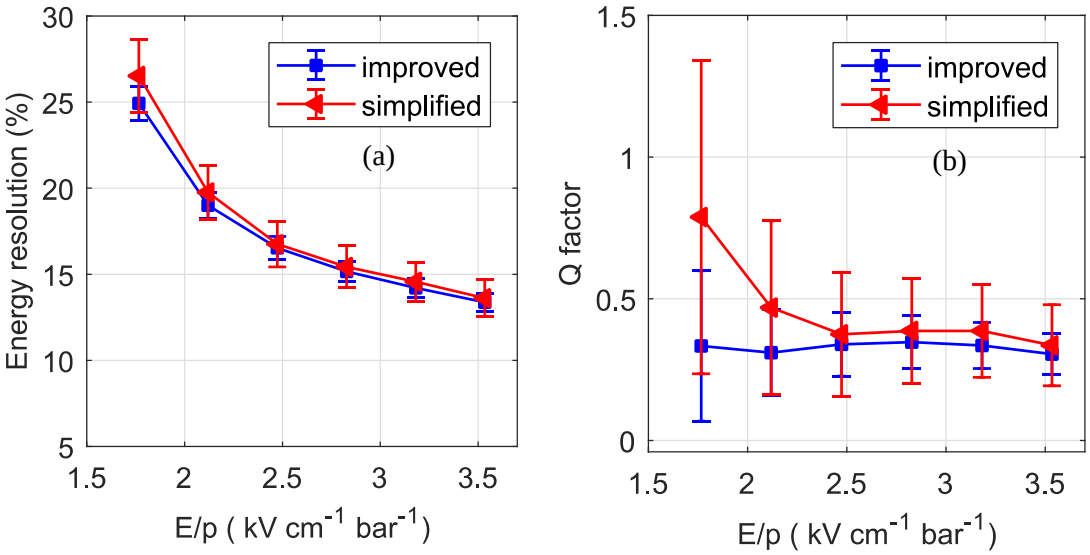

Figure 67: Corrected energy resolution (a) and corresponding Q factor (b) estimated from several pulse-height distributions obtained with different E/p values, using either the improved response function (in blue) or the simplified one (in red). The experimental data were obtained for a CO_2 concentration of 0.33 %, at a pressure of 1.13 bar, irradiated by 5.9 keV x-rays. The linear-amplifier shaping constant was set to 4 µs, the same value used for the modulated linear-amplifier.

In the example of figure 67 (a), ER obtained with the simplified function is slightly overestimated in comparison with ER coming from the improved function. This deviation is larger at lower E/p values, which may be explained by the higher impact of the electronics, since the waveform durations become comparable to the linear-amplifier shaping constant (4 µs). As seen, the mismatch between the ER values of the two data sets has a larger influence on Q, because the latter depends quadratically on ER, and other the contributions are subtracted. The Q factor obtained for the lowest E/p value with the simplified function is almost a factor of 2 higher than the one estimated with the improved function. The results produced by the two fit functions represented in figure 67 are a good example of the trend usually observed for other mixtures.

The reliability of the present method in the estimation of the 2.5-cm Gaussian centroid, the energy resolution and the attachment probability can be summarized as follows. The determination of the attachment probability for 2.5 cm (computed from the η parameter) is generally more precise and accurate than the one provided by the simplified function, since fluctuations between close E/p measurements are smaller, and the results agree often with the values measured directly. Still, we do not consider this method reliable enough to

accurately determine the attachment probability within the full range of studied working conditions. On the other hand, the estimation of the corrected ER is acceptably accurate, at least for the available direct measurements (i.e. the ones listed in table 3), for which the overestimation of ER obtained with the simplified function is still observed, but the relative difference is lower, usually 4 %, reaching 8 % for the highest CF_4 concentration. The relative uncertainty (68 % CL) of the ER fit parameter is usually about 6 %, which is almost a factor of 2 lower than the relative statistical error obtained with the simplified response function.

Since the centroid of the full absorption peak is not significantly affected by the x-ray penetration, the accuracy achieved in the estimation of the 2.5-cm Gaussian centroid is far superior than the other two parameters (energy resolution and attachment coefficient). When the pulse-height distribution is left-tailed (e.g. pure xenon), the centroid of the non-corrected full abortion peak can be 3 % lower than the centroid of the 2.5-cm-Gaussian, while for right-tailed distributions (e.g. high CF_4 concentrations) it can be 8 % higher. Therefore, even without a complex response function based on several Gaussians, the error obtained in the EL yield estimation by simply measuring the centroid of the full absorption peak is lower than 10 %.

8.3 Conclusions

The main motivation for the study of the driftless-GPSC waveforms was to build a detector response function suitable to fit the pulse-height distributions previously obtained with Xe-CO_2, Xe-CH_4 and Xe-CF_4 mixtures. In this way, a better estimation of the energy resolution at fixed x-ray penetration could be computed, and consequently, a more accurate Q factor, which is essential to extrapolate our results for the NEXT-100 TPC, or any other detector.

The information from the experimental PMT waveforms was used, and some processes were modulated, e.g. electron attachment and electronics. Either the preamplifier or the linear amplifier was found to distort significantly the MCA pulse-height distribution in a driftless GPSC. The large EL region in our prototype intensifies this effect, especially at low E/p values due to the longer duration of waveforms. As a result, the left-tail in the pulse-height distribution is decreased for low attachment mixtures, whereas the right-tail is even larger for high attachment mixtures.

Two detector response functions were generated, a simplified version based on rough approximations and an improved one, both delivering similar results, except for low E/p values where the electronics effect that is modulated in the improved function becomes relevant. The energy resolution and Q factor estimated using these response functions were compared with direct measurements obtained for a fixed x-ray penetration. The response function fitting method has shown to be reliable estimating these parameters, within an error of 5 % and 20 % for the energy resolution and Q factor, respectively. This is a huge

improvement with respect to the results obtained when the x-ray penetration is not considered, where Q can be a factor of 3 overestimated.

9 RESULTS FOR CO_2, CH_4 AND CF_4 ADDITIVES

When this work was initiated, CO_2, CH_4 and CF_4 were pointed out as the most promising molecular additives to add to xenon, although each of them have distinct properties. Besides the undesirable effect that the electron cooling itself has on the amount of produced EL photons, for a given electric field, CH_4 also reduces the EL yield due to the quenching of excited states. On the other side, CF_4 is expected to keep almost untouched the scintillation probability of pure xenon, the EL yield being only degraded by the dissociative attachment of electrons. This latter property increases considerably the fluctuations on the number of emitted EL photons, hence degrading the detector energy resolution. CO_2 is expected to induce both effects, quenching and attachment. Therefore, none of these molecules is perfect (i.e. affecting the EL process only though the electron cooling), each one having advantages and disadvantages. Our goal was to find the best candidate for the NEXT experiment, where electron diffusion should be significantly reduced.

In this chapter, the EL yield (section 9.2) and energy resolution (section 9.3) of the detector are reported for different electric fields and additive concentrations, for the three molecular additives investigated. Based on these results we also estimate the squared relative standard deviation on the number of EL photons produced per electron, i.e. the *Q* factor (section 9.4), and the scintillation probability (section 9.5). But first of all, the description of the experimental operation conditions is presented (section 9.1).

9.1 Operation conditions

The performance of the driftless GPSC was evaluated using x-rays from a ^{55}Fe radiative source. An x-ray beam was obtained using a 4 mm thick lead collimator, with 2 mm in diameter, placed ~2.5 cm way from the detector window. In the worst case, the beam

divergence is 1 mm in diameter per mm of length, irradiating the full detector entrance window (8 mm in diameter). Only 5.9 keV x-rays from the Mn K_α line are allowed to interact in the gas, since 6.4 keV x-rays from the Mn K_β line are efficiently absorbed in a chromium film. In this way, a clean 5.9 keV full abortion peak is obtained, making it easier to determine the detector energy resolution.

The NEXT-100 detector will operate at a pressure of 10-15 bar. Since our apparatus cannot sustain such high pressures, our measurements were made at pressures close to the limit of the capacitive pressure gauges installed, rated up to 1000 torr (~1.33 bar). In this way, the possibility of atmospheric air entering into the detector through leaks is reduced. In our setup, the gases are introduced into the system after being cooled down with liquid nitrogen. Therefore, it is technically hard to get always the same final pressure. The pressure of each mixture could differ at most 1.6 %, 2.3 % and 3.2 % with respect to the average pressure, which was 1.13, 1.25 and 1.24 bar for Xe-CO_2, Xe-CH_4 and Xe-CF_4 mixtures, respectively.

The typical operation range of the electric field in the electroluminescence region is covered, i.e. above the secondary scintillation threshold (~0.75 kV/cm/bar) and below the electron avalanche threshold (~4.5 kV/cm/bar) [95]. The PMT is polarized at about 850 V, corresponding to a gain of about 7×10^5, according to the manufacturer specifications.

Before preparing each mixture, the getters are operated at 250 ºC during several hours, thus insuring the maximum purity of xenon. During this time, the RGA additive background is measured, being then used in the calculation of the mixture concentration, as described in chapter 3. Since getters also remove the molecular gases studied, their operation temperature is dropped down to 80 °C for Xe-CO_2 and to 120 °C for Xe-CF_4 and Xe-CH_4, usually one hour before preparing the mixture, to ensure stabilization of temperature inside the getters. In this way, the possible adsorption of these molecules in getters is kept as low as possible, while more reactive gases as O_2 can still be actively removed [127]. Despite the getters performance being not ideal at these temperatures, it is still acceptable. A slight reduction on the pure xenon EL yield (7 % at most) was observed when compared to the one obtained at 250 ºC, after several days of operation. On the other side, no significant degradation of the energy resolution was detected. Thus, a relative systematic error in the measured EL yield of 7 % at most may exist.

The detector total pressure was found to decrease by ~2.1 % and ~1.6 %, when the getters temperature is reduced from 250 ºC down to 80 ºC and 120 ºC, respectively. These changes in pressure are due to the gas average temperature variation, rather than the number of atoms or molecules, inside the chamber. Therefore, the pressure measured for each acquisition with mixtures is corrected according to the difference in the total pressure when the getters temperature is decreased. In this way, all the reduced EL yields and the reduced electric fields are related to the same number density.

The concentrations of CO_2 and CH_4 in the measurements reported in this chapter were obtained using the RGA, following the methodology introduced in chapter 3. The errors represented correspond to the statistical uncertainty of the measurement, nonetheless an additional systematic error may exist. Due to the minute concentrations required for Xe-CF_4 mixtures, the relative error of the RGA measurement was too large, reaching 50 % in some cases. Therefore, the concentrations measured with the pressure gauges at the time the mixture was prepared are used instead (i.e. an upper limit of the real concentration). In this case, the error corresponds to the difference between the initial concentration and the one measured by the RGA during the detector operation.

The range of concentrations studied differs from additive to additive, because the same reduction of the electron diffusion is achieved with different amounts of each molecular additive. According to simulations [16], a 3-dimentional electron spread per drifted meter (D_{3d}) of 2.75 mm (considering a E/p value of 20 V/cm/bar in the drift region, at 10 bar) is reached with concentrations of 0.04 %, 0.22 % and 0.015 % of CO_2, CH_4 and CF_4, respectively. Therefore, in the present experimental work, concentrations that allow to reduce D_{3d} down to at least 4 mm were used, this being the region of interest for the NEXT experiment.

9.2 Electroluminescence yield

Electroluminescent is the main signal amplification mechanism used for the detection of rare events in some TPCs, such as the one used in the NEXT experiment. Therefore, quantifying the effect of molecular additives on the EL yield is a key point. Our experimental apparatus (described in section 4.1, figure 17) allows to measure only relative values of the EL yield (Y). The absolute reduced EL yield (Y/p) is obtained as follows. The simplified response function of the detector (described in section 8.1) is first fitted to the full abortion peak of the MCA pulse-height distribution, and the centroid of the estimated 2.5-cm Gaussian is divided by the respective working pressure. In this way, the relative Y/p is obtained for the several E/p values. The variation of Y/p with E/p is fitted by a straight line (since the dependence is known to be linear [92]), which is used to extrapolate the relative Y/p at a specific E/p value of 2.63 kV/cm/bar. Finally, the absolute pure xenon Y/p at the same E/p value and at a similar pressure (1.52 bar), which can be found in reference [92], is used to compute the normalization constant. Since the electronics and PMT gain remain unchanged across our measurements with mixtures, the same normalization constant is applied to all the experimental relative Y/p values.

The statistical uncertainty associated to our EL yield measurements (i.e. the error coming from the fits to the pulse-height distributions) is negligible, but the relative error of

the absolute Y/p used in the normalization is about 14 % [92]. Consequently, the Y/p values reported in this section are affected by the same relative error. However, this error is not shown in the plots due to readability proposes.

In a driftless GPSC, the primary and secondary scintillation signals are superimposed because the electrons start immediately to drift under the EL electric field after an interaction. However, since the amount of EL photons is usually three orders of magnitude larger than the amount of primary scintillation photons, the last ones can be neglected in the Y/p measurements [87].

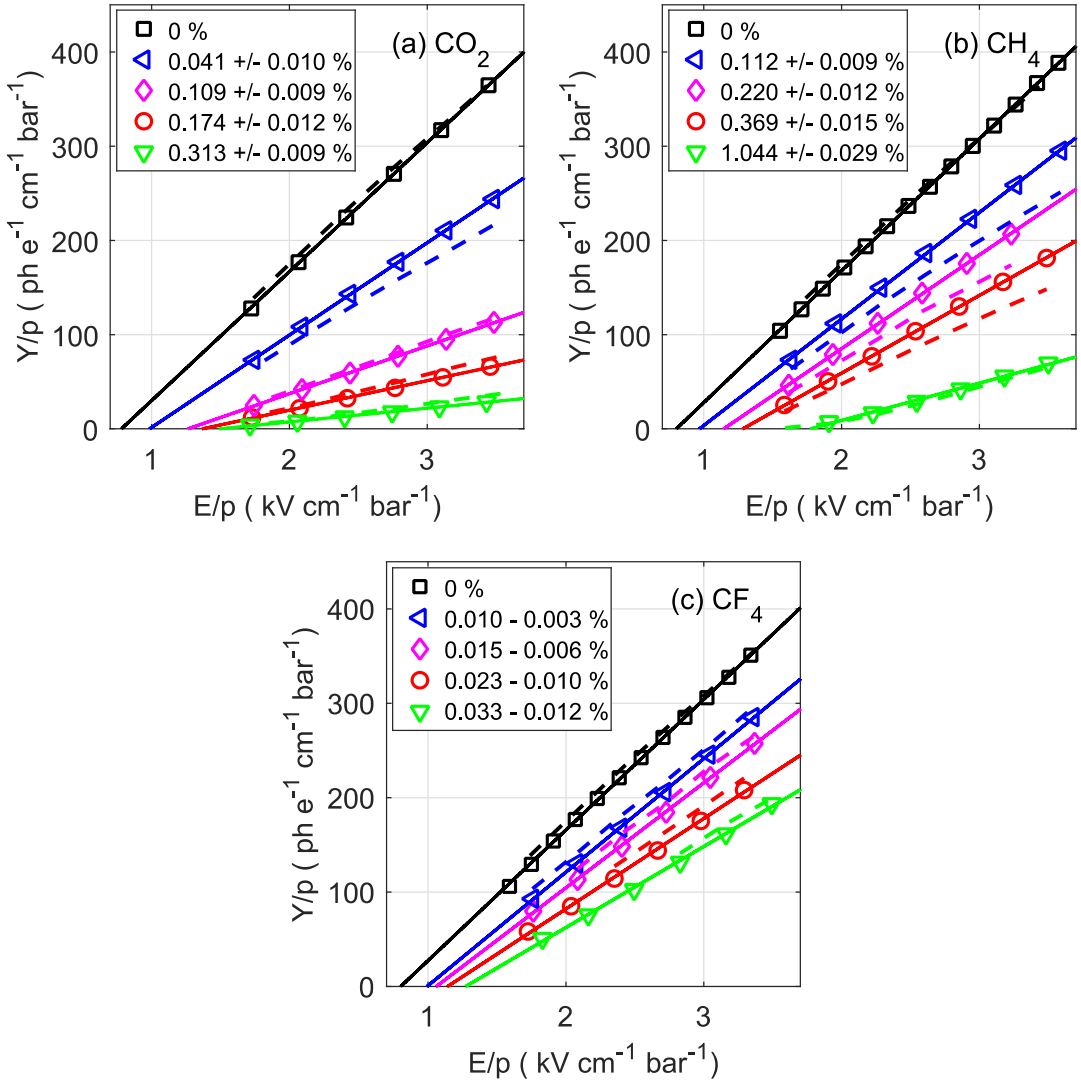

Figure 68: Absolute EL yield (Y/p) as a function of E/p, for different types and concentrations of molecular gases added to pure xenon: (a) CO_2, (b) CH_4, (c) CF_4. Total pressures of 1.13, 1.25 and 1.24 bar were used in average, for Xe-CO_2, Xe-CH_4 and Xe-CF_4 mixtures, respectively. Solid lines show linear fits to the data, while dashed lines are simulation values [16, 70, 113].

In figure 68, Y/p is plotted as a function of E/p for different concentrations of CO_2 (a), CH_4 (b) and CF_4 (c). Several concentration data series were omitted to make data clearer or because they are outside the range of interest for NEXT. The solid lines are fits to the

experimental data points, while the dashed lines represent predictions from simulation, for the same additive concentrations, E/p values and total pressure, according to the method reported in [16, 70].

In a previous experimental study on the emission spectra from Ar-CO_2 and Ar-CH_4 mixtures in a GPSC, a relative reduction of about 80 % and 70 % on the secondary scintillation emission spectra intensity was observed for concentrations as low as 0.004 % and 0.02 % of CO_2 and CH_4, respectively [101]. Even the minute concentrations of CO_2 and CH_4 required to reduce efficiently the electron diffusion were believed to degrade excessively the scintillation signal, making the GPSC useless. However, we demonstrate in this section that the EL-yield reduction is tolerable in xenon-based mixtures, probably because of the faster decay rate of the scintillation process (~100 ns) when compared with argon (~3 µs [104]).

In general, the agreement between the simulated and experimental data is better than 10 %. The simulated Y/p is higher than the experimental one for Xe-CF_4 mixtures, as well as for the higher concentrations of Xe-CO_2. The opposite is observed for the remaining cases. It is important to note that the EL yield observed in Xe-CH_4 mixtures was found to be significantly higher than the previous theoretical prediction reported in [16], although it agrees with other simulation data [17]. On the other side, the Xe-CF_4 data agrees modestly with both theoretical studies [16, 17].

The E/p value required to initiate the electroluminescence process (EL threshold) is higher as more effective the electron cooling is. This behaviour is confirmed by the experimental results of figure 68. Nevertheless, since the attachment coefficient may change with E/p (as demonstrated in figure 47), the EL thresholds extrapolated using the fitted lines could deviate slightly from the real values (because Y/p is no more linearly dependent on E/p). Even so, some conclusions can be drawn from the linear fits, especially for CO_2 where attachment is expected to be roughly constant within the studied E/p range [70]).

The quenching of excited states is expected to be the main source of EL yield reduction in Xe-CH_4 and Xe-CO_2 mixtures. This property is considered to be independent from the electric field [16, 17, 70]. The sharp decrease of the slopes of the fitted lines with the concentration observed in figure 68 (a,b) is mostly attributed to the quenching. On the other hand, the decrease of the line slopes observed in figure 68 (c) is mostly attributed to the dissociative electron attachment, as the quenching in Xe-CF_4 mixtures is expected to be negligible [16, 17, 70]. As seen, the impact of the latter effect is smaller than the quenching effect, at least within the studied range of concentrations. The slopes of the fitted lines are also expected to be slightly affected by gas transparency in CO_2 [70], although this contribution is minute in our detector, due to the low pressure used (~1 bar) and the short length travelled by photons.

9.3 Energy resolution

A good energy resolution (ER) is crucial for the NEXT experiment, since it is an efficient tool to discriminate ββ0ν events against the background, especially from the ββ2ν distribution. Therefore, the impact of molecular additives on ER was also investigated with the driftless GPSC, for the same molecular species and concentrations reported in the previous section.

The present studies with CO_2, CH_4 and CF_4 were carried out using only the standard method, since the direct method and the respective software were not yet developed at the time. Consequently, the energy resolution obtained directly from the available energy spectra contains also the x-ray penetration effect. To minimize this contribution, two detector response functions were built in chapter 8, which have shown similar results, except for low E/p values. Therefore, the following results were obtained using the simplified response function, thus avoiding the use of simulated drift velocities in an experimental work, while the simplicity of the full methodology is kept. Most of acquisitions for E/p bellow 2 kV/cm/bar are omitted because the simplified response function is less accurate in those conditions (as shown in section 8.2.4), since the distortion of the pulse-height distribution induced by electronics is not modulated.

As explained in section 8.1.3, the corrected ER estimated using the simplified response function should be interpreted as an average value, corresponding approximately to the resolution obtained from events occurring at the mean penetration depth (0.25 cm for CO_2 and 0.23 cm for CH_4 and CF_4). This fact is particularly relevant for attachment-inducing mixtures, as ER may change considerably with the total path length drifted by electrons (as demonstrated in figure 65). However, to make our results more intuitive, allowing the direct comparison between the several ER values, the energy resolution is always extrapolated for a path length of 2.5 cm. The correction is performed for each acquisition considering the mean path length expected for the respective total pressure, assuming a linear dependence of the Q factor with the path length. A more detailed description of this procedure can be found in section 8.2.4. In general, this correction leads to a relative increase of the Q factor of about 10 %, and a relative increase of the energy resolution value of about 4 % (this difference is lower when the photosensor relative contribution is high).

In figure 69, the corrected energy resolution extrapolated for a path length of 2.5 cm is depicted as a function of E/p, for the three additives and several concentrations of them. The error bars come from the fit confidence intervals (68 % CL), being strongly affected by the unknown attachment probability, which is also left as a free parameter in the fit. The average attachment probabilities at 2.5 cm estimated for each additive concentration from the lowest to the highest are: 8 %, 30 %, 44 % and 58 % for CO_2 (roughly constant along the entire E/p range); 27 %, 39 %, 60 % and 69 % for CF_4 (decreasing as the E/p value increases, with a

variation of about 25 % between the lowest and the highest values); and near 0 % for all CH_4 concentrations.

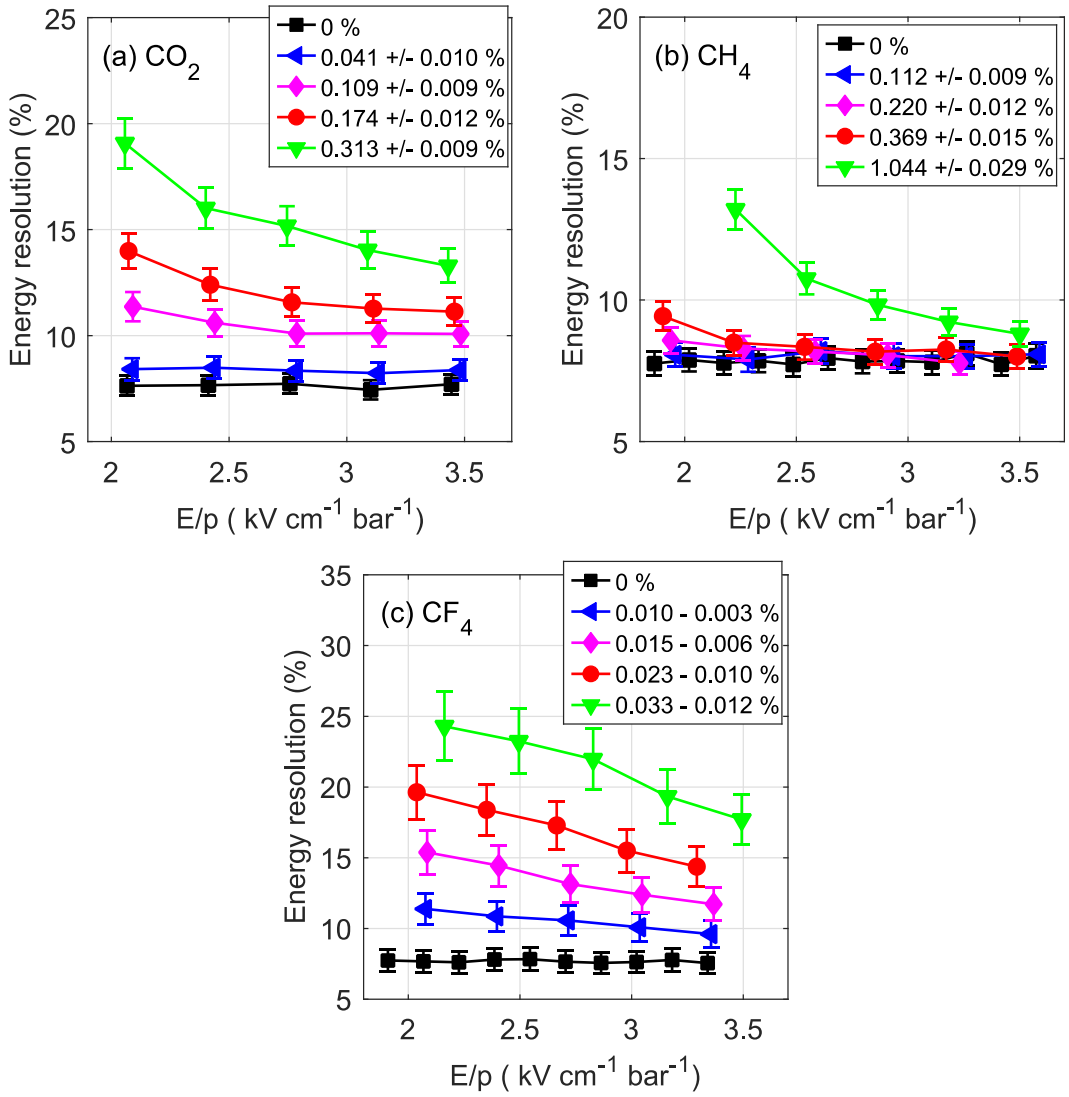

Figure 69: Corrected ER extrapolated for a path length of 2.5 cm, as a function of E/p, for mixtures of xenon with various molecular additives at different concentrations: (a) CO_2; (b) CH_4; (c) CF_4. The solid lines serve only to guide the eye. Total pressures of 1.13, 1.25 and 1.24 bar were used, on average, for Xe-CO_2, Xe-CH_4 and Xe-CF_4 mixtures, respectively.

As seen, ER for Xe-CO_2 and Xe-CH_4 mixtures does not degrade significantly up to concentrations of 0.04 % and 0.4%, respectively, remaining almost unchanged in Xe-CH_4. On the contrary, ER obtained with Xe-CF_4 mixtures is strongly deteriorated even at concentrations as low as 0.01 %. In Xe-CH_4 mixtures, a sharp decrease of ER with E/p is observed, being possible to obtain almost the same ER of pure xenon at high E/p values. Obviously, ER is at some point limited by the charge avalanche threshold. This result suggests that the impact of the CH_4 additive on ER comes mostly from the PMT photon statistics (equation (8)). Therefore, it can be compensated, for instance, by increasing the light collection efficiency. On the other hand, ER has a flatter variation with E/p in Xe-CF_4

mixtures, suggesting that the dissociative electron attachment is the main source of the ER degradation. Despite the attachment coefficient decreasing with E/p in this case (as shown in figure 47), it is most likely impossible to fully recover the pure xenon ER at high E/p values.

9.4 *Q* factor

The *Q* factor is defined as the squared relative standard deviation of the number of EL photons produced per electron. The knowledge of this EL-related parameter is essential to extrapolate the impact of additives for other detectors. To compute *Q*, one needs to exclude from the corrected energy resolution the other sources of fluctuations, i.e. primary charge production (quantified by the Fano factor), and the photosensor related fluctuations.

In chapter 6, the Fano factor and the PMT contribution to the energy resolution were determined for pure xenon through the variation of the EL electric field. These contributions were also determined independently, using the energy resolution obtained at several x-ray energies and the PMT photon statistics obtained with a pulsed LED. The latter method being considered most accurate. The *Q* factor, which is negligible in pure xenon, can now be estimated from the ER obtained with mixtures by subtracting the Fano factor and the PMT contribution previously determined, since they are not expected to change significantly in the presence of additives. The error in the estimation of *Q* is dominated by the larger uncertainties on the ER measurements (figure 69), rather than the possible errors introduced by the method used. Therefore, for the sake of simplicity, the less accurate method (i.e. based on the variation of the electric field, as described in section 6.5.1) is used. Accordingly, the $1/A$ value obtained for each mixture pulse-height distribution is used to estimate the contribution to ER coming from primary charge production and from the PMT, which is given by the line fitted to data in figure 42. Finally, the *Q* factor is computed from equation (8).

The dependence of the *Q* factor on E/p is shown in figure 70, for the three additives at different concentrations. The error bars come from the error in the corrected ER and the two parameters of the linear fit shown in figure 42. Despite we have considered *Q* to be negligible in pure xenon, a measurable growing trend with E/p can be observed in every plot. This odd behaviour is likely produced by additional fluctuations apart from the Fano factor and PMT contributions (i.e. the same effect responsible for the deviation from the linearity at low $1/A$ values observed in figure 42). Because the source of these fluctuations is not clear and the impact on *Q* is small (mostly within the error), *Q* obtained with mixtures is not subtracted by the *Q* factor shown for pure xenon.

As expected, CF_4 induces large fluctuations on the EL light production, most likely due to the high electron attachment, making *Q* larger than the Fano factor for all the studied concentrations. The decrease of Q with E/p is consistent with the decreasing trend of the

attachment coefficient observed in figure 47. On the other hand, Q in CO_2 is still below the Fano factor for the two lowest concentrations, showing almost no dependence on E/p. This behaviour suggests that the electron attachment in Xe-CO_2 mixtures is generally lower than in Xe-CF_4 mixtures (at least for these concentrations), and approximately constant in the studied range of electric fields. In Xe-CH_4 mixtures, the fluctuations on the EL process are negligible, at the level of pure xenon. This is an expected result due to the absence of electron attachment, which is known to have a dramatic impact on the Q factor [70].

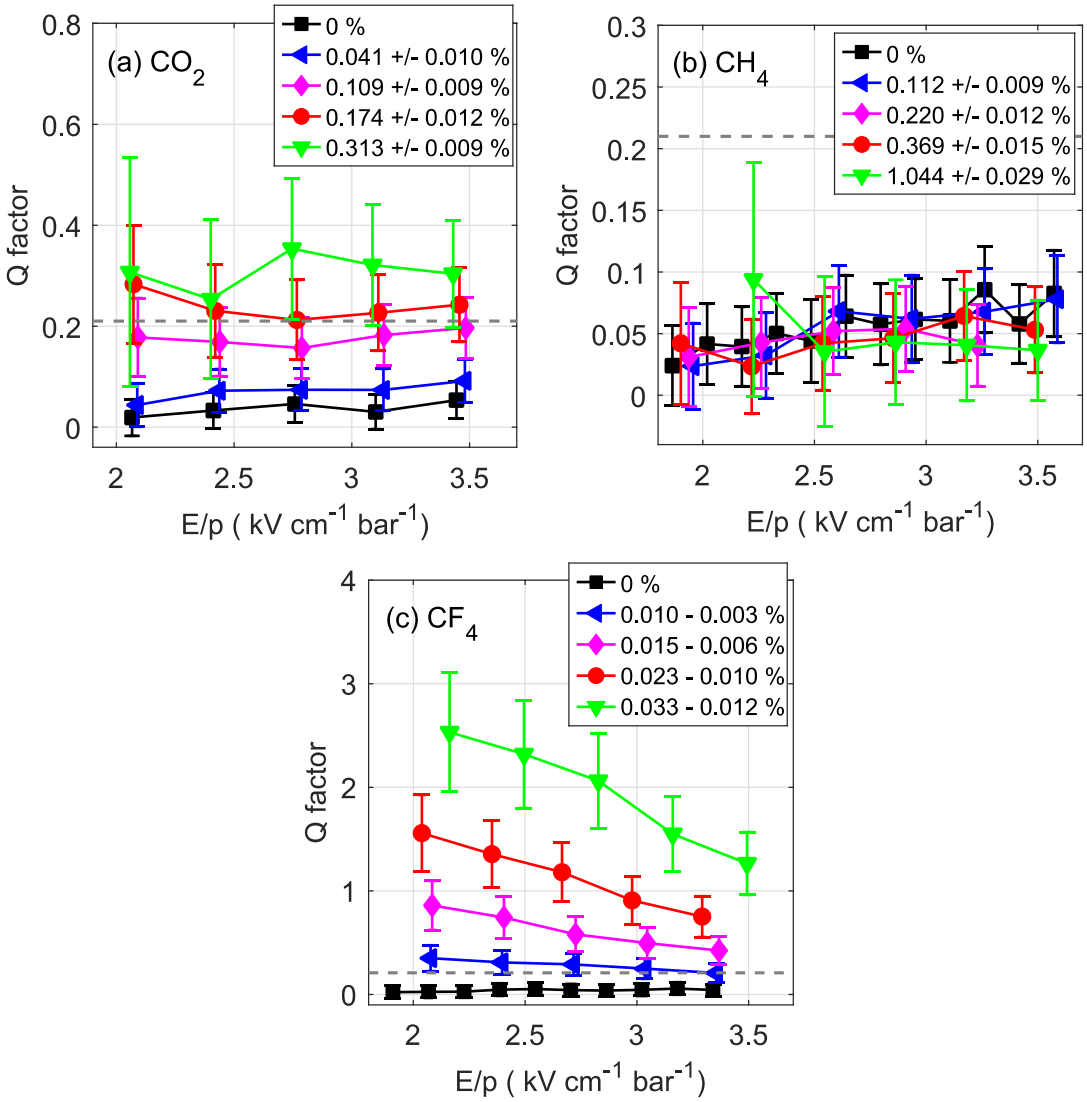

Figure 70: Q factor extrapolated for a path length of 2.5 cm as a function of E/p, for different concentrations of molecular additives: (a) CO_2; (b) CH_4; (c) CF_4. Total pressures of 1.13, 1.25 and 1.24 bar were used, on average, with Xe-CO_2, Xe-CH_4 and Xe-CF_4 mixtures, respectively. The horizontal dashed line shows the Fano factor. The solid lines serve only to guide the eye.

The Q factor was recently obtained for Xe-CO_2 mixtures using a microscopic simulation for the same operation conditions of our experimental study [70]. Those results agree within the errors with data plotted in figure 70 (b) for the full range of CO_2 concentrations and E/p values. Another theoretical study was carried out with Xe-CH_4 and Xe-CF_4 mixtures,

however, considering the NEXT-100 operation conditions (a gas pressure of 10 bar, and an EL gap of 5 mm) [17]. Using the simulation described in appendix D, and considering the solid angle variation along the electron path present in our detector, we estimated that the Q factor in the NEXT TPC would be about 40 % lower than the value measured in our detector for high attachment coefficients, being approximately the same for low attachment coefficients. For CH_4 concentrations up 1 %, the simulated Q factor is below 0.1, which is consistent with our results. For Xe-CF_4 mixtures, the simulated Q factor obtained with a CF_4 concentration of 0.01 % also agrees (within the error) with our results extrapolated for the same conditions of the simulation. The remaining simulated concentrations are outside the range studied experimentally. Even so, the Q factors plotted in figure 70 (c) for the highest CF_4 concentration seem to be higher than the simulated values, especially for low E/p. One should note, the Q factor obtained from the corrected energy resolution estimated with the simplified response function is likely overestimated for high attachment coefficients and low E/p values, as demonstrated in table 3, where a relative systematic error as high as 50 % can be observed. On the other hand, the Q factors obtained using the direct method that are listed in the same table are more consistent with the simulated values of ref. [17] (after applying the proper scaling), even for high CF_4 concentrations and low E/p values.

9.5 Scintillation probability

The scintillation probability (SP) is defined as the ratio between the number of produced VUV photons and the number of excited Xe atoms. In pure xenon, this parameter is known to be near 100 %. However, in mixtures it may severely decrease due to the quenching of excited atoms or excimers. Despite being not possible to measure this parameter directly in our apparatus, the EL-related SP can be estimated from the slopes of Y/p as a function of E/p, if the remaining contributions to the Y/p deterioration are known. Since the scintillation probability of the primary and secondary scintillation processes are expected to be similar, the impact of additives on the intensity of the primary scintillation signal can be also evaluated. Such experimental measurement is of great importance for optical-TPCs, as the NEXT-100 TPC, which relies on this first light burst to access the z-coordinate used in the event topology reconstruction.

In section 7.2, the impact of the electron attachment on Y/p was measured experimentally using data produced with the direct method, allowing the accurate estimation of SP. Unfortunately, the results reported in the present chapter were obtained using the standard method only, preventing us to make this kind of analysis or to measure the attachment probability directly from waveforms. Still, a rough estimation of the attachment probability is provided by the simplified response function that is fitted to the MCA pulse-

height distributions. Then, this parameter can be used to compute the contribution of the electron attachment to the degradation of the EL yield, based on the study described in section 7.1.6 (figure 51) for a path length of 2 cm. Since Y/p is here estimated from the 2.5-cm Gaussian centroid, the relative EL yield reduction (Y_{att}/Y_0) expected for given attachment is estimated considering a path length of 2.5 cm. To maintain the consistency of the present methodology, the simplified response function is used for this propose, as it contains the modulated effect of the attachment on the distribution of Gaussian centroids (section 8.1.1). In this way, the relative reduction of the 2.5-cm Gaussian centroid is directly obtained from this function for the respective attachment probability, with the remaining parameters being fixed.

In Xe-CH_4 mixtures electron attachment is expected to be negligible [16, 17]. Indeed, the attachment probabilities estimated from the simplified response function that is fitted to the pulse-height distributions agree with this prediction. Therefore, for Xe-CH_4 mixtures, SP is directly obtained from the ratio between the slopes of the $Y/p(E/p)$ lines for the several concentrations and the slope for pure xenon, i.e. the lines depicted in figure 68 (b). For Xe-CO_2 and Xe-CF_4 mixtures, the Y/p value corresponding to each E/p is first corrected by the ratio Y_{att}/Y_0 expected for the respected attachment probability. Then, the slopes of the corrected $Y/p(E/p)$ are computed, and SP is estimated as in the case of Xe-CH_4.

The experimental SP estimated for the several additive concentrations are shown in figure 71, together with predictions from simulation [113], obtained as described in ref. [70]. For Xe-CO_2 and Xe-CF_4 mixtures, the vertical error bars come mostly from the large uncertainties on the attachment probability values (estimated from the pulse-height distribution fit), which in turn affects the Y_{att}/Y_0 ratio. For Xe-CH_4 mixtures, the error comes from the $Y/p(E/p)$ linear fit (the systematic error being estimated by excluding the two lowest E/p points). The data series represented in figure 71 were obtained for total pressures of 1.13, 1.25 and 1.24 bar for Xe-CO_2, Xe-CH_4 and Xe-CF_4 mixtures, respectively. The horizontal error bars correspond to the same uncertainties shown in the remaining figures of this chapter.

As anticipated, the quenching of excited states is severe in Xe-CO_2 and Xe-CH_4 mixtures, while it is small or even zero in Xe-CF_4 mixtures. In general, simulation results agree with our experimental results, within the errors. Nevertheless, in contrast to the procedure reported in section 7.2, the low accuracy of the attachment probability values estimated here may have resulted in large systematic errors in SP, for Xe-CF_4 and Xe-CO_2 mixtures. Therefore, the present results cannot be used for an accurate evaluation of the theoretical model. For CO_2, CH_4 and CF_4 concentrations of 0.041 %, 0.220 % and 0.015 % respectively (required to achieve a 3-dimentional electron spread after 1 m drift of 2.75 mm),

SP is decreased by about 30 % in both Xe-CO_2 and Xe-CH_4 mixtures, however, it remains almost the same in Xe-CF_4 mixtures. Therefore, from the scintillation point of view, CF_4 is clearly the best additive. On the other hand, the energy resolution degradation due to the presence of electron attachment is the major limitation for the use of CF_4 as additive, when compared to the other two gases. The impact that CO_2 and CH_4 have on SP could be acceptable for several applications, where the number of collected photons is large. The reduction of the primary scintillation signal intensity is expected to be similar to the values reported here, for the three additives. It is worth mentioning that the scintillation probability may change with the total pressure [70].

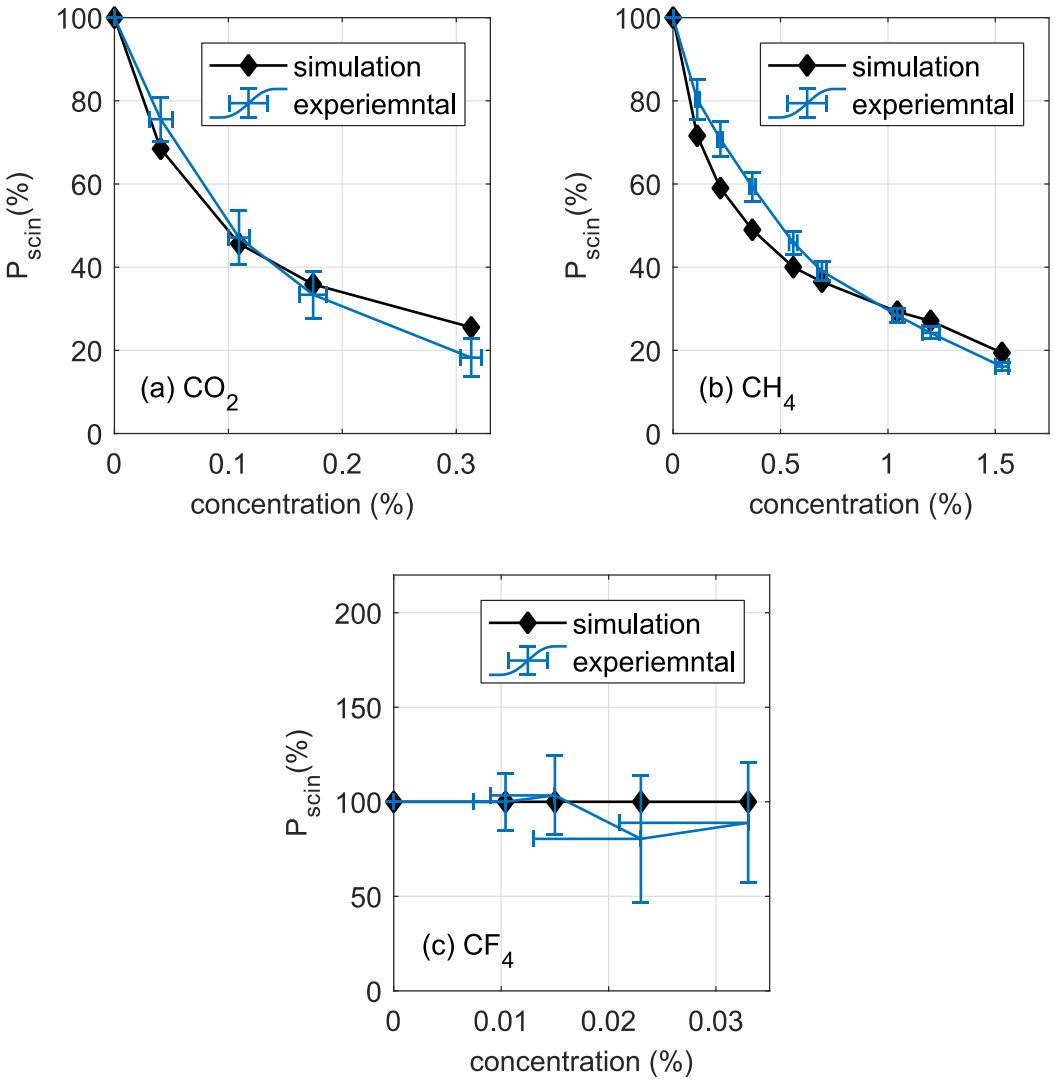

Figure 71: Scintillation probability (P_{scin}) as a function of the additive concentration, obtained for: (a) CO_2; (b) CH_4; (c) CF_4. Experimental values (in blue) were obtained from the Y/p linear dependence on E/p, after the subtraction of the electron attachment contribution. Simulated results are also shown (in black) [70, 113]. Total pressures of 1.13, 1.25 and 1.24 bar were used, on average, with Xe-CO_2, Xe-CH_4 and Xe-CF_4 mixtures, respectively. The solid lines serve only to guide the eye.

10 NEXT-100 EXTRAPOLATION

The ultimate goal of the present study is to find the most suitable molecular additive, to improve the NEXT TPC spatial resolution, which is mainly limited by the large electron diffusion in pure xenon. There are several factors to take into account in this discussion, keeping the energy resolution (ER) at acceptable levels is probably the most important one, since this feature is also crucial for the background discrimination capability. Therefore, the parameters presented in chapter 9 are now used to extrapolate ER to the NEXT-100 detector, filled with xenon admixtures.

The extrapolated ER for every mixture considered must be compared considering the electron diffusion reduction that can be achieved with each additive concentration. However, no experimental results of the electron diffusion are available in the literature for the molecules and working conditions here discussed. Therefore, the electron diffusion is obtained using a Magboltz simulation, since electron transport parameters estimated with these simulations are usually accurate. For instance, in a recent study of the NEXT collaboration, the experimental electron drift velocity, as well as the longitudinal and transversal diffusion coefficients agree within an error of 5 % at most with the predictions from Magbotz simulation. These results were obtained for several drift electric fields, between ~20 and ~50 V/cm/bar, and two different pressures, 7.2 and 9.1 bar [51]. It is important to note that the pressure scaling considered in section 7.3 was confirmed in the same experimental study.

In this chapter, we start by introducing the 3-dimentional diffusion coefficient, obtained from Magboltz simulations. Then, the extrapolation conditions of the experimental results reported in chapter 9 to the NEXT-100 detector are described for each additive. Finally, the extrapolated total number of detected EL photons and the energy resolution are shown, considering also alternative working conditions.

10.1 Three-dimensional electron spread

The transverse (D_T) and longitudinal (D_L) diffusion coefficients can be very different in practice, up to a factor of 4 for pure noble gases at low electric fields (tens of V/cm/bar). Therefore, a point-like charge cloud moving inside a TPC is in general deformed like an ellipsoid. Both coefficients were recently computed within the NEXT collaboration using a Magbotlz simulation, for several concentrations of Xe-CO_2, Xe-CH_4 and Xe-CF_4 mixtures [16]. Since the detailed specifications and working conditions of the NEXT-100 were unknown at the time, published results were obtained at a pressure of 10 bar and a drift field of 30 V/cm/bar. The simulations were also carried out for an E/p value of 20 V/cm/bar and a pressure of 15 bar [128]. These results can be extrapolated to other pressures, using the $\sqrt{P_0/P}$ scaling, where P_0 is the simulated pressure, and P the extrapolated one, the temperature being the same [1].

The simulation results used here are the ones shown in figure 7. According to the formalism adopted in this document, the diffusion coefficients refer to the spread per squared root of the drifted path length, in units of $mm/\sqrt{m}$. Simulation data show that D_T is clearly the most important coefficient to be improved, because it is considerably larger than D_L. Moreover, D_T affects two coordinates of the event topology reconstruction. For convenience, the 3-dimentional diffusion coefficient (D_{3d}) is defined here as the characteristic size of the electron diffusion ellipsoid ($\sqrt[3]{xyz}$) after 1 m drift through the TPC, $D_{3d} = \sqrt[3]{D_L \times D_T \times D_T}$ ($mm/\sqrt{m}$). In this way, the EL-related parameters extrapolated for the three additives can be plotted as a function of a unique diffusion-related parameter, making the comparison between molecules and concentrations more intuitive.

Electron-xenon collisions are mostly elastic, allowing the electrons to gain substantial energy even under modest electric fields, due to the small ratio between the electron and the xenon atom masses. For some noble gases (argon, krypton, and xenon), there is a deep minimum in the electron-atom elastic cross-section, known by Ramsauer-Townsend minimum. In xenon (see figure 6), this quantum mechanical effect leads to a local minimum in the longitudinal diffusion near an E/p of 30 V/cm/bar [54], motivating the use of this electric field in TPCs. However, simulations predict that this point may change in the presence of molecular additives [17, 70]. Therefore, the optimal E/p range to be used in the drift region must be re-evaluated for the desired molecular additive concentration. This study was not performed in the present work, however, a further improvement of D_{3d} may be possible in the future.

In addition to the previous considerations, the choice of the drift field relies also on other factors, such as the electron drift velocity optimization required to reduce the effect of the

electron life-time [7], and charge recombination. Since simulation data are only available for a drift fields of 30 or 20 V/cm/bar, the results shown in the next sections only consider these two possibilities. We focus on the E/p value of 20 V/cm/bar, because lower D_{3d} values are generally reached with molecular additives under this field.

The minimum diffusion achievable in a medium at a given temperature (T) and under a given drift reduced electric field (E_d) is defined by the thermal limit ($D_{L,T}^{min}$), which can be derived from the Einstein-Smoluchowski relation, yielding equation (25) [1].

$$D_{L,T}^{min} = \sqrt{\frac{2\ k_B\ T}{q_e\ P\ E_d}} \tag{25}$$

Where k_B, q_e and P are the Boltzmann constant, electron charge and working total pressure, respectively. $D_{L,T}^{min}$ has units of spread per root square of the drifted path length. Thus, for an E_d value of 20 V/cm/bar, a P = 10 bar and for room temperature, $T = 300\ K$, $D_{L,T}^{min}$ becomes equal to $1.6\ mm/\sqrt{m}$. This limit decreases at higher drift E/p values or operating pressures. For example, at E/p = 30 V/cm/bar and P =10 bar, $D_{L,T}^{min} = 1.3\ mm/\sqrt{m}$, and at E/p = 30 V/cm/bar and $P = 15$ bar, $D_{L,T}^{min} = 1.1\ mm/\sqrt{m}$.

10.2 Extrapolation of the energy resolution

The three molecules studied in this work have distinct properties. Therefore, the approximations made to extrapolate the impact of each additive on the NEXT-100 energy resolution are different. In the next sections, the calculations performed for each additive are described.

10.2.1 Xe-CH_4 mixtures

In Xe-CH_4 mixtures, the EL yield is mainly affected by the quenching of atoms and excimers. This mechanism is expected to depend on the gas pressure, especially if excimer quenching is significant. This behavior still remains a theoretical hypothesis, which was raised and discussed in ref. [70], while a previous simulation work reported in ref. [17] neglects the excimer deexcitation channel, leading to a low dependence of the scintillation probability on the pressure. Here, we consider the more conservative scenario, described in ref. [70].

The NEXT-100 detector will probably operate at 10 bar or 15 bar, which is far larger than the 1.25 bar used in our study. Therefore, the experimental EL reduced yields (Y/p in

[7] The electron drift velocity is usually lower for weak electric fields, although this trend depends on the additive concentration [16]. Recently, an electron lifetime of 1.6 ms was measured in the NEXT-White TPC for an E/p value of ~54 V/cm/bar [51].

figure 68 (b)) are scaled according to the ratio between the simulated scintillation probability at 10 bar and 1.25 bar, for each CH_4 concentration. The full simulation model described in ref. [70] is considered (i.e. accounting for 2 and 3-body collisions as well as atom and excimer quenching). The experimental Y/p includes the contribution of electron cooling that increases the EL threshold, however, it should not affect the slope of Y/p as a function of E/p.

The simulated scintillation probabilities (SP) at 10 and ~1 bar are depicted in figure 72, for Xe-CH_4 (a) and Xe-CO_2 (b) mixtures, together with the ratio between both data series. The black curves show that SP is considerably degraded at 10 bar, within the entire range of studied concentrations, either for Xe-CH_4 or Xe-CO_2 mixtures. Nevertheless, an experimental quantification of the quenching dependence on pressure is still required to validate or refute these predictions.

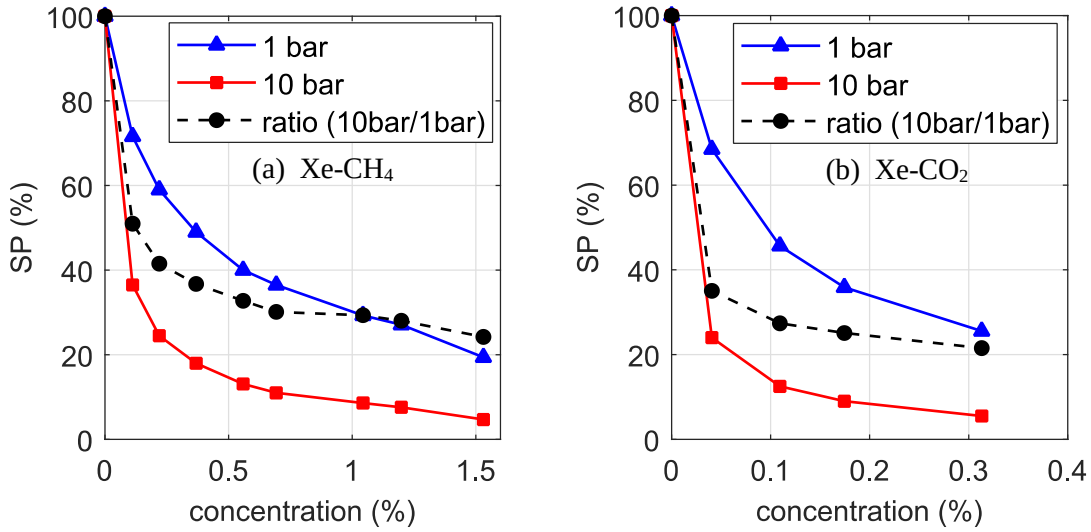

Figure 72: Simulated SP as a function of the additive concentration, (a) for Xe-CH_4 mixtures at 10 bar and 1.25 bar, (b) for Xe-CO_2 mixtures at 10 bar and 1.13 bar [113]. The ratio between the two SP data series is also represented for each additive in the same y-axis (%). The simulation was performed considering the full model described in [70].

The fluctuations on the secondary scintillation production are negligible for the studied concentration range of CH_4, due to the minute attachment probability. For this reason, no Q factor scaling is performed, the Q extrapolated for NEXT-100 being the one measured experimentally (figure 70 (b)). Thus, only the pressure scaling of Y/p is performed for the NEXT-100 energy resolution extrapolation.

10.2.2 Xe-CO_2 mixtures

CO_2 is likely the most complex case due to many mechanisms that degrade the energy resolution. As in Xe-CH_4 mixtures, the quenching of excited states in Xe-CO_2 mixtures is the major process responsible for the Y/p reduction. Therefore, the same pressure scaling computed from the simulated SP is applied to the experimental Y/p obtained with CO_2 (figure

68 (a)). The ratio between SP at 10 bar and 1.13 bar used for the scaling is represented in figure 72 (b).

Besides quenching, the effect of the dissociative electron attachment is also included in the experimental Y/p for Xe-CO_2 mixtures. From equation (19), one would expect the EL yield to decrease linearly with both the drifted path length and the attachment coefficient [70]. In turn, the latter scales linearly with the pressure [1]. Thus, the attachment impact on the NEXT-100 Y/p would be factor of ~2 higher than our experimental results, since the pressure is about 10 times larger, and the EL gap is about 5 times shorter. However, equation (19) is only valid in the limit of low attachment, as demonstrated in figure 51. For this reason, the same simulation described in appendix D is here employed to estimate the scaling of the attachment impact on Y/p.

Since the energy plane is far away from the EL gap in the NEXT-100 TPC, the solid angle along the electron path is nearly constant. Therefore, the additional degradation of Y/p that is produced by the variation of solid angle in our detector should be considered. In figure 73 (a), the ratio between the simulated EL yield including and neglecting the attachment effect ($Y_{att}/\,Y_0$) is plotted as a function of the attachment coefficient (η), considering both situations: the NEXT-100 TPC (black curve), including a constant solid angle, a pressure of 10 bar and an EL gap of 0.6 cm; and our detector (red curve), including the solid angle variation for a 1.3-cm-radius PMT, a pressure of about 1.2 bar and an EL gap of 2.5 cm. For comparison, $Y_{att}/\,Y_0$ was also obtained from the simulated driftless GPSC curve neglecting the solid angle effect (blue curve), after scaling according to equation (19) (dashed green curve in figure 73 (a)). To make the comparison between data more intuitive, η for the two NEXT-100 curves (green and black) was divided by the pressure scaling factor 0.12 ($1.2\ \mathrm{bar}/\ 10\ \mathrm{bar}$).

As discussed in section 7.1.6, the sharp variation of the solid angle in our apparatus leads to a further reduction of the EL yield, as shown from the difference between the blue to the red curve in figure 73 (a). One may still argue that the scaled green curve that was obtained from the blue one through equation (19) is only valid at very low η (below ~0.15 cm^{-1}), being considerably underestimated for larger η (relative to the black curve). Consequently, the expected $Y_{att}/\,Y_0$ in the NEXT-100 TPC is not much different from the one in our detector, in contrast to the equation (19) prediction. Looking at the ratio between the black and red curves of figure 73 (a), one may expect a 20 % reduction of Y/p at most, due to the attachment scaling. Therefore, for the sake of simplicity, the experimental Y/p obtained with Xe-CO_2 is not scaled according to the attachment. Therefore, the extrapolation of the energy resolution for NEXT-100 is underestimated for Xe-CO_2.

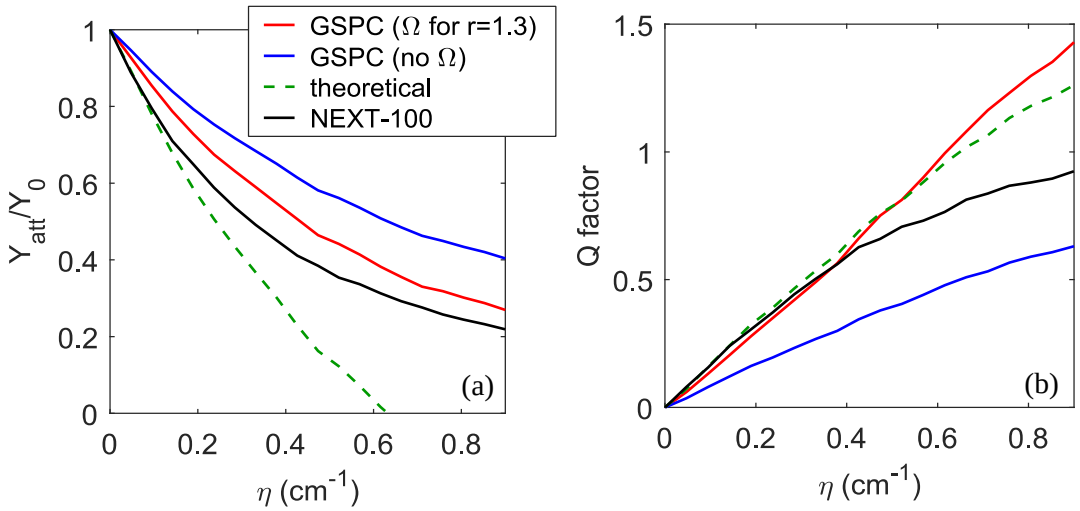

Figure 73: Ratio between the simulated EL yield including (Y_{att}) and neglecting (Y_0) the attachment. (a), and Q factor (b), as a function of the attachment coefficient, considering both the NEXT-100 specifications (black and green curves) and the driftless-GPSC specifications (red and blue curves, assuming the solid angle Ω subtended by a 1.3-cm-radius PMT and not considering the solid angle at all, respectively). The solid curves are obtained directly from simulation (section 7.1.5), while the green dashed curve was scaled from the blue one, according to equation (19).

Despite the Xe-CO_2 transparency to the VUV scintillation being negligible in our compact detector, it may attenuate significantly the primary and the secondary scintillation signals in large scale optical TPCs. The minimum path length travelled by incident EL photos in the NEXT-100 TPC is about 1 m, but reflected photons may travel longer path lengths. Here, we consider the CO_2 transparency to VUV photons after a 2-m travelled length, this being also a more realistic projection for a future tone-scale NEXT experiment. Accordingly, the experimental Y/p for Xe-CO_2 is also multiplied by the expected gas transparency after 2 m for each additive concentration. In figure 74, the transparency of Xe-CO_2 is plotted as a function of the CO_2 concentration. These results were obtained from the experimental photo-absorption coefficient as a function of the photon wavelength, weighted by the respective xenon second continuum spectrum (because the photo-absorption coefficient has a sharp dependence on the wavelength in CO_2, within the VUV scintillation wavelength range) [129].

The dissociative electron attachment induced by CO_2 degrades the energy resolution mainly through the Q factor increase. According to equation (18), one would expect Q to increase by factor of about 2 in NEXT-100, since Δx is about 5 times lower, and η is about 10 times larger. On the other hand, the Q factor further degradation produced in our detector by the solid angle variation (by a factor of about 2) should be absent in NEXT-100. Therefore, the Q scaling with the pressure and the gap length should be broadly cancelled by the solid angle variation effect, resulting in a similar Q factor between our detector and the NEXT-100 TPC. Nevertheless, since equation (18) only holds on the limit of low attachment, a careful quantification of the Q scaling is addressed using the simulation described in appendix D.

In figure 73 (b), the simulated Q (corresponding only to the contribution of attachment) is plotted as function of η, considering either the driftless GPSC or the NEXT-100 specifications. For a η value up to 0.4 cm^{-1}, the Q factor expected for NEXT-100 is roughly the same as for the driftless GPSC. This result is explained by the adverse impact of the solid angle variation on Q in our apparatus. For higher attachment coefficients, Q for NEXT-100 becomes even lower than the driftless GPSC one. The Q factor for NEX-100 was also scaled from the driftless GPSC value excluding the solid angle variation effect (blue curve), according to the approximation of equation (18). The result agrees with the simulated Q factor obtained for NEXT-100 (black curve) up to attachment coefficients of ~0.4 cm^{-1}, then the Q factor scaled according to equation (18) is overestimated.

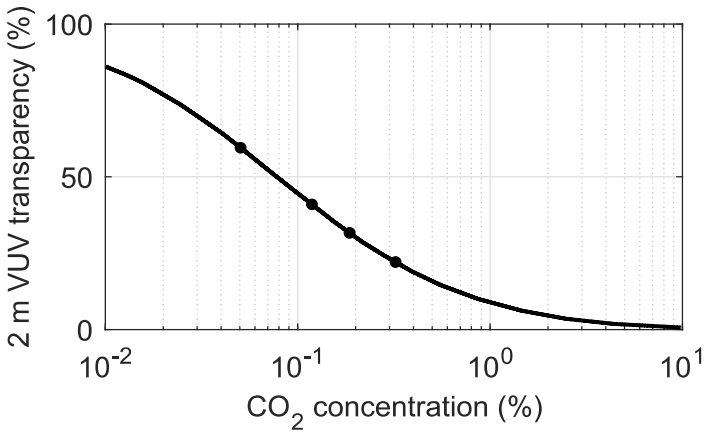

Figure 74: Transparency of Xe-CO_2 mixtures to the Xe scintillation 2nd-continuum after a 2-m travel length as a function of the CO_2 concentration [129]. The black dots mark the studied concentrations.

The experimental Q factor obtained for each E/p value for the several CO_2 concentrations (figure 70 (a)) are multiplied by the ratio between the simulated Q factor for the NEXT-100 and the simulated Q factor for the driftless GPSC including the solid angle variation (black and the red curves of figure 73 (b)). Since this ratio depends on the attachment, η is computed for each concentration from the average attachment probability (at 2.5 cm), which is estimated by the simplified response function fitted to the pulse-height distributions. The Q scaling from our results to the NEXT-100 TPC ranges from 1.25 down to 1, for increasing η values.

In short, the energy resolution is extrapolated for the NEXT-100 TPC filled with Xe-CO_2, considering the scaling of SP on the pressure, the gas transparency to VUV photons for a 2-m travel length, and the Q scaling according to simulation, which includes the solid angle variation effect in our detector.

10.2.3 Xe-CF_4 mixtures

As demonstrated in sections 7.2 and 9.5, the quenching of excited states by CF_4 molecules is negligible, in opposite to the other two additives. Therefore, Y/p in Xe-CF_4 mixtures is

mostly reduced due to the electron attachment. According to the simulation results depicted in figure 73 (a), the larger attachment probability present in NEXT-100 may further reduce the EL yield by 20 %, at most. However, since ER is mainly degraded through the high Q factor in Xe-CF_4 mixtures, the experimental Y/p (figure 68 (c)) is not scaled at all. Thus, the extrapolated ER values are slightly underestimated.

Following the same arguments discussed previously for Xe-CO_2, the experimental Q (figure 70 (c)) obtained with Xe-CF_4 mixtures for the several E/p and CF_4 concentrations are scaled according to the simulated ratio between Q obtained for NEXT-100 and for the driftless GPSC, which are computed from the curves depicted in figure 73 (b), for the respective η values. This scaling ranges from 1.1 down to 0.7 with increasing η.

10.2.4 General considerations

The energy resolution (R_E) expected in NEXT-100 is computed using the general equation (10) introduced in section 2.3.2.2, here rewritten:

$$R_E = 2\sqrt{2\ln 2}\ \sqrt{\frac{F}{\bar{N}_e} + \frac{\mathrm{Q}}{\bar{N}_e} + \frac{1}{k\bar{N}_e\bar{N}_{EL}}\left(1 + \frac{\sigma_q^2}{\bar{G}_q^2}\right)}$$

The mean number of primary electrons produced in the ββ0ν event ($\bar{N}_e$) is given by $\bar{N}_e = Q_{\beta\beta0\nu}/w_i$, where $Q_{\beta\beta0\nu}$ is the energy released in the medium, and w_i average energy required to form an electron-ion pair. For ^{136}Xe, $Q_{\beta\beta0\nu} = 2.458$ MeV, and assuming $w_i = 22$ eV, $\bar{N}_e$ is about $112\ 237$ electrons [12, 86]. For the high energy electrons released in the ββ0ν decay, the Fano factor is likely lower than the values reported in this work, since they were measured with x-rays in the low energy region where sharp discontinuities of the Fano factor are expected [86]. Therefore, a Fano factor of 0.15 is considered for the ER extrapolation to the NEXT-100 TPC, keeping the consistency with previous studies performed by the NEXT collaboration [96]. The Q factor is obtained for each additive as described in the previous sections.

No accurate estimation of the k parameter (i.e. the light collection efficiency) in NEXT-100 is known. In a previous simulation study reported in [96], k was assumed to be in the 0.5-6 % range, while more recently in ref. [16], k was assumed to be 3 %. Therefore, we consider a k parameter of 3 % in our extrapolations. Regarding the relative sigma of the PMT gain, $\sigma_q/\bar{G}_q$, a value of about 0.35 was measured in NEW; accordingly, the same value is considered here.

$\bar{N}_{EL}$ is computed from the experimental Y/p, after the scaling described in previous sections being applied. For convenience, the CO_2 VUV photon absorption is included in the $\bar{N}_{EL}$ parameter. A pressure of 10 bar and an EL gap of 0.6 cm (currently used in NEW) are

considered. The electric field intended to be used in the EL region of the NEXT-100 TPC falls in the 2-3 kV/cm/bar range [12]. Therefore, $\bar{N}_{EL}$ and Q are interpolated from our experimental data considering an $E/p = 2.5$ kV/cm/bar.

10.3 Detected EL photons vs electron diffusion

In this section, the expected number of EL photons detected in a ββ0ν decay (DP) in the NEXT-100 TPC is shown for the several additive concentrations. For Xe-CH_4, DP is computed following the considerations described previously. However, for Xe-CF_4 and Xe-CO_2, the Y/p scaling according to the simulated Y_{att}/Y_0 shown in figure 73 (a) is also considered. For simplicity, the attachment variation with E/p in Xe-CF_4 is neglected, hence the scaling of Y_{att}/Y_0 affects only the slope of the lines fitted to the experimental Y/p as a function of E/p.

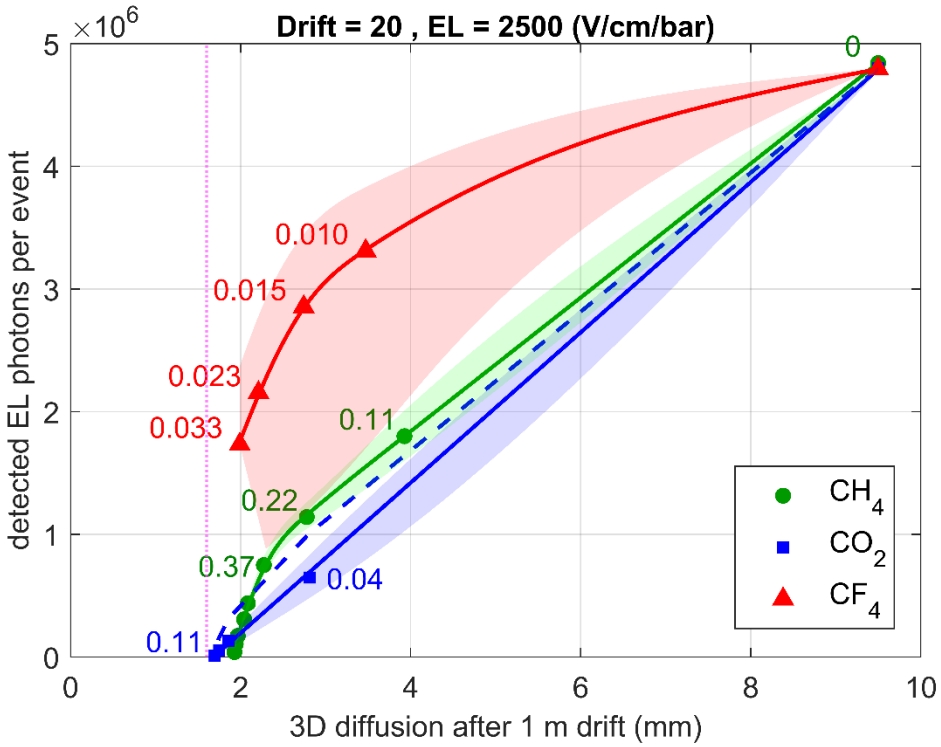

Figure 75: Expected number of EL photons detected per ββ0ν event in the NEXT-100 TPC as a function of the 3-dimentional electron spread after 1 m drift (D_{3d}) for the several additive concentrations (indicated in the plot). Electric fields of 2.5 kV/cm/bar and 20 V/cm/bar were considered in the EL and drift regions, respectively. The dashed blue line was obtained neglecting the CO_2 opacity. The dashed pink line represents the D_{3d} thermal limit. The shadow areas correspond to the experimental error intervals for each additive.

In figure 75, DP for an EL field of 2.5 kV/cm/bar is plotted as a function of D_{3d}, for the three additives at several concentrations. D_{3d} was obtained from Magboltz simulations for a drift field of 20 V/cm/bar. The respective thermal limit (at the room temperature) is also shown in the figure. Since the exact attenuation of the EL signal produced by the CO_2 opacity

is unknow, DP was also extrapolated considering full transparency (blue dashed line). The error associated to each additive data series is represented by a shadow area, which is bounded by the curves corresponding to the best and worst-case scenarios. These curves do not take into account the uncertainty of simulation data (i.e. electron diffusion and scaling), they are computed based solely on experimental data, including the error of the additive concentration, represented in figure 68, and the error from the linear fits performed to $Y/p(E/p)$.

In order to reduce the 3-dimentional spread of electrons down to about 3 $mm/\sqrt{m}$, one may lose about 85 %, 75% and 40 % of EL photons for Xe-CO_2, Xe-CH_4 and Xe-CF_4 mixtures, respectively. This degradation of the EL light is more severe than the one observed in our driftless GPSC, being mainly explained by the large impact of the theoretical SP pressure scaling in Xe-CO_2 and Xe-CH_4, and by the higher attachment probability in Xe-CF_4. The low transparency of CO_2 to scintillation photons is also a determinant factor in large TPCs.

10.4 Extrapolation of ER vs electron diffusion

The energy resolution is probably the most important parameter to take into account on the final judgment of the most suitable additive for the NEXT-100 TPC. ER was estimated for each molecule according to the procedure introduced in section 10.2.

In figure 76, ER extrapolated for the NEXT-100 TPC for an EL field of 2.5 kV/cm/bar is plotted as a function of D_{3d}, for the three additives at several concentrations. D_{3d} was obtained from Magboltz simulations for a drift field of 20 V/cm/bar, like in figure 75. Similarly, the shadow areas represent the error intervals from the experimental measurements. In addition to the error on DP that was discussed in the previous section, the ER uncertainty is also affected by: the error bars of the *Q* factor, represented in figure 70; the systematic errors in Xe-CO_2 and Xe-CF_4 mixtures resulting from not considering the attachment scaling in DP; and the possible overestimation of *Q* in attachment-inducing mixtures, as suggested by the results of table 3.

When the three additives are compared between concentrations for which the electron diffusion is equally reduced, CF_4 reveals to be the worst additive, despite showing smaller deterioration on the electroluminescence signal intensity. For these operating conditions, CH_4 is clearly the most promising candidate for NEXT-100, at least within the region of interest, i.e. D_{3d} between 2 and 3 $mm/\sqrt{m}$. This tendency seems to be well established, even considering the large errors represented by the shadow areas. CO_2 may also be a viable additive, although it does not overtake CH_4, since DP in Xe-CO_2 is still lower than the one extrapolated for Xe-CH_4, even considering a full transparency to VUV light (see figure 75). In addition, ER is further degraded in CO_2 through the *Q* factor.

From figure 76, one may expect the region of interest for the Xe-CH_4 concentration to be between 0.2 and 0.6 %, since D_{3d} is reduced from ~9.5 $mm/\sqrt{m}$ down to the 2.0-2.8 $mm/\sqrt{m}$ range, without an excessive compromise of the TPC energy resolution. For instance, with a CH_4 concentration of 0.37 %, D_{3d} is reduced down to 2.27 $mm/\sqrt{m}$, which is close to the thermal limit (1.6 $mm/\sqrt{m}$), while the ER value is increased from 0.33 to 0.42 %. However, in a complex TPC as the one in NEXT-100, additional fluctuation sources besides the ones considered in equation (10) may exist (e.g. electronics, geometric effects or the systematic error introduced by the spatial energy calibration). Those contributions are likely not affected by the molecular additive. Therefore, in practical terms, the relative degradation of ER induced by the additive will be far lower than the ones depicted in figure 76. For example, in NEXT-DEMO and NEXT-DBDM, ER extrapolated at the $Q_{\beta\beta}$ are 0.5 % [62] and 0.74 % [63], respectively. Those values are substantially higher than the ER value estimated considering only the Fano factor, Q factor and PMT contributions.

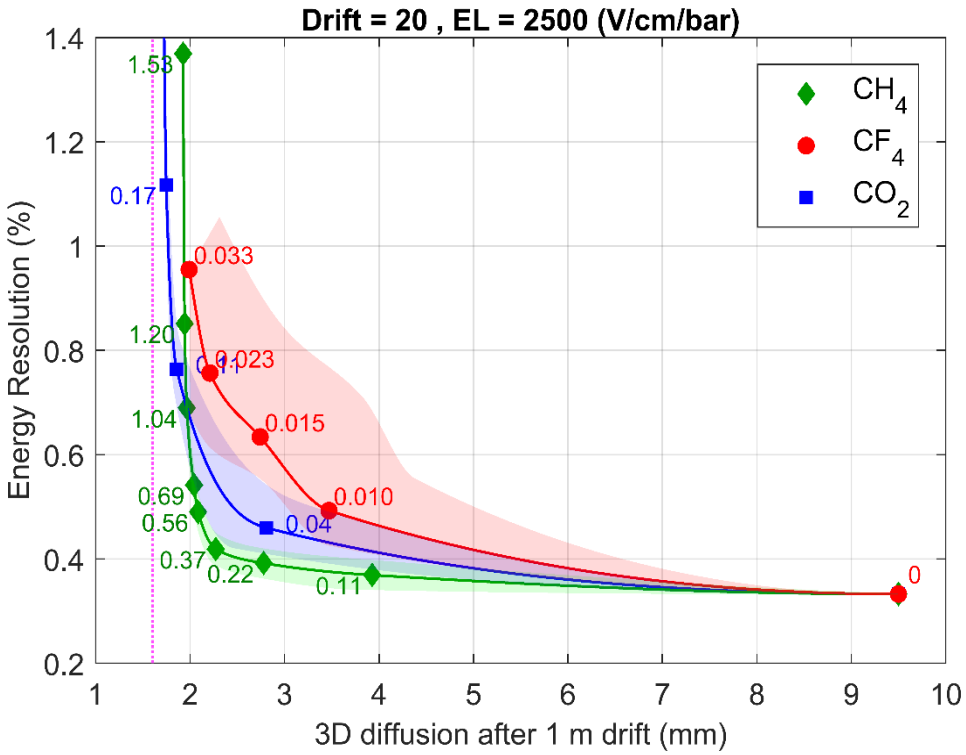

Figure 76: ER extrapolated for NEXT-100 for the ββ0ν energy as a function of D_{3d}, for the several additive concentrations (labelled in the figure), considering an EL electric field of 2.5 kV/cm/bar and a drift electric field of 20 V/cm/bar. The dashed pink line shows the D_{3d} thermal limit. The shadow areas correspond to the experimental error intervals for each additive.

In a preliminary characterization of the NEXT-White TPC reported in [67], the ER extrapolated at the $Q_{\beta\beta}$ was (1.02 ± 0.11) %. The larger contribution to this value comes from a constant term, i.e. not scaling with $1/\sqrt{E}$, which is likely introduced by the corrections of the electron lifetime and local inhomogeneities of the detector. If the NEXT-100 TPC is

limited by the same constant term (0.81 %), which adds quadratically to ER depicted in figure 76, the overall energy resolution could be degraded by a negligible 1.04 factor (from 0.88 % to 0.91 %), for a CH_4 concentration of 0.37 %.

In any case, the figure of merit shown here may be unsatisfactory, as other working conditions could be used in a future NEXT experiment (NEXT-100, or even a ton-scale TPC). Moreover, our experimental work could also be helpful for other kind of EL-based TPCs, where both the spatial and energy resolutions are critical. Therefore, in the following sections, ER is extrapolated considering other working conditions and TPC specifications.

10.4.1 Extrapolation for different EL electric fields

The optimal ER expected from simulation for the NEXT-100 TPC is achieved for an EL field in the region between 3 and 5 kV/cm/bar (depending on the light collection efficiency) [96]. However, the TPC long term stability in these conditions could be compromised, as sparks are likely to occur for such high electric fields. Due to the long drift region, about 1 m, the cathode is at a very high voltage (e.g. 55 kV for a EL field of 2.5 kV/cm/bar and drift field of 40 V/cm/bar). Even a 10 cm-long feedthrough may have problems to hold 50 kV in xenon at 10 bar [130]. Therefore, the EL field in the NEXT-100 will be probably limited by technical issues. An operation E/p range of 2-3 kV/cm/bar is anticipated [12].

In this section, ER is extrapolated for the NEXT-100 TPC according to the same conditions described in section 10.2, except the EL field that is here varied, being either 2 or 3 kV/cm/bar. The results are shown in figure 77. For the sake of clarity, the errors that were represented by shadow areas in figure 76 are no more depicted, but the relative uncertainties of data are similar.

As expected, ER is improved when an E/p value of 3 kV/cm/bar is used in the EL region, while it is considerably degraded for 2 kV/cm/bar. In Xe-CO_2 and Xe-CH_4 mixtures, this result is explained by the linear variation of DP with E/p that affects the PMT photon-statistics contribution. On the other hand, the ER dependence on the EL field observed in Xe-CF_4 is mostly attributed to the experimental Q variation, as seen in figure 70 (c).

Taking again the example of Xe-CH_4 (0.37 %), the ER value can be slightly reduced from 0.42 % down to 0.40 % at 3 kV/cm/bar, while a larger difference is observed for 2 kV/cm/bar, for which ER varies from 0.40 % to 0.49 %. The impact of the EL electric field is more significant for higher CH_4 concentrations, for instance 0.56 %, further reducing D_{3d} from 2.27 down to 2.09 mm. For these conditions, ER can be improved from 0.49 % to 0.44 % at 3 kV/cm/bar and degraded from 0.49 % to 0.59 % at 2 kV/cm/bar. Therefore, the operation of the NEXT-100 TPC at higher E/p values should be a major concern, as it can profit significantly the performance with mixtures.

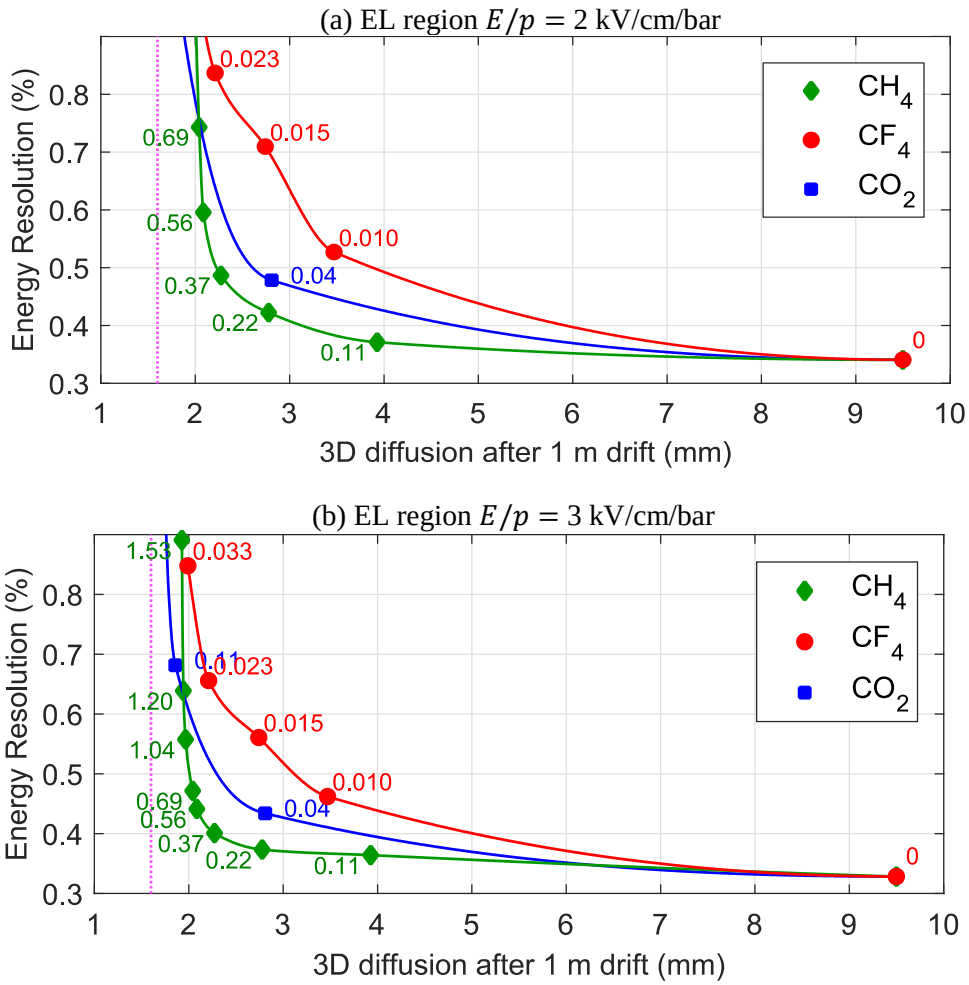

Figure 77: Energy resolution expected for NEXT-100 at the ββ0ν energy as a function of D_{3d}, for several additive concentrations. EL fields of 2 and 3 kV/cm/bar are considered in the top and bottom plots, respectively. The remaining conditions are described in section 10.2. The dashed pink line represents the D_{3d} thermal limit.

10.4.2 Extrapolation for different drift fields

As previously discussed, low drift electric fields may have disadvantages, such as higher electron loss in this region. Therefore, in this section we present the figure of merit for the other simulated E/p value in the drift region, 30 V/cm/bar. In figure 78, ER extrapolated for the NEXT-100 TPC is plotted as a function of D_{3d}, following the conditions described in section 10.2, except the drift E/p value that is 30 V/cm/bar.

Figure 78 shows that the reduction of D_{3d} is more modest when compared with the reduction achieved for the same additive concentrations under a drift field of 20 kV/cm/bar. In general, the relative diffusions provided by the three additives remains similar, with D_{3d} obtained with CH_4 being slightly improved with respect to the other two additives. One may also notice that D_{3d} achievable with molecular additives is further away from the thermal limit, which is in turn smaller.

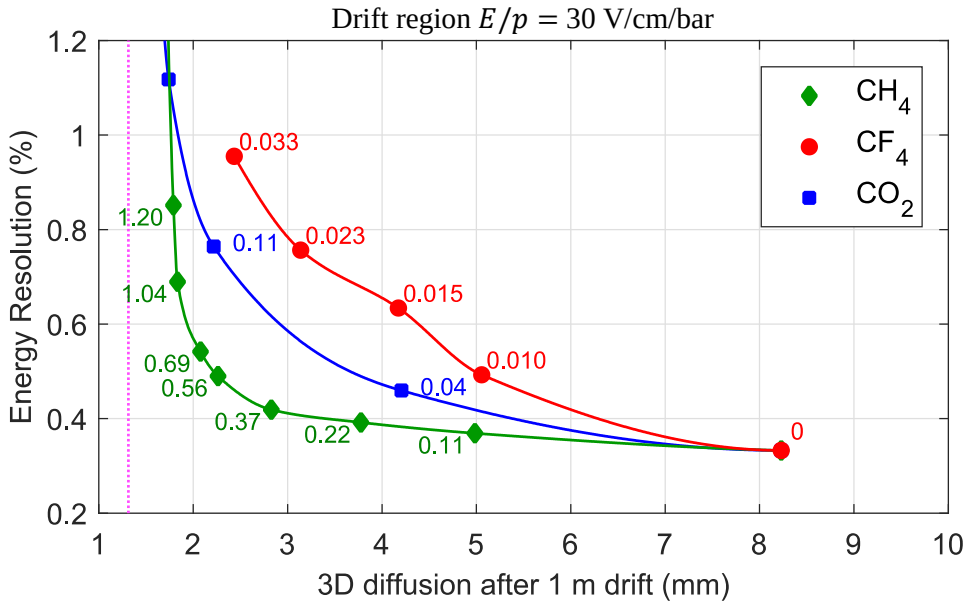

Figure 78: Energy resolution expected for NEXT-100 at the ββ0ν energy as a function of D_{3d}, for several additive concentrations. A drift E/p value of 30 V/cm/bar is considered, the remaining conditions being described in section 10.2. The dashed pink line, representing the D_{3d} thermal limit, is also affected by the drift field.

10.4.3 Extrapolation for a different gas pressure

Operating the NEXT detector at higher pressures has some obvious advantages, such as the larger amount of ^{136}Xe that is contained inside the same volume. The NEXT-100 pressure vessel can hold up to 15 bar [12], this being likely the pressure to be used in the future. In figure 79, ER extrapolated for the NEXT-100 TPC is plotted as a function of D_{3d}, considering a total pressure o 15 bar, for drift fields of 20 and 30 V/cm/bar.

The pressure increase from 10 to 15 bar does not affect only the D_{3d} parameter, it also increases DP by a factor of 1.5, due to the larger number of electron collisions within the same EL gap. DP is also affected through other mechanisms, such as the CO_2 transparency, the pressure scaling of SP, and the Y_{att}/Y_0 ratio scaling. The larger attachment probability at 15 bar may also degrade the Q factor in Xe-CO_2 and Xe-CF_4 mixtures. Since SP was not simulated at 15 bar, the same scaling used for 10 bar is assumed (figure 72). The remaining scaling factors from 10 to 15 bar are also neglected, as they do not affect CH_4. In this way, ER is underestimated in Xe-CO_2 and Xe-CF_4 when compared to Xe-CH_4 mixtures.

The general picture is improved at 15 bar, mostly due to the favourable scaling of electron diffusion with pressure, $D_{3d}(15\ \text{bar}) = D_{3d}(10\ \text{bar})\sqrt{10/15}$. In addition, ER is improved due to the higher DP. For a drift field of 20 V/cm/bar, an impressive D_{3d} of 1.8 $mm/\sqrt{m}$ is achieved with Xe-CH_4 (0.37 %), at the expense of a little degradation in ER, from 0.33 % to 0.38 %. For a drift E/p value of 30 V/cm/bar, D_{3d} can be also reduced to 1.8

$mm/\sqrt{m}$, but with 0.56 % of CH_4, resulting in a larger increase on ER, from 0.33 % to 0.44 %.

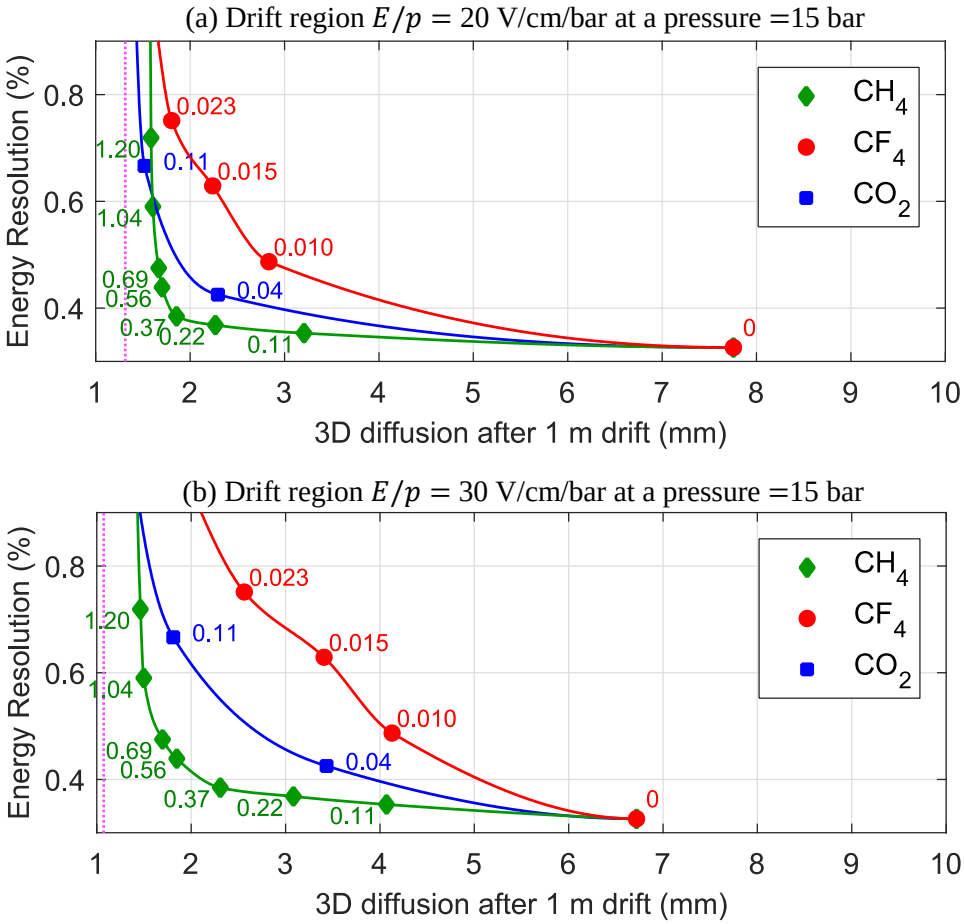

Figure 79: Energy resolution expected for NEXT-100 at the ββ0ν energy as a function of D_{3d}, for several additive concentrations. Drift fields of 20 and 30 V/cm/bar are considered, in the top and bottom plots, respectively. Results are extrapolated for a pressure of 15 bar in both plots, the remaining conditions being described in section 10.2. The dashed pink line, representing the D_{3d} thermal limit, is affected by the pressure and drift field.

10.4.4 Extrapolation to other parameters favoring CF_4

In the previous sections we have depicted the figure of merit for different TPC working conditions. Still, the anticipated tendency has been always confirmed, i.e. CH_4 showing the best performance, while CF_4 seems to be the worst additive. However, since these two molecules degrade the energy resolution through distinct mechanisms, different applications may take advantage from the unique properties of CF_4 over CH_4.

In Xe-CH_4 mixtures, ER is affected mostly by the fluctuations in the PMTs, this contribution being lower in Xe-CF_4 due the higher EL yield. Therefore, if the total number of collected photons is very low, the performance of CH_4 or CO_2 may become worse than the performance of CF_4, despite the large Q factor in the latter case. Such scenario could be induced, for example, by a poor light collection efficiency (k). To demonstrate this behaviour,

ER extrapolated for NEXT-100 is plotted as a function of D_{3d} in figure 80 (a), considering a $k = 0.3$ %, i.e. 10 times lower than the value assumed in the previous plots. The remaining conditions are the ones described in section 10.2. For such high contribution of the PMT fluctuations to ER, CF_4 becomes better than CH_4 and CO_2. Thus, CF_4 may provide the best solution in TPCs with limited photosensor coverage areas. This result shows that the real light collection efficiency achieved in the NEXT TPC might determine the feasibility of molecular additives or decide which one is more advantageous. In order to operate the NEXT-100 TPC with Xe-CH_4 mixtures, the k parameter must be optimized as much as possible, using for instance highly reflective materials.

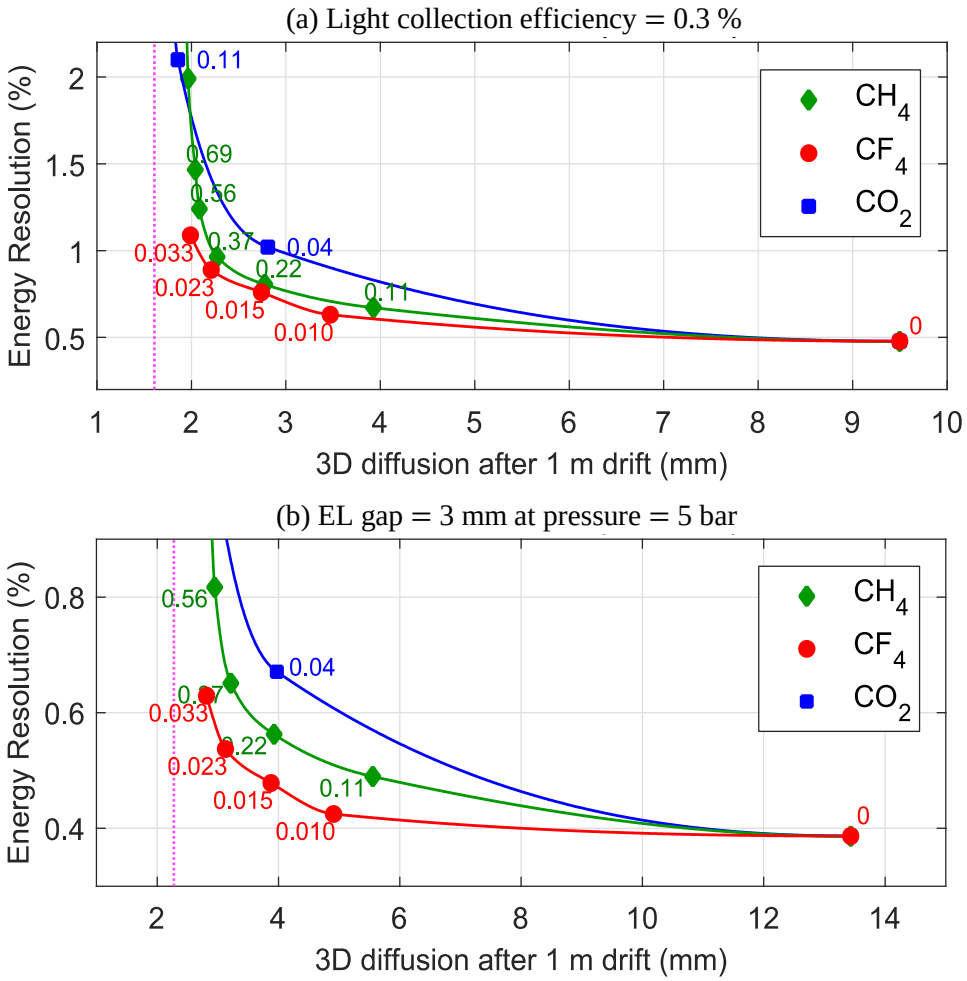

Figure 80: NEXT-100 extrapolated ER as a function of D_{3d} for several additive concentrations. In (a), assuming a 10 times lower light collection efficiency (0.3 %). In (b), considering a 2 times shorter EL gap (0.3 cm) and a 2 times lower gas pressure (5 bar). The remaining conditions are described in section 10.2. The dashed pink line, representing the D_{3d} thermal limit, is affected by the pressure in (b.

It is interesting to note that DP and Q are directly proportional to the EL gap width and the gas pressure (only in the limit of low attachment for Q, equation (18)). Consequently, the contribution of the fluctuations in EL production to ER scales with the squared root of the EL gap and pressure ($\sqrt{P\Delta x}$), whereas the contribution of PMTs to ER scales with the reciprocal

of the same quantity ($1/\sqrt{P\Delta x}$). Therefore, in attachment inducing mixtures, the overall ER might be improved reducing the EL gap or the gas pressure, though this procedure increases the PMT fluctuations. There is a $P\Delta x$ value where ER is optimal, and below this value the PMT contribution becomes asymptotically larger, overtaking the Q factor reduction. In this way, Xe-CF_4 could provide good ER in TPCs where the pressure and/or the EL gap are small. The performance of CF_4 can be better than the other two molecules in such applications. To illustrate this scenario, the NEXT-100 extrapolated ER is plotted as a function of D_{3d} in figure 80 (b), considering a two times shorter EL gap of 0.3 cm and a two times lower gas pressure of 5 bar. The remaining conditions are the ones described in section 10.2. For the sake of simplicity, the Q variation with $P\Delta x$ was assumed to be linear (following equation (18)), and the scaling of SP, $Y_{att}/\,Y_0$ and CO_2 gas transparency from $P = 10\ bar$ and $\Delta x = 0.6\ cm$ to $P = 5\ bar$ and $\Delta x = 0.3\ cm$ were neglected. ER obtained with Xe-CF_4 is considerably better in this case when compared to figure 76. For instance, ER is improved from 0.64 % to 0.48 %, for a 0.015 % CF_4 concentration mixture. On the other hand, ER is degraded in Xe-CH_4 and Xe-CO_2 mixtures, due to the lower DP. Consequently, the performance of CF_4 is far superior than CH_4 and CO_2 for this TPC specifications.

It is still worth highlighting that in none of the cases analysed through this chapter, CO_2 becomes better than CH_4. This observation is explained by the slightly larger impact that CO_2 has on DP within the D_{3d} region of interest (2-3 $mm/\sqrt{m}$), even considering a full transparency (figure 75). In addition, CO_2 deteriorates ER through dissociative electron attachment.

10.5 Final remarks on the use of additives in NEXT-100

In this chapter, the impact of molecular additives on the NEXT-100 TPC performance was evaluated. In general, the degradation of DP and Q revealed to be larger when compared with our driftless GPSC, which is mostly due to the higher electron attachment probability and the lower scintillation probability for higher pressures. Despite the EL signal intensity being still acceptable in Xe-CF_4 mixtures, in Xe-CO_2 and Xe-CH_4 it may be only 20 % of the original EL yield for pure xenon (figure 75), within the 3-dimentional diffusion region of interest, 2-3 $mm/\sqrt{m}$. Even so, the energy of a ββ0ν event is high enough to keep the PMT relative fluctuations low, allowing to reduce D_{3d} down to values close to the thermal limit, at an acceptable expense of ER in the case of Xe-CH_4 (figure 76). Nevertheless, the results shown in this chapter are strongly determined by the simulated SP pressure scaling and the 3 % NEXT-100 light collection efficiency, the latter being highly speculative.

As previously discussed in section 2.2, the electron drift velocity is degraded for high additive concentrations. For instance, considering an E/p value of 20 V/cm/bar in the drift

region and a pressure of 10 bar, the drift velocity falls below that of pure xenon for concentrations of CH_4, CO_2 and CF_4 higher than 0.083 %, 0.014 % and 0.004 %, for which D_{3d} is modestly reduced from 9.5 down to 4.6, 5.5 and 5.9 $mm/\sqrt{m}$, respectively. If one needs to reach a D_{3d} value in the 2-3 $mm/\sqrt{m}$ range, as is the case of NEXT, larger concentrations are required, leading to a relative reduction of the electron drift velocity of (40-50) %, independent of the chosen additive. Fortunately, this drawback is likely not problematic for the NEXT experiment, since the detection rate is low.

Despite some NEXT-100 specifications being less important for operation with pure Xe, they must be reconsidered as priorities for the use of molecular additives, since the TPC performance may be considerably enhanced. Some examples are the drift and electroluminescence fields. The first should be low, at the level of 20 V/cm/bar, due to the better D_{3d} that is possible to reach (figure 78), while the second one should be high, 3 kV/cm/bar or above, thus improving ER (figure 77). This counterbalancing allows keeping the cathode voltage unchanged, avoiding issues related with sparks. The light collection efficiency, here assumed as 3 %, is likely the most relevant parameter and should be maximized as much as possible. This feature is crucial to achieve a good ER in Xe-CH_4 mixtures. In addition, it renders the time detection of the event (t_0) more efficient.

From the three additives studied, CH_4 has shown to be the best candidate for the NEXT experiment, at least for the following conditions: drift fields of 20 to 30 V/cm/bar, EL fields of 2 to 3 kV/cm/bar, pressures of 10 to 15 bar and a light collection efficiency of 3 %. Nevertheless, additional factors must be taken into account in this judgment, such as the primary scintillation signal (S1). From the experimental SP plotted in figure 71, together with the theoretical SP pressure scaling of figure 72, one may extrapolate the impact of additives on the NEXT-100 S1 signal. For Xe-CH_4, Xe-CO_2 and Xe-CF_4 concentrations of 0.220 %, 0.041 % and 0.015 %, respectively, S1 is expected to be reduced down to ~30 %, ~25 % (15 % when the CO_2 transparency is considered) and ~100 %, relative to the one obtained with pure xenon. Despite the large impact of Xe-CH_4 on S1, the signal could still be strong enough to discriminate the ββ0ν start-of-event, t_0, against noise.

The spatial calibration of NEXT-100 is performed using 41.5 keV point-like energy depositions produced by ^{83m}Kr. Assuming an average of 72 eV required to produce a scintillation photon in pure xenon, about 576 photons would be produced per event [87]. However, for Xe-CH_4 (0.37 %), this amount may be reduced by 80 %. Therefore, if the light collection efficiency is 3 %, only an average of 3 photons will be detected per event. Consequently, the probability to identify t_0 is considerably reduced, increasing the number of events needed to perform the ^{83m}Kr calibration. On the other side, the S1 intensity should remain almost unchanged with the addition of CF_4 to pure Xe, rendering it the best choice.

From the technical point of view, CO_2 is hard to implement, since it is reactive with hot getters, even at lower temperatures, as shown in section 3.6. On the other hand, CH_4 is stable at lower getter temperatures, for which the major impurities, such as H_2O, H_2, O_2, CO_2 and N_2 are still removed. The higher concentrations required for the Xe-CH_4 operation are another advantage, since they are easier to prepare and measure, while the minute Xe-CF_4 concentrations are harder to measure, as demonstrated in chapter 3, and probably difficult to maintain homogenous and stable for long periods of time.

The recovery of Xe after mixed with CO_2 is, in principle, straightforward, since it can be frozen at the solid-CO_2 temperature using dry ice. On the other side, this task may be more complex with Xe-CH_4. Still, it should be feasible, as the xenon and CH_4 boiling points are very different, 165 K and 111 K, respectively. In our preliminary tests, we have cooled down a Xe-CH_4 mixture (1.4 %) at liquid nitrogen temperature, pumping out the vapour phase during 10 minutes, assuming that the probability for a CH_4 molecule to escape to the vapour phase would be higher than for xenon atoms. In this way, we have successfully removed 55 % of CH_4, with a minute loss of xenon (1 %). The efficiency of this method could be not good enough for the future NEXT-100 operation with isotope ^{136}Xe. Nevertheless, the separation of CH_4 from xenon should be more efficient using a cooling bath, whose temperature is between the xenon and the CH_4 boiling points, for instance, a mixture of liquid nitrogen with 1,5-hexadiene or n-pentane, with temperatures of 132 K and 142 K, respectively. The effectiveness of this method is expected to decline with decreasing CH_4 concentration, since CH_4 is trapped by the liquid/solid xenon intermolecular forces. Therefore, after most of the CH_4 gas is pumped out, hot getters could be operated at higher temperatures to safely remove the remaining quantities of CH_4, without saturation.

Recently, helium has been pointed out as a viable alternative to molecular additives. The electron momentum transfer to helium is much more efficient compared to xenon because of its small mass, leading to a lower average electron kinetic energy. The use of another noble gas has obvious benefits, such as the negligible degradation of the scintillation signal and ER [72]. Moreover, no further incompatibilities with the system materials or with the getters are expected. Helium is also easy to separate from xenon due to its low boiling temperature.

Magboltz simulations suggest that D_{3d} might be reduced down to 2.65 and 3.16 $mm/\sqrt{m}$ with a Xe-He mixture of 15 % and 10 % helium, respectively, at 15 bar, for a drift E/p value of 20 V/cm/bar [72]. As shown in figure 79 (a), a considerable better D_{3d} value can be achieved with a CH_4 concentration of 0.37 %, 1.8 $mm/\sqrt{m}$, although with a significant degradation of the theoretical ER, from 0.33 % to 0.38 % (a factor of 1.15). However, the real ER in the NEXT-100 TPC will likely contain additional contributions that are not affected by the additive. For instance, if the NEXT-100 detector achieves an overall ER of 0.6 % with

pure xenon, i.e. assuming it is dominated by an additional term of 0.5 % ($(0.60\,\%)^2 = (0.33\,\%)^2 + (0.50\,\%)^2$), the overall ER is only degraded by a factor of 1.05 ($(0.63\,\%)^2 = (0.38\,\%)^2 + (0.50\,\%)^2$) with a CH_4 concentration of 0.37 %. Therefore, despite the many advantages of mixing helium with xenon, CH_4 may still provide an overall better performance, without the 10 % or 15 % ^{136}Xe mass loss (considering the same volume and pressure as in pure xenon), and eliminating the risk of PMT damaging (since helium can easily penetrate through the vacuum tube).

In order to compare the two additives (helium and CH_4), one may evaluate the impact that each solution has on the experiment sensitivity to the electron neutrino effective Majorana mass ($m_{\beta\beta}$), for the same reduction in the D_{3d} value. The $m_{\beta\beta}$ lower limit that an experiment may achieve is given by $S(m_{\beta\beta}) \propto \sqrt{\bar{N}/M}$, where M is the source mass and $\bar{N}$ is the average upper limit of the number of events expected in the experiment under the no-signal hypothesis. For the case of high background, $\bar{N}$ is proportional to the square root of the mean number of background events (b), which is, in turn, proportional to the energy resolution (ΔE) of the detector (as the $\beta\beta 2\nu$ background within ROI is negligible in NEXT-100, b should not be affected by the ^{136}Xe mass loss) [12]. Therefore, $S(m_{\beta\beta}) \propto \Delta E^{1/4}/M^{1/2}$, hence favouring the energy resolution degradation over the ^{136}Xe mass loss. With a CH_4 concentration of about 0.15 % and 0.11 %, D_{3d} can be reduced to 2.65 and 3.16 $mm/\sqrt{m}$ (as shown in figure 79 (a)), respectively, which are similar values as obtained with 15 % and 10 % of helium, considering the same operation conditions (a pressure of 15 bar, and a drift field of 20 V/cm/bar). For these two CH_4 concentrations, the value of the theoretical energy resolution is degraded from 0.33 % to 0.36 % and 0.35 %, respectively. If it is assumed that the real energy resolution in NEXT-100 is dominated by a 0.50 % additional contribution, these differences become smaller, from 0.60 % to 0.63 % and 0.62 %, respectively. In this way, $S(m_{\beta\beta})$ is degraded by a factor of only 1.008 and 1.007 with 0.15 % and 0.11 % of CH_4, which is substantially lower than the 1.085 and 1.054 factors obtained with 15 % and 10 % of helium. Therefore, Xe-CH_4 mixtures are significantly less harmful for the experiment sensitivity, considering the same improvement in the TPC spatial resolution (at least assuming the aforementioned conditions).

11 CONCLUSIONS

The detection of the ββ0ν decay is crucial to clarify some of the most central questions in modern physics, such as the absolute mass scale of neutrinos and their hypothetical Majorana nature. The NEXT experiment is a promising candidate to cover the inverse neutrino mass hierarchy, thanks to its innovative concept of background rejection based on the 3-dimentional topology reconstruction of the events. In this work, we carried out a systematic experimental study regarding the challenge of doping xenon with molecular gases, which is an attractive solution to overcome the high electron diffusion in pure xenon, one of the major limitations of the background discrimination technique.

A driftless GPSC was employed to evaluate the impact of molecular additives in the electroluminescent response of xenon, using an x-ray beam to excite the gas. The undesirable effect on the detector response resulting from the x-ray penetration in xenon motivated us to investigate deeply the driftless GPSC operation. To this end, the photosensor waveforms were sampled and carefully analyzed. Based on this study, we developed a software to turn the driftless GPSC into a powerful spectroscopy instrument, eliminating the x-ray penetration effect. Energy resolutions of 7.23 % at 5.9 keV and 3.69 % at 22.2 keV were obtained with pure xenon, representing one of the best performances reported in literature, even with regular GPSCs.

The waveform analysis of the driftless GPSC allowed to assess some fundamental parameters hitherto unknown. Those include the electron attachment, scintillation probability, electron drift velocity and longitudinal electron diffusion. Although we have not measured these parameters systematically with different mixtures, the proof-of-concept methods to estimate them were developed and validated, by comparison of our results with simulations. In future, these new tools will be extremely useful to evaluate fully the impact of additives on the scintillation, EL fluctuations and electron transport in noble gases. Moreover, we demonstrated that the energy resolution and secondary scintillation yield are further degraded by the variation of the number of EL photons collected by the photosensor along the electron

path way, for electron attachment inducing additives. This geometrical specification must be considered in the design of future detectors operating with such mixtures.

The core of the present work consisted in an extensive study of the electroluminescence degradation promoted by the addition of CO_2, CH_4 and CF_4 molecular additives to pure xenon, for several electric fields and concentrations. The EL yield, energy resolution, fluctuations in the EL photon production and the scintillation probability were estimated using the driftless GPSC. These results were only possible thanks to the complex detector response function developed from the waveform analysis, which allows to modulate both the x-ray penetration and the electron attachment effects.

Considering the electron diffusion obtained from simulations, we demonstrated that a performance near the thermal diffusion limit might be achieved with these additives, at an acceptable expense of electroluminescence yield and energy resolution. Therefore, an enhanced position resolution in a EL optical TPC is compatible with a good energy resolution, in contrast to what was believed up to now.

As expected from theory, the three molecules have shown very different properties. Despite the obvious reduction of the EL yield as a result of electron cooling, CO_2 and CH_4 have shown to quench the xenon excited states, leading to a substantial reduction of both the primary and secondary scintillation. Consequently, the energy resolution is degraded through the photosensor statistics. On the other side, Xe-CF_4 mixtures demonstrated a scintillation probability near 100 %, being the electroluminescence yield only slightly reduced, due to the large dissociative attachment. However, this last feature was found to deteriorate considerably the energy resolution, due to the large fluctuations in the EL photon production.

We have shown that for many applications CH_4 may likely be the most suitable additive to improve the electron diffusion, because the energy resolution can be maintained almost untouched, especially when the light collection efficiency is large. However, due to the unique characteristics of CF_4, it might be preferable in other applications, for instance when the electroluminescence gap is short, or the gas pressure is low. On the other side, CO_2 was never found to be advantageous, because of its opacity to VUV light and dissociative electron attachment, in addition to the high quenching probability that is comparable to the one in Xe-CH_4 mixtures.

For the NEXT-100 working conditions, CH_4 is the preferable solution, either from the physical or technical point of view. For a pressure of 15 bar, a drift field of 20 V/cm/bar and a EL field of 2.5 kV/cm/bar, the 3-dimentional electron spread per drifted meter could be reduced from about 8 mm to an impressive 1.8 mm with 0.37 % of CH_4, while the energy resolution is degraded from 0.33 % to 0.38 %. It is worth highlighting that the practical energy resolution achievable in the NEXT-100 TPC will likely contain a constant term that does not depend on the mixture, thus making the use of the additive almost imperceptible. CH_4 might

be still advantageous over the recently proposed helium alternative, since a large percentage of active Xe-136 mass (10-15 %) would be lost in the latter case. From the technical point of view, CO_2 showed some serious concerns due to its reactiveness with the purification system. In contrast, CH_4 showed to be the most stable additive and easier to control, due to the low reactiveness and larger concentrations needed for the electron diffusion region of interest.

Some unknown parameters were speculated in our calculations of the NEXT-100 TPC performance, when filled with mixtures. However, the true values might change significantly the global picture. Some examples are the maximum EL field and minimum drift field that can be used, the light collection efficiency, and the pressure quenching scaling. For this reason, it is imperative to evaluate experimentally these factors in a prototype under the NEXT collaboration.

11.1 Future work

NEXT-DEMO is currently in the final phase of its rehabilitation. This upgrade of the prototype (named DEMO++) will serve to test and develop several ideas targeted for NEXT-100, such as the enhanced electron diffusion. Xe-He and Xe-CH_4 mixtures are priorities for the near future. In DEMO++, the electron drift velocity, transverse and longitudinal diffusion coefficients will be measured for the first time in mixtures, and the real benefit of additives in the topology identification could be evaluated. Other processes taking place in the drift region that were inaccessible in our driftless GPSC could be also studied for these mixtures, such as the primary charge recombination, electron lifetime, gas transparency, primary ionization and primary scintillation yields.

In this work, we assumed the theoretical dependence of the quenching probability on pressure. However, this hypothesis lacks from experimental confirmation. DEMO++ will allow to inspect this parameter for pressures up to 15 bar. The result might determine the feasibility of Xe-CH_4 mixtures in terms of primary and secondary scintillation yields. Being DEMO a small prototype of the NEXT-100 TPC, the overall degradation in the energy resolution produced by the CH_4 addition will be directly evaluated, allowing to spot the concentration that delivers the best sensitivity to the $\beta\beta0\nu$ decay half-life (i.e. the compromise between spatial resolution enhancement and energy resolution degradation).

Recently, a regular GPSC was installed in parallel with the driftless GPSC used in this study. The complementary operation of the two apparatus will provide a deeper and more complete understanding of the effect of molecular additives in optical EL TPCs. Several molecules including CO_2, CH_4 and CF_4 are planned to be fully characterized in this multifaceted system. The first additive to test is C_2H_6 (starting in a few weeks). Being from the same family of CH_4, C_2H_6 could be a good alternative, perhaps with a lower degradation

on the scintillation yield. Moreover, the quenching probability in CH_4 reveled to be lower than initially predicted, hence it is relevant to verify this parameter in a similar molecule.

The proof-of-concept tools developed in this work for the analysis of the driftless GPSC waveforms will be employed, allowing to measure many parameters for different mixture concentrations. Those include the energy resolution corrected from the x-ray penetration effect, the attachment coefficient and how it affects the energy resolution, the scintillation probability, and the electron drift velocity and longitudinal diffusion for typical EL electric fields. In addition, the same algorithms will be adapted to study the waveforms coming from the regular GPSC. In this way, we intend to measure the primary scintillation yield, electron lifetime, electron drift velocity and longitudinal diffusion for typical drift electric fields. Since the new GPSC has an EL region 5 times thinner than the driftless GPSC, we expect to reach a better understanding of the influence of the attachment probability, EL gap and solid angle variation in the energy resolution, which is in turn obtained directly in the new detector, i.e. without the need for a correction of the x-ray penetration effect. Finally, we intend to vary the operation pressure between 1 bar and the maximum pressure achievable in both detectors, of about 2 bars, in order to evaluate the dependence of the scintillation probability on this variable.

All the aforementioned parameters will allow to validate and refine the electron transport and scintillation theoretical models. Besides that, a more complete collection of information on the benefits and drawbacks of several molecular additives in EL TPCs will be useful for future researchers who seek for the best solution in their application.

APPENDICES

Appendix A: Source of fluctuations on the waveform duration

In this appendix, we describe an attempt to simulate the experimental distribution of the waveform durations that can be observed in figure 31, stemming from the theoretical exponential attenuation of x-rays in xenon.

Several random numbers corresponding to the path length of electrons are generated, following the exponential distribution expected for the attenuation of 5.9 keV x-rays in pure xenon, at a pressure of 1.24 bar and a temperature of 310 K. For comparison purposes, these working conditions are the same used in the run of figure 31. For each path length value, the corresponding waveform duration is randomly generated following a Gaussian distribution. The mean of this distribution is equal to the correspondent event path length divided by the expected drift velocity (estimated from the run of figure 31); and the relative standard deviation of the Gaussian is made constant for all events, being left as a free parameter for fine fitting.

In figure A-1, the simulated histogram of waveform durations is plotted and compared with the distribution obtained experimentally for the same working conditions. To make the results more intuitive, both distributions are depicted in terms of path lengths, directly computed from the waveform durations (as in figure 31). The theoretical exponential distribution of path lengths used in the simulation is also represented.

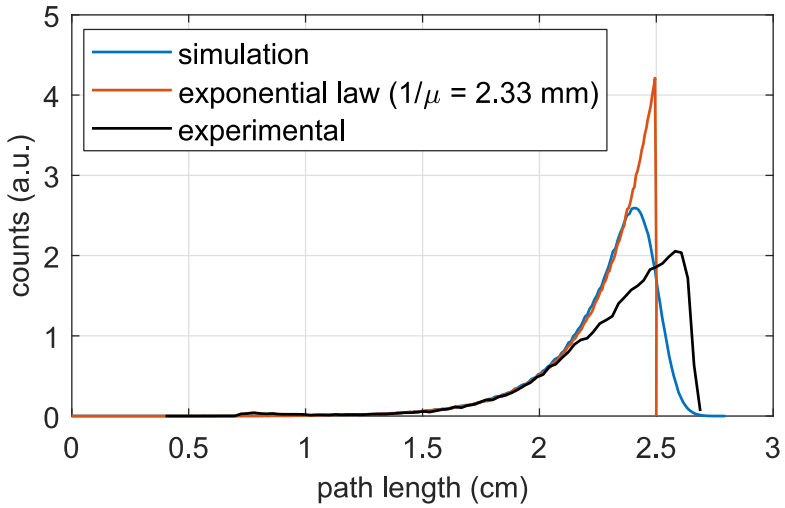

Figure A-1: Comparison between the experimental distribution of path lengths directly obtained from waveform durations (in black) and the simulated one (in blue), considering a Gaussian distribution of waveform durations. The theoretical exponential distribution used in the simulation is also shown (in orange). Experimental data were taken with pure xenon at a pressure of about 1.24 bar and an estimated temperature of about 310 K. The detector was irradiated with 5.9 keV x-rays.

The constant relative standard deviation considered in the random generation of the waveform durations was adjusted so that the simulated distribution matches as much as possible the experimental one. In this way, we are able to estimate the resolution of the photon

burst duration, in ordert to calculate the contribution of this effect to the detector energy resolution. However, as seen in figure A-1, the simulated distribution is completely different from the experimental one, no matter the Gaussian relative standard deviation. From this simulation, we conclude that the waveform duration produced by the same x-ray penetration does not follow a Gaussian distribution, at least for the longest path lengths. However, in the shorter path length region, the simulated distribution fits well the experimental one, as observable in figure A-1.

Additional distributions of waveform durations for the same x-ray penetration were simulated, in particular the uniform and the exponential distributions. Unfortunately, none of our attempts could fully explain the experimental results. Nonetheless, a proper distribution based on several physical effects broadening the PMT waveforms may exist.

For the longer waveform durations, fluctuations as high as 250 ns corresponding to about 1.5 mm in the path length can be observed (see figure 31). This order of magnitude cannot be explained by the excitation and de-excitation times of the xenon scintillation process, which are about 20 and 100 ns, respectively [120]. For 5.9 keV x-rays used in the example of figure 31, 90 % of the ionization electrons are expected to be within a radius of only 100 μm (at 1 bar) [131]. Therefore, these effects alone hardly explain the large fluctuations on the waveform duration for events produced near the detector window.

Such observations rise the possibility of two different sources of fluctuations, one affecting all the waveforms, and the other one affecting only the events taking place just below the detector window. The last one could have a larger impact on the waveform duration, thus explaining the considerable deviation between the experimental and the theoretical curves, observed in figure 31 for longer path lengths. Non-uniformities of the electric field in this region might induce this effect, since the electron cloud could be elongated. When the detector is pressurized, the Kapton window (8 mm in diameter) becomes bent outwards due to the pressure differential. A deflection of about 1 mm from the window central point is observed, likely promoting distortions on the EL electric field. Nonetheless, this source of fluctuations should not have a significant impact on the energy resolution corrected from the x-ray penetration effect, as longer waveforms are excluded from the analysis.

Appendix B: Second-order improvement of the energy resolution

In this appendix, we describe several methods used to further improve the energy spectrum corrected from the x-ray penetration effect. The method delivering the best results is the second organization of waveforms according to their fall-times. Therefore, in section B.1 we describe this method, showing some practical results, while in section B.2 other methods are discussed.

B.1 Second organization of events based on fall-times

First, waveforms with similar durations are gathered, as described in section 5.3. Then, each group of waveforms resulting from the first organization method is also organized, but according to the waveform fall-time. The best results with this method were found when the fall-time is measured between 90 % and 50 % of each single waveform maximum height. In this way, most of the fluctuations produced by the PMT afterpulsing are excluded, remaining the fluctuations of interest, i.e. the ones related with the final electron cloud size. To reduce the signal noise, a large span moving average is done earlier for each single waveform.

After organizing the events according to their fall-times, the histogram of waveform integrals is computed (a different histogram per waveform duration interval and per fall-time interval). A Gaussian function is fitted to the full absorption's peak, and the distribution of centroids along the fall-times is obtained for each waveform duration interval. In figure B-1, we show an example of the centroid distribution obtained for three waveform duration intervals, corresponding to path lengths of 2.34, 2.18 and 2.10 cm (computed directly from the waveform durations, as demonstrated in figure 31). A 2-degree polynomial fit is performed to each centroid distribution, as illustrated in figure B-1. The fitting curve is then used to compensate each single waveform integral, according to the respective fall-time. This second correction is analogous to the first one, described in section 5.5.

The computation of the centroid distribution along the fall-time (figure B-1) is only possible when the number of events within each interval is large enough to fit a Gaussian function to the respective spectrum. Therefore, every time the working conditions or the acquisition times are changed, the waveform duration interval as well as the fall-time interval need to be adjusted accordingly. In figure B-1, those intervals are 120 ns and 6 ns, respectively (used here for demonstration proposes, the waveform duration interval is usually shorter). Naturally, this analysis reduces slightly the detection efficiency, because some fall-time intervals are rejected if the number of events is lower than 100.

In figure B-1, a consistent trend along the waveform fall-time is observed, thus reinforcing the hypothesis that this parameter is somehow correlated with the total number of collected EL photons. The energy of the events is on average higher for longer fall-times. To

understand this behavior let us recall the initial motivation of the second-order improvement of the energy resolution, waveforms having the same duration can be produced by slightly different x-ray penetrations (due to fluctuations on the photon burst duration). Therefore, waveforms with shorter fall-times were likely produced by deeper events, since the electron cloud was less affected by the longitudinal diffusion, despite all of the waveforms having the very same total duration. This logic may explain the results of figure B-1, validating the method here developed.

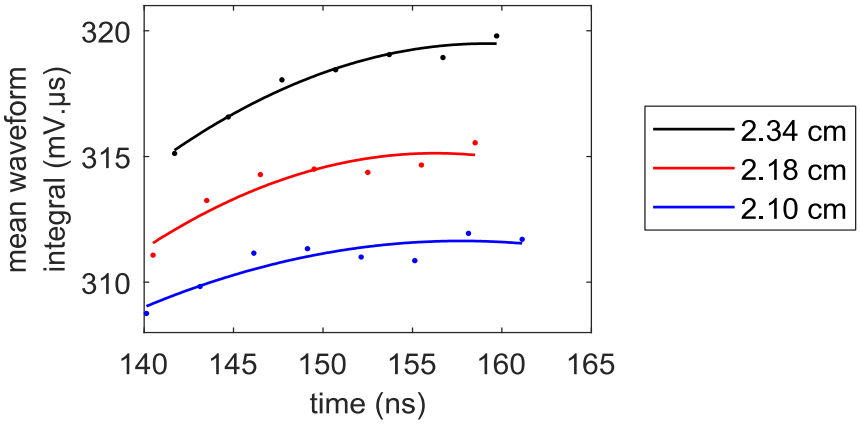

Figure B-1: Distribution of centroids along the waveform fall-time (from 90% to 50% of the waveform maximum height) for three waveform duration intervals, corresponding to mean path lengths of 2.34, 2.18 and 2.10 cm. The respective 2-degree polynomial fits are also shown.

The two-stage correction method can be summarized as follows. For each run, the distribution of centroids along the waveform duration is computed (figure 32). Then, within each duration interval, the distribution of centroids along the waveform fall-time is obtained (e.g. figure B-1). First, the integrals of the single waveforms are divided by the respective centroid of the duration distribution. Second, the waveform integrals within each duration interval are divided by the respective centroid of the fall-time distribution. Finally, the histogram of the two-fold corrected waveform integrals is computed, featuring an improved energy resolution.

This method has successfully improved the driftless GPSC energy resolution. For example, an improvement from (7.42 $\pm$ 0.04) % to (7.23 $\pm$ 0.06) % was observed for the 5.9 keV peak, which is significant given the low error of these measurements [8]. For the 14.3 keV and 21.4 keV Pu L-lines, ER value is improved from (4.59 $\pm$ 0.08) % and (4.23 $\pm$ 0.15) % to

[8] The uncertainties include the statistical uncertainties (68 % CL) of the fit parameters, as well as the systematic uncertainty introduced by the x-ray penetration correction methodology. This was estimated by changing several parameters, such as the interval width of the 1st and 2nd organization algorithms, the range of path lengths that are excluded from the analysis, or the minimum number of events required within each subcategory.

(4.49 ± 0.10) % and (3.87 ± 0.20) %, respectively. For the 22.2 keV and 24.9 keV Ag K-lines, an improvement from (3.82 +/ 0.04) % and (3.69 ± 0.15) % to (3.69 ± 0.12) % and (3.46 ± 0.25) % was obtained, respectively.

From these results, one concludes that the relative improvement on ER is better for higher energies. A possible explanation is the larger electron clouds produced at these energies, which may induce stronger fluctuations on the photon burst duration. Indeed, the expected radial profile of the electron cloud at 1 bar may be more than 400 μm for 25 keV [126].

When multi-energy radioactive sources are analyzed, only the tallest peak is used to compute both distributions of centroids. It is worth mentioning that the tallest peak from longer path lengths could be overtaken by more energetic peaks from shorter path lengths, due to the higher penetration. Therefore, the algorithm that automatically finds the tallest peak for the longest path length should take this into account, so that always the same peak is found for the full path length range.

The possibility of ER being artificially improved by this second order correction is unlikely, since the improvement is observed for every peak in a multi-energy spectrum, despite only the tallest peak being used to compute the distribution of correction factors.

B.2 Additional second-order correction methods

Different types of organization of the waveforms within each path length interval were used, for instance based on the rise time at the beginning of the waveform (from 1 % to 25 % of the waveform average height) or the rise time before the maximum height is reached (from 70 % to 95 % of the waveform maximum height). Both methods improved the energy resolution, probably because these parameters are also somehow correlated with the penetration of x-rays. Nevertheless, this relative improvement of ER is usually worst when compared to the method based on the waveform fall-time.

The x-ray penetration correction of the energy spectrum based on the whole waveform shape would be theoretically the best. In order to perform this kind of analysis, all the waveforms with a given shape within each duration interval were selected. In this way, the energy spectrum could be computed using solely the events that produced a “well-behaved” waveform. The standard shapes were computed from the mean waveforms for each duration interval (i.e. the standard waveforms represented in figure 28), since the probability to find waveforms with similar shapes is expected to be higher. These standard waveforms are modulated by a large degree polynomial function, to reduce the high frequency noise, and to speed up the fitting algorithm. Next, each single waveform is fitted by the standard shape corresponding to the same duration interval. Events whose R-squared is below a given threshold (usually about 0.999) are excluded. Finally, the corrected energy spectrum is built

using only the remaining events, after their energy being compensated by the respective durations.

The energy resolution obtained with this method seems to be better as higher the R-squared threshold is, although the detection efficiency is considerably reduced. Nonetheless, the relative improvement of ER is somewhat below the one achieved with the second-organization method based on waveform fall-times.

Appendix C: PMT single-photon statistics

In this appendix, the PMT single-photon response is obtained using both the direct and the standard method. The results from the two methods are compared and cross checked with the two photon statistics lines of figure 43.

C.1 Single-photon spectra with the direct and standard methods

Single photons were provided by the ambient light when the room was almost dark. Special attention is necessary to detect single photons using only an oscilloscope without any additional amplification stage connected to the PMT. The time division scale of the oscilloscope was set so that each recorded wave has about 50 ns before and after the light pulse. For these measurements the 50 Ω DC coupling of the oscilloscope was used, despite a higher resistance being advantageous to increase the signal amplitude. However, the reflection of the wave in the resistance (as the BNC cable impedance is 50 Ω) would produce a chain of pulses after the first one.

To avoid the noise triggering, a weighted moving average is previously performed. Then, the trigger threshold on the rising edge is set near zero, and several runs are made for slightly increasing thresholds. On the post-processing, the PMT pulses are integrated and the histogram of the integrals is plotted for each threshold. Above a given threshold, the single photon peak becomes distinguishable in the histogram, since noise triggering is reduced. We have found this threshold to be about 150 μV in our setup, which is in the order of magnitude of the oscilloscope baseline fluctuations.

If the trigger threshold is too high, the smaller pulses could be missed, despite they have been produced by photon detection. To check this possibility, the trigger threshold can be slightly decreased. The centroid corresponding to the single photon (in the histogram of integrals) should remain approximately the same, while the area below the background peak becomes larger with respect to the single photon one. Another useful test to know if photons are being correctly detected lays on the variation of the ambient light intensity. The single photon peak area in the histogram should change accordingly, but its centroid must remain about the same.

If the pulses recorded by the oscilloscope are simply integrated, the single-photon peak will be undistinguishable from the background due to the large fluctuations on the oscilloscope baseline. Data post-processing is then crucial. For each recorded pulse, a line is fitted to the signal baseline, excluding a fixed duration interval around the peak, usually between -15 ns and 20 ns. This offset is then subtracted to the full wave. Finally, the integral within the time duration of the pulse is computed (between -15 ns and 20 ns). This procedure is demonstrated in figure C-1.

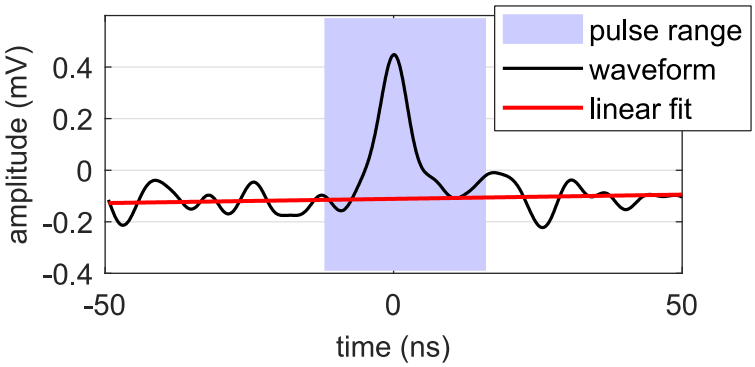

Figure C-1: Example of a PMT pulse (in black) likely produced by a single photon. The oscilloscope base line offset is obtained from the horizontal line (in red) that is fitted to the baseline, excluding the pulse region (area in blue). The pulse integral is computed between -15 ns and 20 ns (area in blue), after the fitted line is subtracted to the full wave.

In figure C-2 (a), the histogram of the pulse integrals obtained in single-photon counting mode with the direct method is shown. A sum of two Gaussian functions was fitted to data to account for the peak with centroid near zero, corresponding to background counts, and the rightmost peak, corresponding to electrons extracted from the photocathode. From the rightmost Gaussian, one may compute the PMT absolute gain (i.e. the conversion factor between A (in $mV \cdot \mu s$) and $\bar{N}_{pe}$), and the respective standard deviation. After performing several runs in similar working conditions, $\bar{G}$ and $\sigma_G/\bar{G}$ were found to be 3.32×10^{-3} mV µs and 0.37, respectively.

The PMT single-photon statistics was also obtained using the standard method, the resulting MCA pulse-height distribution being shown in figure C-2 (b). The linear amplifier shaping constant was set to the minimum, i.e. 500 ns. Therefore, there is a non-negligible probability of two consecutive photons being recorded within the same count, resulting in a second peak whose centroid is twice the single photon one. An additional Gaussian is included in the fit function to account for the double-photon peak (part of this Gaussian is shown in figure C-2 (b)). The fit function does not include the background, since its superposition with the single-photon peak is small. Thus, part of the left side of the single-photon peak was excluded from the fit, as shown in figure C-2 (b).

With the standard method (figure C-2 (b)), $\bar{G}$ and $\sigma_G/\bar{G}$ were found to be about 58.5 (normalized MCA channel) and 0.56, respectively, $\sigma_G/\bar{G}$ being considerably worst that the analogous result obtained with the direct method. This disagreement may result from the different integration intervals used by both methods, 35 ns around the PMT pulse in the direct method, against ~500 ns in the standard method. Consequently, additional fluctuations are integrated in the second case. For this reason, we believe that the $\sigma_G/\bar{G}$ value of 0.37 is a better approximation of the real PMT performance for single photons.

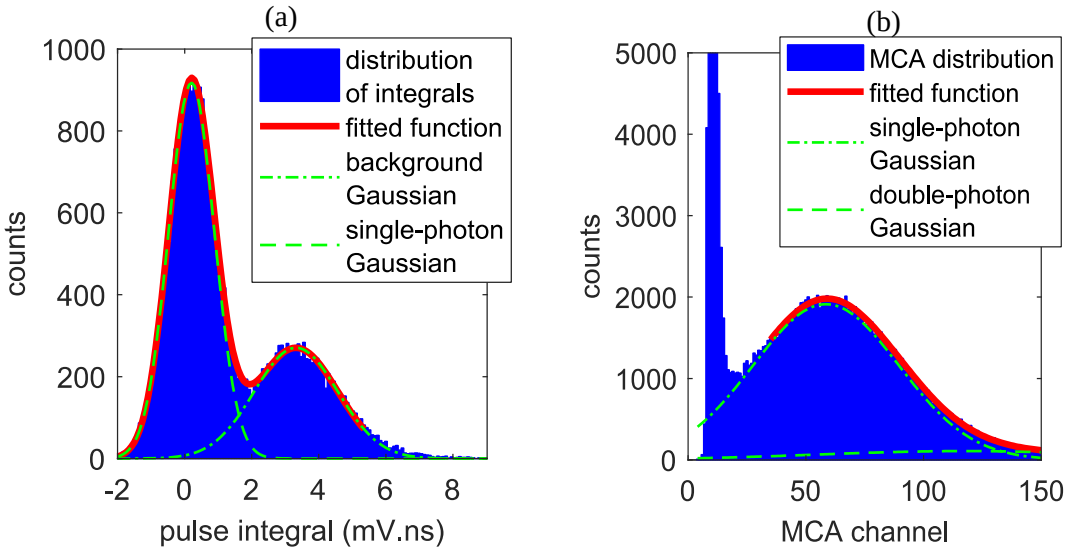

Figure C-2: In (a), the histogram of pulse integrals (blue bars) produced by the PMT in single-photon counting mode obtained with the direct method, together with a double-Gaussian fit (red curve) and the respective two Gaussian functions (green curves), corresponding to background and single-photon counts. In (b), the MCA pulse-height distribution (blue bars) produced by the PMT in single-photon counting mode obtained with the standard method, together with a double-Gaussian fit (red curve) and the respective two Gaussian functions (green curves), corresponding to single- and double-photon counts. In both plots, the PMT was polarized with 1400 V.

The single-photon distributions shown in figure C-2 can also be used to estimate the PMT photon statistics line, through equation (16), providing an independent alternative method to the one demonstrated in figure 43. Therefore, considering $\sigma_G/\bar{G}$ values of 0.37 and 0.56 obtained for the direct and standard methods, respectively, the straight line showing $R_{PMT}^2\left(1/\bar{N}_{pe}\right)$ would have a slope of ~6.3 and ~7.3, respectively. The mismatch between these values and the ones observed in figure 43 (9.3 (a) and 10.8 (b)) might be explained by the PMT strong afterpulsing, which leads to a underestimation of $1/\bar{N}_{pe}$ in figure 43 (a,b). Moreover, afterpulsing degrades further R_{PMT}, increasing even more the disagreement between the slopes of the experimental and expected lines (because these additional fluctuations are not considered in equation (16)).

C.2 Total number of photoelectrons

The absolute mean number of electrons extracted from the PMT photocathode ($\bar{N}_{pe}$) can be computed for any run, using the PMT gain obtained from figure C-2. To demonstrate this procedure, we predict $\bar{N}_{pe}$ produced during the detection of 5.9 keV x-rays, for an E/p value of 2.9 kV/cm/bar. Then we compare this result with the expected one, based on a rough estimation of the detector parameters.

From ref. [92], one can compute the number of EL photons produced in pure xenon per path length and per primary electron for a pressure of 1.24 bar, which is 360

$ph\ cm^{-1}\ electron^{-1}$. Therefore, the total number of EL photons produced in our detector after the electron cloud drifts 2.5 cm is 242 196 photons. Considering that the relative integrated solid angle to the PMT window is 30 %, the transparency of the vacuum-evaporated grid on the PMT window is 80 %, and the photocathode quantum efficiency is 25 %, an average of 14808 photoelectrons are expected to be released on average from the PMT photocathode. However, using the PMT gain from figure C-2, about 17 283 photoelectrons are estimated (for 5.9 keV x-rays and an E/p value of 2.9 kV/cm/bar) using the direct method, while 22 477 photoelectrons are estimated using the standard method.

One would expect that the real number of photoelectrons is lower than the predicted value, since an additional loss of EL photons may occur, for instance due to reflections on the PMT window. However, a significant number of photons could also be reflected on other parts of the detector, and then collected by the PMT. In an experimental study reported in [121], the total reflectivity of stainless steel and aluminum (stainless steel is the main building material of or detector, and aluminum is vacuum evaporated in the entrance window) to the xenon scintillation light was found to be 57 % and 70 %, respectively. Therefore, this effect seems to be a reasonable explanation for the observed discrepancy. Afterpulsing may also contribute to the larger measured N_{pe}, as part of the PMT signal is not produced by real photons. This hypothesis is also compatible with the lower N_{pe} found with the direct method when compared to the standard one, as the later integrates also the afterpulsing at the end of the waveforms.

Even if the aforementioned factors are not significant, at least for the direct method the 23 % relative difference between the measured N_{pe} and the predicted value is tolerable, due to the technical challenges to measure $\bar{G}$ with an oscilloscope (we estimate that $\bar{G}$ may have a relative error of 25 %). Moreover, the detector parameters used to predict N_{pe} from the reduced EL yield are rough estimations.

Appendix D: Simulation of the photon collection statistics

Several random numbers following an exponential distribution are generated, corresponding to the path lengths drifted by single electrons until they become attached, according to a given attachment coefficient η. Since the electric field is uniform, the rate at which the secondary scintillation photons are generated is constant. Therefore, the total number of EL photons produced per electron is given by the integration of the EL yield, along the path length drifted until the electron becomes attached or reach the anode. The EL yield must be weighted by the solid angle variation along the drift path (given by equation (11)).

In figure D-1, the histogram of the normalized total number of collected EL photons per electron obtained for a large number of runs is plotted for two situations: when the number of collected photons is constant along the electron path, and when it varies according to the solid angle. For all the runs, the electrons start at a fixed distance from the PMT, 2.28 cm (the same Δx considered in table 2), drifting along the axis, perpendicular to the circular PMT photocathode, whose radius is 2.4 cm.

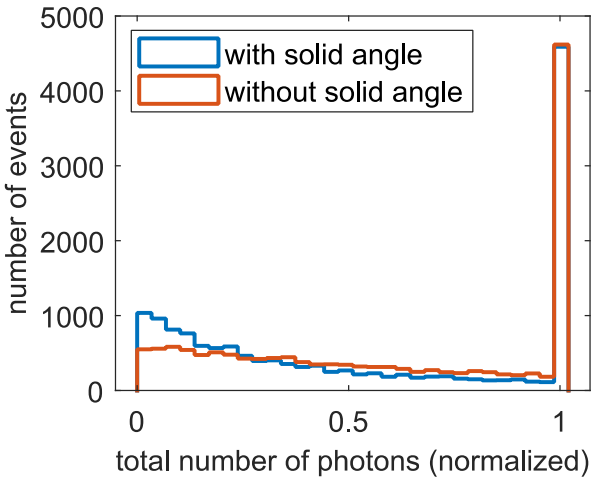

Figure D-1: Comparison between the distributions of the normalized total number of collected EL photons per electron obtained when the solid angle is considered (in blue) and ignored (in orange), obtained by simulation for $\Delta x = 2.28$ cm, $\eta = 0.52$ cm^{-1} and a PMT photocathode radius of 2.4 cm.

The peak on the right side of the two distributions represented in figure D-1 was produced by electrons that survived the full pathway until the anode ($\Delta x = 2.28$ cm), this value being normalized to unity for demonstration proposes. The several counts extending down to zero correspond to events where the electron became attached before reaching the anode. A clear difference between the two distributions is observed, confirming that the solid angle variation plays an essential role in the photon collection statistics. In the example of figure D-1, the mean number of collected photons per electron ($\overline{N}_{cp}$) considering and ignoring the solid angle variation is 0.52 and 0.59, with a standard deviation (σ_{cp}) of 0.39 and 0.36, respectively. Although these differences seem to be small, they have a considerable impact

on the Q factor ($Q = (\sigma_{EL}/\overline{N}_{EL})^2$), which is 0.55 and 0.38 considering and neglecting the solid angle variation, respectively.

Appendix E: The effect of electronics on the detector response

In this appendix, we discuss the effect of electronics (i.e. the pre-amplifier and the linear-amplifier) on the MCA pulse-height distribution, obtained with the standard method. The pre-amplifier and linear-amplifier outputs are modulated by software for the experimental standard waveforms obtained with pure Xe through the direct method. In this way, the electronics impact on the distribution of centroids of the several penetration Gaussians is accounted for, allowing a more accurate reproduction of the MCA pulse-height distributions.

E.1 Preamplifier

In order to understand the influence of the electronics chain on the detector response, the MCA pulse-height distribution was compared to the histogram of waveform integrals obtained with the direct method without any corrections. In theory, the shape of both distributions should be similar. However, for pure xenon, a larger penetration left-tail was observed in the direct method spectrum. This behavior is demonstrated in figure E-1 (a), where the linear-amplifier impact was minimized using a large shaping constant, of 12 µs.

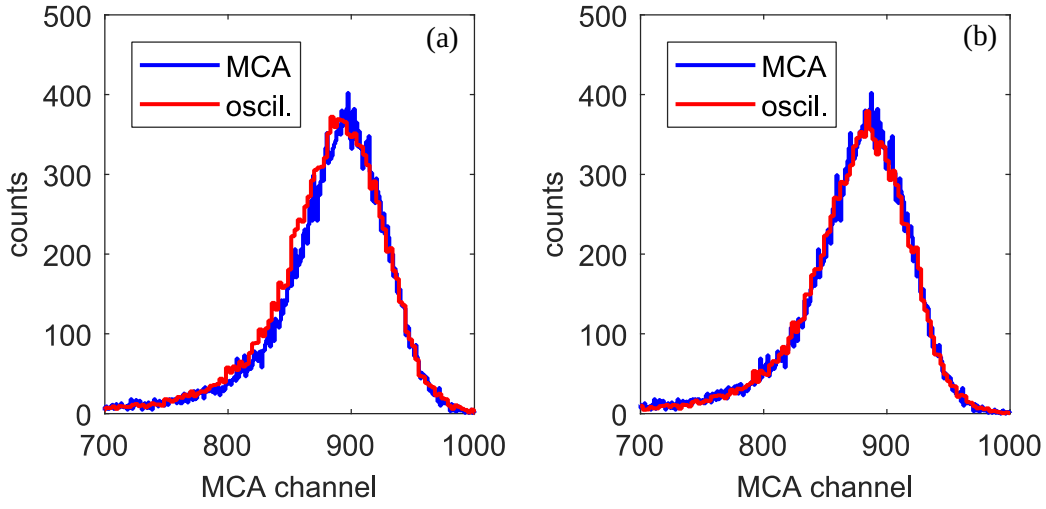

Figure E-1: Pulse-height distributions obtained with the standard method (in blue), and the analogous distributions obtained with the direct method (in red) using either the mathematical integration of waveforms (a) or the simulated preamplifier integration with a time constant of 50 µs (b). 5.9 keV x-rays were absorbed in pure xenon at 1.17 bar, for an E/p value of 2.4 kV/cm/bar. To minimize the linear-amplifier impact on the pulse-height distribution, a large shaping constant of 12 µs was used.

The different methods used to integrate the PMT signal are likely the source of the mismatch between the MCA pulse-height distribution and the histogram of waveform integrals. While our algorithm makes a pure mathematical integration of waveforms within their duration (avoiding part of the afterpulsing), the preamplifier stores the PMT charge in a capacitor, which is slowly discharging through a resistor. One may consider the voltage of the capacitor to be proportional to the charge collected in the preamplifier, since its capacitance is high enough for the current produced by the PMT. On the other hand, despite the

preamplifier decay time constant is 50 µs, i.e. about 10 times longer than waveform durations, it may still have a sizable impact on the energy spectrum.

When an event occurs, the voltage of preamplifier capacitor increases as the waveform is integrated, decreasing slowly at the same time due to the parallel resistor. The maximum voltage reached during this process is used to compute the energy of the event. Consequently, the energy of less penetrating x-rays is underestimated compared with to the energy of the deeper penetrating x-rays, since for the first case, the capacitor loses more charge through the resistor before the maximum voltage is reached. This effect known by *ballistic deficit* may affect any GPSC, being larger as longer the waveforms are with respect to the preamplifier decay time constant.

A numerical integration and differentiation of the PMT waveforms obtained with the direct method is performed to modulate this effect (with a decay time constant of 50 µs). An example of the preamplifier simulated output for an experimental waveform is shown in figure E-2, together with a full integration of the same waveform.

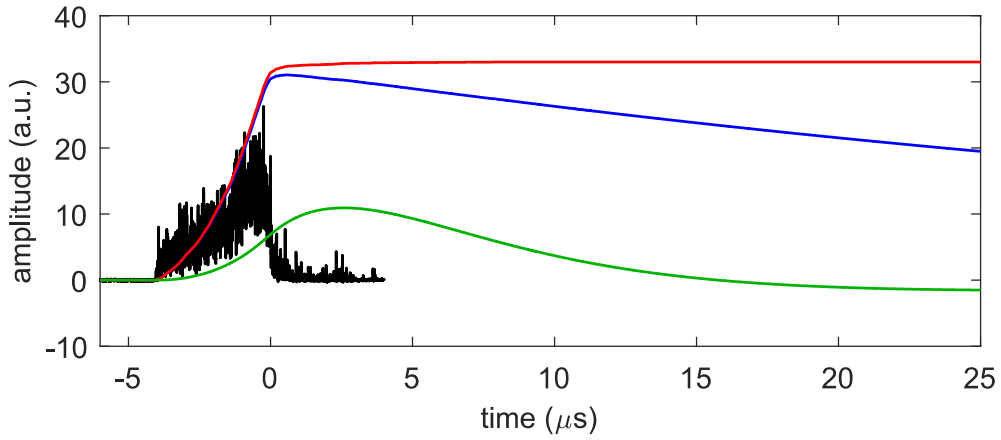

Figure E-2: Experimental waveform obtained with the direct method (in black), together with its full integration as a function of time (in red), and the modulated preamplifier integration for a time constant of 50 µs (in blue), which is then passed through a software-implemented linear-amplifier using a shaping constant of 4 µs (in green). The experimental waveform was obtained with 5.9 keV x-rays absorbed in pure xenon at 1.25 bar, for an E/p value of 2.23 kV/cm/bar.

In figure E-2, one may notice that the maximum height of the preamplifier output (blue) is below the full integration curve (red). This ballistic deficit was produced with a moderate electric field (2.23 kV/cm/bar), however, at lower electric fields, it is expected to be larger due to the longer waveform durations. The result obtained with the modulated preamplifier was compared with the signal measured at the output of the real preamplifier. A good agreement between data was found, thus, validating the simulation.

The ballistic deficit is not the major concern by itself. However, since it depends on the path length, the pulse-height distribution of the driftless GPSC becomes less left-tailed for low attachment mixtures, and even more right-tailed in the presence of high attachment. This

effect is demonstrated in figure E-1 (b), where the distribution of heights of the modulated pulses computed from the PMT waveforms is compared with the MCA pulse-height distribution obtained in the same conditions. The distribution obtained with the direct method using the modulated preamplifier integration has now a shorter left-tail, matching the distribution produced with the standard method.

E.2 Linear amplifier

The inclusion of the preamplifier effect on the energy spectra obtained with the direct method has shown to be insufficient to explain the observed pulse-height distributions obtained with the standard method, especially for low electric fields, high attachment mixtures and short linear-amplifier shaping constants.

In addition to the preamplifier ballistic deficit, a similar effect can be produced by the linear amplifier, when the duration of the waveforms is comparable to the shaping constant. In such cases, the integration of the initial part of the waveform contributes less to the height of pulse generated by the linear-amplifier, which is in turn recorded by the MCA. Thus, the pulse-height distribution relies mostly on the total number of photons produced during the last stages of the electron path. As before, in the absence of attachment, this effect leads to the decrease of the left-side tail of the energy spectrum. However, in the presence of high attachment, the right-tail may become significantly larger, since the number of electrons crossing the region near the PMT depends strongly on the x-ray penetration. This behaviour is demonstrated in figure E-3, where two experimental MCA pulse-height distributions produced by a Xe-CF_4 mixture (with a high CF_4 concentration of 0.066 %) are depicted, being obtained with two different linear-amplifier shaping constants, 12 μs and 2 μs.

As seen, when the linear amplifier shaping constant is short (2 μs) compared with the waveform duration (~ 4.3 μs, measured with the direct method), the pulse-height distribution has a longer tail on the right side, in contrast to the distribution obtained with a longer shaping constant (12 μs). For even shorter shaping constants (e.g. 50 ns as used in [116]), the pulses at the linear amplifier output becomes similar to the PMT waveforms rather than to the Gaussian function. Consequently, the energy spectrum accounts only for the waveform maximum heights. On the other hand, if the shaping constant is made much longer than the waveform duration, the linear amplifier distortion induced on the pulse-height distribution is negligible, even for high attachment mixtures.

The CO_2 campaign was carried out with a linear amplifier shaping constant of 4 μs. This fact, in combination with the CO_2 electron attachment resulted in a large distortion of those MCA acquisitions, for low electric fields. On the other hand, the runs with CH_4 and CF_4 were performed with a larger shaping constant, of 8 μs. Even so, this effect can still be observed

for the lowest E/p values and the highest CF_4 concentrations. Therefore, the linear amplifier must be also modulated in the improved version of the detector response function.

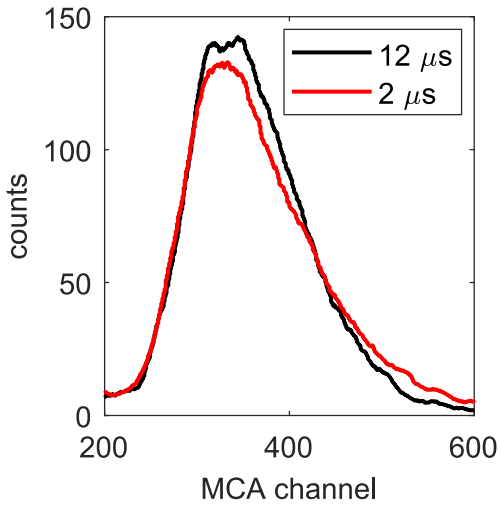

Figure E-3: Two experimental pulse-height distributions (smoothed) obtained with a linear amplifier shaping constant of 12 μs (black) and 2 μs (red). Data were obtained with 5.9 keV x-rays, absorbed in a Xe-CF_4 mixture with a CF_4 concentration of 0.066 %, at 1.22 bar, for a E/p value of 2.27 kV/cm/bar.

Due to the slow discharge of the preamplifier capacitor, upcoming x-ray detections would result in pile-up when the detection rate is high. Consequently, the heights of the preamplifier pulses would also depend on previous events. A capacitor-resistor (CR) differentiator (i.e. a high-pass filter) can be used to minimize this problem. However, the maximum heights of the differentiated pulses are held for a short time, making any subsequent MCA height analysis very sensitive to fluctuations. Moreover, the high-frequency noise may still pass through the CR filter. Therefore, a resistor-capacitor (RC) integrating stage (i.e. a low-pass filter) is usually placed after the CR differentiator to reduce these weaknesses. This combination of a differentiator and an integrator is commonly used in linear amplifiers, where the differentiator and integrator time constants ($\tau = RC$) are often made equal. Accordingly, the response of our linear amplifier can be modulated in approximation using the differential equations (26) and (27), which corresponds to the differentiation and integration stages, respectively.

$$V_o + \tau \frac{dV_o}{dt} = \tau \frac{dV_i}{dt} \tag{26}$$

$$V_o + \tau \frac{dV_o}{dt} = V_i \tag{27}$$

V_o and V_i are the output and input voltage signals, respectively. Since the pulse produced by the preamplifier (blue curve of figure E-2) cannot be approximated to a step-function, equations (26) and (27) are computed numerically for the modulated preamplifier output obtained for each PMT waveform.

An example of the simulated linear amplifier output for a given experimental waveform is demonstrated in figure E-2 (V_o being obtained from equations (26) and (27) for the modulated preamplifier signal, V_i, represented in the same figure), where a τ of 4 μs was used. The experimental pulses at the output of the real linear amplifier were compared with the modulated ones, for several shaping constants. An acceptable agreement was found, thus validating the simulation.

The standard waveforms obtained with pure xenon (e.g. figure 28 (b)) for the several path lengths can now be passed through the software-implemented preamplifier and linear-amplifier. The heights of the resulting pulses are then used to compute the centroid distribution of the several Gaussians, necessary to build the improved response function of the detector.

BIBLIOGRAPHY

[1] D. González-Díaz, F. Monrabal, and S. Murphy, "Gaseous and dual-phase time projection chambers for imaging rare processes," *Nucl. Instrum. Methods Phys. Res. A*, vol. 878, pp. 200–255, (2018).

[2] NEXT Collaboration, J. J. Gómez Cadenas, *et al.*, "Present Status and Future Perspectives of the NEXT Experiment," *Adv. High Energy Phys.*, vol. 2014, no. October 2013, pp. 1–22, (2014).

[3] X. Chen, C. Fu, *et al.*, "PandaX-III: Searching for neutrinoless double beta decay with high pressure 136Xe gas time projection chambers," *Sci. China Physics, Mech. Astron.*, vol. 60, no. 6, p. 061011, (2017).

[4] S. Pan, "AXEL: High pressure xenon gas Time Projection Chamber for neutrinoless double beta decay search," *J. Phys. Conf. Ser.*, vol. 718, no. 6, p. 062047, (2016).

[5] EXO Collaboration, J. B. Albert, *et al.*, "Search for Majorana neutrinos with the first two years of EXO-200 data," *Nature*, vol. 510, no. 7504, pp. 229–234, (2014).

[6] LUX Collaboration, D. S. Akerib, *et al.*, "Results from a Search for Dark Matter in the Complete LUX Exposure," *Phys. Rev. Lett.*, vol. 118, no. 2, p. 021303, (2017).

[7] PandaX-II Collaboration, A. Tan, *et al.*, "Dark Matter Results from First 98.7 Days of Data from the PandaX-II Experiment," *Phys. Rev. Lett.*, vol. 117, no. 12, p. 121303, (2016).

[8] F. J. Iguaz, J. G. Garza, *et al.*, "TREX-DM: a low background Micromegas-based TPC for low-mass WIMP detection," *J. Phys. Conf. Ser.*, vol. 718, p. 042026, (2016).

[9] XENON Collaboration, M. J. Xiao, *et al.*, "First dark matter search results from the PandaX-I experiment," *Science China: Physics, Mechanics and Astronomy*, vol. 57, no. 11. American Physical Society, pp. 2024–2030.

[10] E. Daw, J. R. Fox, *et al.*, "Spin-dependent limits from the DRIFT-IId directional dark matter detector," *Astropart. Phys.*, vol. 35, no. 7, pp. 397–401, (2012).

[11] D. Santos, J. Billard, *et al.*, "MIMAC : A micro-tpc matrix for dark matter directional detection," *J. Phys. Conf. Ser.*, vol. 460, no. 1, p. 012007, (2013).

[12] NEXT Collaboration, J. Martín-Albo, *et al.*, "Sensitivity of NEXT-100 to neutrinoless double beta decay," *JHEP*, vol. 2016, no. 5, p. 159, (2016).

[13] J. J. Gómez-Cadenas, J. Martín-Albo, M. Mezzetto, F. Monrabal, and M. Sorel, "The search for neutrinoless double beta decay," *Riv. del Nuovo Cim.*, vol. 35, no. 2, pp. 29–98, (2012).

[14] KamLAND-Zen Collaboration, A. Gando, *et al.*, "Search for Majorana Neutrinos Near the Inverted Mass Hierarchy Region with KamLAND-Zen," *Phys. Rev. Lett.*, vol. 117, no. 8, p. 082503, (2016).

[15] NEXT Collaboration, J. Renner, *et al.*, "Background rejection in NEXT using deep neural networks," *JINST*, vol. 12, no. 01, pp. T01004–T01004, (2017).

[16] C. D. R. Azevedo, L. M. P. Fernandes, *et al.*, "An homeopathic cure to pure Xenon large diffusion," *JINST*, vol. 11, no. 02, pp. C02007–C02007, (2016).

[17] J. Escada, T. Dias, P. Santos, M. Rachinhas, N. Conde, and D. Stauffer, "A Monte Carlo study of the fluctuations in Xe electroluminescence yield: Pure Xe vs Xe doped with CH4 or CF4 and planar vs cylindrical geometries," *JINST*, vol. 6, no. 8, pp. P08006–P08006, (2011).

[18] M. C. Gonzalez-Garcia and M. Maltoni, "Phenomenology with massive neutrinos," *Phys. Rep.*, vol. 460, no. 1, pp. 1–129, (2008).

[19] G. L. Fogli, E. Lisi, A. Marrone, A. Palazzo, and A. M. Rotunno, “Evidence of θ13>0 from global neutrino data analysis,” *Phys. Rev. D - Part. Fields, Gravit. Cosmol.*, vol. 84, no. 5, p. 053007, (2011).

[20] R. N. Mohapatra and G. Senjanović, “Neutrino Mass and Spontaneous Parity Nonconservation,” *Phys. Rev. Lett.*, vol. 44, no. 14, pp. 912–915, (1980).

[21] M. Fukugita and T. Yanagida, “Barygenesis without grand unification,” *Phys. Lett. B*, vol. 174, no. 1, pp. 45–47, (1986).

[22] M. Goeppert-Mayer, “Double Beta-Disintegration,” *Phys. Rev.*, vol. 48, no. 6, pp. 512–516, (1935).

[23] M. G. Inghram and J. H. Reynolds, “Double Beta-Decay of Te 130,” *Phys. Rev.*, vol. 78, no. 6, pp. 822–823, (1950).

[24] S. R. Elliott, A. A. Hahn, and M. K. Moe, “Direct evidence for two-neutrino double-beta decay in Se 82,” *Phys. Rev. Lett.*, vol. 59, no. 18, pp. 2020–2023, (1987).

[25] W. H. Furry, “On Transition Probabilities in Double Beta-Disintegration,” *Phys. Rev.*, vol. 56, no. 12, pp. 1184–1193, (1939).

[26] S. R. Elliott and P. Vogel, “Double Beta Decay,” *Annu. Rev. Nucl. Part. Sci.*, vol. 52, no. 1, pp. 115–151, (2002).

[27] A. Giuliani and A. Poves, “Neutrinoless Double-Beta Decay,” *Adv. High Energy Phys.*, vol. 2012, pp. 1–38, (2012).

[28] S. R. Elliott, “Recent Progress in Double Beta Decay,” *Mod. Phys. Lett. A*, vol. 27, no. 07, p. 1230009, (2012).

[29] W. Maneschg, “Review of neutrinoless double beta decay experiments: Present status and near future,” *Nucl. Part. Phys. Proc.*, vol. 260, pp. 188–193, (2015).

[30] I. Ostrovskiy and K. O’Sullivan, “Search for neutrinoless double beta decay,” *Mod. Phys. Lett. A*, vol. 31, no. 18, p. 1630017, (2016).

[31] O. Cremonesi, “Neutrinoless Double Beta Decay,” *J. Phys. Conf. Ser.*, vol. 718, no. 2, p. 022006, (2016).

[32] S. Dell’Oro, S. Marcocci, M. Viel, and F. Vissani, “Neutrinoless Double Beta Decay: 2015 Review,” *Adv. High Energy Phys.*, vol. 2016, pp. 1–37, (2016).

[33] J. D. Vergados, H. Ejiri, and F. Šimkovic, “Neutrinoless double beta decay and neutrino mass,” *Int. J. Mod. Phys. E*, vol. 25, no. 11, p. 1630007, (2016).

[34] J. Schechter and J. W. F. Valle, “Neutrinoless double-β decay in SU(2)×U(1) theories,” *Phys. Rev. D*, vol. 25, no. 11, pp. 2951–2954, (1982).

[35] S. M. Bilenky and C. Giunti, “Neutrinoless double-beta decay: A probe of physics beyond the Standard Model,” *Int. J. Mod. Phys. A*, vol. 30, no. 04n05, p. 1530001, (2015).

[36] E. Lisi, A. M. Rotunno, and F. Šimkovic, “Degeneracies of particle and nuclear physics uncertainties in neutrinoless ββ decay,” *Phys. Rev. D - Part. Fields, Gravit. Cosmol.*, vol. 92, no. 9, p. 093004, (2015).

[37] J. . Gómez-Cadenas, J. Martín-Albo, *et al.*, “Sense and sensitivity of double beta decay experiments,” *J. Cosmol. Astropart. Phys.*, vol. 2011, no. 06, pp. 007–007, (2011).

[38] KamLAND-Zen Collaboration, A. Gando, *et al.*, “Measurement of the double-β decay half-life of 136-Xe with the KamLAND-Zen experiment,” *Phys. Rev. C*, vol. 85, no. 4, p. 045504, (2012).

[39] EXO Collaboration, M. Auger, *et al.*, “The EXO-200 detector, part I: Detector design and construction,” *JINST*, vol. 7, no. 5, pp. P05010–P05010, (2012).

[40] GERDA Collaboration, M. Agostini, *et al.*, “Improved Limit on Neutrinoless Double-β Decay

of 76Ge from GERDA Phase II," *Phys. Rev. Lett.*, vol. 120, no. 13, p. 132503, (2018).

[41] Majorana Collaboration, C. E. Aalseth, *et al.*, "Search for Neutrinoless Double-β Decay in 76 Ge with the Majorana Demonstrator," *Phys. Rev. Lett.*, vol. 120, no. 13, p. 132502, (2018).

[42] CUORE Collaboration, C. Alduino, *et al.*, "First Results from CUORE: A Search for Lepton Number Violation via 0νββ Decay of 130Te," *Phys. Rev. Lett.*, vol. 120, no. 13, p. 132501, (2018).

[43] A. A. Klimenko and N. S. Rumyantseva, "Limits of Majorana neutrino mass from combined analysis of data from 76Ge and 136Xe neutrinoless double beta decay experiments," *Phys. Part. Nucl.*, vol. 48, no. 1, pp. 21–26, (2017).

[44] nEXO Collaboration, J. B. Albert, *et al.*, "Sensitivity and discovery potential of the proposed nEXO experiment to neutrinoless double-β decay," *Phys. Rev. C*, vol. 97, no. 6, p. 065503, (2018).

[45] S. Obara, "Status of balloon production for KamLAND-Zen 800 kg phase," *Nucl. Instrum. Methods Phys. Res. A*, vol. 845, pp. 410–413, (2017).

[46] S. Andringa, "SNO+ status and plans for double beta decay search and other neutrino studies," *J. Phys. Conf. Ser.*, vol. 665, no. 1, p. 012080, (2016).

[47] SuperNEMO Collaboration, A. S. Barabash, *et al.*, "Calorimeter development for the SuperNEMO double beta decay experiment," *Nucl. Instrum. Methods Phys. Res. A*, vol. 868, pp. 98–108, (2017).

[48] H. S. Jo, S. Choi, *et al.*, "Status of the AMoRE Experiment Searching for Neutrinoless Double Beta Decay Using Low-Temperature Detectors," *J. Low Temp. Phys.*, vol. 193, no. 5–6, pp. 1182–1189, (2018).

[49] D. R. Artusa, A. Balzoni, *et al.*, "The LUCIFER/CUPID-0 demonstrator: Searching for the neutrinoless double-beta decay with Zn82Se scintillating bolometers," *J. Phys. Conf. Ser.*, vol. 888, no. 1, p. 012077, (2017).

[50] NEXT Collaboration, V. Álvarez, *et al.*, "NEXT-100 Technical Design Report (TDR). Executive summary," *JINST*, vol. 7, no. 06, pp. T06001–T06001, (2012).

[51] NEXT Collaboration, A. Simón, *et al.*, "Electron drift properties in high pressure gaseous xenon," *JINST*, vol. 13, no. 07, pp. P07013–P07013, (2018).

[52] EXO Collaboration, J. B. Albert, *et al.*, "Improved measurement of the 2νββ half-life of 136 Xe with the EXO-200 detector," *Phys. Rev. C*, vol. 89, no. 1, p. 015502, (2014).

[53] D. Nygren, "Optimal detectors for WIMP and 0νββ searches: Identical high-pressure xenon gas TPCs?," *Nucl. Instrum. Methods Phys. Res. A*, vol. 581, no. 3, pp. 632–642, (2007).

[54] D. Nygren, "High-pressure xenon gas electroluminescent TPC for 0-ν ββ-decay search," *Nucl. Instrum. Methods Phys. Res. A*, vol. 603, no. 3, pp. 337–348, (2009).

[55] K. A. Olive, "Review of Particle Physics," *Chinese Phys. C*, vol. 38, no. 9, p. 090001, (2014).

[56] NEXT Collaboration, V. Álvarez, *et al.*, "The NEXT-100 experiment for neutrinoless double beta decay searches (Conceptual Design Report)," *http://arxiv.org/abs/1106.3630*, (2011).

[57] J. J. Gomez-Cadenas, "The NEXT experiment," *Nucl. Part. Phys. Proc.*, vol. 273–275, pp. 1732–1739, (2016).

[58] M. Nebot-Guinot, P. Ferrario, J. Martín-Albo, J. Muñoz Vidal, and J. J. Gómez-Cadenas, "Backgrounds and sensitivity of the NEXT double beta decay experiment," *Nucl. Part. Phys. Proc.*, vol. 273–275, pp. 2612–2614, (2016).

[59] NEXT Collaboration, T. Dafni, *et al.*, "Results of the material screening program of the NEXT experiment," *Nucl. Part. Phys. Proc.*, vol. 273–275, pp. 2666–2668, (2016).

[60] NEXT Collaboration, S. Cebrián, *et al.*, "Radiopurity assessment of the tracking readout for

the NEXT double beta decay experiment," *JINST*, vol. 10, no. 05, pp. P05006–P05006, (2015).

[61] NEXT Collaboration, S. Cebrián, *et al.*, "Radiopurity assessment of the energy readout for the NEXT double beta decay experiment," *JINST*, vol. 12, no. 08, pp. T08003–T08003, (2017).

[62] NEXT Collaboration, V. Álvarez, *et al.*, "Near-intrinsic energy resolution for 30-662keV gamma rays in a high pressure xenon electroluminescent TPC," *Nucl. Instrum. Methods Phys. Res. A*, vol. 708, pp. 101–114, (2013).

[63] NEXT Collaboration, D. Lorca, *et al.*, "Characterisation of NEXT-DEMO using xenon Kα X-rays," *JINST*, vol. 9, no. 10, pp. P10007–P10007, (2014).

[64] NEXT Collaboration, P. Ferrario, *et al.*, "First proof of topological signature in the high pressure xenon gas TPC with electroluminescence amplification for the NEXT experiment," *JHEP*, vol. 2016, no. 1, p. 104, (2016).

[65] NEXT Collaboration, V. Álvarez, *et al.*, "Operation and first results of the NEXT-DEMO prototype using a silicon photomultiplier tracking array," *JINST*, vol. 8, no. 09, pp. P09011–P09011, (2013).

[66] NEXT Collaboration, F. Monrabal, *et al.*, "The Next White (NEW) detector," *http://arxiv.org/abs/1804.02409*, (2018).

[67] NEXT Collaboration, J. Renner, *et al.*, "Initial results on energy resolution of the NEXT-White detector," *JINST*, vol. 13, no. 10, pp. P10020–P10020, (2018).

[68] NEXT Collaboration, A. D. McDonald, *et al.*, "Demonstration of Single-Barium-Ion Sensitivity for Neutrinoless Double-Beta Decay Using Single-Molecule Fluorescence Imaging," *Phys. Rev. Lett.*, vol. 120, no. 13, p. 132504, (2018).

[69] NEXT Collaboration, C. A. O. Henriques, *et al.*, "Secondary scintillation yield of xenon with sub-percent levels of CO2 additive for rare-event detection," *Phys. Lett. B*, vol. 773, pp. 663–671, (2017).

[70] NEXT Collaboration, C. D. R. Azevedo, *et al.*, "Microscopic simulation of xenon-based optical TPCs in the presence of molecular additives," *Nucl. Instrum. Methods Phys. Res. A*, vol. 877, pp. 157–172, (2018).

[71] NEXT Collaboration, C. A. O. Henriques, *et al.*, "Electroluminescence TPCs at the thermal diffusion limit," *JHEP (accepted) http://arxiv.org/abs/1806.05891*, (2018).

[72] NEXT Collaboration, R. Felkai, *et al.*, "Helium–Xenon mixtures to improve the topological signature in high pressure gas xenon TPCs," *Nucl. Instrum. Methods Phys. Res. A*, vol. 905, pp. 82–90, (2018).

[73] NEXT Collaboration, A. Simón, *et al.*, "Application and performance of an ML-EM algorithm in NEXT," *JINST*, vol. 12, no. 08, pp. P08009–P08009, (2017).

[74] V. Palladino and B. Sadoulet, "Application of classical theory of electrons in gases to drift proportional chambers," *Nucl. Instrum. Methods* , vol. 128, no. 2, pp. 323–335, (1975).

[75] L. Huxley and R. Crompton, "The diffusion and drift of electrons in gases," *http://cds.cern.ch/record/102745*, (1974).

[76] P. Segur, M. Yousfi, M. H. Kadri, and M. C. Bordage, "A survey of the numerical methods currently in use to describe the motion of an electron swarm in a weakly ionized gas," *Transp. Theory Stat. Phys.*, vol. 15, no. 6–7, pp. 705–757, (1986).

[77] R. . Robson, M. Hildebrandt, and B. Schmidt, "Electron transport theory in gases: must it be so difficult?," *Nucl. Instrum. Methods Phys. Res. A*, vol. 394, no. 1–2, pp. 74–86, (1997).

[78] Y. Tanaka, "Continuous Emission Spectra of Rare Gases in the Vacuum Ultraviolet Region," *J. Opt. Soc. Am.*, vol. 45, no. 9, p. 710, (1955).

[79] M. Suzuki and S. Kubota, "Mechanism of proportional scintillation in argon, krypton and xenon," *Nucl. Instrum. Methods* , vol. 164, no. 1, pp. 197–199, (1979).

[80] J. W. Keto, R. E. Gleason, and G. K. Walters, “Production mechanisms and radiative lifetimes of argon and xenon molecules emitting in the ultraviolet,” *Phys. Rev. Lett.*, vol. 33, no. 23, pp. 1365–1368, (1974).

[81] C. A. B. Oliveira, V. Gehman, A. Goldschmidt, D. Nygren, and J. Renner, “Measurements of Charge and Light in Pure High Pressure Xe towards the Study of Xe+TMA Mixtures with Dark Matter Directionality Sensitivity and Supra-intrinsic Energy Resolution for 0νββ Decay Searches,” *Phys. Procedia*, vol. 61, pp. 742–749, (2015).

[82] M. Suzuki, J. Ruan(Gen), and S. Kubota, “Time dependence of the recombination luminescence from high-pressure argon, krypton and xenon excited by alpha particles,” *Nucl. Instrum. Methods Phys. Res.*, vol. 192, no. 2–3, pp. 565–574, (1982).

[83] NEXT Collaboration, L. Serra, *et al.*, “An improved measurement of electron-ion recombination in high-pressure xenon gas,” *JINST*, vol. 10, no. 03, pp. P03025–P03025, (2015).

[84] F. L. R. Vinagre and C. A. N. Conde, “A technique for the absolute measurement of the W-value for X-rays in counting gases,” *Nucl. Instrum. Methods Phys. Res. A*, vol. 450, no. 2, pp. 365–372, (2000).

[85] S. J. C. do Carmo, F. I. G. M. Borges, F. L. R. Vinagre, and C. A. N. Conde, “Experimental Study of the w-Values and Fano Factors of Gaseous Xenon and Ar-Xe Mixtures for X-Rays,” *IEEE Trans. Nucl. Sci.*, vol. 55, no. 5, pp. 2637–2642, (2008).

[86] T. H. V. T. Dias, J. M. F. dos Santos, P. J. B. M. Rachinhas, F. P. Santos, C. A. N. Conde, and A. D. Stauffer, “Full-energy absorption of x-ray energies near the Xe L- and K-photoionization thresholds in xenon gas detectors: Simulation and experimental results,” *J. Appl. Phys.*, vol. 82, no. 6, pp. 2742–2753, (1997).

[87] L. M. P. Fernandes, E. D. C. Freitas, *et al.*, “Primary and secondary scintillation measurements in a Xenon Gas Proportional Scintillation Counter,” *JINST*, vol. 5, no. 09, pp. P09006–P09006, (2010).

[88] K. N. Pushkin, N. Hasebe, *et al.*, “A scintillation response and an ionization yield in pure xenon and mixtures of it with methane,” *Instruments Exp. Tech.*, vol. 49, no. 4, pp. 489–493, (2006).

[89] P. Lindblom and O. Solin, “Atomic near-infrared noble gas scintillations I: Optical spectra,” *Nucl. Instrum. Methods Phys. Res. A*, vol. 268, no. 1, pp. 204–208, (1988).

[90] C. A. B. Oliveira, H. Schindler, *et al.*, “A simulation toolkit for electroluminescence assessment in rare event experiments,” *Phys. Lett. B*, vol. 703, no. 3, pp. 217–222, (2011).

[91] F. P. Santos, T. H. V. T. Dias, A. D. Stauffer, and C. A. N. Conde, “Three-dimensional Monte Carlo calculation of the VUV electroluminescence and other electron transport parameters in xenon,” *J. Phys. D*, vol. 27, no. 1, pp. 42–48, (1994).

[92] C. M. B. Monteiro, L. M. P. Fernandes, *et al.*, “Secondary scintillation yield in pure xenon,” *JINST*, vol. 2, no. 05, pp. P05001–P05001, (2007).

[93] M. S. S. C. P. Leite, “Radioluminescence of rare gases,” *Port. Phys*, vol. 11, pp. 53–73, (1980).

[94] A. J. P. L. Policarpo, “Light production and gaseous detectors,” *Phys. Scr.*, vol. 23, no. 4, pp. 539–549, (1981).

[95] J. M. F. dos Santos, J. A. M. Lopes, *et al.*, “Development of portable gas proportional scintillation counters for x-ray spectrometry,” *X-Ray Spectrom.*, vol. 30, no. 6, pp. 373–381, (2001).

[96] C. A. B. Oliveira, M. Sorel, J. Martin-Albo, J. J. Gomez-Cadenas, A. L. Ferreira, and J. F. C. A. Veloso, “Energy resolution studies for NEXT,” *JINST*, vol. 6, no. 05, pp. P05007–P05007, (2011).

[97] E. D. C. Freitas, M. R. Jorge, L. M. P. Fernandes, and C. M. B. Monteiro, “R&D Studies on the influence of the addition of percentage quantities of CH4 to pure xenon,” *(NEXT internal*

report) http//next.ific.uv.es/next/talks.html#InternalReports, (2014).

[98] M. R. Jorge, "Experimental measurement of the electroluminescence yield of pure xenon and mixtures of xenon with percentage quantities of CH 4," *(Master degree thesis) University of Coimbra: http://hdl.handle.net/10316/28098*. .

[99] E. D. C. Freitas, R. D. P. Mano, L. M. P. Fernandes, and C. M. B. Monteiro, "Electroluminescence studies on the influence of percentage quantities of CO2 added to pure xenon," *(NEXT internal report) http//next.ific.uv.es/next/talks.html#InternalReports*, (2015).

[100] R. D. P. Mano, "Experimental measurement of the Electroluminescence Yield, Electron Drift Velocity and Intrinsic Energy Resolution for mixtures of Xenon with sub-percentage quantities of CO2 for the NEXT Experiment," *(Master degree thesis), University of Coimbra: http://hdl.handle.net/10316/29816*. .

[101] T. Takahashi, S. Himi, M. Suzuki, J. Ruan(Gen), and S. Kubota, "Emission spectra from Ar-Xe, Ar-Kr, Ar-N2, Ar-CH4, Ar-CO2 and Xe-N2 gas scintillation proportional counters," *Nucl. Instrum. Methods Phys. Res.*, vol. 205, no. 3, pp. 591–596, (1983).

[102] R. Veenhof, "Choosing a gas mixture for the ALICE TPC," *(ALICE internal note) http//web-docs.gsi.de/~jcastill/docs/REF04-Choosing_Veenhof.pdf*, (2003).

[103] L. G. Christophorou, D. L. McCorkle, D. V. Maxey, and J. G. Carter, "Fast gas mixtures for gas-filled particle detectors," *Nucl. Instrum. Methods* , vol. 163, no. 1, pp. 141–149, (1979).

[104] E. Morikawa, R. Reininger, P. Gürtler, V. Saile, and P. Laporte, "Argon, krypton, and xenon excimer luminescence: From the dilute gas to the condensed phase," *J. Chem. Phys.*, vol. 91, no. 3, pp. 1469–1477, (1989).

[105] C. A. N. Conde and A. J. P. L. Policarpo, "A gas proportional scintillation counter," *Nucl. Instrum. Methods* , vol. 53, pp. 7–12, (1967).

[106] E. D. C. Freitas, C. M. B. Monteiro, *et al.*, "Secondary scintillation yield in high-pressure xenon gas for neutrinoless double beta decay (0νββ) search," *Phys. Lett. B*, vol. 684, pp. 205–210, (2010).

[107] A. J. P. L. Policarpo, M. A. F. Alves, M. Salete, S. C. P. Leite, and M. C. M. dos Santos, "Detection of soft X-rays with a xenon proportional scintillation counter," *Nucl. Instrum. Methods* , vol. 118, no. 1, pp. 221–226, (1974).

[108] J. A. M. Lopes, J. M. F. dos Santos, R. E. Morgado, and C. A. N. Conde, "A xenon gas proportional scintillation counter with a UV-sensitive large-area avalanche photodiode," in *IEEE*, 2001, vol. 1, no. 3, p. 5/72-5/76.

[109] D. F. Anderson, T. T. Hamilton, W. H.-M. Ku, and R. Novick, "A large area, gas scintillation proportional counter," *Nucl. Instrum. Methods* , vol. 163, no. 1, pp. 125–134, (1979).

[110] J. M. F. Dos Santos, A. C. S. S. Bento, and C. A. N. Conde, "A simple, inexpensive gas proportional scintillation counter for x-ray fluorescence analysis," *X-Ray Spectrom.*, vol. 22, no. 4, pp. 328–331, (1993).

[111] A. Peacock, R. D. Andresen, E.-A. Leimann, A. E. Long, G. Manzo, and B. G. Taylor, "Performance characteristics of a gas scintillation spectrometer for X-ray astronomy," *Nucl. Instrum. Methods* , vol. 169, no. 3, pp. 613–625, (1980).

[112] F. M. Mao and J. Leck, "The quadrupole mass spectrometer in practical operation," *Vacuum*, vol. 37, no. 8–9, pp. 669–675, (1987).

[113] D. González-Díaz and C. D. R. Azevedo, *private communication*. .

[114] D. G. Simons and P. A. J. de Korte, "Soft X-ray energy resolution and background rejection in a driftless gas scintillation proportional counter," *Nucl. Instrum. Methods Phys. Res. A*, vol. 277, no. 2–3, pp. 642–656, (1989).

[115] P. C. P. S. Simões, J. M. F. Dos Santos, and C. A. N. Conde, "Driftless gas proportional

scintillation counter pulse analysis using digital processing techniques," *X-Ray Spectrom.*, vol. 30, no. 5, pp. 342–347, (2001).

[116] P. C. P. S. Simões, D. S. Covita, J. F. C. A. Veloso, J. M. F. dos Santos, and R. E. Morgado, "A new method for pulse analysis of driftless-gas proportional scintillation counters," *Nucl. Instrum. Methods Phys. Res. A*, vol. 505, no. 1, pp. 247–251, (2003).

[117] H. Inoue, K. Koyama, M. Matsuoka, T. Ohashi, Y. Tanaka, and H. Tsunemi, "Properties of gas scintillation proportional counters for soft X-rays," *Nucl. Instrum. Methods* , vol. 157, no. 2, pp. 295–300, (1978).

[118] D. G. Simons, P. A. J. de Korte, A. Peacock, and J. A. M. Bleeker, "Energy Resolution Limitations In A Gas Scintillation Proportional Counter," 1986, vol. 0597, p. 190.

[119] Y. Guan, "Photomultiplier Tubes in Biosensors," in *Methods in molecular biology (Clifton, N.J.)*, vol. 503, 2009, pp. 375–387.

[120] P. Millet, A. Birot, H. Brunet, J. Galy, B. Pons-Germain, and J. L. Teyssier, "Time resolved study of the UV and near UV continuums of xenon," *J. Chem. Phys.*, vol. 69, no. 1, pp. 92–97, (1978).

[121] S. Bricola, A. Menegolli, *et al.*, "Noble-gas liquid detectors: measurement of light diffusion and reflectivity on commonly adopted inner surface materials," *Nucl. Phys. B - Proc. Suppl.*, vol. 172, pp. 260–262, (2007).

[122] J. A. Bearden and A. F. Burr, "Reevaluation of X-Ray Atomic Energy Levels," *Rev. Mod. Phys.*, vol. 39, no. 1, pp. 125–142, (1967).

[123] R. D. Dewey, R. S. Mapes, and T. W. Reynolds, *Handbook of X-ray and Microprobe Data*. Pergamon Press, 1969.

[124] T. H. V. T. Dias, F. P. Santos, A. D. Stauffer, and C. A. N. Conde, "The Fano factor in gaseous xenon: a Monte Carlo calculation for X-rays in the 0.1 to 25 keV energy range," *Nucl. Instrum. Methods Phys. Res. A*, vol. 307, no. 2–3, pp. 341–346, (1991).

[125] G. C. Damián, *private communication*. .

[126] T. H. V. T. Dias, F. P. Santos, A. D. Stauffer, and C. A. N. Conde, "Monte Carlo simulation of x-ray absorption and electron drift in gaseous xenon," *Phys. Rev. A*, vol. 48, no. 4, pp. 2887–2902, (1993).

[127] A. Dobi, D. S. Leonard, *et al.*, "Study of a zirconium getter for purification of xenon gas," *Nucl. Instrum. Methods Phys. Res. A*, vol. 620, no. 2–3, pp. 594–598, (2010).

[128] C. D. R. Azevedo, *private communication*. .

[129] W. H. Parkinson, J. Rufus, and K. Yoshino, "Absolute absorption cross section measurements of CO2 in the wavelength region 163–200 nm and the temperature dependence," *Chem. Phys.*, vol. 290, no. 2–3, pp. 251–256, (2003).

[130] B. Rebel, C. Hall, *et al.*, "High voltage in noble liquids for high energy physics," *JINST*, vol. 9, no. 08, pp. T08004–T08004, (2014).

[131] T. H. V. T. Dias, F. P. Santos, and C. A. N. Conde, "The primary electron cloud in xenon for X-rays in the 0.1 to 10 keV range," *Nucl. Instrum. Methods Phys. Res. A*, vol. 310, no. 1–2, pp. 137–139, (1991).